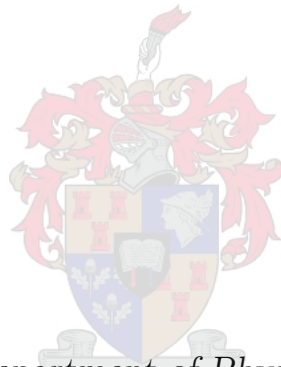


Spectroscopy of ^{22}Mg Relevant to Explosive Nucleosynthesis in Classical Novae and X-Ray Bursts

by

Johann Wiggert Brümmer

*Dissertation presented for the degree of Doctor of Natural Philosophy
in the Faculty of Science at Stellenbosch University*



*Department of Physics
Stellenbosch University
Private Bag X1, Matieland 7602, South Africa*

Supervisors:

Dr P. Adsley	Prof P. Papka	Dr F.D. Smit
University of the Witwatersrand	Department of Physics Stellenbosch University	iThemba Laboratory for Accelerator-Based Science

March 2020

Declaration

By submitting this dissertation electronically, I declare that the entirety of the work contained therein is my own, original work, that I am the sole author thereof (save to the extent explicitly otherwise stated), that reproduction and publication thereof by Stellenbosch University will not infringe any third party rights and that I have not previously in its entirety or in part submitted it for obtaining any qualification.

March 2020

Copyright © 2020 Stellenbosch University
All rights reserved.

Abstract

Spectroscopy of ^{22}Mg Relevant to Explosive Nucleosynthesis in Classical Novae and X-Ray Bursts

J.W. Brümmer

Department of Physics

Stellenbosch University

Private Bag X1, Matieland 7602, South Africa

Dissertation: PhD (Physics)

March 2020

This thesis discusses the spectroscopy of ^{22}Mg . This was done by performing the $^{24}\text{Mg}(p,t)^{22}\text{Mg}$ reaction at iThemba LABS using the K600 magnetic spectrometer in coincidence with the CAKE silicon-detector array. Using this experimental setup, resonances in ^{22}Mg were studied and proton decays from this nucleus to the ground state and excited states in ^{21}Na were detected with the CAKE.

The ^{22}Mg nucleus was studied for two different reasons. Firstly, it is the compound nucleus in the $^{18}\text{Ne}(\alpha,p)^{21}\text{Na}$ HCNO breakout reaction in X-ray bursts (XRBs). Secondly, the $^{24}\text{Mg}(p,t)^{22}\text{Mg}$ dataset also revealed that it is possible to use the excitation energy spectrum below the α -particle separation threshold, S_α , at 8.142 MeV to study the $^{21}\text{Na}(p,\gamma)^{22}\text{Mg}$ reaction.

The $^{18}\text{Ne}(\alpha,p)^{21}\text{Na}$ reaction is one of a number of crucially-important reactions that greatly influence the energy generation in XRBs. Therefore, it also affects the shape of the lightcurve considerably which is the only realistic observable of these events and only means to detect and study stellar XRBs.

Direct measurements of this reaction are challenging and, to date, many studies have performed a variety of different types of measurements to determine the thermonuclear reaction rate. In particular, one such study performed the time-reversed reaction. The data from that study were used and reevaluated in this thesis.

The resultant excitation energy spectrum from the $^{24}\text{Mg}(p,t)^{22}\text{Mg}$ experiment was analysed in two sections. Above S_α the spectrum was analysed in 100-keV bins up to an excitation energy of 13 MeV. The proton branching ratios B_{p_i} ($i \in [0, 4]$) were calculated for each bin. A moving-average function

was determined for the proton branching ratio to the ground state, B_{p_0} , to calculate the cross section as a function of energy, $\sigma(E)$, using cross section data from the previous study of this reaction. This was used to recalculate the thermonuclear reaction rate of $^{18}\text{Ne}(\alpha, p)^{21}\text{Na}$.

From this study it is concluded that the reaction rate varied by no more than a factor of 2.3 higher as compared to the average reaction rate from the previous study that performed the time-reversed reaction. The recalculated rate is in good agreement, within uncertainties, with another study that made an estimate of this rate by means of evaluating all pre-existing data. In that study, the reaction rate was determined by evaluation of the uncertainties from previous $^{18}\text{Ne}(\alpha, p)^{21}\text{Na}$ reaction-rate measurements and determining the regions where those uncertainties overlap. Results from this thesis were used with a stellar simulation code, MESA, to simulate the lightcurve of a particular XRB event. Clear changes to the lightcurve, due to the recalculated reaction rate, were apparent.

The $^{21}\text{Na}(p, \gamma)^{22}\text{Mg}$ thermonuclear reaction rate is linked to the production of ^{22}Na by means of β emission from the ^{22}Mg nucleus. The production of ^{22}Na plays an important role in the ability of astronomers to detect and study the astrophysical phenomenon of classical novae.

For the $^{21}\text{Na}(p, \gamma)^{22}\text{Mg}$ reaction the compound nucleus is also ^{22}Mg . The region of the excitation energy spectrum below S_α was resolved and as a result isolated, narrow resonances were studied. The resonance energies and widths were determined by fitting the spectrum using Gaussian and Voigt functions. The proton branching ratios were calculated and possible J^π assignments were discussed.

However, owing to the physical and electronic thresholds of the silicon-detector array, the protons from the decay of resonances in the astrophysically-relevant Gamow energy region were too low in energy to detect successfully. Therefore, it was not possible to use their branching ratios to calculate the thermonuclear reaction rate of $^{21}\text{Na}(p, \gamma)^{22}\text{Mg}$. To achieve this, subsequent experiments that aim to calculate this rate may need to use silicon detectors that can operate at lower thresholds. Alternatively, active-target detectors can be used as they have very low energy thresholds coupled with high detection efficiencies.

Uittreksel

Spektroskopie van ^{22}Mg Relevant tot Plofbare Kernsintese in Klassieke Novae en X-Straal Ontploffings.

J.W. Brümmer

Fisika Departement

Universiteit van Stellenbosch

Privaatsak X1, Matieland 7602, Suid-Afrika

Proefskrif: PhD (Fisika)

Maart 2020

Hierdie tesis bespreek die spektroskopie van ^{22}Mg . Dit is moontlik gemaak deur 'n eksperiment waarin die $^{24}\text{Mg}(p, t)^{22}\text{Mg}$ reaksie uitgevoer is by iThemba LABS met die K600 magnetiese spektrometer in voorwaartse hoeke en die CAKE silikondetektor opstelling gelyktydig in terugwaartse hoeke. Met hierdie eksperimentele opstelling was resonans toestande in ^{22}Mg bestudeer. Proton verval van hierdie kern na die grond toestand en verskeie opgewekte toestande in ^{21}Na was gevolglik opgespoor met die CAKE.

Die ^{22}Mg kern is bestudeer vir twee afsonderlike redes. Eerstens, dit is die saamgestelde kern in die $^{18}\text{Ne}(\alpha, p)^{21}\text{Na}$ HCNO wegbreek reaksie in X-straal ontploffings in sterre. Tweedens, data vanuit die $^{24}\text{Mg}(p, t)^{22}\text{Mg}$ eksperiment het aan die lig gebring dat dit moontlik is om die opwekkings-energie spektrum tot en met S_α te gebruik om die $^{21}\text{Na}(p, \gamma)^{22}\text{Mg}$ reaksie te bestudeer.

Die $^{18}\text{Ne}(\alpha, p)^{21}\text{Na}$ reaksie is een van 'n aantal hoogs-belangrike reaksies wat die energie produksie in hierdie astrofisiese ontploffings grootliks beïnvloed. Om hierdie rede beïnvloed die reaksie ook die vorm van die X-straal ontploffing ligkurwe aansienlik. Dit is die enigste prakties-waarneembare maatstaaf van hierdie gebeurtenisse en die enigste manier om hierdie soort ontploffings op te spoor en te bestudeer.

Direkte metings van hierdie reaksie is uitdagend and tot op hede het menigde vorige studies hierdie reaksie op verskillende wyse ondersoek om so-doende die reaksietempo te probeer meet. Een so 'n spesifieke studie het die tyd-omgekeerde reaksie uitgevoer. Die data van daardie studie is in hierdie tesis gebruik en herevalueer.

Die gevolglike opwekkings-energie spektrum van die $^{24}\text{Mg}(p, t)^{22}\text{Mg}$ reaksie is in twee afdelings geanaliseer. Bo die α -deeltjie verval drumpel, S_α , by

8.142 MeV is die spektrum in 100-keV energie gedeeltes geanaliseer tot by 'n opwekkings-energie van 13 MeV. Die proton vertakkings verhoudinge B_{p_i} ($i \in [0, 4]$) was vir elke 100-keV energie gedeelte bereken. 'n Bewegende-gemiddelde funksie is bepaal vir die proton vertakkings verhoudinge na die grond toestand, B_{p_0} , om die reaksiekansvlak as 'n funksie van energie, $\sigma(E)$, te bereken m.b.v. data vanuit 'n vorige studie van hierdie reaksie. Die kansvlak was gebruik om die nuwe reaksietempo van die $^{18}\text{Ne}(\alpha, p)^{21}\text{Na}$ reaksie te bereken.

Die reaksietempo wat gevolglik in hierdie tesis bereken is is hoogstens 2.3 maal groter as die reaksietempo wat bereken is deur die vorige studie wat die tyd-omgekeerde reaksie uitgevoer het. Die herberekende reaksietempo vergelyk baie goed, binne die onsekerheidsvlakke, met 'n vorige studie wat 'n skatting van hierdie reaksietempo uitgewerk het deur alle vorige data van hierdie reaksie te herevalueer. Die skatting is bepaal deur die mees waarskynlike oorvleueling van die onsekerhede van datapunte vir die $^{18}\text{Ne}(\alpha, p)^{21}\text{Na}$ reaksietempo te neem. Resultate vanuit hierdie tesis is gebruik in 'n astrofisiese simulasië program, MESA, om die ligkurwe van 'n spesifieke X-straal ontplofing gebeurtenis te simuleer. Duidelike verskille in die ligkurwe is opgemerk weens die verskille in die nuwe reaksietempo.

Die $^{21}\text{Na}(p, \gamma)^{22}\text{Mg}$ reaksietempo is gekoppel aan die produksie van ^{22}Na d.m.v. β verval van die ^{22}Mg kern. Die produksie van ^{22}Na speel 'n baie belangrike rol in die vermoë van sterrekundiges om die astrofisiese verskynsel van klassieke novae op te spoor en te bestudeer.

Die saamgestelde kern van die $^{21}\text{Na}(p, \gamma)^{22}\text{Mg}$ reaksie is ook ^{22}Mg . Die gedeelte van die opwekkings-energie spektrum tot en met S_α was opgelos vanweë die goeie eksperimentele resolusie. Dit was dus moontlik om die geïsoleerde, vernoude resonans toestande te bestudeer. Die resonans energieë en wydtes was bereken deur 'n passing te maak in die spektrum met Gaussian en Voigt funksies. Hierdeur was dit moontlik om die proton vertakkings verhoudinge te bereken en om moontlike J^π toekennings te bespreek.

Dit was egter nie moontlik om resonans toestande in die astrofisies-relevante Gamow-energie gebied suksesvol te verken nie omdat die toestande te laag in energie is. Dit is vanweë die fisiese en elektroniese drumpels in die silikon detektors. Dus kon hul proton vertakverhoudings nie gebruik word om die $^{21}\text{Na}(p, \gamma)^{22}\text{Mg}$ reaksietempo te bereken nie. Om hierdie probleem te oorkom in moontlike daaropvolgende eksperimente kan silikon detektors gebruik word wat by laer fisiese en elektroniese drumpels kan funksioneer. As 'n alternatief kan aktiewe-teiken detektors gebruik word omdat hierdie soort toerusting by baie lae-energie drumpels kan meet met 'n baie hoë doeltreffendheid.

Acknowledgements

With your permission the author will use the first-person personal pronoun for this section.

There have been many that have supported me and stood by my side, academically and personally, since I have started my studies. Firstly, I would like to thank the Department of Physics at Stellenbosch University. I am immensely proud to have been affiliated with the university and department. I also want to express my gratitude towards the National Research Foundation (NRF) for supporting this PhD financially through the PDP and Top-up grants and thank you to iThemba LABS that has been such a wonderful place to conduct my PhD research. The CAKE silicon-detector array used in this experiment was funded by the NRF through the NEP grant 86052.

I want to thank the entire K600 group, Dr Neveling, and all the members that have been part thereof over the years. A special thank you to Dr Smit who, along with being my iThemba LABS promoter, was also the administrator of my PDP grant which allowed me to complete this PhD. Thank you to the ever-enthusiastic Prof Papka who has been my promoter for my MSc and PhD.

To Dr Phil Adsley, thank you for the endless academic support and proposing the experiment that this thesis is based on. Not only have you been a great source of knowledge and wit but you have been a good friend. You always answered each and every question, email and message without fail and for that I am truly grateful.

A very special thank you to my lovely mother Lynette, sister Suné, my father Danie, and my wonderful dog Liefie that have been there for me from the very start. You have always been supportive of me. I love you more than words can describe.

Finally, to Helen: you have been my best friend when I needed it most. You have stood by my side since the beginning of this PhD and never once did you doubt in my ability to complete it. Our wonderful adventures together have brought happiness and meaning to my life. Thank you for everything you have done for me. And to my dearest Molly, Nyla and Lola that were always so jubilant every time I came home: you are synonymous with love, laughter and joy.

Dedication

For my beautiful family: Helen, Molly, Lola and Nyla.

Contents

Declaration	ii
Abstract	iii
Uittreksel	v
Acknowledgements	vii
Dedication	viii
Contents	ix
List of Figures	xii
List of Tables	xvi
1 Astrophysical Motivation	1
1.1 Introduction	1
1.2 Evolution of the stars	2
1.2.1 Protostars	3
1.2.2 The pp chains	3
1.2.3 The CNO cycles	4
1.2.4 The hot CNO cycles	6
1.2.5 The 3α process	6
1.3 Dying stars	8
1.3.1 Red giant formation	8
1.3.2 White dwarf formation	10
1.3.3 Supernovae and neutron star formation	10
1.4 Binary systems with compact objects	12
1.4.1 The Roche lobe	13
1.4.2 X-ray bursts	13
1.4.3 Breakout reactions and thermonuclear runaway	16
1.4.4 Classical novae	18
1.5 Calculation of the $^{18}\text{Ne}(\alpha, p)^{21}\text{Na}$ and $^{21}\text{Na}(p, \gamma)^{22}\text{Mg}$ Reaction Rates	19

1.5.1	Reaction rate of $^{18}\text{Ne}(\alpha, p)^{21}\text{Na}$ information from literature	20
1.6	The $^{24}\text{Mg}(p, t)^{22}\text{Mg}$ reaction	24
2	Theory	25
2.1	Introduction	25
2.2	Cross sections	25
2.3	Resonance properties	26
2.4	Thermonuclear reaction rates	27
2.4.1	Coulomb penetrability	29
2.4.2	The Gamow window	31
2.4.3	Resonances and reaction rates	31
2.5	Introduction to TALYS statistical models and Hauser-Feshbach Theory	33
2.6	Principle of detailed balance	34
2.7	Nuclear reaction theory	37
2.7.1	ℓ Values	37
2.7.2	Angular correlation functions	38
2.7.3	Spin-parity (J^π) assignments	39
3	Experimental Setup and Method	41
3.1	Introduction	41
3.2	iThemba LABS SSC facility and the K600 magnetic spectrometer	42
3.3	The K600 magnetic spectrometer	43
3.3.1	Dispersion matching	46
3.3.2	The small-angle mode scattering chamber	47
3.3.3	The VDC detection system	48
3.3.4	Scintillating detectors	52
3.4	The CAKE array	53
3.4.1	Properties of silicon detectors	57
3.4.2	GEANT4 simulations for the CAKE	59
3.4.3	Parameters for the CAKE during PR254	62
3.5	DAQ electronic module setup	64
3.5.1	The CAKE electronics	64
3.6	Target-ladder setup	69
4	Experimental Data Analysis	71
4.1	Introduction	71
4.2	The particle identification (PID) spectrum	72
4.3	Focal-plane calibration	74
4.4	Energy calibration	82
4.5	The CAKE calibration	85
4.6	Coincidence analysis	88
4.7	Excitation energy spectra fits	97

5	Analysis Results	106
5.1	Introduction	106
5.2	Yield corrections	107
5.3	Analysis of states below S_α	111
5.3.1	Coincidence fit results	111
5.3.2	Angular correlation spectra	112
5.3.3	ℓ -Value assignments	113
5.3.4	Angular correlation functions	116
5.3.5	Branching ratios of states below S_α	119
5.3.6	Spin-parity (J^π) assignments	120
5.4	Analysis of states above S_α	122
5.4.1	Singles and coincidence spectra	123
5.4.2	Spectra gated on p_i	125
5.4.3	Corrected angular correlation spectra	130
5.4.4	ℓ -Value per bin	131
5.4.5	Angular correlation functions	131
5.4.6	Branching ratios	134
6	Astrophysical Calculations and Impact	136
6.1	Introduction	136
6.2	Resonances below S_α	137
6.3	Reaction rate of Salter <i>et al.</i>	138
6.3.1	TALYS calculations of $^{18}\text{Ne}(\alpha, p)^{21}\text{Na}$	139
6.4	Recalculation of the Salter reaction rate	141
6.5	Calculation of reaction rates using B_{p_0}	145
6.6	MESA simulations	148
7	Conclusions	153
	Appendices	155
A	Monte Carlo Simulations for the CAKE	156
A.1	Running the simulation	156
A.2	Calculation of ring efficiencies for the CAKE	160
A.3	Efficiency uncertainties	161
B	Log-Normal Distributions	162
B.1	Definition and use	162
	List of References	166

List of Figures

1.1	The pp chains	4
1.2	The four CNO cycles	5
1.3	The four HCNO cycles	7
1.4	Hertzsprung-Russell diagram	9
1.5	Supernova 1994D	12
1.6	Illustration of a Roche-lobe around a binary star system	14
1.7	Scientific illustration of an X-ray burst	15
1.8	Breakout reaction pathway by $^{14}\text{O}(\alpha, p)^{17}\text{F}(p, \gamma)^{18}\text{Ne}(\alpha, p)^{21}\text{Na}$. . .	17
1.9	The first instance of XRB detection	18
1.10	The first image of a classical nova	19
1.11	Reaction rate of $^{18}\text{Ne}(\alpha, p)^{21}\text{Na}$ from Salter <i>et al.</i>	22
1.12	Comparison of reaction rate of $^{18}\text{Ne}(\alpha, p)^{21}\text{Na}$ from Matic and Mohr	23
2.1	The Gamow window	32
2.2	Level scheme for the population of states in ^{22}Mg from the HCNO breakout reaction	36
2.3	Level scheme for the population of states in ^{22}Mg	36
2.4	Inverse level scheme for the population of states in ^{22}Mg	37
2.5	The first four even Legendre polynomials	38
3.1	The iThemba LABS facility layout	42
3.2	Schematic representation of the K600 Magnetic Spectrometer	44
3.3	Photo of the beamstop position during (p, t) measurements	45
3.4	The SPEXCIT program interface	46
3.5	Schematic lateral dispersion	47
3.6	The beam-attenuation meshes	48
3.7	The small-angle mode scattering chamber inner design	49
3.8	Design of the VDC wire-plane detectors	50
3.9	Schematic top-view cross section of a VDC	50
3.10	Illustration of drift electrons under influence of guard-wire potentials	51
3.11	The scintillating detectors during the assembly phase	53
3.12	Diagram of the CAKE array in the scattering chamber	54
3.13	Upstream view of the CAKE array in the scattering chamber	55
3.14	Downstream view of the CAKE array in the scattering chamber	56

3.15	Illustration of the process of reverse biasing a silicon detector	58
3.16	Schematic diagram of an MMM-type detector in the CAKE	59
3.17	Simulated solid angle subtended by the CAKE rings	60
3.18	Simulated solid angle subtended by the CAKE sectors	61
3.19	Simulated upstream view of the CAKE	61
3.20	Simulated side view of the CAKE	62
3.21	DSSSD leakage current graph	63
3.22	DAQ configuration for experiment PR254	65
3.23	MMM detector cable	66
3.24	Mesytec modules used for the electronics setup of the CAKE	67
3.25	Diagram of electronics and cabling for the CAKE	68
3.26	Target-ladder setup for experiment PR254	70
4.1	Particle identification spectrum	73
4.2	The empty-frame spectrum	74
4.3	$X1_{pos}$ spectrum before calibration	75
4.4	Illustrative definition of θ_{SCAT}	75
4.5	θ_{FP} versus $X1_{pos}$ spectrum	76
4.6	θ_{FP} slope and offset as a function of X (mm)	76
4.7	θ_{FP} to θ_{SCAT} conversion parameters	77
4.8	θ_{SCAT} vs $X1_{pos}$ spectrum	78
4.9	Corrected θ_{SCAT} spectrum	79
4.10	Corrected $X1_{pos}$ spectrum	80
4.11	Wire-plane position plotted against trigger-event number	81
4.12	Corrected $X1_{pos}$ spectrum of all runs	82
4.13	Focal plane energy calibration	84
4.14	Excitation energy spectrum	85
4.15	The ^{228}Th decay chain	86
4.16	α -particle decay loci in the CAKE front-back coincidence calibration spectrum	87
4.17	α particles in the ^{228}Th decay chain	88
4.18	Polar diagram of all events in the CAKE	89
4.19	Ring hit pattern in the CAKE	90
4.20	Sector hit pattern in the CAKE	90
4.21	Separation-energy spectrum in the CAKE	91
4.22	Time spectrum of particle decays detected in the CAKE	92
4.23	Front-back coincidence events in the CAKE	93
4.24	Front-back coincidence events with energy gate in the CAKE	93
4.25	p-Side TDC channel number vs Time offset spectrum	94
4.26	CAKE vs K600 Coincidence spectrum	95
4.27	Coincidence spectrum gated on ring 7	96
4.28	Target attenuation as seen with the CAKE	96
4.29	Gaussian, Lorentzian and Voigt profiles comparison	98
4.30	Singles excitation energy spectrum with Voigt fit	99

4.31	Coincidence excitation energy spectrum with Voigt fit	99
4.32	Coincidence excitation energy spectrum gated on p_0 decay with fit .	100
4.33	Coincidence excitation energy spectrum gated on p_1 decay with fit .	100
4.34	Coincidence excitation energy spectrum with p_0 and p_1 spectra superimposed	101
4.35	Excitation energy spectrum gated on p_0 decay and CAKE rings 1 to 4 with fit	102
4.36	Excitation energy spectrum gated on p_0 decay and CAKE rings 5 to 8 with fit	102
4.37	Excitation energy spectrum gated on p_0 decay and CAKE rings 9 to 11 with fit	103
4.38	Excitation energy spectrum gated on p_0 decay and CAKE rings 12 to 15 with fit	103
4.39	Excitation energy spectrum gated on p_1 decay and CAKE rings 1 to 4 with fit	104
4.40	Excitation energy spectrum gated on p_1 decay and CAKE rings 5 to 8 with fit	104
4.41	Excitation energy spectrum gated on p_1 decay and CAKE rings 9 to 11 with fit	105
4.42	Excitation energy spectrum gated on p_1 decay and CAKE rings 12 to 15 with fit	105
5.1	Yield spectrum for the ADC channels corresponding to the CAKE rings	108
5.2	Yield spectrum for the ADC channels corresponding to the CAKE sectors	109
5.3	Corrected efficiencies of the rings of the CAKE	110
5.4	Corrected and uncorrected GEANT4 simulation results	111
5.5	Angular correlation spectrum from GEANT4 simulations	113
5.6	Corrected yield spectrum of the 6.767 MeV state (p_0 decay)	114
5.7	Corrected yield spectrum of the 7.218 MeV state (p_1 decay)	114
5.8	Legendre fit for the p_0 6.767-MeV state	115
5.9	Legendre fit for the p_1 7.218-MeV state	116
5.10	Full Legendre fit for the p_0 6.229-MeV state	117
5.11	Full Legendre fit for the p_0 6.875-MeV state	117
5.12	Angular correlation function for $\ell = 1$	118
5.13	Angular correlation function for $\ell = 2$	119
5.14	Coincidence spectrum indicating punch through limits of the CAKE and focal limits of the VDCs	124
5.15	Singles and coincidence spectrum with resonance labels	124
5.16	Higher order decay loci in the coincidence spectrum	126
5.17	Coincidence spectrum showing individual p_i decay loci	127
5.18	Excitation energy spectrum for states above S_α for p_0 decay	128
5.19	Excitation energy spectrum for states above S_α for p_1 decay	128

5.20	Excitation energy spectrum of states above S_α for p_1 decay gated on ring 9	129
5.21	Excitation energy spectrum of states above S_α for p_1 decay gated on ring 9 with grouped bins	129
5.22	Corrected angular distribution spectrum for p_0 bin 7	130
5.23	Corrected angular distribution spectrum for p_1 bin 7	131
5.24	Corrected angular distribution spectrum for p_0 bin 7 with Legendre fit	132
5.25	Corrected angular distribution spectrum for p_1 bin 7 with Legendre fit	132
5.26	Angular correlation function for p_0 bin 7	133
5.27	Angular correlation function for p_1 bin 7	134
5.28	B_{p_i} for states above S_α	135
5.29	B_{p_0} for states above S_α	135
6.1	Talys B_{p_0} calculation comparing α OMPs	139
6.2	Talys branching-ratio calculations using α OMP1	140
6.3	Talys B_{p_0} calculation with α OMP1	141
6.4	Cross section data for the $^{18}\text{Ne}(\alpha, p)^{21}\text{Na}$ reaction from Salter <i>et al.</i>	142
6.5	Gamow Window for $T_9 = 1.05$	143
6.6	Reproduction of $^{18}\text{Ne}(\alpha, p)^{21}\text{Na}$ reaction rates from Salter <i>et al.</i>	144
6.7	Difference between reaction-rate values from literature and reproduced in this study	144
6.8	Moving average function for $B_{p_0}(E)$	146
6.9	Reaction rates calculated with present data versus results from Salter <i>et al.</i>	147
6.10	Reaction rates calculated with present data, with upper and lower limits, versus values from literature	148
6.11	XRB lightcurve simulation using the default reaction rate	149
6.12	XRB lightcurve simulation using the Salter <i>et al.</i> reaction rate	151
6.13	XRB lightcurve simulation using reaction rate calculated in this thesis	151
6.14	XRB lightcurve simulation using upper-limit reaction rate calculated in this thesis	152
6.15	XRB lightcurve simulation using lower-limit reaction rate calculated in this thesis	152
A.1	Points of measurement to determine the CAKE arm distance	157
A.2	α particles simulated with the CAKE simulation package	159
B.1	Log-normal probability density function	163
B.2	Log-normal cumulative density function	165

List of Tables

1.1	The pp chains for nucleosynthesis	5
1.2	The CNO fusion cycles in stars	6
1.3	The HCNO fusion cycles	7
3.1	Detector threshold for the CAKE	63
4.1	Table of values for the linear lineshape component	78
4.2	Table of values for the quadratic lineshape component	79
4.3	Table of position and energies for energy calibration	83
4.4	Table of parameters for conversion from wire-plane position to excitation energy	84
4.5	Half-lives of elements in the ^{228}Th decay chain	87
5.1	Voigt and Gaussian fit parameters for states below S_α	112
5.2	ℓ value results for p_0 and p_1 resonances below S_α	116
5.3	Branching ratios for resonances below S_α	120
5.4	J^π possibilities for p_0 decay and different ℓ values	122
5.5	J^π possibilities for p_1 decay and different ℓ values	122
5.6	Table of states for the singles and coincidence spectrum above S_α	125
6.1	Gamow window for $^{21}\text{Na}(p, \gamma)^{22}\text{Mg}$ at $T_9 = 0.5, 0.75$ and 1.0	137

Chapter 1

Astrophysical Motivation

Your reward will be the
widening of the horizon as you
climb. And if you achieve that
reward, you will ask no other.

Cecilia Payne

1.1 Introduction

This thesis discusses the determination of the $^{18}\text{Ne}(\alpha, p)^{21}\text{Na}$ reaction rate which is one of three important nuclear reactions in the energy production of Type-I X-ray bursts (XRBs) [1, 2]. XRBs are characterised by sudden and large increases in X-ray flux that can last from a few seconds to hundreds of seconds. These phenomena were first observed in 1976 [3, 4]. In the same year, it was postulated [5] that their origin is the accretion of matter from a red giant companion star to a neutron star that leads to thermonuclear runaway on the surface of the neutron star.

As a result, it is now known that Type-I¹ XRBs are an astrophysical phenomenon in which hydrogen- and helium-rich material is accreted from a red giant star to a neutron star in a compact binary system. This results in thermonuclear runaway that causes periodic and distinct X-ray emissions. The X-ray flux is large enough to be detected by X-ray telescopes that orbit Earth as the atmosphere is opaque to them.

Due to the nature of the neutron star and its strong gravitational field, it is unlikely that XRBs contribute to observed galactic isotope abundances by ejecting matter during the burst [8]. The only realistic observable to study XRBs is the lightcurves of X-ray flux. This thesis will, therefore, reanalyse

¹Type-II XRBs also exist but are caused by a different mechanism. They occur due to instabilities in the accretion disk of neutron-star binary systems [6, 7]. These bursts are not caused by nuclear reactions and are not discussed further in this thesis.

the $^{18}\text{Ne}(\alpha, p)^{21}\text{Na}$ reaction rate and recalculate the lightcurves by means of a simulation to determine the effect of the rate re-evaluation.

This thesis will also discuss the determination of the $^{21}\text{Na}(p, \gamma)^{22}\text{Mg}$ reaction rate which is important during classical novae. These are transient astrophysical phenomena during which a sudden emission of light occurs. It is caused by a sequence of events during which hydrogen- and helium-rich material is accreted from a red giant star onto the surface of a white dwarf resulting in thermonuclear runaway.

To discuss the behaviour of XRBs the evolution of stars into a compact binary system will be discussed. This will include discussions on red giants, supernovae and neutron stars. White dwarfs and classical novae will also be discussed. The spectroscopy of ^{22}Mg above the proton-decay threshold, S_p , at 5.502 MeV has relevance to the reaction rate of $^{21}\text{Na}(p, \gamma)^{22}\text{Mg}$ as this is important in the production of ^{22}Na . Isotopic abundances of ^{22}Na are used to study the properties of classical novae as radiative proton capture reactions on ^{21}Na occur in these stellar explosions [9].

1.2 Evolution of the stars

The first stage of stellar evolution begins with the formation of protostars. During this formative period, the initial mass of the star is established. The star will then remain constant in size whilst it burns its hydrogen fuel by means of the pp chains, CNO cycles, and HCNO cycles until hydrogen is depleted and the next phase of its evolution starts. Protostars are discussed in Subsection 1.2.1 whilst the various stages of hydrogen burning are discussed in Subsections 1.2.2 to 1.2.5.

The final stages of stellar evolution depends greatly on the initial mass of a star. Stars with an initial mass $0.4M_{\odot} < M < 11M_{\odot}$ ($M_{\odot} = 1$ solar mass) become red giant stars near the end of their life. In this case the hydrogen in the core of the star has been consumed leaving a helium core. Hydrogen burning and eventually helium burning will then commence in a shell around the helium core which causes a drastic increase in the surface area of the star. The increase in surface area also results in a decrease in temperature resulting in the wavelength of the visible light emitted from the star to increase making it appear red. Red giant stars are discussed further in Subsection 1.3.1.

White dwarfs are formed by stars with $0.4M_{\odot} < M < 2M_{\odot}$. In this case a red giant star undergoes significant mass loss after it has gone through the phases of hydrogen and then helium burning. If helium burning is the final stage a carbon-oxygen (CO) white dwarf will remain. These stars still contain approximately half of the initial mass of the star but with much lower luminosities due to its small size. White dwarfs are discussed further in Subsection 1.3.2.

Stars heavier than $11M_{\odot}$ will end their life cycle through a supernova. At this point the hydrostatic equilibrium between the inward gravitational force and outward nuclear force can no longer be maintained. The result of a supernova can be a neutron star - a compact object supported by the neutron degeneracy pressure left as a remnant after the explosion. This will be discussed further in Subsection 1.3.3.

1.2.1 Protostars

Gravitational collapse of molecular cloud fragments, that contain mainly hydrogen with some helium, into very dense clumps form what is known as a protostellar core with a mass of up to $0.01M_{\odot}$. Additional accretion of surrounding gas and dust from the interstellar medium increases its mass and completes the process of protostar formation [10]. This is the first stage of stellar evolution. At this point the temperature is not high enough to initiate hydrogen burning or nucleosynthesis. Protostars are not detectable at visible wavelengths as they are concealed beneath gas and dust. Instead, infrared or microwave wavelengths are used to study these small, faint objects.

Gravitational potential energy that is liberated, owing to the contraction, causes the kinetic energy of the collapsing gas particles to rise and the volume over which the energy is spread to decrease. This causes the temperature of the protostar to rise. This initial stage can last for 10^5 to 10^7 years depending on the size of the star. For protostars with a mass of less than $0.08 M_{\odot}$ it is not possible to initiate hydrogen burning, leaving it shrouded in gas and dust [11]. This is called a brown dwarf.

However, if the mass of a protostar exceeds $0.08 M_{\odot}$ the temperature and density in the core will be sufficient to initiate deuterium burning ${}^2\text{H}(p, \gamma){}^3\text{He}$ and become a main sequence star. The resultant nuclear fueled force released will start to counteract the gravitational collapse. Once the star is massive enough, the density and temperature in the core of the star will have reached a point where the rate of nuclear fusion is large enough to produce a force that counterbalances the gravitational contraction. This is known as a hydrostatic equilibrium. Stars maintain this equilibrium as they burn protons to form ${}^4\text{He}$ in their cores by means of the pp chains or CNO cycles. The following sections will describe these various stages of hydrogen burning.

1.2.2 The pp chains

The proton-proton (pp) chains represent 3 reaction sequences which describe various ways in which the conversion of 4 protons proceeds to form ${}^4\text{He}$. From each such sequence, about 26 MeV is released. The pp chains are one of the simpler means of nucleosynthesis as they cannot make nuclei heavier than ${}^4\text{He}$. The reason for this is due to the absence of stable nuclei for masses $A = 5$ and $A = 8$. For stars with lower mass or stars without carbon, nitrogen,

or oxygen (CNO) catalytic nuclei, the pp chains represent the only means of nucleosynthesis. The reactions involved are slow. It takes longer for the star to exhaust its supply of hydrogen allowing it to burn for millions of years more than stars that can initiate the CNO cycles making it possible to form heavier nuclei. The pp chains are shown in Figure 1.1. Stable nuclei are shaded in grey, unbound nuclei in white and β^- emitters in pink. The reaction sequences are listed in Table 1.1 [12].

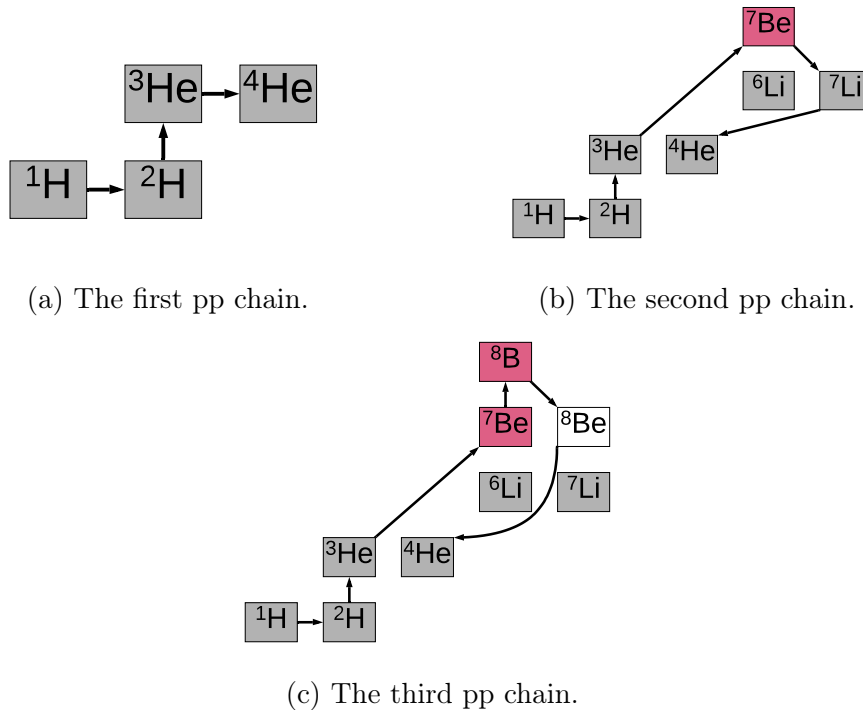


Figure 1.1: The pp chains. Stable nuclei are shaded in grey, unbound nuclei in white and β^- emitters in pink. In the second and third pp chains ${}^7\text{Be}$ is formed by the thermonuclear fusion of ${}^3\text{He}$ and ${}^4\text{He}$, the product of the first pp chain.

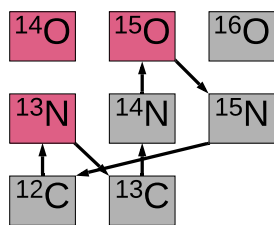
1.2.3 The CNO cycles

The CNO cycles fuse hydrogen into helium. When a star is formed there may be small isotopic abundances of ${}^{12}\text{C}$, ${}^{14}\text{N}$, ${}^{15}\text{N}$, and ${}^{16}\text{O}$ nuclei that were accreted from the interstellar medium. It is also possible for ${}^{12}\text{C}$ to have formed during the 3α fusion process which will be discussed later in this chapter. During nucleosynthesis these elements act as seed nuclei and are catalytic in the CNO processes. The CNO nuclei can undergo various proton captures and subsequent β emissions. At the end of each cycle α -particle emission occurs and the seed nuclei are regenerated. The four different CNO cycles

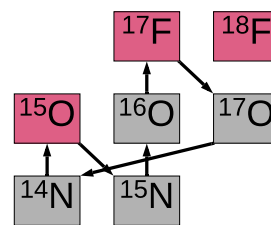
1 st pp chain	2 nd pp chain	3 rd pp chain
$p(p, \beta^+ \nu)d$	$p(p, \beta^+ \nu)d$	$p(p, \beta^+ \nu)d$
$d(p, \gamma)^3\text{He}$	$d(p, \gamma)^3\text{He}$	$d(p, \gamma)^3\text{He}$
$^3\text{He}(^3\text{He}, 2p)\alpha$	$^3\text{He}(\alpha, \gamma)^7\text{Be}$	$^3\text{He}(\alpha, \gamma)^7\text{Be}$
	$^7\text{Be}(\beta^-, \nu)^7\text{Li}$	$^7\text{Be}(p, \gamma)^8\text{B}$
	$^7\text{Li}(p, \alpha)\alpha$	$^8\text{B}(\beta^+ \nu)^8\text{Be}$
		$^8\text{Be}(\alpha)\alpha$

Table 1.1: The nuclear sequences in stars that form the pp chains in order to fuse hydrogen to helium.

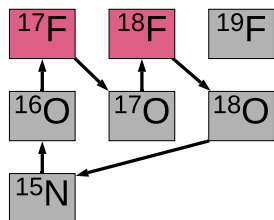
are shown in Figure 1.2 [12]. The reaction sequences are listed in Table 1.2. These reaction sequences are also referred to as the cold CNO cycles as they operate at temperatures of the order of 10 MK. The CNO cycles can operate as a network because of branching points like ^{15}N which can undergo proton capture and then either α emission $^{15}\text{N}(p, \alpha)^{12}\text{C}$ to end the first cycle or γ -ray emission $^{15}\text{N}(p, \gamma)^{16}\text{O}$ to start the third.



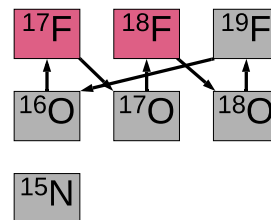
(a) The CNO1 cycle.



(b) The CNO2 cycle.



(c) The CNO3 cycle.



(d) The CNO4 cycle.

Figure 1.2: The four CNO cycles. The colour scheme is the same as for the pp chains.

1 st CNO cycle	2 nd CNO cycle	3 rd CNO cycle	4 th CNO cycle
$^{12}\text{C}(p, \gamma)^{13}\text{N}$	$^{14}\text{N}(p, \gamma)^{15}\text{O}$	$^{15}\text{N}(p, \gamma)^{16}\text{O}$	$^{16}\text{O}(p, \gamma)^{17}\text{F}$
$^{13}\text{N}(\beta^+\nu)^{13}\text{C}$	$^{15}\text{O}(\beta^+\nu)^{15}\text{N}$	$^{16}\text{O}(p, \gamma)^{17}\text{F}$	$^{17}\text{F}(\beta^+\nu)^{17}\text{O}$
$^{13}\text{C}(p, \gamma)^{14}\text{N}$	$^{15}\text{N}(p, \gamma)^{16}\text{O}$	$^{17}\text{F}(\beta^+\nu)^{17}\text{O}$	$^{17}\text{O}(p, \gamma)^{18}\text{F}$
$^{14}\text{N}(p, \gamma)^{15}\text{O}$	$^{16}\text{O}(p, \gamma)^{17}\text{F}$	$^{17}\text{O}(p, \gamma)^{18}\text{F}$	$^{18}\text{F}(\beta^+\nu)^{18}\text{O}$
$^{15}\text{O}(\beta^+\nu)^{15}\text{N}$	$^{17}\text{F}(\beta^+\nu)^{17}\text{O}$	$^{18}\text{F}(\beta^+\nu)^{18}\text{O}$	$^{18}\text{O}(p, \gamma)^{19}\text{F}$
$^{15}\text{N}(p, \alpha)^{12}\text{C}$	$^{17}\text{O}(p, \alpha)^{14}\text{N}$	$^{18}\text{O}(p, \alpha)^{15}\text{N}$	$^{19}\text{F}(p, \alpha)^{16}\text{O}$

Table 1.2: The CNO fusion cycles in stars.

1.2.4 The hot CNO cycles

As the name suggests, the hot CNO (HCNO) cycles operate at temperatures higher than the CNO cycles. For the HCNO cycles the temperature is of the order of $T > 100$ MK. The difference in temperature has an effect on the reaction rates. Proton capture reactions are no longer the limiting step. At these temperatures β decays become the limiting factor as they are temperature independent. The HCNO cycles, therefore, show no temperature dependence as opposed to the CNO cycles that strongly do so. Therefore, any explosive behaviour and resultant increase in energy output cannot be as a result of a temperature increase [13].

The HCNO cycles are shown in Figure 1.3. The reaction sequences are listed in Table 1.3. Nuclei such as ^{14}O , ^{15}O , and ^{18}Ne are waiting points in these cycles. Proton capture on these nuclei would proceed to the proton-unbound nuclei ^{15}F , ^{16}F , and ^{19}Na , respectively. Therefore, at lower temperatures β decay is the only possibility. The α capture reactions $^{14}\text{O}(\alpha, p)^{17}\text{F}$, $^{15}\text{O}(\alpha, \gamma)^{19}\text{Ne}$, and $^{18}\text{Ne}(\alpha, p)^{21}\text{Na}$ only become significant at higher temperatures. The latter two form the breakout reactions and are discussed later on in the text. Therefore, β decay from these nuclei is the only possibility in this context. They are the slowest steps which limit the HCNO reaction rates. The β -decay half-life of the ^{14}O , ^{15}O , and ^{18}Ne nuclei are $t_{1/2} = 70.6$ s, $t_{1/2} = 122.2$ s, and $t_{1/2} = 1.7$ s, respectively [14].

1.2.5 The 3α process

The pp chains are unable to synthesize elements heavier than helium. Therefore, a different reaction mechanism was needed to explain the formation of heavier nuclei. This is, of course, an important mechanism in stars as it allows for the eventual formation of life. The 3α process was proposed [15] in 1952 whereby a small equilibrium abundance of the unbound ^8Be nucleus is present

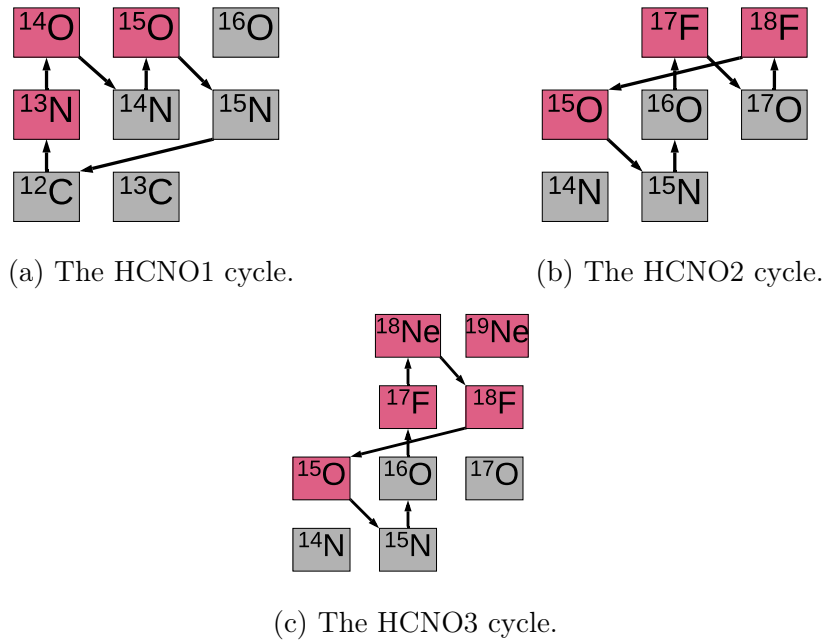


Figure 1.3: The four HCNO cycles. The terminating reactions are $^{15}\text{N}(p, \alpha)^{12}\text{C}$ for HCNO1 and $^{18}\text{F}(p, \alpha)^{15}\text{O}$ for HCNO2 and HCNO3.

1 st HCNO cycle	2 nd HCNO cycle	3 rd HCNO cycle
$^{12}\text{C}(p, \gamma)^{13}\text{N}$	$^{15}\text{O}(\beta^+ \nu)^{15}\text{N}$	$^{15}\text{O}(\beta^+ \nu)^{15}\text{N}$
$^{13}\text{N}(p, \gamma)^{14}\text{O}$	$^{15}\text{N}(p, \gamma)^{16}\text{O}$	$^{15}\text{N}(p, \gamma)^{16}\text{O}$
$^{14}\text{O}(\beta^+ \nu)^{14}\text{N}$	$^{16}\text{O}(p, \gamma)^{17}\text{F}$	$^{16}\text{O}(p, \gamma)^{17}\text{F}$
$^{14}\text{N}(p, \gamma)^{15}\text{O}$	$^{17}\text{F}(\beta^+ \nu)^{17}\text{O}$	$^{17}\text{F}(p, \gamma)^{18}\text{Ne}$
$^{15}\text{O}(\beta^+ \nu)^{15}\text{N}$	$^{17}\text{O}(p, \gamma)^{18}\text{F}$	$^{18}\text{Ne}(\beta^+ \nu)^{18}\text{F}$
$^{15}\text{N}(p, \alpha)^{12}\text{C}$	$^{18}\text{F}(p, \alpha)^{15}\text{O}$	$^{18}\text{F}(p, \alpha)^{15}\text{O}$

Table 1.3: The four HCNO cycles.

when two α particles collide in stars. A third α particle would then be able to collide with the ^8Be nucleus to form ^{12}C :



The negative Q value for the first reaction ($Q_{\alpha+\alpha \rightarrow ^8\text{Be}} = -92.1 \text{ keV}$) is the reason why ^8Be is unbound as it is unstable. The breakup is much faster than the fusion of two α particles. For this reason the 3α process is very

slow. However, Hoyle suggested in 1953 [16] that this process could only exist through means of a strong s -wave or d -wave resonance around 7 MeV in ^{12}C . The Hoyle state was subsequently discovered at 7.65 MeV [17, 18]. The Hoyle state is at a lower excitation energy relative to the $\alpha+^8\text{Be}$ system. It dominates the reaction rate at most temperatures.

1.3 Dying stars

After the formation of a protostar and the onset of hydrogen burning via the pp chains and CNO cycles, a star becomes part of the main sequence. However, as the hydrogen in the core of the star is consumed, the star will leave the main sequence and enter various stages depending on its initial mass. At this point, the star can become a red giant. As the red giant cycles through the various possible burning stages, it may end up either as a white dwarf or it may undergo a supernova explosion and become a neutron star.

Other outcomes for main-sequence stars are possible but will not be considered here as the XRBs discussed in this thesis only occur in binary systems with a red giant and a neutron star. Similarly, classical novae only occur in binary systems with a red giant and a white dwarf. Therefore, this section will expand on the formation and evolution of compact objects.

The different stars under discussion in this section can also be compared using a simplified Hertzsprung-Russell diagram shown in Figure 1.4 [19]. Each star is plotted on the diagram according to its temperature and luminosity - the total amount of radiation emitted per unit time. It is evident that most stars fall into one of several distinct groups. The correlation between stellar luminosity and temperature is the most important relationship of stellar properties used to study the stars.

Red giants (discussed in Subsection 1.3.1) do not form part of the main sequence stars as they are very luminous for their associated temperature. Contrarily, white dwarfs (discussed in Subsection 1.3.2) have much higher temperatures but lower luminosities. One reason for this is their small size (comparable to the Earth) whereas red giants can be multiple magnitudes larger than our Sun (which falls under the classification of main sequence stars under the spectral class G). The diagram is used for active stars. Neutron stars (discussed in Subsection 1.3.3) are remnants of stars. They have essentially no luminosity or visual magnitude and no spectral class and, therefore, do not form part of the diagram.

1.3.1 Red giant formation

The onset of red giant formation starts with the final stages of hydrogen burning in the core of stars with $0.4M_{\odot} < M < 11M_{\odot}$. Once the hydrogen in the core has been consumed, hydrogen burning will continue in an outer shell

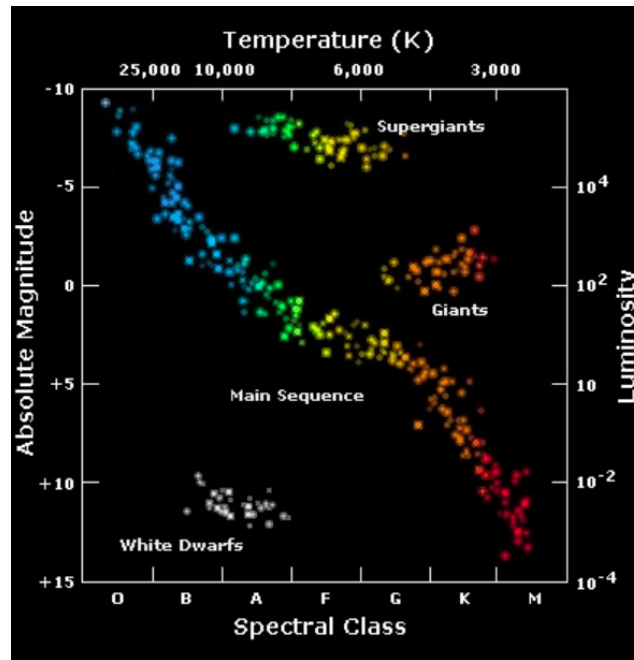


Figure 1.4: The Hertzsprung-Russell diagram. It compares the luminosity and temperature of various types of stars. This figure is taken from Ref. [19].

around the core. Without any burning regime in the core, it starts to contract under the influence of gravity. At this point, the energy source that kept the core in hydrostatic equilibrium, and resisted gravity, is absent. The core contraction causes the density to increase. As a result, the temperature in the hydrogen burning shell around the core also increases. This increases the rate of energy generation from hydrogen burning around the core. It creates an outward nuclear force causing the star to increase in size drastically due to the core contraction. As a result, the surface area of the star increases and the temperature decreases making the star become red. At this point the star has become a red giant.

The outer layers of the star is still rich in hydrogen and helium. Due to prolonged hydrogen burning in the core, it is now made up of mostly helium. The core will contract until it reaches an electron degenerate state - a point where the electrons start to resist the gravitational contraction as the nuclei are forced closer together. This degeneracy, described by the Pauli exclusion principle, may be lifted with the onset of helium burning in the core in a thermonuclear runaway event. Larger stars with $2M_{\odot} < M < 4M_{\odot}$ have enough mass to prevent an electron degenerate state as helium burning is ignited quiescently in the core. As the helium burning phase stops when the helium supply is exhausted, further and more complicated burning stages and dredge ups will begin in the star. During the dredge-up periods in the evolution of the star a convection zone from the inner regions of the star, where nuclear fusion has occurred, can extend outward to the surface. These materials and

fusion products are mixed convectively through the stellar envelope to form part of its atmosphere which can be seen in the spectrum of the star [12]. For lower mass stars like the Sun, the red giant will be transformed into a white dwarf. Depending on the initial mass, the smaller remnant star can either be a CO or ONe white dwarf. The mechanism whereby these stars are formed is discussed in the following section.

1.3.2 White dwarf formation

White dwarfs are the final stage of evolution for lower mass stars. A white dwarf is approximately as large as the Earth but has a mass roughly equivalent to M_{\odot} giving it a strong gravitational field. It is formed as the outer envelope of a red giant star is ejected into the interstellar medium. Eventually, the entire hydrogen envelope disappears as the hydrogen burning shell is extinguished. As a result, a rapid decrease in size and luminosity ensues. Gravitational contraction continues as hydrostatic equilibrium cannot be sustained without nuclear burning. The mass of these stars are high enough for it to contract to a point where the size is sustained only by the electron degeneracy pressure. The outer layers of the star are expelled to form a planetary nebula leaving a small, dense core. Henceforth the volume remains constant as the electron degeneracy resists further contraction. After their formation, white dwarfs exist for billions of years more whilst cooling slowly by radiating away thermal energy.

The maximum mass that a star can have where the hydrostatic equilibrium between the degeneracy pressure and gravitational contraction is sustained is called the Chandrasekhar limit. For white dwarfs this is $M \approx 1.41M_{\odot}$ caused by the electron degeneracy [12]. Sirius B is an example of a well-known white dwarf with its companion, Sirius A, that is the brightest star in the night sky. The Sun is an example of a star that will become a red giant. Towards the end of its evolution as it completes the hydrogen and then helium burning phases, it will turn into a white dwarf.

Different types of white dwarfs exist. One such type is a carbon-oxygen (CO) white dwarf. In this case, the initial mass of the star was too low to start carbon burning leaving behind a white dwarf comprised of the remnants of helium burning - carbon and oxygen. Certain stars can leave behind an oxygen-neon (ONe) white dwarf when the star is massive enough to make heavier α -conjugate nuclei.

1.3.3 Supernovae and neutron star formation

For stars with an initial mass $M > 11M_{\odot}$ helium burning is not the final thermonuclear stage. The evolution of these stars extend beyond that of the lower-mass red giants discussed in the previous sections. More massive stars will be able to ignite carbon, oxygen, neon, and silicon burning under the im-

mense pressure exerted by gravity. The thermonuclear processes will continue to burn the CNO nuclei until the iron-peak nuclei are reached and the core is made of mostly these materials. These nuclei have the highest binding energy per nucleon making it energetically unfavourable to continue fusion of heavier nuclei.

For higher-mass stars, the core is supported partially by the electron degeneracy pressure as was the case for red giant stars. However, the core is too massive to be fully supported [20]. Consequently, the core of the star will collapse further. Electron capture on iron-peak nuclei will result. This process is energetically favourable as the mass difference between protons and neutrons are lower than the electron degeneracy energy. This is an inverse β -decay process [21]. Due to this process the electrons fill up all available states so as to make neutron decay impossible: the electron formed during neutron decay will have no available state to occupy. The core of the star, therefore, continues to collapse until the magnitude of the nuclear density in the core becomes such that infalling matter bounces and creates an outward shockwave. The resultant shockwave is forceful enough to strip the star of its envelope and outer layers leaving a dense, compact neutron-star remnant behind supported by the neutron degeneracy pressure.

The typical mass of a neutron star is $1.5M_{\odot} < M < 2M_{\odot}$ with a radius of about 10 km [7]. The combination of these factors gives the star a very high mass density and consequently a very strong gravitational field. Over time, an isolated neutron star will slowly radiate its thermal energy and start to cool to the same temperature as the universe. As it rotates and radiates it also loses angular momentum. The star will gradually slow down and eventually become a completely inert, dark, and undetectable object.

The expulsion of matter from a supernova into the interstellar medium is thought to be a source of element synthesis in the galaxy [12]. It has been suggested in literature that supernovae produce a neutron flux great enough to support the r-process during the brief and powerful explosion. The sheer amount of energy produced during a supernova event creates so much light that it rivals the brightness of the entire galaxy which it is part of. Figure 1.5 shows supernova 1994D (the fourth supernova discovered in 1994 by the Hubble space telescope) and the immense luminosity from the event. More recently, neutron star mergers have been discovered to be a better candidate to support the r-process [22].



Figure 1.5: Supernova 1994D (bottom left) as seen by the Hubble space telescope [23].

1.4 Binary systems with compact objects

Binary star systems are a very common occurrence in space where two stars orbit each other with a distinct orbital period and distance between the two. Isolated stars like the Sun are far less common². Two different types of compact binary systems will be discussed in this chapter. The first is a red giant and neutron star binary in which XRBs can occur. The second type is a red giant and white dwarf binary that can give rise to classical novae. Apart from these events, binary stars are studied extensively as they offer the most reliable way to study stellar mass. As has been established in this chapter, the mass of a star is critical to its evolution and ultimate end. Using Newtonian mechanics, the gravitational effect that one star has on another can be calculated. The period of the orbit and the distance between the stars can be derived using telescopes. The mass of a star is then determined by taking all of these factors into consideration [7].

The sections that follow will discuss some of the most important aspects of compact binaries which can lead either to XRBs or to classical novae. The

²Binary systems are thought to make up 85% of all stars where some stars are in triple or even higher-multiple systems [24].

Roche lobe will be discussed along with thermonuclear runaway and HCNO breakout reactions. XRBs and classical novae will also be discussed.

1.4.1 The Roche lobe

The Roche lobe is a hypothetical surface boundary surrounding stars that marks the gravitational domain of the binary system. Within the tear-drop shape of the lobe, material will be bound to the star by its gravity. However, if matter is able to move out of this region one of three possible outcomes can occur. The matter can either leave the binary system entirely given enough velocity or it can orbit the binary system or it can fall into the smaller neutron star and accrete onto the surface. Each of these possibilities is, of course, dependent on the initial location, energy, and momentum of the particles. These scenarios occur more often in close binaries that orbit within a few radii of each other or that may even share a common envelope. This is called a contact binary.

Red giant stars form part of both the XRB and classical novae binaries. The reason is that the star is large enough for loosely bound hydrogen- and helium rich material from its atmosphere to move out of the Roche lobe. Another reason is due to the expansion of the red giant: the mass of the star is concentrated at the core. The expansion of the outer surface area implies that the gravitational influence experienced by the atmospheric hydrogen and helium is smaller.

Figure 1.6 shows two scenarios involving a binary system. In the first, the star is completely contained within the Roche lobe. In the second scenario, the outer atmosphere of a larger, companion star can accrete onto the neutron star as the loosely bound hydrogen and helium feels a greater gravitational attraction from the smaller neutron star. The momentum of the particles during this accretion phase often gives rise to an accretion disk. The overflow from the Roche lobe occurs at the inner Lagrangian point where the gravity and rotation of the two stars cancel and the two Roche lobes touch. These events lead to various astrophysical phenomena such as novae, Type Ia supernovae, and X-ray binaries [12].

1.4.2 X-ray bursts

XRBs occur in compact stellar binary systems that contain a neutron star and a red giant star. Both of these stars and their formation have been discussed earlier. The red giants are very large stars with loosely-bound hydrogen- and helium-rich outer layers that are able to approach the inner Lagrangian point of the Roche lobe. For close binaries where the neutron star is in relative close proximity, the strong gravitational field will begin to funnel matter from the red giant onto the neutron-star surface.

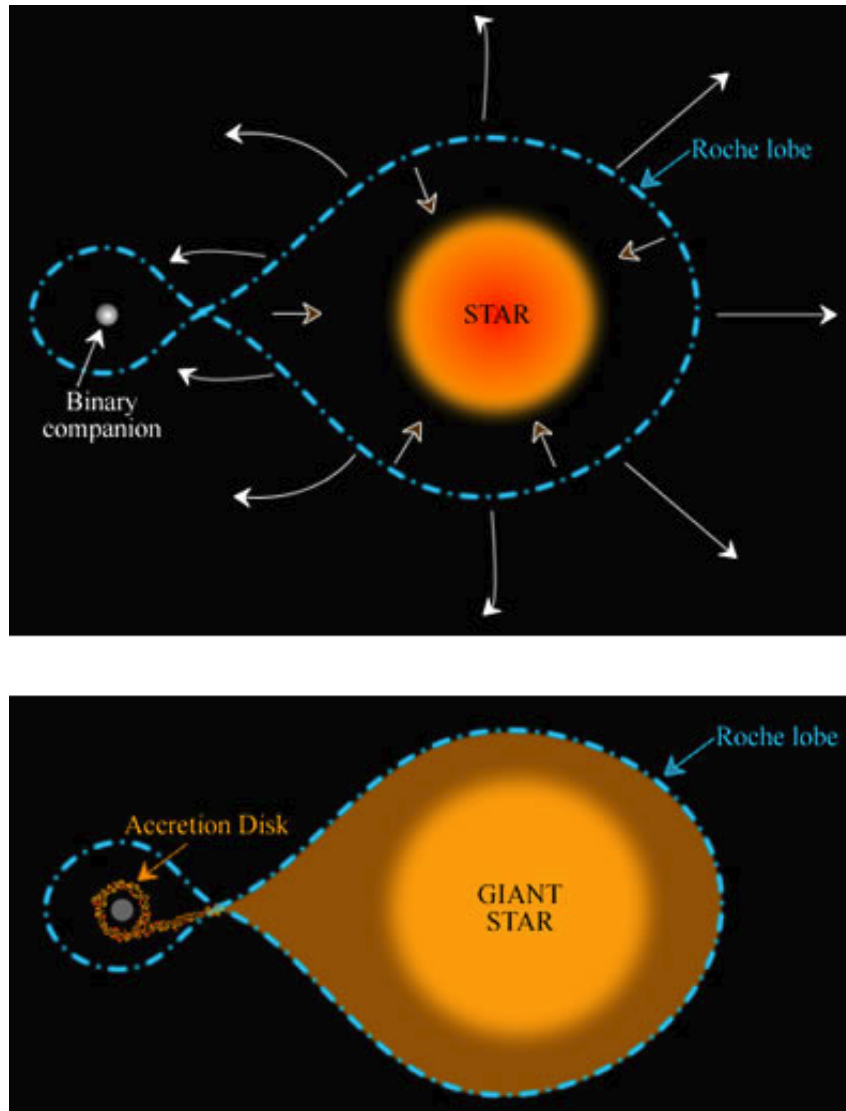


Figure 1.6: An illustration of a Roche-lobe around a binary star system [25].

After formation, certain neutron stars may spin at a rate of 200 rotations per second - much faster than typical neutron stars [7]. Due to this the star becomes highly magnetised (known as a magnetar) as a dynamo effect is created helping to establish a much stronger magnetic field. In these cases, the material from the red giant will be channelled along the magnetic field lines. This gives a constant X-ray flux seen as hotspots at certain points on the surface of the neutron star. During the XRB light is emitted constantly. However, it is observed as a pulsar because the rotation of the neutron star may obscure parts of the lightcurve periodically as the hotspot where the XRB takes place rotates with the neutron star.

Neutron stars that are not highly magnetised will rather form an accretion disk of material from the red giant. From this disk, matter slowly accretes onto the surface of the star. This also gives a constant X-ray flux but no hotspots are observed as the emission proceeds isotropically as shown in Figure 1.7. It shows a conceptual illustration of what an XRB would look like if the X-ray part of the electromagnetic spectrum was also visible. The infalling hydrogen- and helium-rich matter creates an electron-degenerate atmosphere on the surface of the neutron star. The surface temperature begins to rise as thermonuclear reactions in the atmosphere commence. Eventually, the temperature and, therefore, the reaction rates become high enough for thermonuclear runaway to occur. The mechanisms by which XRBs occur are discussed in the following section.



Figure 1.7: A conceptual illustration of an X-ray burst [26].

1.4.3 Breakout reactions and thermonuclear runaway

This section will discuss the reaction sequences leading up to and following an XRB. Hydrogen- and helium-rich matter accreted onto compact objects such as a neutron star ignites hydrogen burning on the surface of the star due to its strong gravitational field. Accretion of additional matter may lead to the onset of thermonuclear runaway on the surface of the neutron star. Three distinct phases exist during an XRB. The first stage is the onset of the CNO cycles in the atmosphere of the neutron star that starts energy production by means of the thermonuclear fusion reactions. The second stage is the breakout reactions from the HCNO cycles that greatly increases the energy generation. The third stage is a series of proton-capture reactions that uses the hydrogen available in the burst [21].

In the pre-burst burning phase, the accreted material forms an electron degenerate atmosphere. The density and temperature of the atmosphere rises to a point where the CNO cycles are initiated. The energy generated causes the density and temperature of the atmosphere to increase. However, as the atmosphere is electron degenerate the typical mechanism of thermal expansion and cooling is not possible. This would typically have limited the thermonuclear reaction rate as it is temperature dependent. As the pre-burst phase depends on the CNO cycles, it can also be affected by the isotopic abundances of the material accreted from the red giant and whether it is rich in CNO seed nuclei. Typically, about 75% of the abundance is composed of ^1H with the rest being ^4He and small amounts of the waiting-point nuclei ^{14}O and ^{15}O [21].

The material from the red giant may not be rich in CNO seed nuclei. However, the atmospheric densities and temperatures at this point in the neutron star is sufficient to ignite the 3α process to produce ^{12}C . The energy generation is, therefore, dependent on the amount of CNO seed nuclei and the initial abundances accreted from the red giant. However, as bursts occur periodically the reaction products of previous bursts can alter the initial abundance of CNO seed nuclei for later XRB bursts.

The second phase of the XRB is the breakout: at this point the CNO cycles are well established and causing the temperature to increase. To have an increase in energy generation to cause a burst, there must be a reaction that provides a pathway to breakout from the HCNO cycles and into a new burning regime. For the breakout to happen, the waiting-point nuclei have to be bypassed. These are ^{14}O , ^{15}O and ^{18}Ne . The waiting points exist as radiative proton capture from these nuclei are to proton-unbound nuclei. In the case of ^{18}Ne , the proton-unbound nucleus is ^{19}Na [27]. α -capture reactions provide a way to bypass the waiting points. However, these can only occur at higher temperatures as the Coulomb barrier for α -induced reactions is higher than for proton-induced reactions. The first breakout reaction is $^{15}\text{O}(\alpha, \gamma)^{19}\text{Ne}(p, \gamma)^{20}\text{Na}$. The second breakout reaction, relevant to this thesis, is $^{14}\text{O}(\alpha, p)^{17}\text{F}(p, \gamma)^{18}\text{Ne}(\alpha, p)^{21}\text{Na}$. It is shown in Figure 1.8.

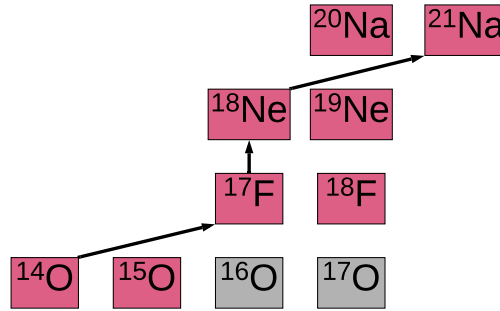


Figure 1.8: The $^{14}\text{O}(\alpha, p)^{17}\text{F}(p, \gamma)^{18}\text{Ne}(\alpha, p)^{21}\text{Na}$ breakout reaction.

The $^{14}\text{O}(\alpha, p)^{17}\text{F}$ reaction surpasses the β^+ -decay rate from around $T \approx 0.4$ GK. However, the $^{18}\text{Ne}(\alpha, p)^{21}\text{Na}$ reaction only surpasses the β^+ -decay rate from around $T \approx 0.8$ GK. Due to this difference, the $^{14}\text{O}(\alpha, p)^{17}\text{F}$ reaction processes more material which increases the ^{15}O abundance making the $^{15}\text{O}(\alpha, \gamma)^{19}\text{Ne}$ breakout reaction more likely. Once the temperature increases and the $^{14}\text{O}(\alpha, p)^{17}\text{F}(p, \gamma)$ reaction becomes stronger, the abundance of ^{18}Ne will increase until the temperature is high enough for it to undergo α capture and be destroyed.

During the final phase of the XRB, the processes have left the CNO cycles and explosive nucleosynthesis continues by the rp-process and αp -process by means of the (p, γ) and (α, p) reactions, respectively. The binding energy per nucleon increases for nuclei until the iron-peak nuclei are reached. This is the origin of the burst energy during the rapid capture reactions. Once past the iron-peak nuclei, the temperature is still sufficient to drive the (p, γ) reactions up to the ^{100}Sn region [21]. The size of the burst also determines the nature of the nuclear reactions following breakout. Larger bursts with more energy can sustain (α, p) reactions if the (p, γ) reaction is weaker and if the β^+ -decay lifetime is long. The end of the burst occurs when the hydrogen is consumed. This can happen at different stages of nucleosynthesis and thus different regions of the nuclear chart depending on the thermodynamic profile of the burst and the initial amount of hydrogen available to drive the burst.

As discussed earlier, the atmosphere of the Earth is opaque to X-rays. Therefore, XRBs can only be detected by space-based telescopes. X-ray light emitted from the burst is regarded as the only practical observable for these events. This is due to the nature of the stellar binary that is needed for these bursts to occur. The gravitational field of the neutron star and the energy output from the bursts make it unlikely that XRBs contribute to galactic isotopic abundances. However, from observation the frequency of bursts, how long they last, their characteristic timescale (defined as the total energy produced per unit area at peak flux), and the decay timescale can be studied. Figure 1.9 shows the first spectrum of an XRB detected from space.

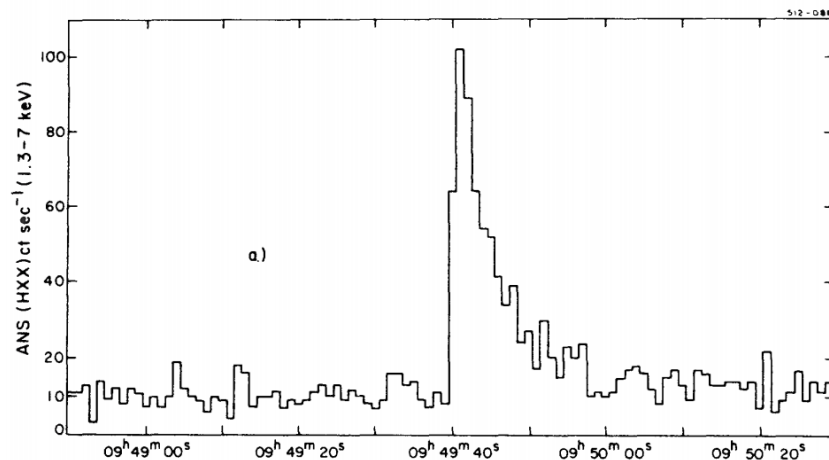


Figure 1.9: Signal detected from an XRB [3] in the constellation Sagittarius near the centre of the Milky Way galaxy.

1.4.4 Classical novae

Classical novae are stellar events that occur in a compact binary system that has a white dwarf and red giant companion. The name was historically given as ancient astronomers saw a classical nova (Latin for new) which they perceived to be a new star. In this situation, hydrogen- and helium-rich matter is accreted from the red giant star as the pair orbit in relative close proximity. The material is accreted in a swirling plate-like disk onto the surface of the white dwarf. The strong gravitational field then starts to condense the matter which causes it to rise in temperature. If enough matter is accreted onto the surface of the white dwarf the temperature will be sufficient to ignite thermonuclear hydrogen burning. The result is a thermonuclear runaway event on the surface that leads to an explosion. This produces a bright but short-lived burst of light known as a nova. The spinning disk of matter being accreted to the white dwarf surface can be ejected during the explosion leaving the cycle to start again. These cycles can be repeated over the course of many hundreds to thousands of years [7].

Classical novae produce observable amounts of the radioactive isotope ^{22}Na during the thermonuclear event [9]. This nucleus, in particular, is important in trying to study these events. It has a long-lived β -decay half-life of $t_{1/2} = 2.6$ years which decays with the emission of a characteristic γ ray of 1.275 MeV. The long half-life and characteristic, high-energy γ ray makes this nucleus possible to detect with γ -ray telescopes beyond the opacity window in classical novae. The presence of ^{22}Na is, therefore, used to infer that such an event has occurred. Figure 1.10 shows two images of the same nova taken 7 months apart. It shows the unburnt hydrogen ejected from the surface of the white dwarf in a rapidly-expanding shell [28].

A reliable prediction of novae outbursts relies on certain key thermonuclear

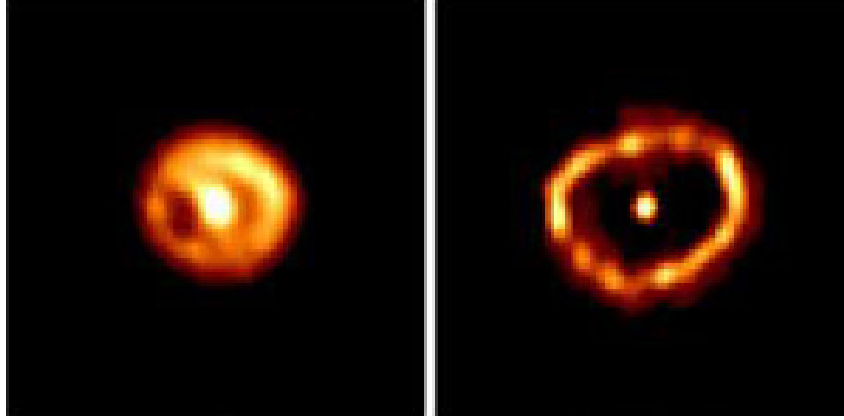


Figure 1.10: Nova Cygni 1992 as seen by the Hubble space telescope [28], taken 7 months apart.

reaction rates. One of the most important rates amongst these is proton capture on ^{21}Na [29]. Therefore, the $^{21}\text{Na}(p, \gamma)^{22}\text{Mg}$ reaction rate has relevance to classical novae as it is a main pathway in producing ^{22}Na . It is produced by the excited ^{22}Mg nucleus through $^{22}\text{Mg}(\beta^+\nu)^{22}\text{Na}$. It can also be produced, after ^{22}Mg has undergone proton decay to ^{21}Na , via radiative proton capture on ^{21}Ne : $^{21}\text{Na}(\beta^+\nu)^{21}\text{Ne}(p, \gamma)^{22}\text{Na}$ [9]. This reaction and the determination of the rate will be discussed further in the following section.

1.5 Calculation of the $^{18}\text{Ne}(\alpha, p)^{21}\text{Na}$ and $^{21}\text{Na}(p, \gamma)^{22}\text{Mg}$ Reaction Rates

The primary objective of this thesis is to make corrections to the $^{18}\text{Ne}(\alpha, p)^{21}\text{Na}$ HCNO breakout reaction. The secondary objective will be to determine the $^{21}\text{Na}(p, \gamma)^{22}\text{Mg}$ reaction rate. This will be possible as the experiment performed in this study involves the $^{24}\text{Mg}(p, t)^{22}\text{Mg}$ reaction. Both reactions being studied have ^{22}Mg as its compound nucleus. By examining states below the α -particle separation threshold, S_α , at 8.142 MeV the $^{21}\text{Na}(p, \gamma)^{22}\text{Mg}$ reaction rate can be studied and above S_α the $^{18}\text{Ne}(\alpha, p)^{21}\text{Na}$ reaction is relevant. This is explained further in Chapter 2 Section 2.6 with the level diagrams shown in Figures 2.2 to 2.4.

Using a silicon detector array, proton decays from ^{22}Mg to ^{21}Na can be detected and the proton branching ratios, B_{p_i} , can be calculated. Proton decays from ^{22}Mg to the i 'th state in ^{21}Na are denoted by p_i . Consequently, the $^{24}\text{Mg}(p, t)^{22}\text{Mg}$ reaction and the analysis thereof will be discussed in this thesis to determine the proton branching ratios.

The theory of thermonuclear reactions will be discussed in Chapter 2. In that discussion, two equations will be presented. The first calculates the thermonuclear reaction rate when using narrow resonances. This will be used for

the $^{21}\text{Na}(p, \gamma)^{22}\text{Mg}$ reaction as the resonances that affect this rate are narrow [30] and the density of states below S_α is low. This makes it possible to study the resonances individually. The second equation is the thermonuclear reaction-rate equation. This uses the cross section as a function of energy $\sigma(E)$. The equation is used when the resonances are difficult to resolve experimentally. The measurements then yield an average cross section that varies smoothly with energy. The following section will discuss the reaction rates that are available from literature.

As discussed earlier, the $^{18}\text{Ne}(\alpha, p)^{21}\text{Na}$ reaction is one of the three crucial breakout reactions from the HCNO cycles to the rp process at peak temperature $T \simeq 1 - 2$ GK. Estimations of the rate [31] were initially made based on sparse experimental information on the level structure of the compound nucleus ^{22}Mg . A study by Salter *et al.* [32] performed the time-reversed reaction $^{21}\text{Na}(p_0, \alpha)^{18}\text{Ne}$ for the first time in the Gamow energy region (discussed in Chapter 2) relevant to the breakout reaction. The measured cross section from the experiment, $\sigma_{(p_0, \alpha)}$, was then transformed to the cross section of interest, $\sigma_{(\alpha, p_0)}$, for the $^{18}\text{Ne}(\alpha, p_0)^{21}\text{Na}$ reaction using the principle of detailed balance [33, 34]. The reaction rates were then determined using this cross section. The nature of this time-reversed reaction meant that the data were limited to $\sigma_{(\alpha, p_0)}$ and did not include any higher proton decay channels. Compared to theoretical predictions based on Hauser-Feshbach calculations, the rate was scaled up by a factor of 3. It is for this reason that the objective of this study is to determine the p_i branching ratios, B_{p_i} , and in particular B_{p_0} to make corrections to the reaction rate of $^{18}\text{Ne}(\alpha, p)^{21}\text{Na}$.

Calculation of the $^{18}\text{Ne}(\alpha, p)^{21}\text{Na}$ reaction rate will take precedence in this thesis. In order to calculate the rate and make corrections to the existing reaction rate, the $^{24}\text{Mg}(p, t)^{22}\text{Mg}$ reaction will be performed in an experiment that will be discussed in Section 1.6. The resultant excitation energy spectrum of ^{22}Mg above S_α will be analysed. The resonance yields per energy region will be determined to get the angular correlation spectrum and ℓ value of the decay to reconstruct the full angular correlation function. In doing so, corrections can be made to the missing solid angle where the ancillary detector system cannot operate. By calculating the true yield for each p_i decay and comparing it with the singles yield in the same energy region, the branching ratios B_{p_i} can be calculated. The branching ratios will be used to make corrections to the reaction rate. States below S_α will be studied in order to calculate the $^{21}\text{Na}(p, \gamma)^{22}\text{Mg}$ reaction rate. The same analysis procedure will be followed.

1.5.1 Reaction rate of $^{18}\text{Ne}(\alpha, p)^{21}\text{Na}$ information from literature

Owing to the importance of the $^{18}\text{Ne}(\alpha, p)^{21}\text{Na}$ breakout reaction, multiple studies [2, 13, 32, 35, 36] have endeavoured to determine its reaction rate. This

1.5. CALCULATION OF THE $^{18}\text{Ne}(\alpha, p)^{21}\text{Na}$ AND $^{21}\text{Na}(p, \gamma)^{22}\text{Mg}$ REACTION RATES

21

section will discuss the reaction rates determined in literature and compare it to the calculations that will be done in this thesis.

The $^{18}\text{Ne}(\alpha, p)^{21}\text{Na}$ cross section at astrophysical energies is small. Additionally, the intensity of available radioactive beams of ^{18}Ne is very low ($\leq 10^6$ pps) and the use of a helium gas target is also difficult making direct measurements of this reaction challenging. Certain studies have performed the direct reaction [1, 2]. Therefore, some studies have performed the time-reversed reaction $^{21}\text{Na}(p, \alpha)^{18}\text{Ne}$ to infer the cross section of the forward reaction. Others have populated states in the compound nucleus ^{22}Mg to study this reaction.

Figure 1.11 [32] shows the reaction rates calculated in various studies by Matic *et al.* [35], Groombridge *et al.* [2], and Salter *et al.* [32]. The study by Matic populated states in the compound nucleus ^{22}Mg . This is the same reaction as presented in this thesis. However, one important difference is the use of a silicon detector array in this study to detect proton decays from ^{22}Mg which was not part of the experiment by Matic. Secondly, the study by Groombridge performed the direct reaction by inverse kinematics - a radioactive ^{18}Ne beam was impinged onto a helium gas cell target. However, the study can only give an experimental lower limit to the reaction rate as the minimum experimental energy was $E_{c.m.} = 1.7$ MeV. This is still too high compared to the region $E_{c.m.} \leq 1.5$ MeV of interest to HCNO breakout in XRBs [32].

The time-reversed study by Salter *et al.* [32] improved upon the results of Groombridge *et al.* [2] by extending the energy range from $1.7 \text{ MeV} \leq E_{c.m.} \leq 2.9$ MeV to $1.2 \text{ MeV} \leq E_{c.m.} \leq 2.6$ MeV. In that study, the reaction that was performed gave a lower estimation of the rate as the reaction was only sensitive to the p_0 channel. Consequently, the rate was estimated to be a factor of 3 higher to include other proton decay channels. This was determined by comparison to Hauser-Feshbach calculations (theory discussed in Chapter 2).

A study by Matic and Mohr [36] compared all experiments that were performed to determine the $^{18}\text{Ne}(\alpha, p)^{21}\text{Na}$ reaction rate. That study aimed to resolve discrepancies of at least one order of magnitude in the data from those experiments. Figure 1.12 shows the comparison of all of the data as ratios between reaction rate factors normalised to a reference rate. The reference rate chosen was from Matic *et al.* [35]. It was concluded that a rate which is a factor of 0.55 smaller than the reference rate should be recommended for use in further astrophysical calculations. The estimate of 0.55 originates from the most realistic overlap from the uncertainties in the various studies. Another, more recent study by Mohr *et al.* [37] used Monte Carlo calculations whilst taking into account uncertainties from all the nuclear physics input quantities. The suggested rate from that study also closely resembles the findings of Matic and Mohr [36] at higher temperatures.

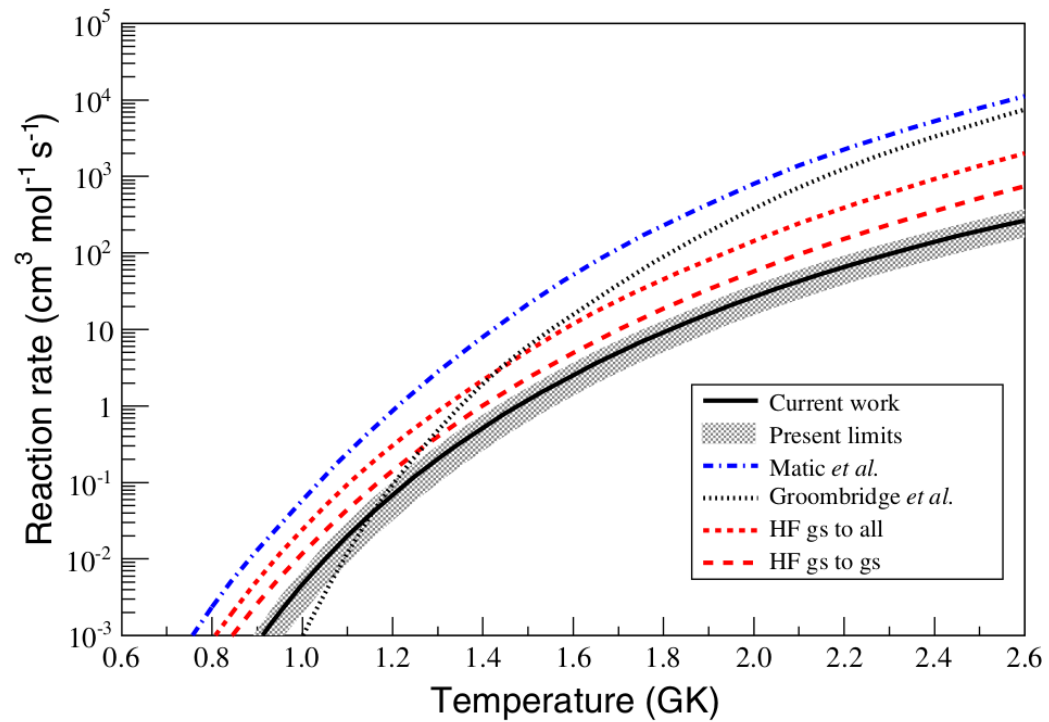


Figure 1.11: Reaction rate of $^{18}\text{Ne}(\alpha, p_0)^{21}\text{Na}$ from Salter *et al.* The figure is from Ref. [32].

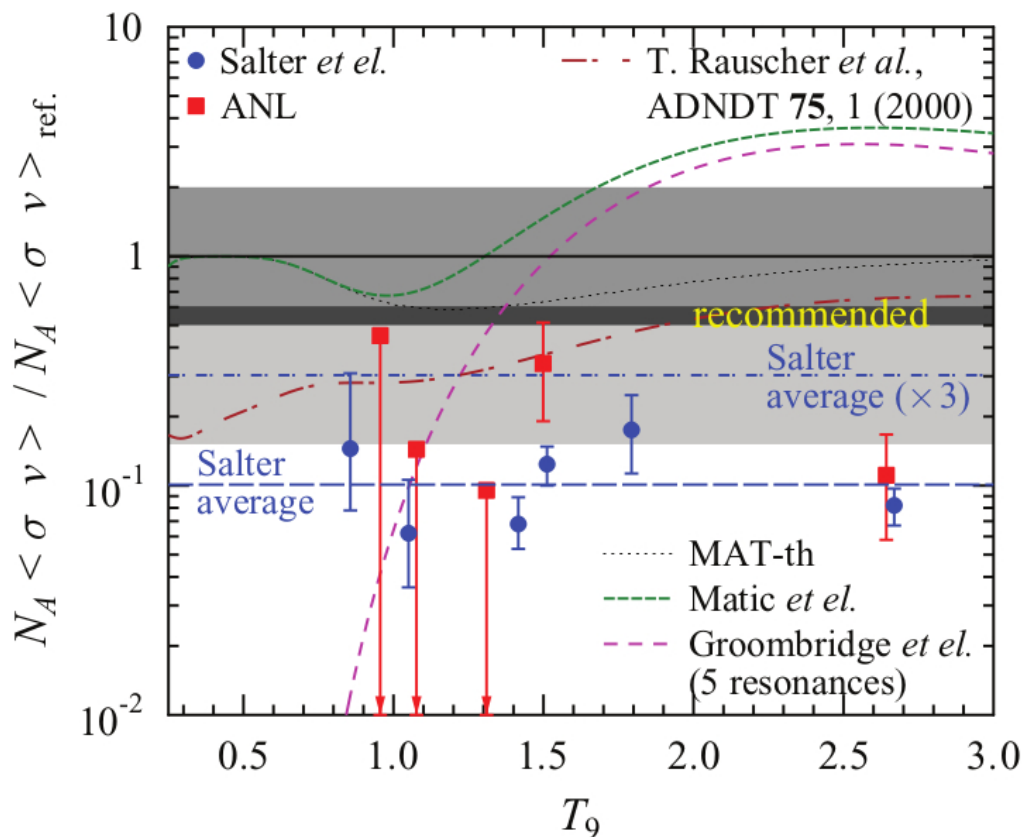


Figure 1.12: Comparison of reaction rates of $^{18}\text{Ne}(\alpha, p)^{21}\text{Na}$ from Matic and Mohr. The reaction rates are normalised to a reference rate by Matic *et al.* (MAT) [35]. Data also included in this figure are by Rauscher and Thielemann [38] and unpublished data from Argonne National Laboratory (ANL). The figure is from Ref. [36].

1.6 The $^{24}\text{Mg}(p, t)^{22}\text{Mg}$ reaction

This thesis will discuss the $^{24}\text{Mg}(p, t)^{22}\text{Mg}$ reaction. It was performed in an experiment using a magnetic spectrometer in coincidence with a silicon-detector array. The reaction populated excited states in ^{22}Mg . Proton decays from ^{22}Mg to states in ^{21}Na were detected using the silicon-detector array. This decay information was used to determine proton branching ratios B_{p_i} to ^{21}Na .

The main objective of the experimental proposal is to study the decay of states from ^{22}Mg to correct for the $^{18}\text{Ne}(\alpha, p)^{21}\text{Na}$ reaction rate. This will be the main objective of this thesis. The excitation energy spectra for states above the α -particle separation threshold, S_α , were generated using the $^{24}\text{Mg}(p, t)^{22}\text{Mg}$ dataset. The spectra were gated on different proton decays - decays to the ground state and first four excited states in ^{21}Na . The experiment had a fairly low resolution and the density of states in this region is high. Therefore, the spectra were analysed in energy regions of 100 keV. The angular correlation spectra were generated with the corrected yields from the excitation energy spectra. The ℓ value of the decay for each excitation energy region was determined by fitting the angular correlation spectra with the Legendre polynomials. The ℓ values were used to construct the angular correlation functions for each energy bin to determine the true proton-decay yield in the relevant energy region. Consequently, the branching ratios for p_i ($i \in [0, 4]$) were calculated. The p_0 branching ratio was used to make corrections to the thermonuclear reaction rate from literature [32].

Data regarding states below S_α were also available and, therefore, analysed. This is relevant to the $^{21}\text{Na}(p, \gamma)^{22}\text{Mg}$ reaction rate. For these data, individual resonances were studied as the density of states below S_α is lower and the states were resolved. Using the same $^{24}\text{Mg}(p, t)^{22}\text{Mg}$ dataset the coincidence excitation energy spectra were generated for p_0 and p_1 decay. The analysis for each resonance proceeded as is described in Chapter 5. The data were used to determine B_{p_0} and B_{p_1} . The ℓ values were also used to determine possible spin-parity (J^π) assignments for each resonance in this region.

The theory needed to calculate the thermonuclear reaction rates is discussed in Chapter 2. The experimental setup and data analysis are discussed in Chapters 3 and 4, respectively. The results from the analysis are presented in Chapter 5. Calculations with the branching ratios to make corrections to the thermonuclear reaction rates are shown in Chapter 6. Finally, the conclusion and outlook for this study is given in Chapter 7.

Chapter 2

Theory

I much prefer the sharpest
criticism of a single intelligent
man to the thoughtless
approval of the masses.

Johannes Kepler

2.1 Introduction

Nucleosynthesis and energy generation in stellar environments are generally as a result of thermonuclear reactions. These reaction rates depend strongly on the temperature and properties of the nuclei involved. In this chapter, the cross section will first be defined briefly and the basic nuclear properties introduced. Thereafter, resonances will be discussed along with the connection between resonance properties and the thermonuclear reaction rates. Hauser-Feshbach theory and the TALYS statistical model will also be introduced briefly. Finally, the theory of angular correlations and relative orbital angular momentum, or ℓ , values which are needed for analysis will be discussed.

2.2 Cross sections

The cross section, σ , is defined as the probability that two particles collide and cause a reaction. This is defined as:

$$\sigma = \frac{\text{Number of interactions per unit time}}{\text{Number of beam particles per unit time and area} \times \text{target areal density}}. \quad (2.2.1)$$

The areal density is seen as the number of target particles that the beam particles are able to collide with. The cross section has units of area and are typically small and in the order of 10^{-28} m^2 , which is called a barn. The

cross section can, to an extent, be compared to the geometric cross section. This is the physical area covered by each nucleus from the viewpoint of the incident beam particles. However, the nuclear cross section can be several orders of magnitude smaller or larger than the geometric cross section. For instance, ^{135}Xe has a very large neutron-capture cross section as it is close to a neutron shell closure. Therefore, it is better to describe the cross section as a probability of interaction. Time invariance and the principle of detailed balance, which relates the cross section of a reaction to the cross section of the time-reversed reaction, is discussed later in this chapter in Section 2.6.

For completeness, the differential cross section, $\frac{d\sigma}{d\Omega}$, is also a measure of probability. It is the probability that a flux of reactants, $d\sigma$, goes into a certain infinitesimally small part of the total solid angle, $d\Omega$. The shape of the differential cross section function can yield information on different reaction mechanisms such as angular momentum transfer. However, this is not used further in this thesis.

2.3 Resonance properties

Resonances are states that are considered to be nearly bound. Each resonance is characterised by a certain number of properties: spin-parity (J^π), resonance energy (E_r), resonance width (Γ_r), and branching ratios for each exit channel (B_i). The resonance width is a measure of the decay rate as it is related to the resonance lifetime, τ , by:

$$\Gamma = \frac{\hbar}{\tau}, \quad (2.3.1)$$

where \hbar is the reduced Planck constant. The total resonance width is the sum of the partial widths of each exit channel indexed as i :

$$\Gamma = \sum_i \Gamma_i. \quad (2.3.2)$$

Therefore, for decay into each open exit channel the partial width relates the branching ratio with the total resonance width by:

$$B_i = \frac{\Gamma_i}{\Gamma}. \quad (2.3.3)$$

In the following section the thermonuclear reaction-rate equations are introduced. Therefore, the Breit-Wigner equation is given here. It describes the cross section for resonant reactions proceeding through a resonance in the compound nucleus by an incoming channel, i , and an outgoing channel, f . It is used in the calculation of broad- and narrow-resonance cross sections and is given by:

$$\sigma_{i,f}(E) = \frac{\lambda^2}{4\pi} \frac{2J+1}{(2j_a+1)(2j_b+1)} (1 + \delta_{ab}) \frac{\Gamma_i \Gamma_f}{(E - E_r)^2 + \frac{\Gamma^2}{4}}. \quad (2.3.4)$$

In this equation, λ is the de Broglie wavelength of the incoming particle. The subscripts a and b denote the reactants and the Kronecker-delta factor accounts for when the particles are identical. The $(2J + 1)$ spin factors account for averaging over the incoming spins and for summing over the outgoing spins. This factor thus allows for summing over all of the possible final projections of the spin. In this case J is the spin of the compound resonance with j_a and j_b being the initial spins [39]. The resonance strength is defined by:

$$\omega\gamma_{ij} = \frac{2J + 1}{(2j_a + 1)(2j_b + 1)} \frac{\Gamma_i\Gamma_f}{\Gamma}. \quad (2.3.5)$$

It is proportional to the area under the resonance cross section or alternatively to the product of maximum cross section [12]:

$$\begin{aligned} \Gamma \cdot \sigma_{BW} &= \Gamma \cdot \frac{\lambda_r^2}{\pi} \omega \frac{\Gamma_a\Gamma_b}{\Gamma^2} \\ &= \frac{\lambda_r^2}{\pi} \omega\gamma \end{aligned} \quad (2.3.6)$$

The resonance strength factor is also an important part of the narrow-resonance reaction rate discussed in Subsection 2.4.3. The cross section at all incident energies can be calculated if all the properties of all resonances in the energy region are known.

2.4 Thermonuclear reaction rates

Reaction rates are defined in terms of unit volume and unit time. An expression for the rate equation can be derived using the cross section definition discussed earlier. In the simplest case, the reaction rate of an incident particle beam of velocity v can be expressed as [12]:

$$\frac{N_r}{Vt} = \sigma(v) \frac{N_{target}}{V} \frac{N_{beam}}{At}. \quad (2.4.1)$$

The number of reactions is given by N_r and the unit time is given by t . The unit volume and cross-sectional area are given by V and A , respectively. The cross section as a function of the velocity is given as $\sigma(v)$ and the number of target and beam particles are given by N_{target} and N_{beam} , respectively.

The number of beam ions per unit time per area gives the beam current density, i.e. $\frac{N_{beam}}{At}$. With a beam velocity v , the beam current density can be rewritten as $\frac{vN_{beam}}{V}$ so that:

$$\frac{N_r}{Vt} = \sigma(v) \frac{N_{target}}{V} \frac{vN_{beam}}{V}. \quad (2.4.2)$$

Equation 2.4.2 can be written in terms of the number densities of the reactants, $n_0 = \frac{N_{target}}{V}$ and $n_1 = \frac{N_{beam}}{V}$. This gives an expression of the reaction rate as:

$$R = \sigma(v)vn_0n_1. \quad (2.4.3)$$

Equation 2.4.3 is still relevant to the scenario of an incident beam particle of velocity v impinging on a stationary target particle. Here, v is the relative velocity between the two particle species. Equation 2.4.3 can, therefore, be used in its current form to calculate the total reaction rate in a plasma. The subscripts denote a reaction involving four particle species: $0 + 1 \rightarrow 2 + 3$. In this definition, 0 and 1 are the target and projectile (reactants) whereas 2 and 3 are the products.

In a thermonuclear environment the velocities of the reactant particles will not be single-valued. They can have a large range of energies (and velocities v) which correspond to the temperature of the plasma. The velocity is then described by a Maxwell-Boltzmann distribution. In this case, the reaction rate is written as:

$$R = \langle \sigma v \rangle_{01} n_0 n_1, \quad (2.4.4)$$

where $\langle \sigma v \rangle_{01}$ can be considered as the reaction rate per particle pair [12]. This is defined by:

$$\langle \sigma v \rangle_{01} = \int_0^\infty P(v) v \sigma(v) dv. \quad (2.4.5)$$

The interpretation of the probability function is that $P(v)dv$ is the probability that the relative velocity, between two particles of a particle pair, is between v and $v + dv$ such that:

$$\int_0^\infty P(v) dv = 1. \quad (2.4.6)$$

We can then write the reaction rate as:

$$\begin{aligned} R &= n_0 n_1 \int_0^\infty v P(v) \sigma(v) dv \\ &\equiv \langle \sigma v \rangle_{01} n_0 n_1. \end{aligned} \quad (2.4.7)$$

In the relative-velocity equation the Maxwell-Boltzmann distribution is:

$$P(v)dv = 4\pi v^2 \left(\frac{\mu_{01}}{2\pi kT} \right)^{3/2} \exp\left(\frac{-\mu v^2}{2kT} \right) dv. \quad (2.4.8)$$

In Equation 2.4.8, k is the Boltzmann constant, T is the temperature in Kelvin, and $\mu_{01} = \frac{m_1 m_2}{m_1 + m_2}$ is the reduced mass of a particle pair. The masses of the two particles involved in the reaction are given by m_1 and m_2 . The scale of the thermal energy from the Maxwell-Boltzmann distribution is proportional to $kT = 86.3T_9$ keV with T_9 being the temperature in GK. The final step is to convert the velocity to energy, E , using the non-relativistic kinetic energy equation with the reduced mass:

$$E = \frac{1}{2} \mu v^2, \quad (2.4.9)$$

which can then be used in Equation 2.4.8 to yield:

$$P(E)dE = \frac{2}{\sqrt{\pi}} \frac{1}{(kT)^{3/2}} \sqrt{E} \exp\left(-\frac{E}{kT} \right) dE. \quad (2.4.10)$$

This distribution will be shown along with the definition of the Gamow window later in the text. The Maxwell-Boltzmann energy distribution (Equation 2.4.10) is substituted into Equation 2.4.5 and used with the Avagadro constant, N_A , to calculate the total reaction rate, $N_A\langle\sigma v\rangle$, [12, 21]:

$$N_A\langle\sigma v\rangle = \left(\frac{8}{\pi\mu_{01}}\right)^{1/2} \frac{N_A}{(kT)^{3/2}} \int_0^\infty \sigma(E)E \exp\left(-\frac{E}{kT}\right) dE. \quad (2.4.11)$$

This is the expression for the total reaction rate that will be used in Chapter 6 to calculate the rate of the $^{18}\text{Ne}(\alpha, p)^{21}\text{Na}$ reaction. The reaction rate has units of $\text{cm}^3 \text{s}^{-1} \text{mol}^{-1}$. The Avagadro constant is introduced in order to calculate the reaction rate per mol instead of per reaction pair thereby making the rate a density-invariant quantity.

In order to calculate the reaction rate the cross section, $\sigma(E)$, has to be determined. Two different contributions make up the cross section. The first, which is small and influences the cross section to a lesser extent, is the contribution from non-resonant direct capture. The main, resonance contribution is from capture reactions into resonances in the compound nucleus. The latter contribution will be discussed in Subsection 2.4.3 along with the narrow-resonance reaction rate.

2.4.1 Coulomb penetrability

The thermal energy scale in stellar environments mentioned earlier is of the order of $kT \sim 86.3T_9 \text{ keV}$. The Coulomb barrier that two nuclei will experience is:

$$B_{Coulomb} = \frac{e^2}{4\pi\epsilon_0} \frac{Z_1 Z_2}{R_0} = 1.44 \frac{Z_1 Z_2}{R_0} \text{ MeV}, \quad (2.4.12)$$

where the number of protons of the two nuclei is given by Z_1 and Z_2 . The distance at which two nuclear surfaces can start interacting is given by the radius R_0 in fm. It is, therefore, evident that the Coulomb barrier is of the order of a few MeV. The thermal energy alone is thus not sufficient to force nuclei close enough to react. The reason is that the temperatures in stellar environments are in the range of 10 MK to 100 MK. The only possible mechanism by which the nuclear surfaces can come into close enough contact to react with each other is by means of quantum-mechanical tunnelling [21] through the barrier. Therefore, the theory of nuclear penetrabilities is discussed in this section.

The nuclear penetrability can be calculated by regarding the total transmission probability, Θ , through a finite square well with height V_0 [12]:

$$\Theta \approx \left(-\frac{2}{\hbar} \sqrt{2m(V_0 - E)} \delta r\right). \quad (2.4.13)$$

Here the thickness of the barrier is given by δr with the incident particle having energy E . In the limit where the width of the barrier approaches zero, $\delta r \rightarrow 0$,

the above equation becomes:

$$\Theta_i = \exp\left(-\frac{2}{\hbar}\sqrt{2m(V_i - E)}(r_{i+1} - r_i)\right). \quad (2.4.14)$$

This can be interpreted as tunnelling through an infinitesimally-thin barrier of a square potential well. In this definition, the Coulomb barrier is regarded as a series of infinitesimally-thin square potential wells. The width of the barrier is rewritten so that $r_{i+1} = \delta r + r_i$ and the potential is equal to the Coulomb barrier:

$$V_i = \frac{e^2}{4\pi\epsilon_0} \frac{Z_1 Z_2}{r_i}, \quad (2.4.15)$$

where Z_1 and Z_2 are defined as before and r_i is the interaction radius between two nuclei in fm. As the entire Coulomb barrier is a series of the potential wells, the total transmission probability can be calculated as the product of the partial transmission probabilities from Equation 2.4.14. In effect, this means that:

$$\Theta_{total} = \prod_i \Theta_i. \quad (2.4.16)$$

Given the mathematical identity:

$$\prod_i e^{a_i} = e^{\sum_i a_i}, \quad (2.4.17)$$

the total transmission probability can be rewritten as:

$$\Theta_{total} = \exp\left(-\frac{2}{\hbar} \sum_i \sqrt{2m(V_i - E)}(r_{i+1} - r_i)\right). \quad (2.4.18)$$

In the limit $\delta r \rightarrow 0$, the difference between the interaction radii become infinitesimally small and the sum becomes an integral:

$$\Theta_{total} = \exp\left(-\frac{2}{\hbar} \int_{R_0}^{R_c} \sqrt{2m(V(r) - E)} dr\right). \quad (2.4.19)$$

Here, the lower limit, R_0 , is the nuclear radius. The upper limit, R_c , is the radius at which point the incoming particle energy is equivalent to the Coulomb barrier. This integral can be evaluated (see Appendix A of [21]) to show that the Gamow factor is:

$$\Theta_{total} \approx e^{-2\pi\eta}, \quad (2.4.20)$$

with the Sommerfeld parameter, η , equal to:

$$\eta = \frac{1}{\hbar} \frac{Z_1 Z_2 e^2}{4\pi\epsilon_0} \sqrt{\frac{m}{2E}}. \quad (2.4.21)$$

2.4.2 The Gamow window

The Gamow energy E_0 and Gamow window $E_0 \pm \Delta E/2$ corresponds to the energy region where astrophysical reactions are likeliest to take place. The origin of the Gamow window is shown in Figure 2.1 [12]. It illustrates the energy region where the product of the Maxwell-Boltzmann distribution and penetrability function is at a maximum. As discussed in the previous sections, the Gamow window is of importance as stellar reactions occur at temperatures where the fraction of particles with a high energy is very low. Additionally, particles with lower energy are not as likely to tunnel through the Coulomb barrier. The Gamow window is, in essence, a compromise between these two factors and it is a region where a much higher probability of reaction exists. The energy of the maximum in the Gamow peak can be calculated by:

$$E_0 = 0.122(Z_1 Z_2 \mu)^{1/3} T_9^{2/3} \text{ MeV}, \quad (2.4.22)$$

and the width can be calculated by:

$$\Delta E = 0.2368(Z_1 Z_2 \mu)^{1/6} T_9^{5/6} \text{ MeV}. \quad (2.4.23)$$

The Gamow window can be approximated as a Gaussian function. The variables μ , Z_1 , and Z_2 are as defined previously. The temperature in GK is given as T_9 . The Gamow window shows that direct measurements of astrophysical reactions are difficult as the astrophysically relevant energies in the Gamow window are small. Measurements of the cross section are often very small and unfeasible to measure. This is one of the main challenges in performing astrophysical measurements. In the case of the $^{18}\text{Ne}(\alpha, p)^{21}\text{Na}$ reaction, as well as other α -particle induced reactions, direct measurements are often not possible. One reason is that the radioactive ion beams have very low intensities and the ^4He gas targets have very low areal densities. That coupled with the low reaction energies result in very low reaction yields making it very difficult to give accurate estimations of these reaction rates.

2.4.3 Resonances and reaction rates

Resonant reactions proceed to the compound nucleus via a resonance. Resonances can cause large increases in the cross section by orders of magnitude. For the case where these resonant states lie within the Gamow window, the resonant state dominates the reaction rate as it is populated more often than any other state within the astrophysically-relevant energy region.

A resonance is considered to be isolated when it does not overlap with another. Additionally, a resonance is considered to be narrow if, over the entire resonance width, the Maxwell-Boltzmann distribution and penetrability remain nearly constant [12]. In these instances, it is possible to calculate the

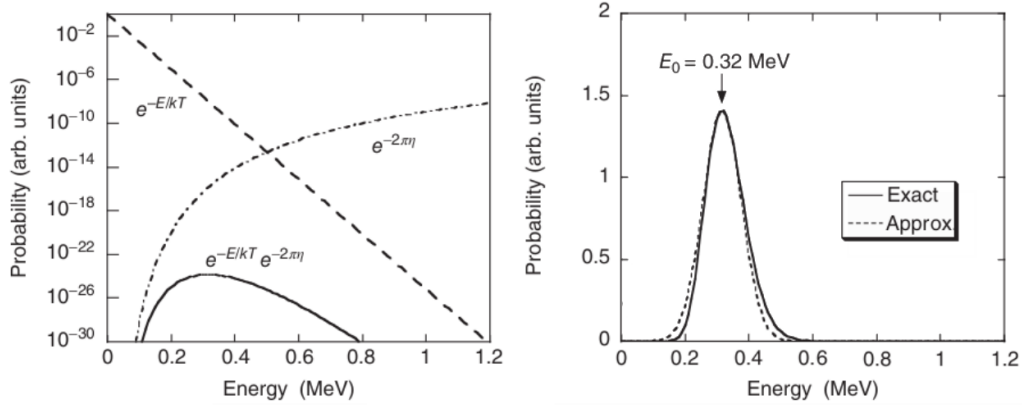


Figure 2.1: Origin of the Gamow window. This figure is taken from Ref. [12]. The figure on the left shows the region, on a logarithmic scale, where the Maxwell-Boltzmann distribution ($\sqrt{E}e^{-E/kT}$) overlaps maximally with the penetration probability ($e^{-2\pi\eta}$) that results in the Gamow factor ($e^{-E/kT}e^{-2\pi\eta}$). The figure on the right shows the Gamow window in linear scale. The region where the Gamow window reaches a maximum is indicated. This example is for the $^{12}\text{C}(\alpha, \gamma)^{16}\text{O}$ reaction.

resonance reaction rate as [12]:

$$N_A \langle \sigma v \rangle = \frac{1.5399 \times 10^{11}}{(\mu T_9)^{3/2}} \sum_i (\omega \gamma)_i e^{-11.605 E_i / T_9}. \quad (2.4.24)$$

In this equation, E_i is the resonance energy of the i th resonance and $(\omega \gamma)_i$ is the resonance strength for the i th resonance which was defined previously in Equation 2.3.5. Both are in units of MeV. The temperature T_9 is in GK and μ is the reduced mass. This reaction rate is calculated by substituting the Breit-Wigner expression for the cross section in Equation 2.3.4 into the reaction rate given in Equation 2.4.11.

It is clear that this reaction rate depends strongly on the resonance properties such as the resonance energies, widths, and the spin-parities. The determination of these properties for resonances below S_α in the ^{22}Mg excitation energy spectrum is discussed in detail in Chapter 5.

For broad resonances, numerical integration is required to account for variations in the Maxwell-Boltzmann distribution and in the penetrabilities. The reaction rate is then determined by the expression given previously in Equation 2.4.11. For even higher excitation energies, the resonance widths start to increase and they are closer to each other to the extent that the resonances start to overlap. In this case, statistical models are used to determine a level density to estimate the number of resonances per MeV at a given excitation energy. This is discussed in more detail in the following section.

2.5 Introduction to TALYS statistical models and Hauser-Feshbach Theory

The TALYS calculation code [40] can be used to calculate cross sections of various nuclear reactions. The underlying Hauser-Feshbach (HF) theory that TALYS is based on relies on accurate descriptions of the level densities in nuclei. The study by Salter *et al.* [32] compensated for the fact that they could only measure cross sections sensitive to p_0 transitions. They did so by comparison to calculations based on HF predictions after which their reaction rate was scaled up by a factor of 3. In Chapter 6 the validity of these estimations are discussed. This section will briefly introduce HF theory and the statistical models used in TALYS.

Resonant reactions with isolated, narrow states were discussed earlier in Subsection 2.4.3. As nuclear excitation energies increase, the level density increases as well. At ever higher excitation energies the resonances are broader and they begin to overlap into what is referred to as the continuum. At this point, there is not any structure in the cross section as it reaches a point where the excitation energy is high enough that it varies more evenly with energy. At such a point, the estimation of the actual number of levels and level density becomes more important. In 1952 Hauser and Feshbach [41] proposed a means by which the level density can be estimated. This is done by:

$$\sigma_{ab} = \frac{\pi}{k_a^2} \frac{T_a T_b}{\sum_c T_c} W_{ab} = \sigma_{ab}^{HF} W_{ab}, \quad (2.5.1)$$

where σ_{ab} is the energy average cross section from channels a to b . The HF cross section is given by σ_{ab}^{HF} and the correction factor due to the width fluctuation is given by W_{ab} . The kinematic factor $\frac{\pi}{k_a^2}$ contains the projectile wave number, k_a , and T_i is the transmission coefficient in channel i .

Various statistical models exist for predicting cross sections. They are used at excitation energies where accurate information of the level structure is either unavailable or incomplete due to an absence of experimental information. TALYS uses six different level density models in order to make predictions of the cross sections in energy regions where the necessary level density information may be absent. The models it uses can range from phenomenological analytical expressions to tabulated values for the level densities based on theoretical models [42].

The various models express the level density as a number of nuclear levels per MeV energy. This is written as $\rho(E_x, J, \pi)$. The level density changes with changing excitation energy. Therefore, it is calculated at a particular excitation energy for spin J and parity π . By summing the contributions over all spins and parities for a particular excitation energy, the total level density per MeV evaluated at a particular excitation energy is given as:

$$\rho^{tot}(E_x) = \sum_J \sum_{\pi} \rho(E_x, J, \pi). \quad (2.5.2)$$

The first three level density models in TALYS use analytical expressions to determine a value for the level density. These are the constant-temperature Fermi gas model, the back-shifted Fermi gas model, and the generalised superfluid model. Level-density models 4 and 5 use microscopic level densities determined with the Skyrme force. The last model uses microscopic level densities determined with the temperature-dependent Hartree-Fock-Bogolyubov calculations using the Gogny force.

The TALYS calculations are discussed further in Chapter 6 and will be used to calculate the $^{18}\text{Ne}(\alpha, p_0)^{21}\text{Na}$ cross section using the α optical model potentials (OMPs). An OMP is a schematic model in nuclear scattering theory and they are used for simulations of nuclear cross sections. An OMP simplifies the calculation of a nuclear-scattering experiment by simply regarding incident and scattered particles as plane waves where the particles are scattered from a spherical potential well that represents the potential between two particles.

2.6 Principle of detailed balance

Certain reaction measurements may not be possible due to their challenging nature. Alternatively, the time-reversed measurement of that reaction may well be achievable. In such instances, which can often be the case for astrophysical measurements, the time-reversed reaction is performed and the principle of detailed balance is used to get the cross section of the forward reaction. This is possible as resonance properties like the energy, width, spin, and parity (as discussed in Section 2.3) are time invariant. This means that a simpler experiment with a higher chance of success can be performed and that direct measurements of the more challenging reactions do not necessarily have to impede the measurement of their cross sections.

The $^{18}\text{Ne}(\alpha, p)^{21}\text{Na}$ reaction is exactly one such reaction which is difficult to perform experimentally for reasons already discussed. The study by Salter *et al.* [32] performed the inverse-kinematic time-reversed $p(^{21}\text{Na}, ^{18}\text{Ne})\alpha$ reaction where a ^{21}Na radioactive beam was impinged on a CH_2 target. Here, the chemistry and low first-ionisation potential of ^{21}Na (as well as other Group-I alkali metals) means that beam intensities at the ISAC II facility [32] are more intense at 10^9 to 10^{10} pps, almost reaching stable-beam intensities [39]. Furthermore, CH_2 targets present fewer challenges than ^4He gas-cell targets. Therefore, the time-reversed reaction is easier to perform successfully than the $^{18}\text{Ne}(\alpha, p)^{21}\text{Na}$ direct reaction.

The reason for the inverse-kinematic experiment is merely because the time-reversed reaction would have required a ^{21}Na target but it is unstable. In that study, the $^{21}\text{Na}(p_0, \alpha)^{18}\text{Ne}$ reaction cross section was measured and then related to the $^{18}\text{Ne}(\alpha, p_0)^{21}\text{Na}$ cross section by using the principle of detailed balance. This is discussed in the following paragraph.

Firstly, consider the general reaction $A + a \rightarrow b + B$ or $\alpha \rightarrow \beta$. This can also be written as $A(a, b)B$. To relate the cross section $\sigma_{\alpha \rightarrow \beta}$ to the time-reversed cross section $\sigma_{\beta \rightarrow \alpha}$ the principle of detailed balance is used [33]:

$$\sigma(\alpha, \beta) = \left[\frac{(2J_B + 1)(2J_b + 1)k_\beta^2}{(2J_A + 1)(2J_a + 1)k_\alpha^2} \right] \sigma(\beta, \alpha), \quad (2.6.1)$$

where k_α and k_β are the asymptotic wavenumbers. The J_i are the spins of the nuclei involved in the reaction.

Figure 2.2 shows the level scheme of the $^{18}\text{Ne}(\alpha, p)^{21}\text{Na}$ HCNO breakout reaction. In that reaction direct α capture on ^{18}Ne populates an excited state in the compound nucleus ^{22}Mg . The compound nucleus undergoes de-excitation by proton emission either to the ground state or various excited states in ^{21}Na .

The time-reversed reaction is shown schematically in Figure 2.3. This is the reaction performed by Salter *et al.* [32]. The reaction populates some excited state in the ^{22}Mg compound nucleus which decays by α emission to ^{18}Ne . As the ^{21}Na beam and protons from the target were all in their ground state, the true reaction was only sensitive to Γ_{p0} . It is for this reason that the $^{24}\text{Mg}(p, t)^{22}\text{Mg}$ direct reaction was performed. It allows for the analysis of resonances in ^{22}Mg which is the compound nucleus in both the HCNO breakout reaction of interest as well as its time-reversed reaction.

Figure 2.4 shows the reaction scheme for $^{24}\text{Mg}(p, t)^{22}\text{Mg}$. Here, some excited state in ^{22}Mg is also populated but detecting decays to various excited states or the ground state in ^{21}Na allows for the calculation of the branching ratios as the partial widths of the resonances are essentially being measured. Consequently, the time-reversed reaction by Salter *et al.* [32] can be corrected for by taking into account higher-order proton-decay exit channels.

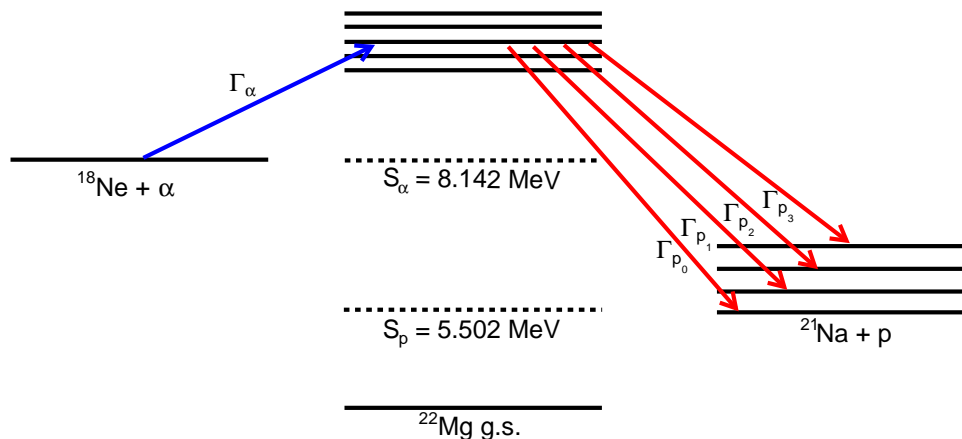


Figure 2.2: The population of excited states above S_α in ^{22}Mg from direct α capture. This level scheme illustrates the $^{18}\text{Ne}(\alpha, p)^{21}\text{Na}$ HCNO breakout reaction. The compound nucleus decays by proton emission to the ground state or various excited states in ^{21}Na . Γ_i gives the decay width for a particle i .

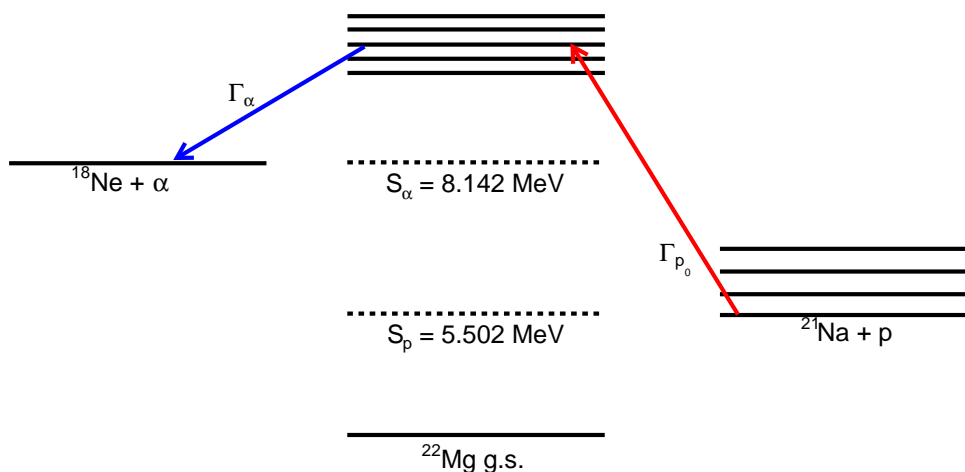


Figure 2.3: The population of excited states above S_α in ^{22}Mg from ^{21}Na . These states decay by α emission to the ^{18}Ne nucleus.

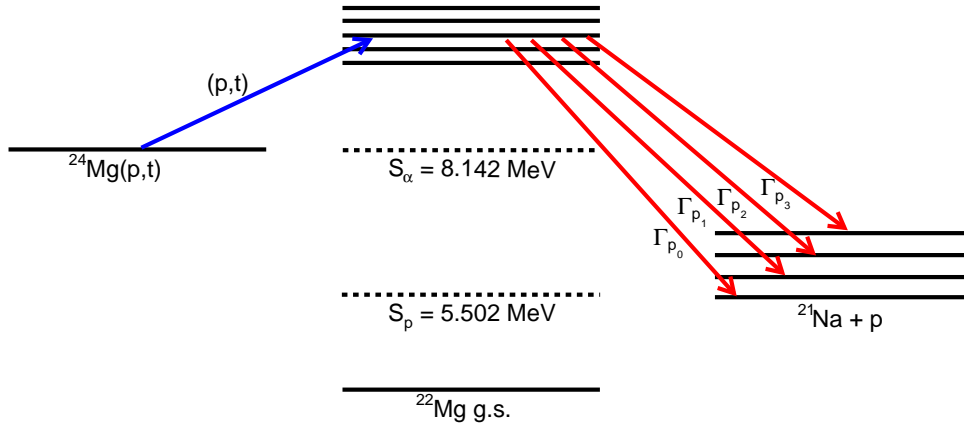


Figure 2.4: The population of excited states above S_α in ^{22}Mg from the direct reaction $^{24}\text{Mg}(p,t)^{22}\text{Mg}$. Proton decays from the excited ^{22}Mg nucleus to ^{21}Na are detected by the CAKE.

2.7 Nuclear reaction theory

This section will discuss the theory used in the analysis in Chapter 5. It will include the theoretical discussions of ℓ values, angular correlation functions, and J^π assignments.

2.7.1 ℓ Values

The ℓ value is the relative orbital angular momentum between a pair of nuclei. In this context where the recoil reaction is $^{22}\text{Mg} \rightarrow ^{21}\text{Na} + p$, it relates the relative orbital angular momentum between the recoil nucleus ^{21}Na and the proton. It has possible values of $\ell = 0, 1, 2, 3, \dots$ etc. The symmetric, even-numbered Legendre polynomials are used to fit the corrected angular distribution spectra in Chapter 5. The ℓ value of the decay is determined by the fit. The assignment is made as the lowest ℓ value where $\chi_{red}^2 \sim 1$. A general Legendre polynomial of order ℓ is expressed in Equation 2.7.1. The first four even Legendre polynomials are shown in Figure 2.5. The Legendre polynomials,

$$P_\ell(x) = \frac{1}{2^\ell \ell!} \frac{d^\ell}{dx^\ell} [(x^2 - 1)^\ell], \quad (2.7.1)$$

form the complete set of solutions to the differential equation [43]:

$$\frac{d}{dx} \left[(1 - x^2) \frac{d}{dx} P_\ell(x) \right] + \ell(\ell + 1) P_\ell(x) = 0. \quad (2.7.2)$$

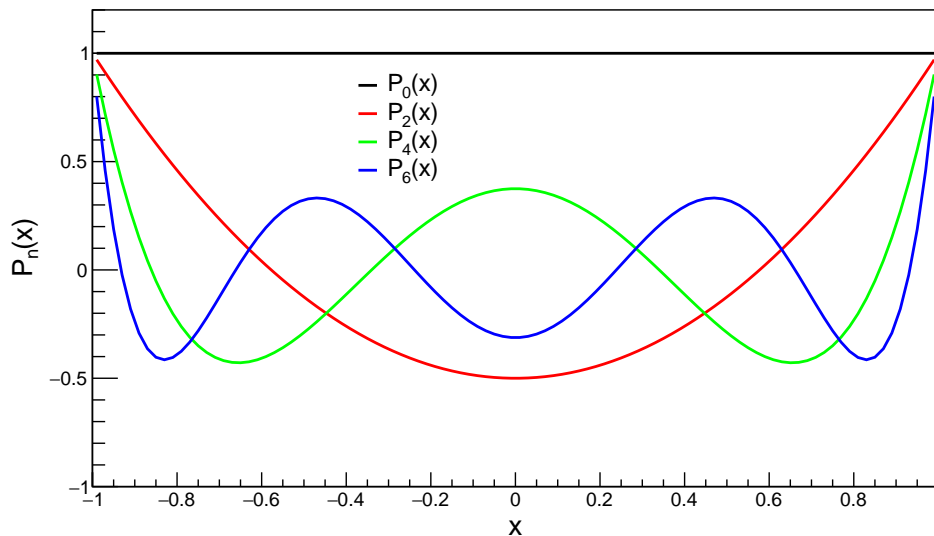


Figure 2.5: The first four even Legendre polynomials $P_{2l}(x)$ for a unitless variable x . These even-numbered, symmetric polynomials are solutions to the angular correlation function.

In the analysis the ℓ value is used to construct the angular correlation function to correct for the missing solid angle of the silicon detector array. This will be discussed in the next section.

2.7.2 Angular correlation functions

Angular correlation measurements are used to determine the angular momenta of nuclei that form part of a particular nuclear reaction. The angular correlations influence the nonuniform intensity distribution of the decay from the recoil nucleus [12] which can be described by an angular correlation function. Reconstruction of the angular correlation function allows for corrections to the differential yields detected by ancillary detector systems that do not cover the entire solid angle and, therefore, do not detect all particles from the reaction of interest. Angular correlations can be expressed as a linear combination of Legendre polynomials:

$$W(\theta) = \sum_{\ell=0,2,\dots}^{\ell_{max}} A_{\ell} P_{\ell}(\cos(\theta)), \quad (2.7.3)$$

where A_{ℓ} are numerical coefficients from the Legendre fits when determining the ℓ values, P_{ℓ} are the even-numbered Legendre polynomials and $\theta_{c.m.}$ is the polar angle in the centre-of-mass reference frame of the recoil nucleus.

A general function $f(x)$ which is finite and single valued in a specified region can be expressed as a series of Legendre polynomials as they form a complete

orthogonal basis. This is the origin of the angular correlation function:

$$f(x) = \sum_{n=0}^{\infty} A_n P_n(x) \quad x \in [-1, 1]. \quad (2.7.4)$$

This is equivalent to:

$$f(\theta) = \sum_{n=0}^{\infty} A_n P_n(\cos\theta) \quad x \in [0, \pi]. \quad (2.7.5)$$

The angular correlation function is used to calculate the yield in an angular region:

$$Y = 2\pi \int_0^{\pi} W(\theta) \sin\theta d\theta. \quad (2.7.6)$$

Equation 2.7.6 can be transformed by substitution of $x = \cos\theta$. Thus $dx = -\sin\theta d\theta$ with $\cos(0) = +1$ and $\cos(\pi) = -1$. The equation becomes:

$$Y = -2\pi \int_{+1}^{-1} W(\theta) dx = 2\pi \int_{-1}^{+1} W(\theta) dx. \quad (2.7.7)$$

From Equation 2.7.7 the true yield of p_i decay can be calculated by integration of the reconstructed angular correlation function. It is this yield which, with the singles yield for the same resonance or same energy region, is used to calculate the p_i branching ratios, B_{p_i} .

2.7.3 Spin-parity (J^π) assignments

Spin-parities (J^π) of resonances are based on the ℓ -value assignments for the decays and the angular momentum selection rules. The selection rules that will be used here that determine the way in which the spins couple and how the parity is determined are shown in Equations 2.7.8 and 2.7.9. They are [12]:

$$\vec{J} = \vec{\ell} + \vec{j}_1 + \vec{j}_2 = \vec{\ell} + \vec{s}, \quad (2.7.8)$$

and

$$\Pi = \pi_1 \pi_2 (-1)^\ell, \quad (2.7.9)$$

where $\ell = 0, 1, 2, \dots$ is the orbital angular momentum of the pair of decay nuclei and the channel spin is given by the vector sum $\vec{s} = \vec{j}_1 + \vec{j}_2$ [12]. The individual spins \vec{j}_p and $\vec{j}_{21\text{Na}}$ can only couple to a unique value of \vec{s} so that:

$$s = |\vec{j}_p - \vec{j}_{21\text{Na}}|, |\vec{j}_p - \vec{j}_{21\text{Na}}| + 1, \dots, \vec{j}_p + \vec{j}_{21\text{Na}}. \quad (2.7.10)$$

The channel spin \vec{s} and orbital angular momentum of the decay ℓ are able to couple in such a way that:

$$\vec{j} = \vec{\ell}_p \pm \vec{s}. \quad (2.7.11)$$

The different possible ways for an initial state with spin j to decay via $\vec{\ell}$ and couple to \vec{s} is given by [12]:

$$|\vec{j} - \vec{s}| \leq \ell \leq \vec{j} + \vec{s}. \quad (2.7.12)$$

These equations will be used in Chapter 5 Subsection 5.3.6 to determine the possible J^π assignments given a certain ℓ value.

Chapter 3

Experimental Setup and Method

Nature is our kindest friend and best critic in experimental science if we only allow her intimations to fall unbiased on our minds.

Michael Faraday

3.1 Introduction

The experiment for this study impinged a 100-MeV proton beam onto a ^{24}Mg target. The two-nucleon pick-up reaction (p, t) was the focus of the experiment in order to populate states in ^{22}Mg . This requires detecting triton ejectiles at the focal plane of the K600 magnetic spectrometer. Various experiments have studied the $^{24}\text{Mg}(p, t)^{22}\text{Mg}$ reaction in past years [13, 32, 35]. These experiments have been used to elucidate the structure of ^{22}Mg which has implications for the astrophysically relevant $^{21}\text{Na}(p, \gamma)^{22}\text{Mg}$ and $^{18}\text{Ne}(\alpha, p)^{21}\text{Na}$ reactions. The aim of this study was to use a novel approach of performing the $^{24}\text{Mg}(p, t)^{22}\text{Mg}$ reaction in order to determine the proton branching ratios from ^{22}Mg to ^{21}Na .

This experimental method is novel because it uses a high-resolution spectrometer in coincidence with a silicon-detector array to examine the structure of ^{22}Mg . This led to the collection of information regarding the proton decays from the excited ^{22}Mg nucleus. In this chapter the experimental apparatus and techniques used to perform the $^{24}\text{Mg}(p, t)^{22}\text{Mg}$ reaction at the iThemba Laboratory for Accelerator Based Sciences (LABS) will be discussed. The K600 magnetic spectrometer and the Coincidence Array for K600 Experiments (CAKE), that were crucial in performing this experiment, will be discussed in detail.

3.2 iThemba LABS SSC facility and the K600 magnetic spectrometer

The Separated-Sector Cyclotron (SSC) facility at iThemba LABS predominantly provides light-ion stable beams to the K600 experimental vault and other experimental vaults at iThemba LABS. The SSC can also generate heavy-ion beams such as ^{136}Xe which is used for predominantly high-spin state physics. This isochronous sector cyclotron has four sectors and can accelerate proton beams to 200 MeV. A layout of the facility is shown in Figure 3.1. This section will discuss the components that form part of the beamline before reaching the spectrometer since it is regarded as an entity that forms a single ion-optical system.

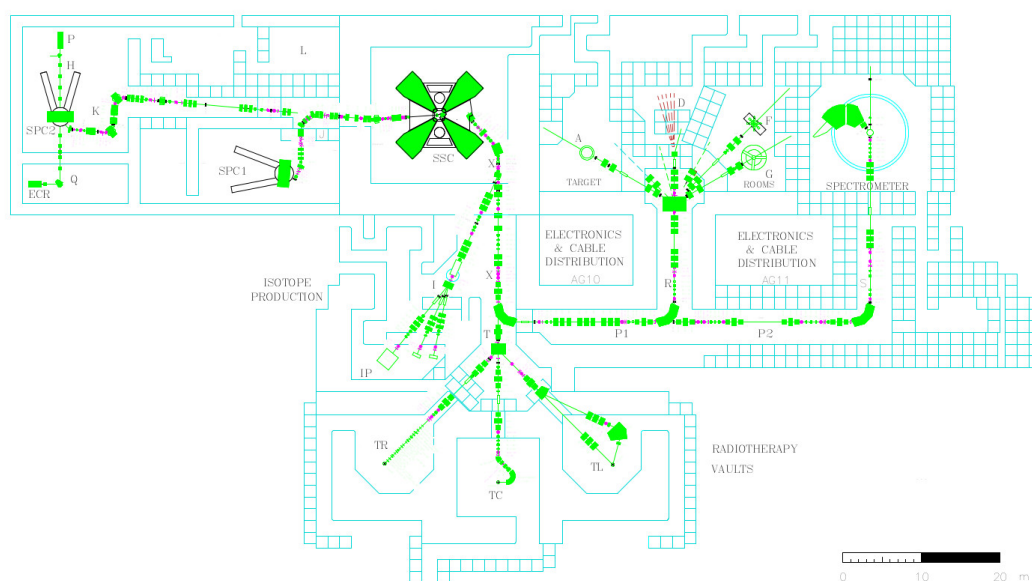


Figure 3.1: The diagram shows the layout of the SSC facility at iThemba LABS.

Ions are initially injected to the beamline at the Electron Cyclotron Resonance (ECR) ion source where the particles are completely ionised. The ECR causes electrons to undergo circular motion due to the Lorentz force when placed in a static, uniform magnetic field. Ionisation occurs due to the injection of microwaves into the ion source volume at the corresponding resonance frequency. The free electrons within the volume are excited to above the ionisation energy of the hydrogen atom which results in a stream of protons being produced and that can be extracted from the ECR. The ions can be confined for longer periods of time inside the ECR and heavier ions undergo multiple collisions to become multiply charged.

After ionisation the charged particles travel to a Split-pole Cyclotron (SPC2), with an energy constant $K=8$, which serves as an injector cyclotron to the SSC. The SSC has a characteristic radio frequency (RF) that is used as a rapidly alternating electric potential applied to its dipoles in order to change the direction of the field which is needed for acceleration. The SSC emits the beam as a stream of discrete beam packets. Choosing to work with pulse selection of 1 in 5 for this experiment means only every 5th beam packet was allowed to travel down the beamline and impinge upon the target. By using pulse selection the time gap between events is larger to allow emitted protons from the decay of excited ^{22}Mg nuclei to reach the CAKE before the next pulse arrives.

After full acceleration by the SSC the beam moves into the X line. Once exiting the X line the beam moves to the P line using a bending magnet (B1P) before reaching a second bending magnet (B3P) to enter the S line that leads to the spectrometer. The presence of two bending magnets reduces the amount of lower-energy "halo" particles because most of these particles will have rigidities that result in them being deflected out of the beam and not able to reach the spectrometer.

The proton beam obeys the law of phase-space conservation which is known as Liouville's theorem, i.e. the area within the phase space contour is conserved [44]. This describes the beam emittance. Emittance is one of the properties of charged particle beams and is defined as the area of the beam spot which resembles the shape of an ellipse [45]. The area of the ellipse corresponds to the average spread of particles and their associated coordinates in position and momentum phase space.

Of particular importance are slits 9X and 12X (before B1P) and 1P (after B1P). 9X is an object slit and 12X is an emittance slit. These greatly affect the resolution and halo downstream at the target due to the divergence the slits cause. Consequently, the beamline from slit 9X to the spectrometer focal plane forms a single ion-optical system. Slits 9X and 12X affect the beam divergence whereas slit 1P cuts down on the energy range of the beam to ensure that it is monoenergetic so as to cut down on beam dispersion. They are therefore important due to their effect on the position and energy resolution of the beam which is crucial in a high-resolution spectrometer experiment operating at $\theta_{\text{lab}}=0^\circ$. All slit positions can be determined in Figure 3.1. They are checked by the beam operators during the experiment to see if they are set properly which is partially done by checking the halo level and beamspot on the beam viewers and harps.

3.3 The K600 magnetic spectrometer

This experiment was performed with the K600, high-resolution, low-acceptance ($\Omega=3.48$ msr) magnetic spectrometer with a quadrupole-dipole-dipole (Q2D)

configuration. The K600 functions as a momentum analyser of energetic charged particles. Particles that enter the spectrometer have a specific momentum and magnetic rigidity based on their energy, charge and mass. Particles with varying momenta will consequently have different flight paths through the spectrometer (see Figure 3.5).

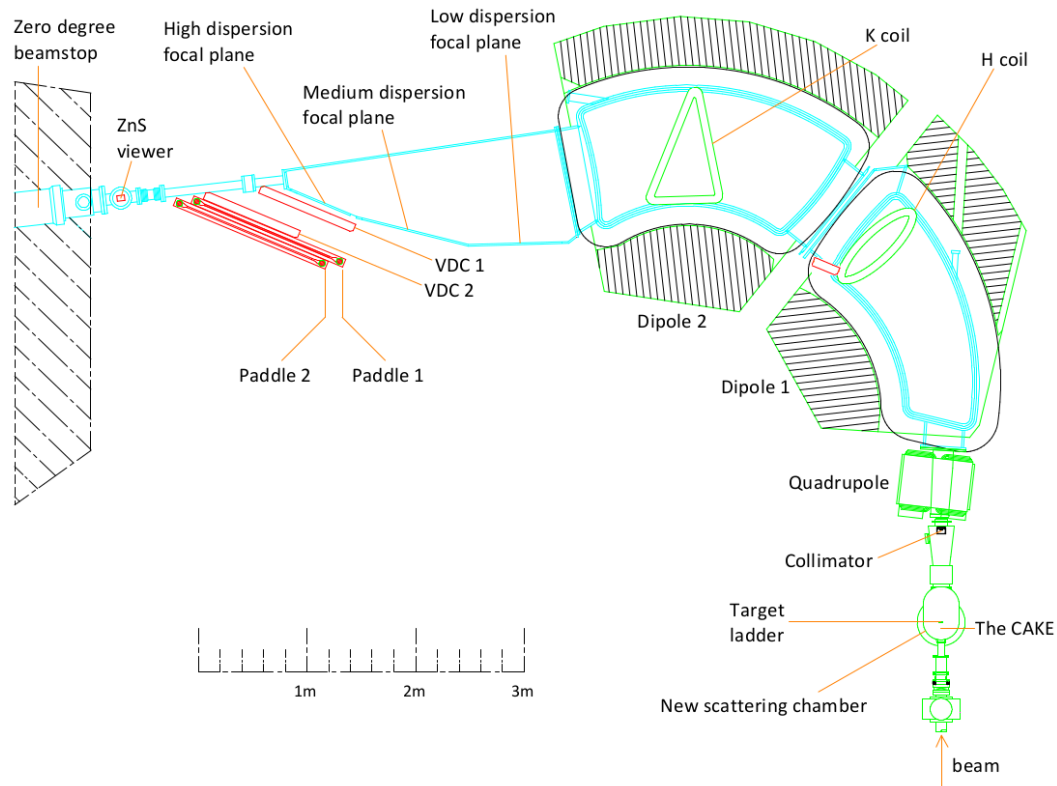


Figure 3.2: The diagram shows the layout of the K600 magnetic spectrometer at $\theta_{\text{lab}}=0^\circ$. It has an angular acceptance of $\pm 2^\circ$.

A special (p, t) beamstop inside the first dipole, instead of the zero-degree beamstop, was used to stop the unscattered beam of protons since the rigidity of the unscattered proton beam is higher than that of the triton ejectiles. The beamstop is shown in Figure 3.3. Additionally, the focal-plane detectors were moved to the medium-dispersion focal plane for this experiment. The reason for this was to cover the correct momentum range of interest relevant to this experiment.

Before the start of this experiment, the position where the beamstop should be placed was determined by using the program TRACK v8.6. It was used to calculate the trajectory of scattered and unscattered particles within the spectrometer by taking into account the magnetic-field settings of the experiment as well as the magnetic rigidity of the particles. The beamstop position is thus inferred. Having an accurate indication of where the beamstop should be placed is important. Without it being placed in the correct position the

unscattered protons would cause a large amount of unwanted activation within the spectrometer and at the focal plane. It would also cause a large amount of background events to be present in the dataset. Additionally, the sheer amount of particles would cause the focal-plane detectors and the data acquisition system to crash.

The two dipoles, D1 and D2, are the primary bending magnets that steer the scattered triton ejectiles onto the focal plane. The quadrupole vertically focusses the ejectiles that enter the K600 aperture after collimation. The H coil (in D1) and K coil (in D2) are used to correct for higher-order aberrations in the magnetic field. The K coil corrects for first-order aberrations using dipole and quadrupole components. The H coil makes a second-order correction using a dipole and hexapole component. All of these components working in unison are vitally important as they act as a unit in order to separate the flight paths of the various particles based on their momenta.



Figure 3.3: The (p, t) beamstop situated in the first dipole magnet D1 is shown. The beamstop is removed only after a few days once the experiment has ended given its high initial activity after being bombarded with 100-MeV protons.

A program developed for the K600 called Spexcit is used to calculate the magnetic fields for the quadrupole and two dipoles that will steer tritons with a $+1$ charge state onto the focal plane. The graphical user interface thereof is shown in Figure 3.4. Once the currents, and thus magnetic fields, have been determined, the values are input to the system which starts to set them by driving the magnetic field through a hysteresis loop [44]. This starts a setting cycle to cancel out the memory of the previous magnetic field setting.

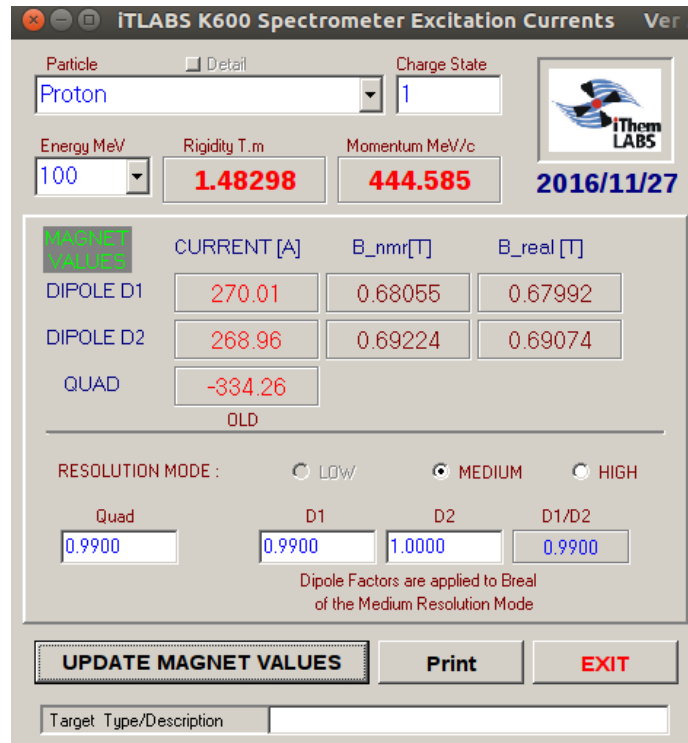


Figure 3.4: SPEXCIT allows the user to select various stable-beam projectiles in various charge states. After the beam energy, in MeV, is selected the program is able to calculate the required current and magnetic-field values for both dipoles and the quadrupole.

3.3.1 Dispersion matching

The inherent momentum distribution Δp of the incoming beam limits the energy resolution measured in the K600 focal plane. However, despite the properties and limitations of the beam, there is a solution to this. Dispersion matching is the process whereby the energy resolution can be improved and optimised up to the limit of the resolving power of the analysing spectrometer [44]. This occurs when the beamline and spectrometer are properly dispersion matched so that the resolution measured at the focal plane of the K600 is improved to a point where it is better than the energy (momentum) spread Δp of the proton beam used for this experiment. It is, therefore, evident that dispersion matching was an important part of this experiment as it is necessary to have an optimised spectral resolution to resolve states.

As the energy (momentum) of the incoming beam increases the spread in energy (momentum) Δp also increases. Lateral dispersion matching is achieved by using the spectrometer beam optics to focus the different energies of the beam of scattered particles at the focal plane. The different energies of the scattered beam correspond to different energies of the initial incoming proton beam. To achieve this form of dispersion matching the trajectories of scat-

tered beam particles with different momenta have to be separated spatially. Particles with less momentum ($-\Delta p$) move along the inner gyroradius of the spectrometer and travel a shorter distance through the spectrometer to the focal plane. Particles with higher momentum ($+\Delta p$) travel along the outer gyroradius and have a larger distance to travel to the focal plane. This effect is shown schematically in Figure 3.5 [46]. The position resolution is thus improved. However, this form of focussing creates a momentum dependence of the trajectory angle of the ejectiles through the focal plane (θ_{FP} , see Section 4.3 for further explanations). To compensate for this and to remove the dependence, angular dispersion matching is used in addition to lateral dispersion matching. This allows for a more accurate reconstruction of the initial scattering angle of the particles [47].

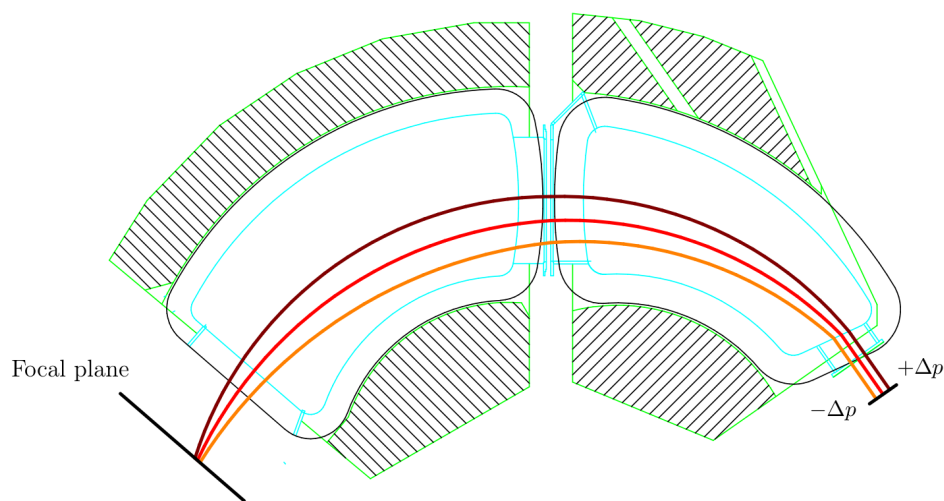


Figure 3.5: Triton ejectiles with varying momenta travel along different bending radii through the spectrometer to the focal plane so as to achieve lateral dispersion matching.

In order to optimise the focal-plane resolution with the dispersion-matched 100-MeV proton beam, a greatly reduced beam is steered directly onto the focal plane. It has a lowered intensity using beam-attenuation meshes as shown in Figure 3.6. These are placed between the ECR source and SPC2 injector cyclotron (see Figure 3.1). The meshes lower the beam intensity without altering the beam profile. The intensity lowers from 10^9 pps to 10^2 - 10^3 pps at the focal plane. The faint beam method was initially found to be effective for simultaneous lateral and angular dispersion matching when $\theta_{K600} = 0^\circ$.

3.3.2 The small-angle mode scattering chamber

After moving into the S-line the beam enters the small-angle mode scattering chamber (see Figure 3.7) just before it reaches the spectrometer. The chamber

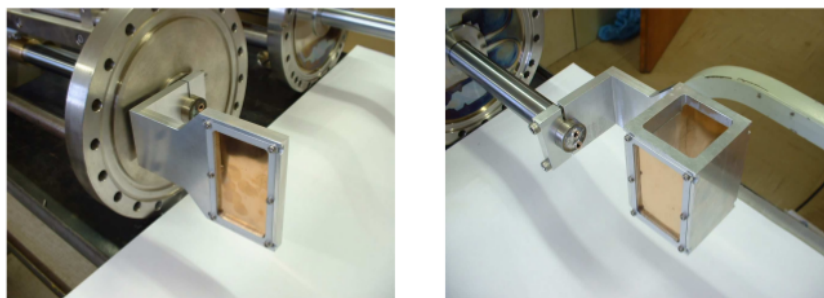


Figure 3.6: The beam-attenuation meshes [44] only allow a fraction of the beam to pass through to enable faint-beam tuning. This method is used to optimise the resolution.

was designed with the intention of having an MMM-type silicon-detector array called the CAKE (see Section 3.4) placed inside it. The chamber initially operated at only two fixed angles: 0° and 4° . The functionality of the chamber was improved in 2017 by adding a flange to the side of the chamber that now allows it to operate within a 7° - 31° range.

Mounting the silicon-detector array has been greatly simplified since all MMMs are mounted on an aluminium frame that, in turn, is directly mounted onto the scattering chamber frame when needed. The net result is a significant decrease in the time taken to setup the MMM array within the scattering chamber. For a different view of the scattering chamber, the silicon-detector array inside the chamber is shown in Figure 3.14 (see Section 3.4).

The target ladder is shown vertically upright inside the chamber in Figure 3.7. The target ladder connects to its control mechanism which is fixed onto the frame of the chamber with a PVC flange for electrical isolation. The LEMO feedthrough connectors are used to relay the signals from the CAKE array to their respective preamplifiers. The mounting bracket of the CAKE array attaches directly to the frame of the chamber. Beyond the chamber exit it is connected by a flange to the collimator which selects ejectiles within a scattering angle of $\pm 2^\circ$. The charged particles that consequently move past the spectrometer aperture and through the spectrometer itself are then detected at the focal plane.

3.3.3 The VDC detection system

Magnetic spectrometers momentum-analyse scattered beam particles. The focal plane detector system of the K600 consists of two plastic scintillating paddles (discussed in the following section) and two vertical drift chambers (VDCs) to track these beam particles. The VDCs are wire-plane detectors that determine the physical wire-plane position of the charged particle ejectiles in order to infer their magnetic rigidity and, ultimately, the excitation energy

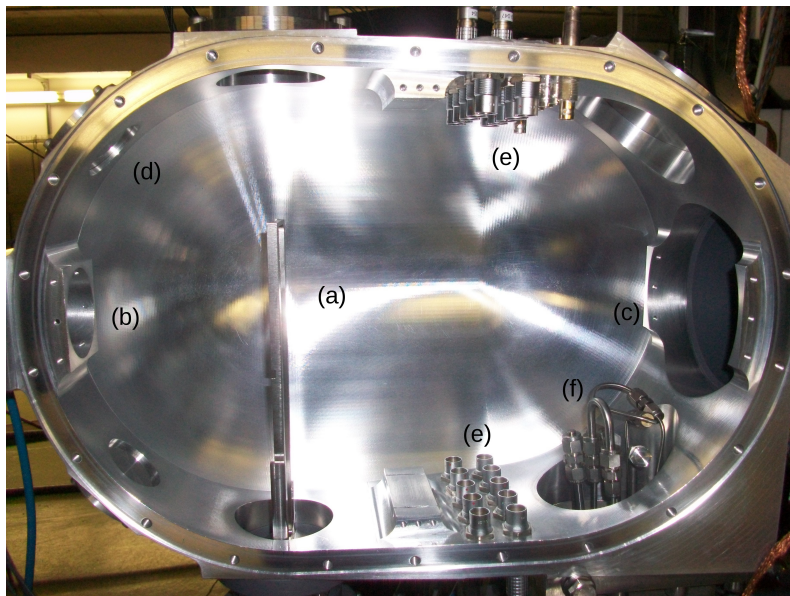


Figure 3.7: A side view of the scattering chamber (upstream on left-hand side). It was milled from aluminium to minimise the amount of activation during experiments. The target ladder is shown vertically upright at (a). The chamber entrance is at (b) and the chamber exit is at (c). A perspex window is used at (d) to close the opening. The LEMO feedthrough connectors are shown with labels (e). Various inlet/outlet pipes are labelled (f) that can be used to channel gas or liquid into or out of the chamber. However, this wasn't used during this experiment.

of the ^{22}Mg recoil nucleus (see Section 4.4). The VDCs are, therefore, a crucial part of the K600. This section will discuss the operating principle of the VDCs.

Various VDCs can be used in the focal plane detector system. The older set of VDCs only has an X wireplane to reconstruct horizontal position information. The newer set (which is used as per default) has an X and U wireplane (for partial vertical position reconstruction). For this study, one new VDC and one older VDC was used to have a sequence of wireplanes of XUX mounted on the medium-dispersion focal plane. The design of the newer VDCs is shown in Figure 3.8. The detectors are made up of various layers. The two planes that can be seen protruding from the top are the X and U wireplanes which are inserted in between three high voltage cathode planes. The opening of the detector is comparable in surface area to the vacuum exit of the K600 and allow for the scattered beam particles to pass through the VDC and reach the scintillating detectors. The spectrometer vacuum exit is sealed by a frame that has a $75\text{-}\mu\text{m}$ thick Kapton window mounted on it. Kapton is used because of its strength to withstand the differential pressure between the spectrometer vacuum ($\sim 10^{-5}$ mbar) and atmospheric pressure. Therefore, it is chosen to ensure the integrity of the spectrometer vacuum. Tritons with $E \gtrsim 50$ MeV

have enough energy to pass through the focal plane detectors.



Figure 3.8: The design layout of one of the new VDC detectors [44].

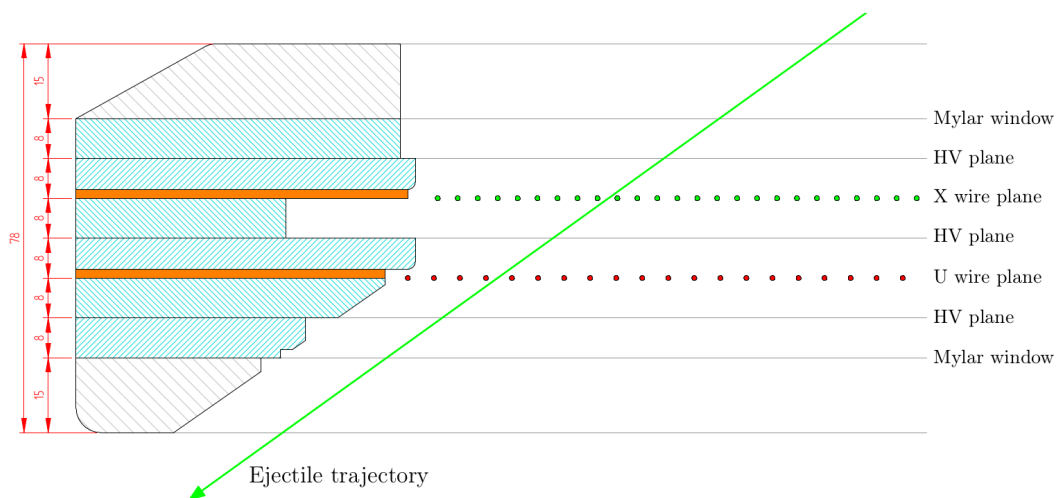


Figure 3.9: A schematic top-view cross section of a VDC [46]. The wireplanes and high-voltage planes are all spaced 8 mm apart. The entire assembly is enclosed by two frames with 25- μm thick Mylar ($(\text{C}_{10}\text{H}_8\text{O}_4)_n$) windows to isolate the internal chamber and detection gas from outer atmosphere.

The X wireplane is used to infer the horizontal position of the ejectiles. It has 198 signal wires interspersed with 201 guard wires (2 additional guard wires at the extremities of the wireplane). The wires are vertically parallel to each other. The signal wires are 4 mm apart, with a guard wire in between. All

wires are made of gold-plated tungsten for its conductivity and strength. The diameter of the signal wires were chosen to be as small as practically possible to have strong electric-field gradients. This causes the electrons to accelerate as they approach the signal wires. As their energy increases they are able to ionise other Ar atoms (see end of this section) liberating more electrons along the way. This quickly leads to an electron avalanche which is large enough to be detected by the signal wires. Consequently, the signal wires are all $20\text{-}\mu\text{m}$ thick with the guard wires being $50\text{-}\mu\text{m}$ thick. The boundary guard wires are $100\text{-}\mu\text{m}$ thick. The guard wires have applied potential differences of 500 V and the signal wires are grounded through the preamplifiers [44]. Figure 3.10 shows the working principle of the VDCs in tracing the trajectory of a particle. The drift electrons will move under the influence of the electric field towards the signal wires. The electric field gradient increases exponentially nearest the signal wires, causing the electron avalanche.

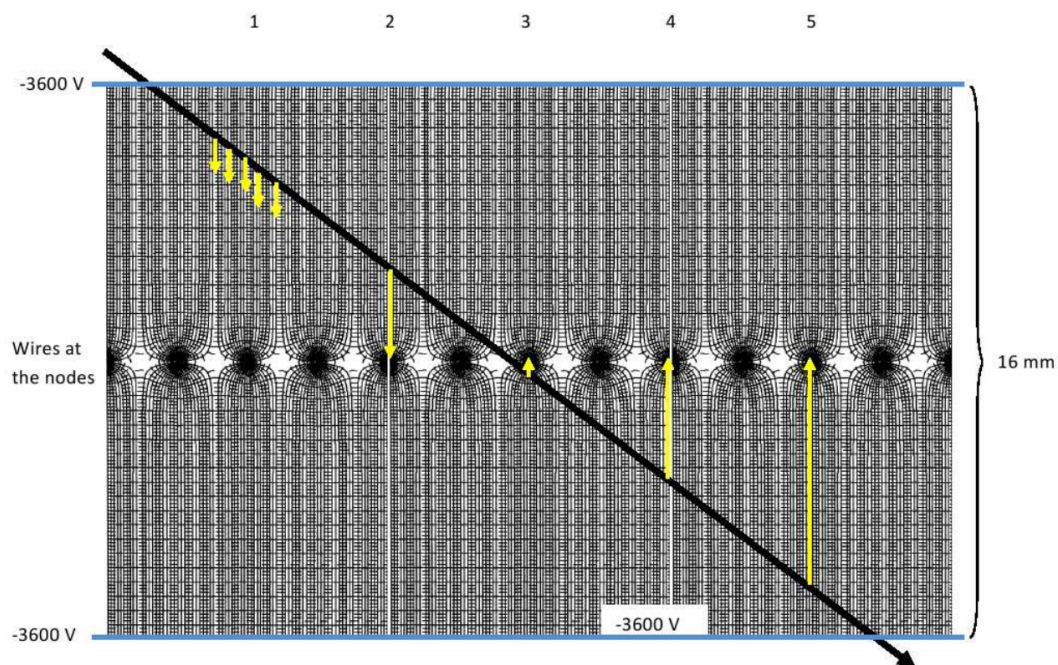


Figure 3.10: A particle trajectory through one of the VDC wireplanes. The electric fields of the signal and guard wires are included in this illustration to show the effect they have on the liberated drift electrons. A hypothetical scenario of five signal wires being triggered is shown.

The U wireplanes have 143 signal and 146 guard wires (also including two outer guard wires) and are used for partial vertical position reconstruction. The wires are parallel to each other and at an angle of 50° relative to horizontal. The perpendicular distance between these wires is also 4 mm.

The delicate high-voltage planes are made from ordinary grocery store aluminium foil (27- μm thick). The foil has to be perfectly smooth to ensure an even electric field distribution which is necessary for uniform electron drift and signal detection in the detector. Upon assembling these planes, a specialised mounting frame is used to place the foil over one of the empty high-voltage frames. A vacuum pump is connected to the foil mount which makes it contract over the empty frame, thereby removing all creases. The foil is secured to the frame with 24-hour slow-drying epoxy.

The detection medium for the K600 VDCs is Ar quenched with CO_2 (9:1 ratio) that is circulated through the detector continuously at atmospheric pressure. Tritons that pass through the gaseous detection medium of the VDCs will collide with argon and liberate electrons creating electron-ion pairs. It is these electrons that drift under the influence of the electric field to the signal wires that register an event. The CO_2 prevents charge build-up within the detectors that may damage it and prevents unwanted background signals.

Signals from the wireplanes are first relayed to preamplifier cards that connect directly onto the wireplanes. These are P-TM 005 16-channel preamplifier/discriminator cards from the Technoland Corporation Ltd company [44]. 13 preamplifiers are needed for all of the X-plane signal wires whereas 9 preamplifiers connect to the U plane. The data is then sent from the preamplifiers to multiple TDC modules using 50-pin ribbon cables.

During the experiment, the high-voltage planes of the first (new) VDC had a potential difference of -3.56 kV whereas the second (old) VDC high-voltage planes were set to -3.65 kV. VDC detector efficiencies of 90%+ were recorded for the duration of the experiment.

3.3.4 Scintillating detectors

An important feature of the K600 focal plane is the scintillating detectors. They provide the K600 with a trigger signal that is relayed to the DAQ so that information regarding each event can be stored. The trigger signal relative to the Radio Frequency (RF) of the SSC gives the time-of-flight (TOF) through the spectrometer for a particle. For (p, t) reactions the triton locus in the spectrum is separated completely from other events such as unscattered particles that have not interacted with the target or that have scattered within the spectrometer. A gate on the events of interest therefore included relatively few background events. A PID plot for this experiment is shown in Figure 4.1 which illustrates the points mentioned.

The scintillators operate on the basis of energy conversion: energy deposited in the material by charged particles is converted into light energy. As a result of the interaction between the charged particle and scintillator material, a certain amount of photons are released depending on the energy and identity of the particle. The resultant photons travel through the scintillating material and the lightguides to two photomultiplier tubes (PMTs), one

mounted on each end of the detector. The lightguides bend through 90° and are used to mount the detectors closer to the beamline and thus reduce the unmeasured low excitation region to a minimum.

Photocathodes convert the scintillator photons to electrons by way of the photoelectric effect. This signal is amplified by the dynode chain of the PMT and further processed into a trigger pulse. A valid event is recorded when a signal is detected at both ends of the detector. As a result, the final charge is dependent on the initial charge and thus the number of scintillation photons. Therefore, the output signal from the detector is proportional to the energy deposited by the particle in the scintillating material.

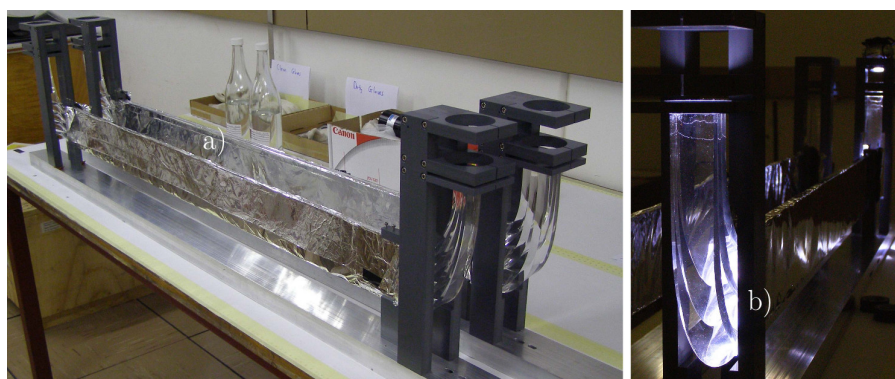


Figure 3.11: The plastic scintillating detectors during assembly [46]. The scintillator has to be wrapped in mylar, as seen in (a), to allow more of the scintillator light to be collected at the ends. The 90° adiabatic twisted lightguides are highlighted in (b) which connect the scintillator to the PMTs. The entire assembly is covered in black material during final assembly to limit background light contamination.

Various types of scintillator detectors with various properties exist with the type of detector chosen being dependent on the experiment at hand. The K600 focal plane contains as standard two scintillating detectors: one with a width of $\frac{1}{2}$ " and $\frac{1}{4}$ ". The surface area of each scintillator is $1219.2 \times 101.6 \text{ mm}^2$. For this experiment both detectors were used.

3.4 The CAKE array

The Coincident Array for K600 Experiments (CAKE) is a silicon-detector array in a lampshade configuration. The array has 5 MMM-type double-sided silicon-strip detectors (DSSSDs) with each having a thickness of $400 \mu\text{m}$. The detector array is mounted as a unit inside the small-angle mode scattering chamber of the K600 magnetic spectrometer and is used to detect charged-particle decays from the recoil nuclei of the nuclear reaction. For this study,

the CAKE was used to detect protons from the recoil nucleus ^{22}Mg after the triton ejectile was emitted following the direct, two-nucleon transfer (p, t) reaction. The CAKE is mounted upstream relative to the ^{24}Mg target to limit the amount of radiation damage to it and to limit the amount of halo detected by it. A diagram that shows the CAKE and how it is mounted in the scattering chamber is shown in Figure 3.12.

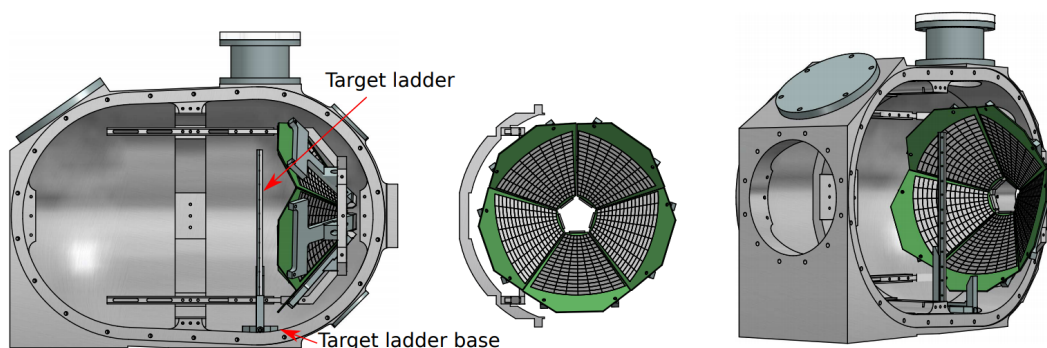


Figure 3.12: Three computer-generated diagrams of the CAKE [48] at different viewpoints. The left image shows the CAKE inside the small-angle mode scattering chamber from beam-left side. The position of the target ladder relative to the detector is indicated. The beam direction is from right to left. The centre image shows the upstream view of the full lampshade geometry and the right image shows the upstream view of the CAKE mounted in position.

The detector setup within the scattering chamber is shown in Figure 3.13. The various openings of the chamber are closed with either transparent perspex or aluminium flanges. The transparent flanges are covered in black paper to prevent any light from entering the chamber and creating leakage currents within the detectors which may damage them if the current is great enough. These flanges are used to be able to view the ZnS target with a camera when tuning the beam.

The K600 is a low-acceptance, high-resolution spectrometer that can operate at 0° to select low angular-momentum transfer reactions. Using the CAKE in coincidence with the K600 provides a very powerful way of studying nuclear reactions and simultaneously observing decay from the recoil nucleus to deduce the nature of other nuclear structures. ^{22}Mg and subsequent proton decay therefrom reveals information regarding the decay of states to the ^{21}Na nucleus which controls the rates of the $^{21}\text{Na}(p, \gamma)^{22}\text{Mg}$ and $^{18}\text{Ne}(\alpha, p)^{21}\text{Na}$ reactions. It is due to that reason that this experimental setup is so powerful for studies in the field of nuclear astrophysics.



Figure 3.13: The CAKE seen inside the small-angle mode scattering chamber looking upstream. The IDE (Integrated Drive Electronics) connectors and ribbon cables that relay the detected signals from the CAKE to the Mesyttec preamplifiers through various 16-pin LEMO-feedthrough connectors are visible. The target ladder is not installed at this point.

A downstream view of the CAKE can be seen in Figure 3.14. The entrance to the spectrometer and the quadrupole can be seen to the right of the scattering chamber.

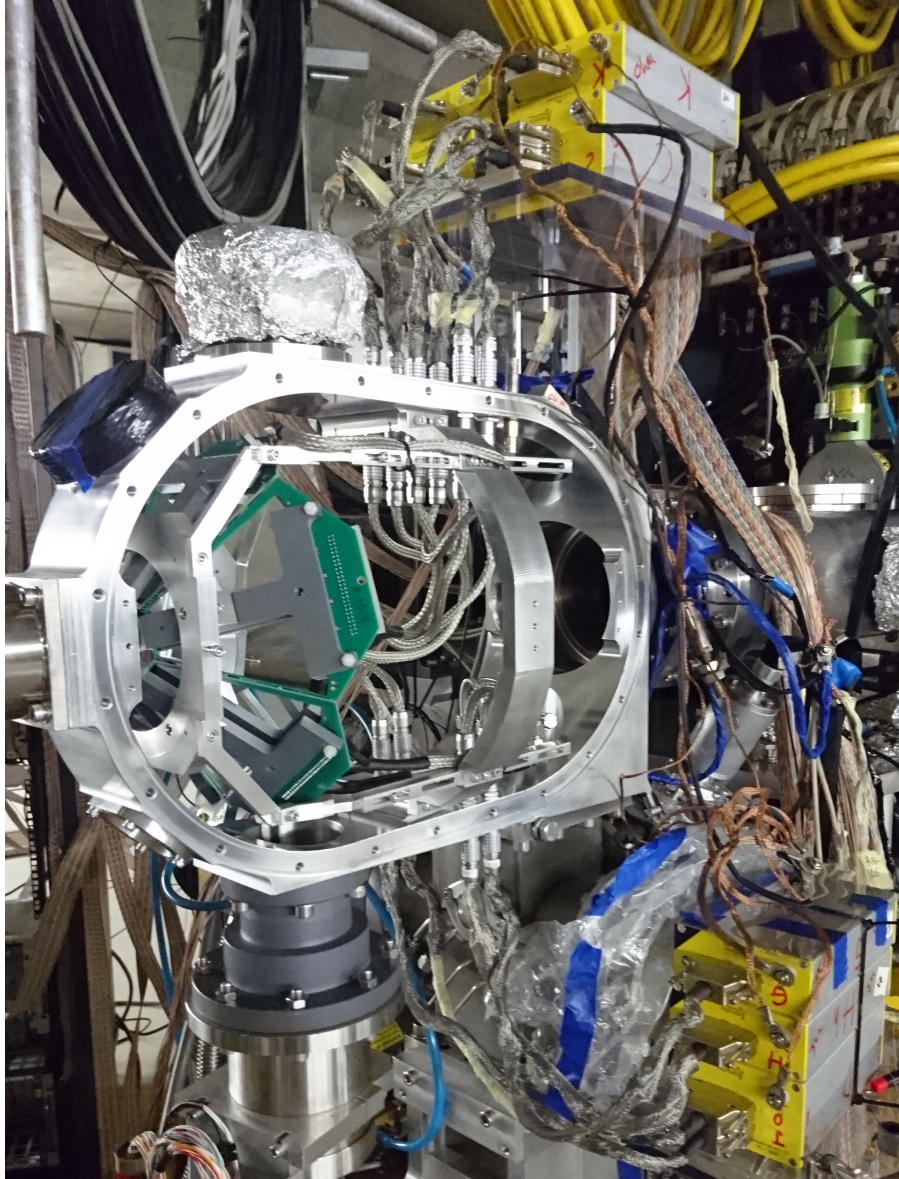


Figure 3.14: The CAKE, in the small-angle mode scattering chamber, seen looking downstream. The entrance to the quadrupole of the K600 spectrometer is also shown. The beam direction is from left to right.

3.4.1 Properties of silicon detectors

Semiconductor detectors such as silicon detectors are used to measure energy deposition from impinging charged particles such as protons or α particles. The density of charge created in the detector can be used in identifying the particle species. This section will expand on the operating principle of these detectors [21].

Electrons in semiconductor materials can exist in one of two different types of energy bands. These are the valence and conduction bands. The valence electrons are comprised of the outer electrons in fixed points of the semiconductor crystal. In contrast, electrons that occupy the conduction band of the crystal are able to move freely through it. In order for an electron to be promoted from the valence to the conduction band it must overcome the bandgap: the difference in energy between the aforementioned two energy bands. An electron can receive energy either from an incoming photon or from a charged particle. The promoted electron leaves a hole behind thus creating an electron-hole pair. The gap left behind by the promoted electron can be filled by another electron. Applying an electric field to the material will cause the electrons and holes to move in opposite directions. This movement of charge, according to the Shockley-Ramo theorem [49, 50], creates the signal which is measured on the contacts of the detector.

Electron-hole pairs are destroyed by recombination which leads to an incomplete signal being detected. Recombination occurs when an electron moves from the conduction band back to the valence band and fills a hole [21]. The efficiency of the detector is improved when this effect is reduced. This is done by increasing the drift velocity of charge carriers. To do so, the strength of the applied electric field is increased thereby minimising the charge-collection time.

In order to maximise the charge-collection efficiency of semiconductor detectors, two doped materials are used to achieve the high electric field strengths at which these detectors need to operate. The act of doping silicon, which is a Group IV element, with either Group III elements (such as boron) or Group V elements (such as phosphorous) will either increase or decrease the number of available electrons artificially. Within a silicon crystal, each atom is bonded to four others. When silicon is doped with pentavalent impurities such as phosphorous a surplus of valence electrons are present which creates an n-type semiconductor material. However, when silicon is doped with trivalent impurities like boron, a deficiency of valence electrons exist. More charge-carrying holes are thus created in this case. This is called a p-type semiconductor [12]. A semiconductor junction, more commonly called a p-n junction, is made when these two types of semiconductor materials are combined. In this scenario, the n-type semiconductor has a high concentration of electrons and the p-type semiconductor has a high concentration of holes (or a low concentration of electrons). Electrons will flow freely from the n-type to the p-type semicon-

ductor to recombine with the holes. In the n-type semiconductor, phosphorous will remain as a stationary positive ion within the crystal lattice after donating an electron. Alternatively, boron will exist as a negative ion in the p-type material when an electron combines with a hole. The presence of these ions within the p-type and n-type semiconductor materials establishes an electric field over the p-n junction, creating the depletion zone. This region is empty of all charge carriers and acts as an insulator to prevent a current from flowing across the junction. Current that does flow across the junction is called a leakage current. When the p-type semiconductor has a negative potential applied to it and the n-type semiconductor has a positive potential applied to it, the detector is reverse biased. This effect is illustrated in Figure 3.15. Biasing the detector in this way causes the electrons to flow to the n-type semiconductor whereas the holes will flow to the p-type semiconductor, increasing the size of the depletion zone. Determining the voltage at which the CAKE becomes fully depleted is discussed in Section 3.4.3.

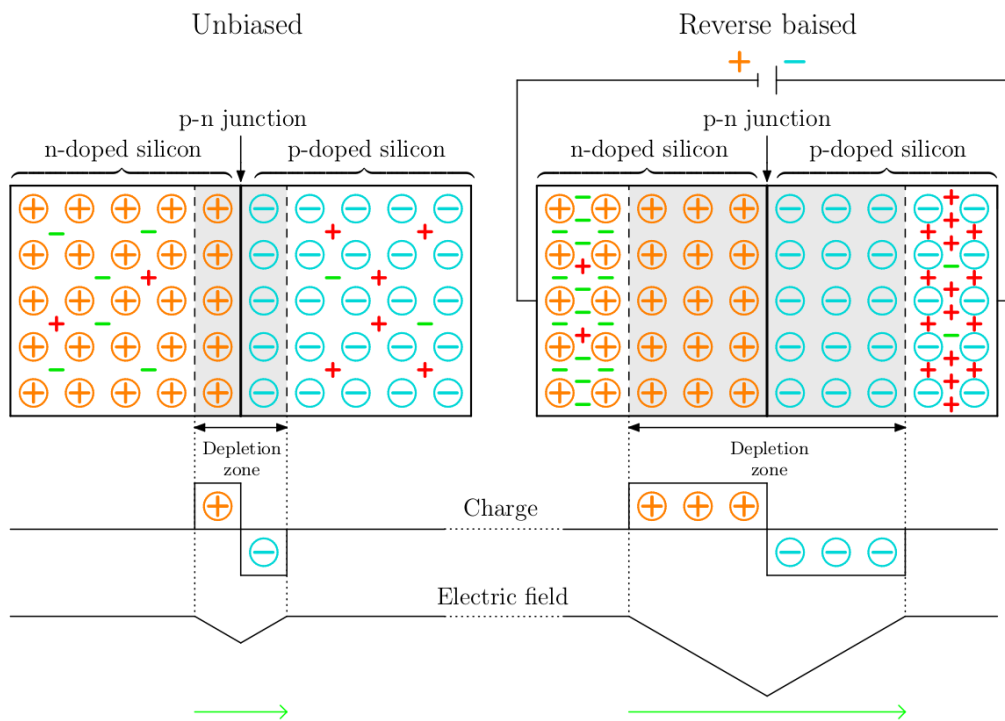


Figure 3.15: Illustration of the p-n junction of a silicon detector and the process of reverse biasing the detector [46]. The grey areas represent the depletion zone over the p-n junction. The encircled positive and negative symbols represent the stationary ions within the p- and n-doped semiconductor materials. The green and red charges represent the freely-moving electrons and holes, respectively. The direction of the electric field is indicated with green arrows.

Each MMM detector in the CAKE has 16 rings that form the p-doped side and 8 sectors which form the n-doped side. A diagram of the rings and sectors is shown in Figure 3.16. The p-side is regarded as the front as the resolution thereof is superior to that of the n-side which is the reason that silicon detectors are normally mounted with the p-side facing the beam target. The n-side is used to determine front-back coincidence with the p-side (which designates a valid event) and to provide additional timing gates in order to eliminate as many unrelated events as possible. The simulations for the CAKE and the parameters thereof during the experiment are discussed in detail in the following two sections. Additionally, the calibration process for the CAKE is discussed in Chapter 4 under Section 4.5.

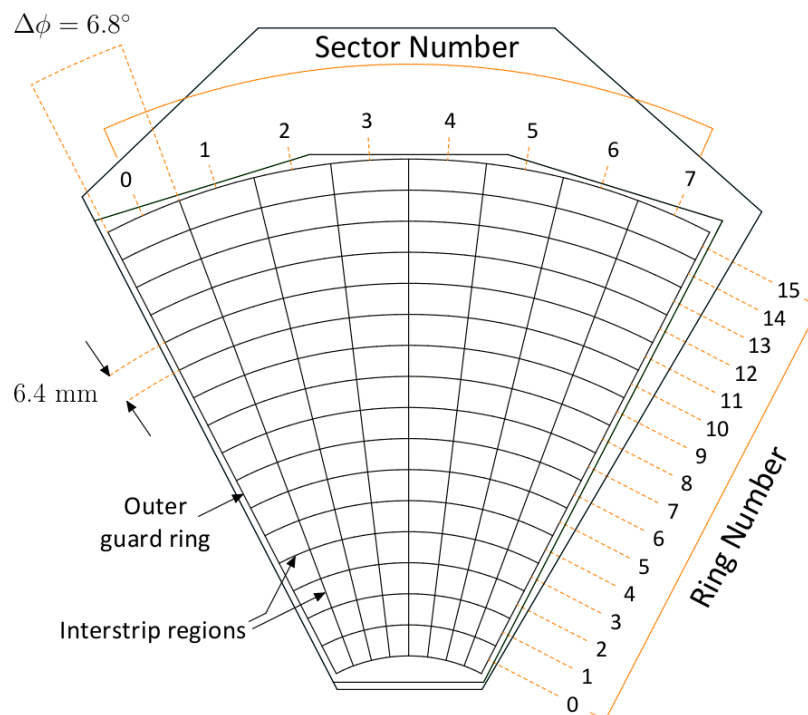


Figure 3.16: A schematic diagram of an MMM-type detector in the CAKE [46]. The numbering of ring and sectors is shown with the outer guard ring and interstrip regions indicated.

3.4.2 GEANT4 simulations for the CAKE

A Monte Carlo (or probability) simulation was previously written with GEANT4 for the CAKE silicon detector array [51]. This was modified and used for this experiment to simulate the efficiency of the CAKE as well as the solid angle subtended by each ring and sector. The simulation also calculates the kinematics of the reaction to determine the kinetic and excitation energy of

the ejectile and recoil nuclei. An excitation energy region of 6-16 MeV was simulated using random values for the recoil excitation energy. The region was chosen to be above the proton-decay threshold of 5.502 MeV, taking into account detector thresholds of about 500 keV. Figure 3.17 shows the simulation results for the solid angle subtended by the rings of the CAKE. Similarly, Figure 3.18 shows the simulation results for the solid angle subtended by the sectors of the CAKE.

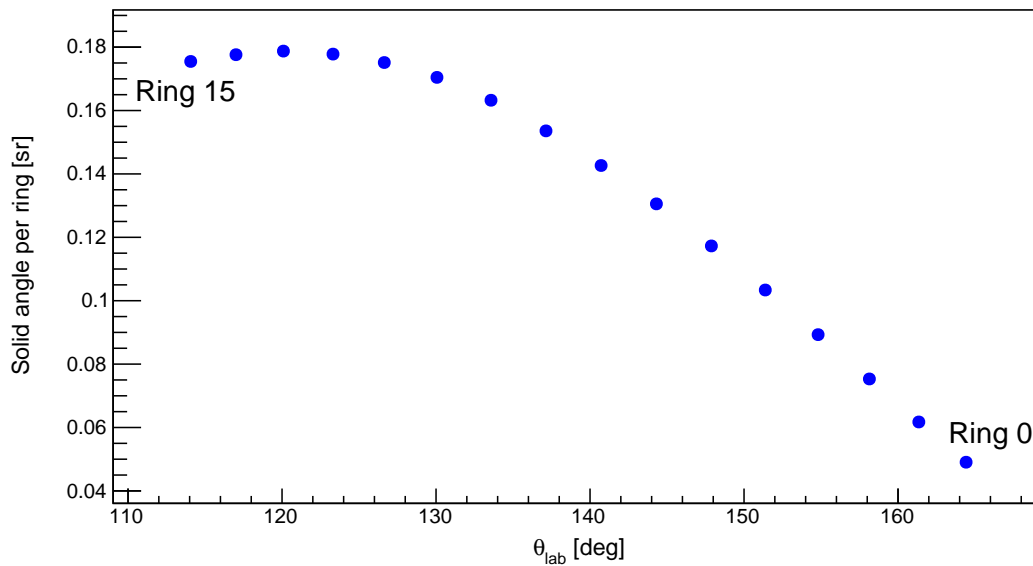


Figure 3.17: Solid angle (in steradians) subtended by each ring of the CAKE plotted against the lab angle relative to the beam axis of each ring. The efficiency of each ring is related to the solid angle by a factor of 4π . The inner rings are smaller and thus cover a smaller solid angle whereas the opposite is true for the outer rings.

The average geometric efficiency was determined to be 26.9% which is in close agreement with the findings of Ref. [48]. The position error, which influences the geometric-efficiency calculation, is discussed in Section A.3. Calculations are also shown in Section A.2 that determine the effective efficiency for each ring of the CAKE. The simulation kinematics show that the recoil has an approximate energy of 650-950 keV which is very low relative to the emitted proton. Due to this the boost effect is diminished which is evident from Figure 3.19. The protons emitted from the recoil nucleus have significantly more energy and are thus able to exit the target material and reach the CAKE. The side view of this simulation is shown in Figure 3.20.

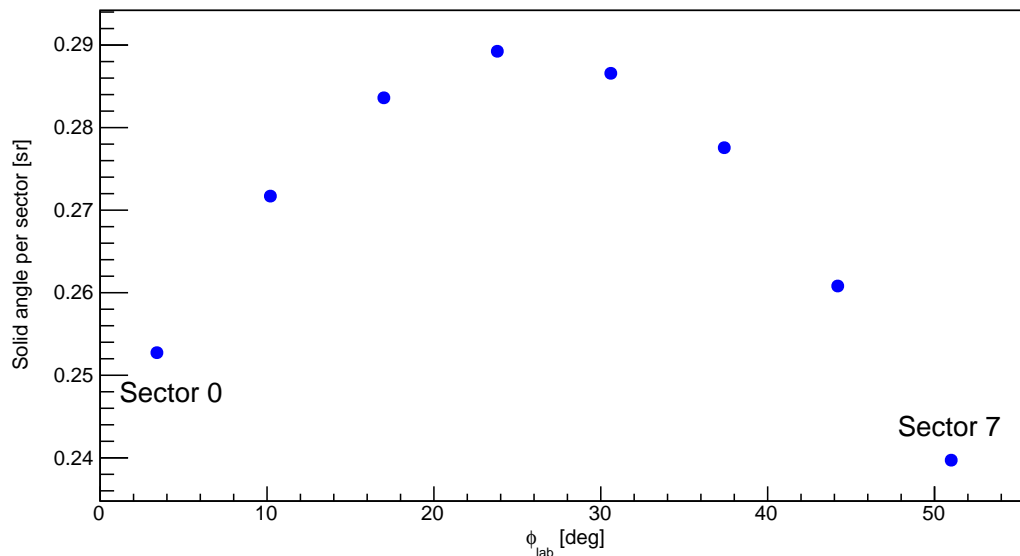


Figure 3.18: Solid angle (in steradians) subtended by each sector of the CAKE plotted against the ϕ lab angle relative to the beam axis of each sector. All sectors have the same area but the middle sectors are closer to the target and effectively cover a greater solid angle.

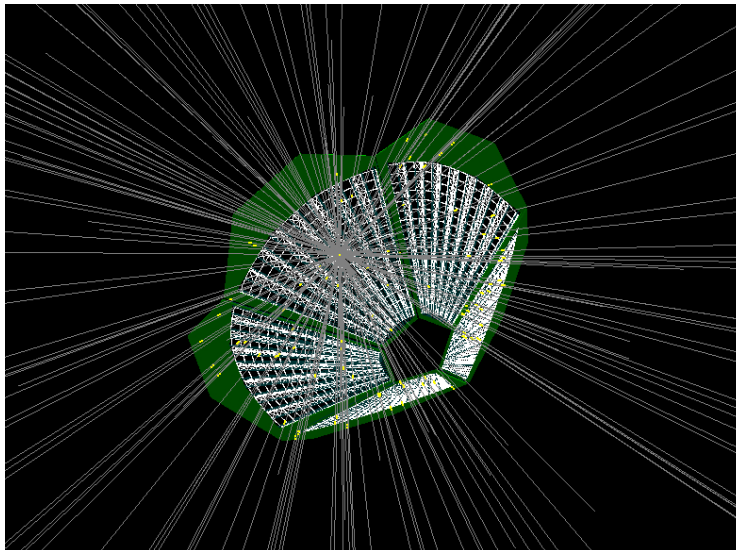


Figure 3.19: OpenGL output of the GEANT4 Monte Carlo simulation of the CAKE [52]. The code for this simulation was edited for the parameters of this particular experiment. Each line represents the trajectory of a decay proton and each yellow point on the array is where that particular event proton impinged upon the detector. The origin of these events is the simulated target position. See Appendix A for further discussions on this code.

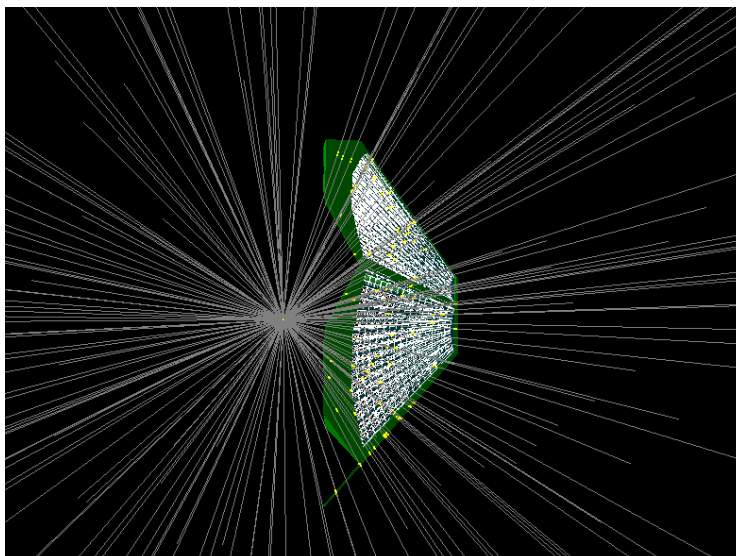


Figure 3.20: OpenGL output of the simulation side view of the CAKE. It was generated during the same simulation by changing the polar and azimuthal angles of the viewpoint to $\theta = 90^\circ$ and $\phi = 0^\circ$, respectively.

3.4.3 Parameters for the CAKE during PR254

Determining the optimal settings and parameters for the MMM-type silicon detectors of the CAKE formed a vital part of the experimental preparation. The setup of the electronics used for the CAKE is explained in more detail in Section 3.5.1. Before attempting a calibration run, a diode-response check has to be done and the detectors have to be biased. The diode response ensures that each side has the correct polarity - negative for the junction (p-side) and positive for the ohmic (n-side) [44]. To determine the bias level for each detector, a leakage-current graph was generated for each to find at which point they become fully depleted. Full depletion occurs when the leakage current remains relatively constant with an increase of applied voltage. The graph for detector one is shown in Figure 3.21. The other four detectors showed a similar response. Consequently, each detector was biased to -80 V and a diode-response check was completed for each to see if they were functioning properly. A series of 32- and 16-channel preamplifiers were used to connect to the silicon detectors. Each preamplifier was set to a gain of 25 MeV maximum range.

The thresholds for the p- and n-sides are listed in Table 3.1. One objective of this study was to search for possible α -particle decay from the recoil nucleus. For that purpose, the detection thresholds for the CAKE were set to be as low as reasonably possible without triggering the silicon detectors in the noise region. The purpose was to measure or place upper limits on the α -particle branching ratio for the resonances within the region of interest for the ^{22}Mg

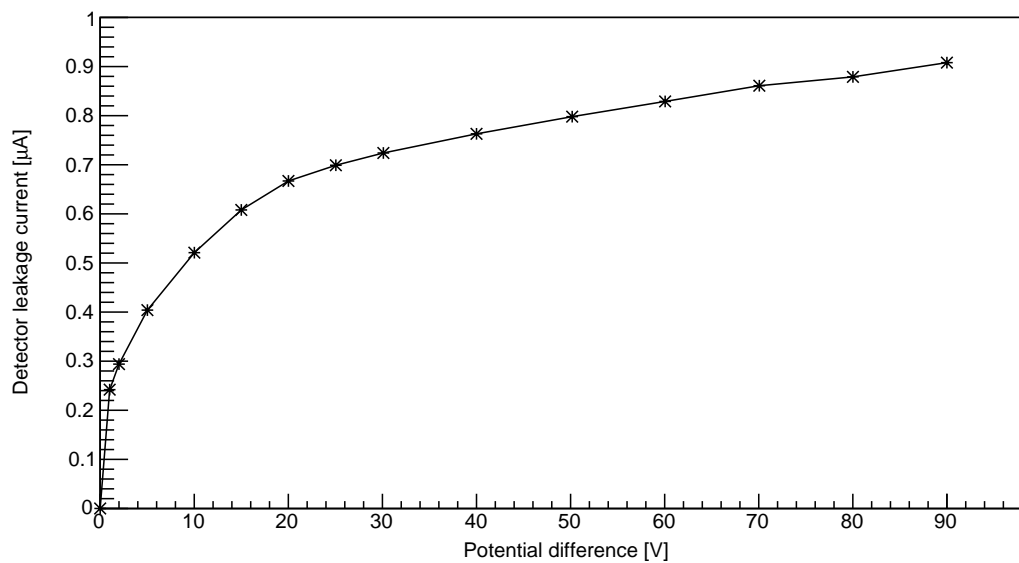


Figure 3.21: Leakage-current graph from detector one in the CAKE. The graph was used to determine the optimal potential difference to be applied to each detector. A detector bias of -80 V was used for each detector in the CAKE for the duration of this experiment since saturation had already been reached.

nucleus. Finally, the CFD settings on the Mesytec MSCF-16 amplifier module should optimally be 60 ns and 40% threshold [44].

Detector(Side)	Threshold (mV)
D1(p)	-50
D2(p)	-50
D3(p)	-85
D4(p)	-42
D5(p)	-64
D1,2(n)	-65
D3,4(n)	-57
D5(n)	-20

Table 3.1: The thresholds for the p and n sides of the five MMM detectors of the CAKE. Note that D1(n) and D2(n) were powered by the same module. Similarly, D3(n) and D4(n) were powered by the same module giving these pairs the same thresholds.

3.5 DAQ electronic module setup

The VME-based data acquisition (DAQ) system of the K600 which was used for this experiment allowed for the simultaneous collection of experimental data from the K600 focal plane as well as the silicon-detector array. A diagram of the complete DAQ, which is modified slightly for each experiment depending on the experimental setup and the hardware used, is shown in Figure 3.22. This particular diagram was modified to include a coincidence trigger and the ADC modules used with the CAKE. The shaped-energy output and emitter-coupled logic (ECL) timing output signals from the Mesytec MSCF-16 amplifiers that the CAKE is connected to (see Section 3.5.1) are relayed to the 12-bit CAEN V785 analogue-to-digital converters (ADCs) and the CAEN V1190 time-to-digital converter (TDC) modules in the DAQ. The TDCs have a 100 ps time resolution. A total of 4 ADC modules (120 channels) and the equivalent of one full module worth of TDC channels were used. In Figure 3.22 there is also a CAEN V792 charge-to-digital converter (QDC) in the VME which has a fullscale range of 400 pC [44]. The ADCs, TDCs and QDCs records data on an event-by-event basis.

3.5.1 The CAKE electronics

Various Mesytec modules are used in conjunction with the CAKE. The detectors are biased using two MHV-4 high-voltage supplies to bias the five MMM detectors as each MHV-4 can only bias four. The MPR-16/32 preamplifiers and MSCF-16 constant-fraction discriminator (CFD) amplifiers are used to give shaped energy signals as output. The MHV-4 module as well as the amplifiers draw their power from the electronics tower in which they are housed. The preamplifiers are powered by the amplifiers and are grounded to the scattering chamber by a cable braid. This can be seen in Figure 3.14. The MSCF-16 modules are directed to the CAEN V785 analogue-to-digital converters (ADCs) in the VME crate of the K600 DAQ.

Figure 3.23 shows the cables that are used to connect the CAKE to the preamplifiers along with other, external cables. One 50-pin connector is plugged into each MMM detector. The signals from each connector is then split into two groups and connected to one of two LEMO connectors - one for the junction (p) side and one for the ohmic (n) side. The LEMO connectors are secured into the LEMO feedthroughs on the inside of the chamber. Importantly, these in-vacuum cables have to be secured to the mounts of the CAKE inside the scattering chamber as they may stray into the beam path (see Figure 3.13). Separate cables are then used to connect to the external part of the feedthrough which in turn are then connected to the preamplifiers. The Mesytec modules used for this experimental setup is shown in Figure 3.24.

The MHV-4 modules have high-voltage cables that supply power to the

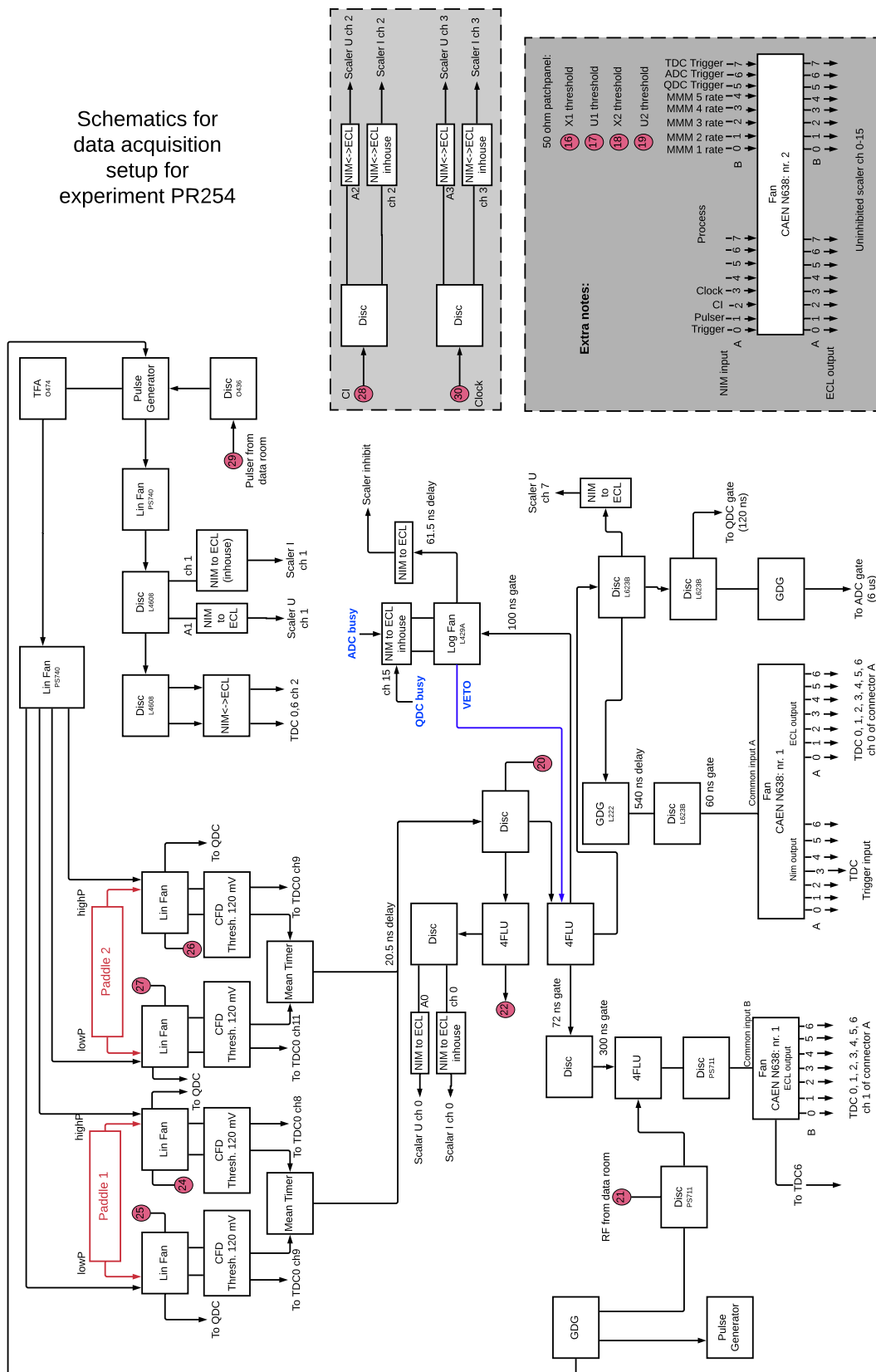


Figure 3.22: The diagram schematically shows the configuration of various electronic modules in the data acquisition (DAQ) system of the K600 during this experiment [44].



Figure 3.23: The cable that connects to the printed circuit board (PCB) of an MMM detector using a 50-pin connector. The wires from the connector is shielded by a metal braid and split into two groups: one group of 18 for the ring channels and one group of 9 for the sector channels. The two LEMO connectors plug into feedthrough connectors on the inside of the scattering chamber. The upper cable and connector relays signals from and power to the p-side whereas the lower cable and connector is used for the n-side in the same way.

MMM detectors via the MPR-16/32 preamplifiers. A standard LEMO BNC connector is used. The power is then relayed to the MMM detectors by the LEMO connectors shown in Figure 3.23. The actual preamplifier modules are powered by the MSCF-16 amplifiers using a normal 9-pin connector. The MSCF-16 amplifiers are used for signal shaping and timing. In Figure 3.24, the amplifier is the module in the centre. The lower IDE connector is for input from the preamplifier. The top-right connector is for output to the TDCs in the DAQ tower whereas the top-left connector is for output to the ADCs. The detector thresholds are set using this module. A diagram showing the electronic and cabling layout for the CAKE setup is shown in Figure 3.25.



Figure 3.24: The different types of Mesytec modules used in the electronics setup of the CAKE is shown. Multiple MPR-16/32 and MSCF-16 units were used to connect a total of 80 ring channels and 40 sector channels and relay the information to the ADC and TDC modules of the K600 DAQ tower. The potentials shown on the MHV-4 module are merely illustrative.

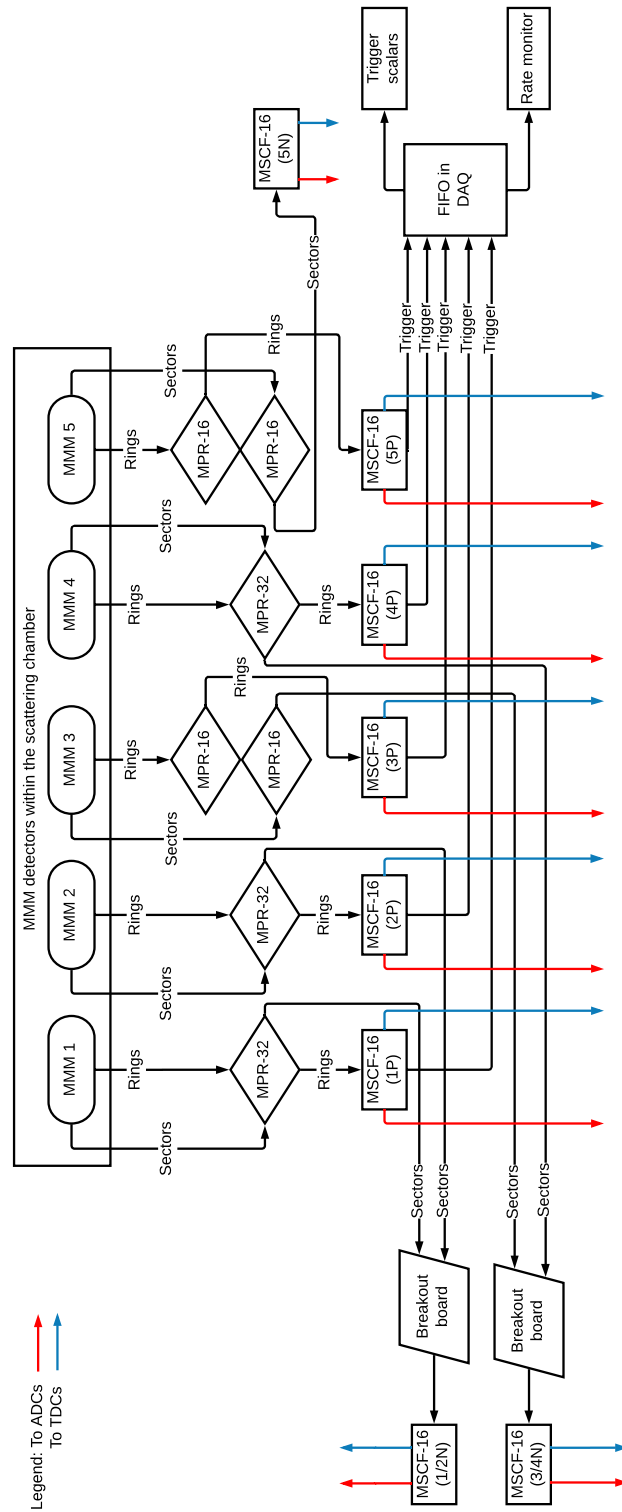


Figure 3.25: This diagram shows the electronics and cabling scheme for the setup of the CAKE during the experiment. Some sector channels had to be combined using a breakout board in order to have enough amplifier modules.

3.6 Target-ladder setup

A target ladder that can hold up to six target frames was used for this experiment. The primary target for this experiment was a $700 \mu\text{g}/\text{cm}^2$ -thick ^{24}Mg target. A thinner $230 \mu\text{g}/\text{cm}^2$ -thick target was also mounted on the target ladder in the event that the resolution in the CAKE was insufficient with the thicker target. The thicker target was used in order to have a count rate high enough to overcome the low cross section in the excitation energy region of interest. A more detailed discussion that compares and contrasts the use of either target can be found in Chapter 4. The following targets are listed according to the position of each target as shown in Figure 3.26.

- The first target was a ZnS viewer that is used for beam tuning. When the proton beam hits the ZnS viewer it starts to fluoresce and the beamspot becomes visible.
- The second target on the ladder is the thinner ^{24}Mg target. The target had a thickness of $230 \mu\text{g}/\text{cm}^2$. However, due to a failure in the vacuum-control system, the vacuum inside the scattering chamber was compromised and the target was lost. As a result, only one dataset was generated using it.
- The third and main target used in the experiment was a ^{24}Mg target that had a thickness of $700 \mu\text{g}/\text{cm}^2$. The targets used for this experiment was formed from a single piece of magnesium bought from Oak Ridge National Laboratory (ORNL). Both targets have an isotopic enrichment of 99.94%.
- A $500 \mu\text{g}/\text{cm}^2$ -thick Diamond-Like Carbon (DLC) target, mounted in position four, was used for background runs to make a background subtraction to remove carbon contaminants from the spectrum after all the data had been collected. However, that too was lost when the chamber vacuum failed.
- The fifth target frame had a $200 \mu\text{g}/\text{cm}^2$ Mylar target mounted on it. Mylar, also known as poly(ethylene terephthalate) with the chemical formula $(\text{C}_{10}\text{H}_8\text{O}_4)_n$, is used because of the carbon and oxygen that it contains which are the two most common types of contaminants in an excitation energy spectrum. The Mylar spectra can, therefore, be used to subtract contaminant peaks from the spectrum. However, this wasn't necessary during the analysis due to low background conditions.
- An empty target frame in position six was used to take background runs to determine the rate of background charged particles, called halo, that is transported with the proton beam. An advantage of using the (p, t) reaction is that very little background radiation reaches the focal plane

at all. This effectively means that a background subtraction is in some cases not necessary.



Figure 3.26: The target ladder used during the experiment with the targets mounted on it. It is used with the target-ladder mechanism to select and move a certain target remotely into the beam path whilst under vacuum in the scattering chamber. The target ladder has six positions. It can also be rotated to increase the effective target thickness that the beam impinges upon. The empty target frame seen next to target number 2 was merely used to prevent the delicate targets from touching the glass surface underneath. The target-ladder mechanism can be seen in Figure 3.14. It is connected to the scattering chamber by a PVC flange to keep the chamber electrically isolated.

Chapter 4

Experimental Data Analysis

I have loved the stars too fondly
to be fearful of the night.

Galileo Galilei

4.1 Introduction

Various program packages were used to analyse the coincident K600 data. The MIDAS [53] and ROOT [54] software packages were used along with the K600 analyser code [55] that sorts data into various ROOT trees. Lastly, an experiment-dependent online database (ODB) file is needed to store experimental parameters to be read by the K600 analyser. These parameters include gates on the particle time-of-flight (TOF) and on the scintillating paddle energies.

The ODB forms part of the MIDAS data acquisition system (DAQ) [44]. During the experiment each run is stored in an event-by-event format in a MIDAS-type (.mid) file which is analysed by the K600 analyser and in turn generates the ROOT files. These are used to analyse the data and draw the resultant spectra.

This study is the first instance in which a K600 and CAKE coincidence experiment was performed using the two-nucleon transfer reaction (p, t). Consequently, this chapter will discuss all of the necessary steps that were taken to analyse the coincidence dataset for this experiment. All of the methods used to extract the necessary information and spectra from the raw dataset will be outlined. This will include the fitting procedures for the excitation energy spectra that are generated.

One important aspect of this analysis was that the excitation energy spectra and coincidence spectra were not generated from chained runs. Each run was analysed individually and then the histograms were added to create a full spectrum. The reason is that the resolution was lower when the runs were

chained together as different runs had slightly different field settings. The total resolution (FWHM) of the excitation energy spectrum was more than 10 keV higher than the resolution of individual runs. However, the alternative method of analysing runs individually showed a total resolution of 2-3 keV higher than the resolution of individual runs.

4.2 The particle identification (PID) spectrum

The first step after successfully analysing all of the runs and events is to draw the PID spectra. They plot the integrated charge from paddle 1 against the particle TOF. The TOF, which is a parameter calculated by software, is measured relative to the radio frequency (RF) of the separated-sector cyclotron (SSC). The trigger signal, which initiates event recording, is transmitted once a particle hit is detected by the plastic scintillators. The following beam packet signals the end of the event. The true event is then reconstructed by calculating the time from the RF retroactively. The reason for this is that not every beam particle interacts with the target and, as such, it lowers the rate in the DAQ. This is also the reason why pulse selection is required - for adequate separation in time between events to simplify the data output. A plot from all the combined runs of the third experimental weekend is shown in Figure 4.1 (no display thresholds are set for any of the following 2D spectra unless specified). The well-defined triton locus shows that the field settings during the third weekend were very stable.

The basic purpose of the PID spectrum is to select for analysis only the events of interest by means of a software gate. In doing so the analysis will only focus on these events and exclude any unrelated data. This step in the analysis is a necessity because there are a myriad of reactions and interactions that are possible. Many of these are a result of halo interactions with the target frame. However, carbon deposits are also virtually always present on the target and oxygen is also a common contaminant as the ^{24}Mg target may have oxidised. Most of the background events associated with these contaminants will be eliminated once the PID gate is in place. The beam may interact with these naturally-abundant contaminants and cause background events. Possible scattering of halo particles from the target frame may also occur. Other sources of background may include scattering from the proton beamstop in the spectrometer or different exit channels from the compound nucleus to produce (p, p') , (p, d) or other possible reactions.

Tritons have a lower charge-to-mass ratio. This means that the spectrometer fields have to be set higher for the tritons to reach the focal plane. Most other particles that enter the spectrometer aperture have less rigidity and will not reach the detectors. As an indication thereof, various empty-frame runs are made during the experiment. This is also used to ensure that the level of halo background is low. The empty-frame spectrum proves the efficacy of

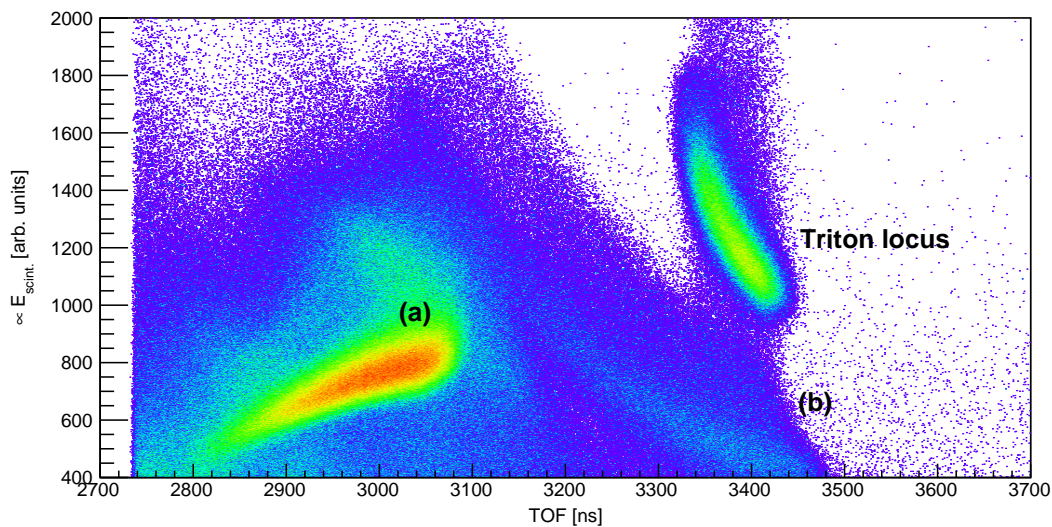


Figure 4.1: The particle identification (PID) spectrum. These types of spectra may show various loci depending on the experiment. The locus of interest can be selected and gated upon. In this instance, the rigidity of the triton ejectiles is highest making the decay locus easily identifiable in the spectrum. The triton locus is labelled. The locus labelled (a) is due to (p, d) reactions where the deuterons are able to reach the focal plane. The locus labelled (b) is a broad, beamstop-related background. This is due to scattering from the (p, t) beamstop that is located in D1 of the K600. A display threshold of >1 is imposed.

using (p, t) reactions since the entire chain of runs had only 181 counts from random background events in it. This is shown in Figure 4.2.

Another important advantage of using PID cuts to gate upon events of interest is that they can be used to minimise computing times. By using the specific cut related to each run, the events that fall outside that gate can be discarded and new ROOT trees created that contain much less data and are faster to process when drawing spectra. The PID gate is then included automatically when drawing spectra that use the new trees.

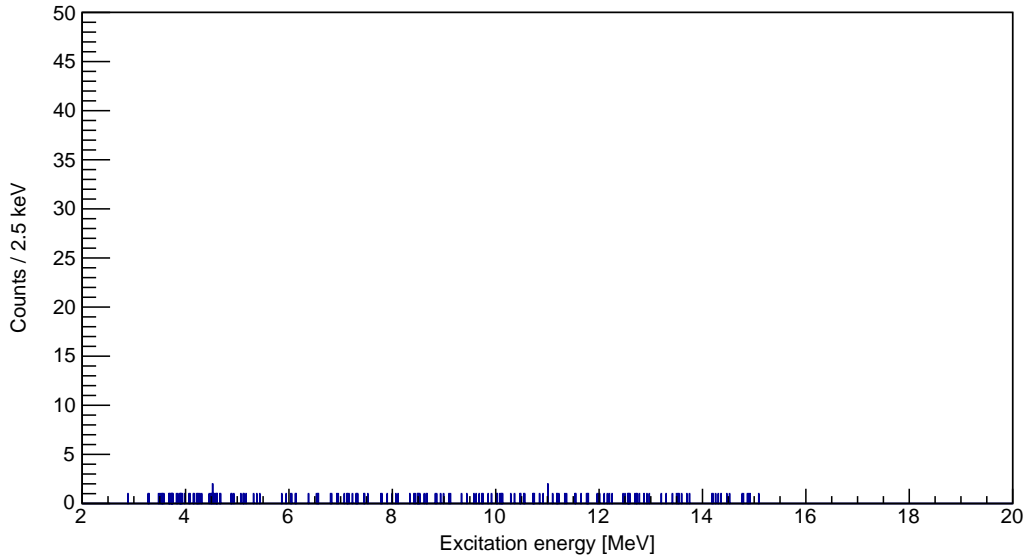


Figure 4.2: The calibrated empty-frame excitation energy spectrum with PID gate. The spectrum shows all the events seen by the focal plane detectors when the empty frame was selected. The total run time of all 36 runs is about 3.5 hours. It is thus evident that the background was low during the experiment as the spectrum has a total of 181 counts over an 18-MeV range. Adding the silicon-time gate (see Section 4.6) reduces that number to 3.

4.3 Focal-plane calibration

The focal-plane position spectrum can be drawn by analysing the new ROOT trees that only contain events from the relevant triton ejectiles. An example of a raw X1-position ($X1_{pos}$) spectrum is shown in Figure 4.3.

The resolution can be improved by taking into account the scattering angle θ_{SCAT} of ejectiles entering the spectrometer aperture. It is defined as the angle between the beam axis and the projection of the ejectile direction onto the $\hat{z}\hat{x}$ plane [46]. Figure 4.4 serves to illustrate this definition along with equation 4.3.1. θ_{SCAT} is calculated in the K600 analyser using the $X1_{pos}$ value from the X1 wireplane and θ_{FP} , the trajectory angle from the focal plane calculated from the U wireplanes of the VDCs. The parameters a_0 to a_3 are experiment-specific and determined by the slope and offset of states in the θ_{FP} spectrum as shown in Figure 4.5.

$$\theta_{SCAT} = \theta_{FP}(a_0 + a_1 X1_{pos}) + a_2 + a_3 X1_{pos}. \quad (4.3.1)$$

Parameters a_0 and a_1 are taken from the offset and slope, respectively, of Figure 4.6(a) whereas a_2 and a_3 are taken from the offset and slope, respectively, of Figure 4.6(b). To determine whether the conversion is successful, values from θ_{SCAT} and θ_{FP} are plotted against each other and checked for collinearity by

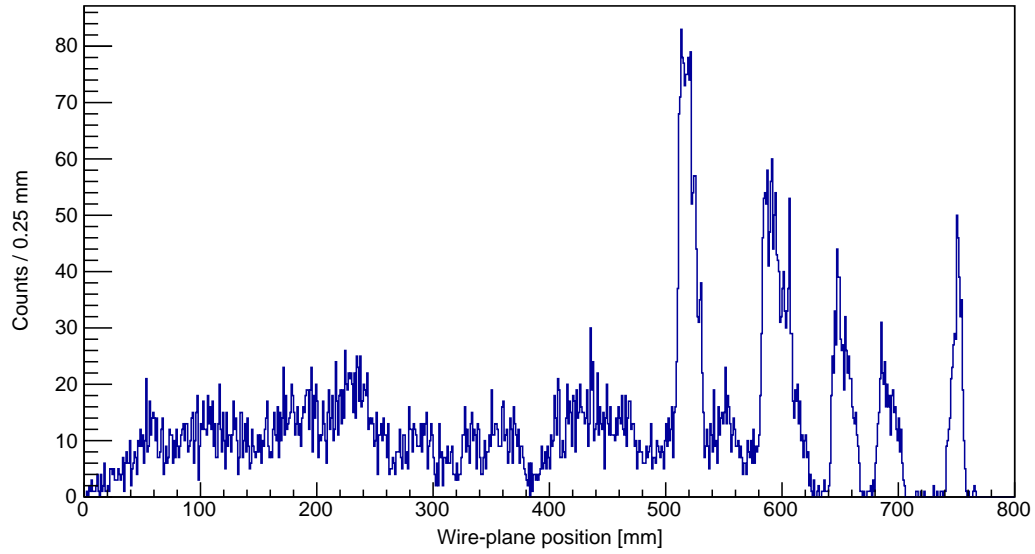


Figure 4.3: The spectrum shows the wire-plane position of hits from triton ejectiles that were detected in the X1 wireplane of the first VDC in the K600 focal plane during run 3025. Less energetic tritons are bent more by the spectrometer dipoles and have a higher wire-plane position as their magnetic rigidity is less.

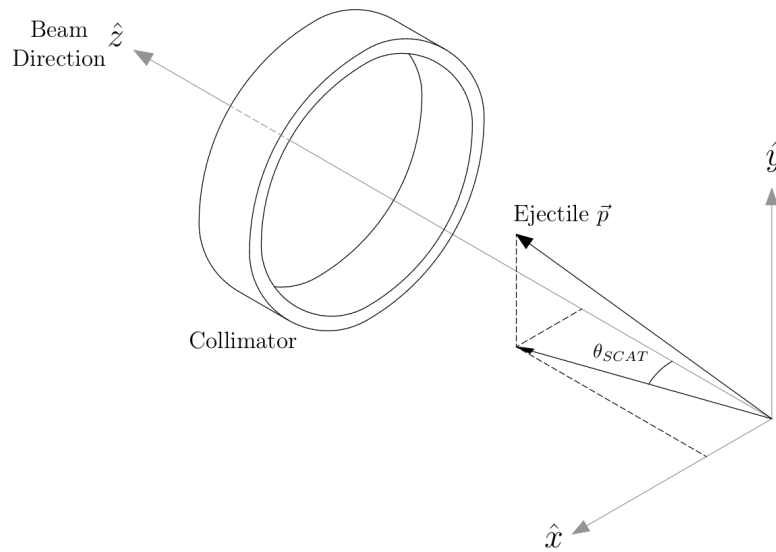


Figure 4.4: Illustration of the definition of θ_{SCAT} . It is defined as the angle between the beam direction and the laboratory plane, $\hat{z}\hat{x}$ in this illustration [46].

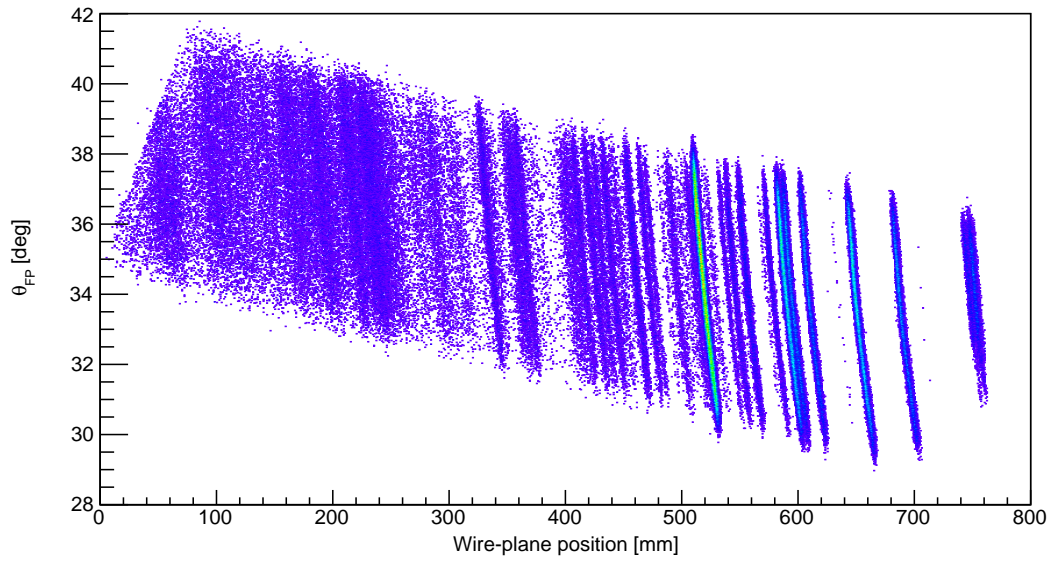


Figure 4.5: The spectrum shows the focal plane angle, θ_{FP} , plotted against the wire-plane position $X1_{pos}$. The slope of the dominant states are taken to determine the parameters used to calculate θ_{SCAT} . A display threshold of >3 is imposed.

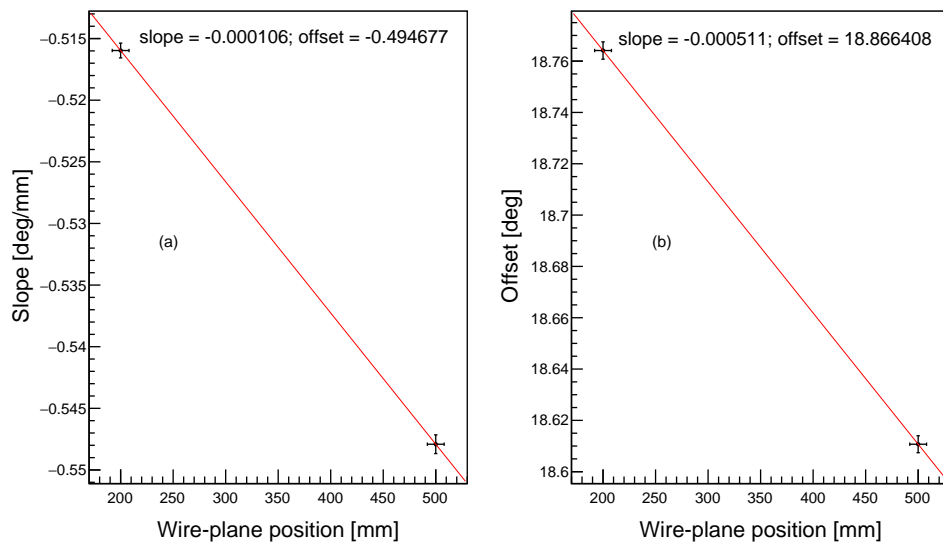


Figure 4.6: The slope and offset of two states in the θ_{FP} spectrum at different $X1$ -plane positions.

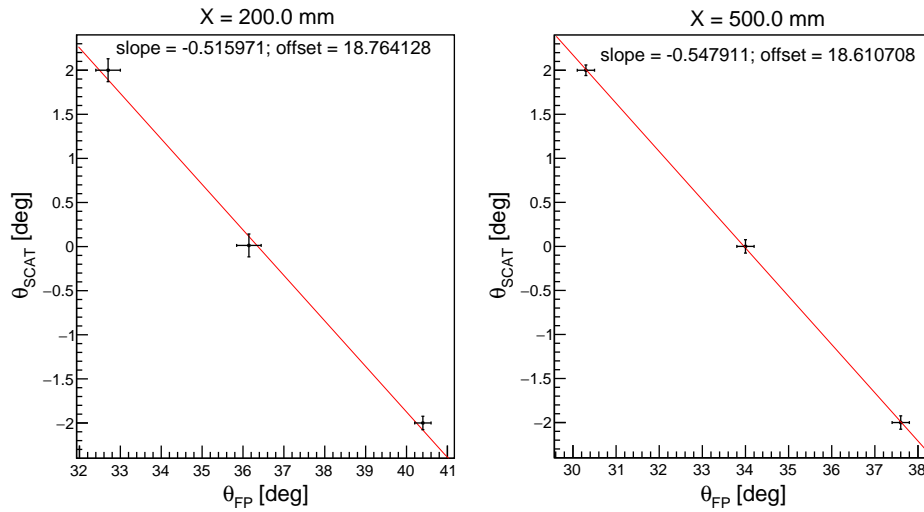


Figure 4.7: This spectrum shows the conversion from θ_{FP} to θ_{SCAT} by using the parameters calculated in Figure 4.6. If this is neglected then the spectrum in Figure 4.8 is not centered around 0° with an acceptance of $\pm 2^\circ$ to reflect the true acceptance of the K600 spectrometer.

fitting the points and determining χ_{red}^2 as illustrated in Figure 4.7. The values calculated for θ_{SCAT} are plotted against the wire-plane positions $X1_{pos}$ and are shown in Figure 4.8. The spectrum shows that each state is represented by an unbroken, slanted line. The collimator of the K600 is situated after the scattering chamber and imposes a restriction of $\pm 2^\circ$ centred around 0° to constrain the value of θ_{SCAT} to: $-2.0^\circ \leq \theta_{SCAT} \leq 2.0^\circ$. A gate that reflects this constraint is applied to the spectrum.

By correcting for the angle in these states using a second-order polynomial, the resolution of all states in the $X1_{pos}$ spectrum improves. However, it was found that the fields varied over the range of the spectrum. Therefore, multiple lineshape corrections were performed for states across the spectrum. The standard corrections needed to this spectrum are:

$$X1_{posCorr} = X1_{pos} - b_1\theta_{SCAT} - b_2\theta_{SCAT}^2, \quad (4.3.2)$$

It was found that the parameters b_1 and b_2 have a quadratic dependence as well over the range of $X1_{pos}$, just like the states in the spectrum. After the lineshape corrections were made individually, a plot was made of all the b_1 parameters against the average $X1_{pos}$ of their associated state. This generated a quadratic expression for the linear lineshape parameter, p_1 . A similar procedure was followed for the quadratic lineshape parameter, p_2 . The data to calculate the parameters are listed in Table 4.1 and Table 4.2.

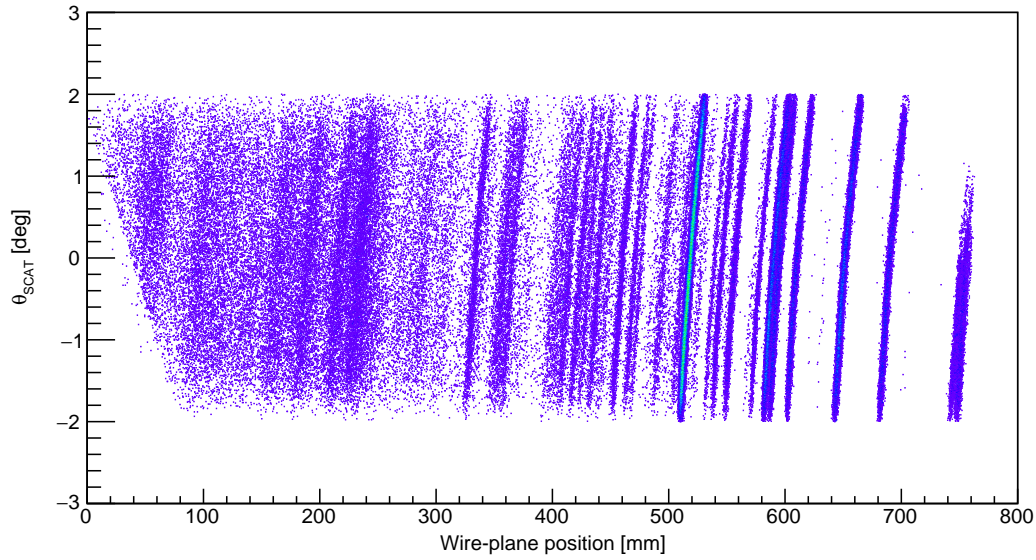


Figure 4.8: The θ_{SCAT} vs $X1_{pos}$ spectrum is shown. The nature of the poor resolution in the raw spectra is due to the slant seen here. By using a second-order correction and applying it to the $X1_{pos}$ spectrum, the resolution can be corrected. Note that the spectrum is subject to the acceptance of the focal plane. The cut offs can be seen by the slant at the front and back of the spectrum which diminishes the strength of the ^{10}C ground state and 3.308 MeV ($J^\pi = 4^+$) state in ^{22}Mg . A display threshold of >1 is imposed.

Lineshape $X1_{pos}$ (mm)	b_1 (deg/mm)
752.321	4.93913
688.711	5.90801
651.461	5.56165
609.054	5.56777
595.301	5.53425
589.57	5.44545
519.083	5.28034
460.236	5.39411
333.901	5.13626
189.312	6.50313

Table 4.1: The lineshape $X1_{pos}$ against the value of the associated linear lineshape parameter. A quadratic fit was made with these values.

The quadratic fits using the data in Table 4.1 and Table 4.2 revealed that:

$$\begin{aligned}
 p_1 &= c_0 + c_1 X1_{pos} + c_2 (X1_{pos})^2 \\
 &= 7.18767 - 0.0062587(X1_{pos}) + 5.40746 \times 10^{-6}(X1_{pos})^2 \quad (4.3.3)
 \end{aligned}$$

Lineshape $X1_{pos}$ (mm)	b_2 (deg/mm ²)
752.321	0.423637
688.711	0.813115
651.461	0.645751
609.054	0.432713
595.301	0.530757
589.507	0.549764
519.083	0.421654
460.236	0.291612
333.901	0.580396
189.312	0.550050

Table 4.2: The lineshape $X1_{pos}$ against the value of the associated quadratic lineshape parameter. A quadratic fit was also made with these values.

and

$$\begin{aligned}
 p_2 &= d_0 + d_1 X1_{pos} + d_2 (X1_{pos})^2 \\
 &= 0.748924 - 0.00131276(X1_{pos}) + 1.52377 \times 10^{-6}(X1_{pos})^2, \quad (4.3.4)
 \end{aligned}$$

with c_0 and d_0 in mm, c_1 and d_1 in mm/deg and c_2 and d_2 in mm/deg².

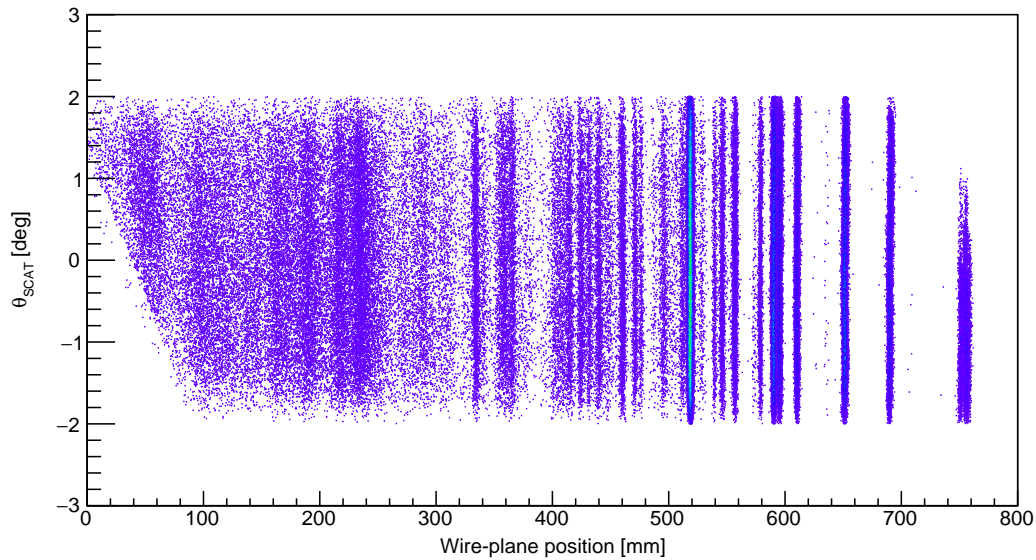


Figure 4.9: The corrected θ_{SCAT} spectrum is shown. The correction is made by applying equation 4.3.1. A display threshold of >1 is imposed.

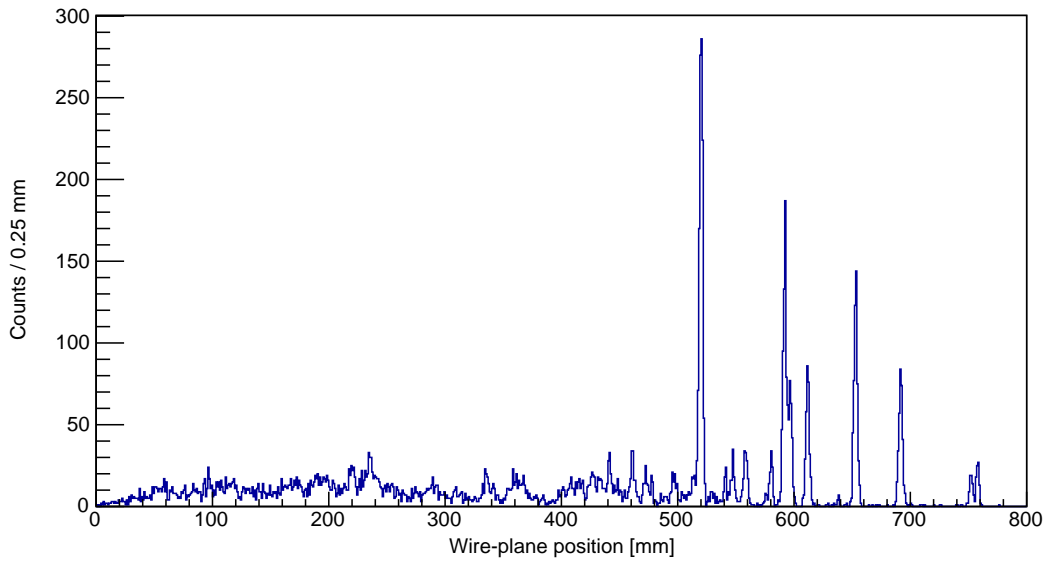


Figure 4.10: The corrected $X1_{pos}$ spectrum for run 3025 is shown. After implementation of the second-order correction from the θ_{SCAT} versus $X1_{pos}$ spectrum in the previous figure (which fundamentally amounts to a projection in the x axis) the resolution is quite noticeably improved. Compare with Figure 4.3.

Using the results from the quadratic fits of the linear and quadratic lineshape correction parameters, the second-order corrections needed due to θ_{SCAT} and the vertical position dependence can be written explicitly as follows:

$$X1_{posCorr} = X1_{pos} - p_1\theta_{SCAT} - p_2\theta_{SCAT}^2, \quad (4.3.5)$$

Henceforth, the corrected wire-plane position $X1_{posCorr}$ will be referred to as $X1_{pos}$. The corrected θ_{SCAT} spectrum is shown in Figure 4.9 and the corrected $X1_{pos}$ spectrum is shown in Figure 4.10.

During the course of an experiment it is usual to have varying magnetic field settings (for the SSC and K600), especially between different experimental weekends. This change in fields is the cause of the triton locus shifting in the PID spectrum from run to run, but it also affects the wire-plane position of states. This has to be corrected for using $X1_{pos}$ offsets in the K600 analyser before chaining all runs with different magnetic field settings together. Should this not be done, the small variation of the wire-plane position of each state from run to run will degrade the resolution and obscure many states. A useful visualisation plotting the wire-plane positions against the trigger-event number illustrates whether the states are aligned from run to run as shown in Figure 4.11. Each horizontal line represents a state at the corresponding wire-plane position which has been aligned correctly. The complete corrected $X1_{pos}$ spectrum is shown in Figure 4.12. The following section will show how the $X1_{pos}$ spectrum is used with an energy calibration to generate the excitation

energy spectrum.

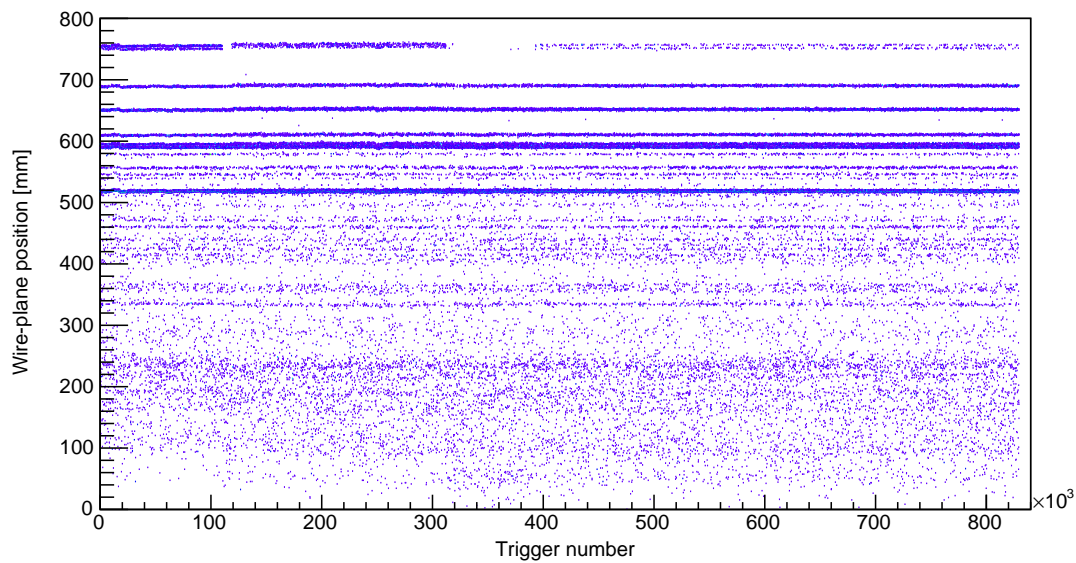


Figure 4.11: This plot shows the wire-plane position plotted against trigger-event numbers. Each horizontal line represents a state at that corresponding energy. When all states appear to be aligned the $X1_{pos}$ offsets have been added to the K600 analyser code accurately. Consequently, runs can be combined together in the full analysis. Due to varying fields, the momentum range near 750 mm was not always covered to detect the 3.308 MeV state or the ^{10}C g.s. which shows up as a broken line. A display threshold of >1 is imposed.

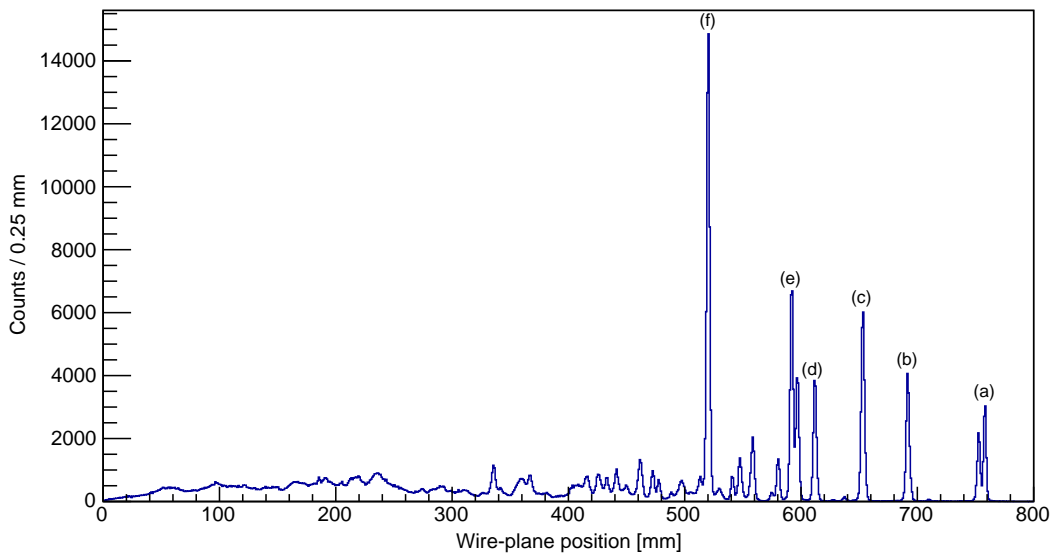


Figure 4.12: The combined corrected $X1_{pos}$ spectrum for all runs are shown. Each $X1_{pos}$ spectrum is drawn separately by finding the offset relative to a fixed state position (520 mm in this case for the dominant state) and drawing the resultant spectrum. The histograms are added to generate the complete $X1_{pos}$ spectrum. The resolution of states in the complete spectrum was found to be within 2-3 keV of states in an individual spectrum as shown previously in Figure 4.10. This will be discussed further in the following section regarding the energy calibration. The dominant states in this spectrum will be used there and are thus labelled (a)-(f), for ease of reference, in order of ascending excitation energy.

4.4 Energy calibration

The wire-plane position spectrum shown in Figure 4.12 in the previous section implicitly hints at the core function of spectrometers. Spectrometers are used to momentum-analyse ejectiles in order to relate a physical focal-plane position to magnetic rigidity and then ultimately to excitation energy. The triton ejectiles are separated by the ion-optics of the K600 on the basis of their magnetic rigidity,

$$B\rho = \frac{p}{q}. \quad (4.4.1)$$

The ratio between the particle charge, q , and linear momentum, p , is equal to the product of the gyroradius ρ and magnetic field, B , that the triton is subjected to. The corrected $X1_{pos}$ spectrum reflects the rigidity of states. The wire-plane position can be interpreted directly in terms of linear momentum as the spectrum is charge independent as only tritons are selected. Therefore,

the excitation energies of states can be determined simply by calibrating in terms of momentum. As such, the dominant states were used for calibration and are labelled (a)-(f) as in Figure 4.12. The wire-plane positions and corresponding excitation energies of these states will be used to determine the energy calibration. These values are listed in Table 4.3.

Resonance label	Position [mm]	Error [mm]	E_x [MeV]	J^π
(a)	757.6	0.028	3.308(6)	4^+
(b)	692.1	0.011	4.402(29)	2^+
(c)	653.4	0.008	5.035(5)	2^+
(d)	612.2	0.010	5.711(5)	2^+
(e)	592.3	0.009	6.040(8)	(3^-)
(f)	520.4	0.005	7.218(9)	0^+

Table 4.3: The approximate wire-plane positions, corresponding excitation energies and spin-parities for the dominant states in the focal plane spectrum are listed. These are used to determine the energy calibration.

The states in the $X1_{pos}$ spectrum were associated with their respective excitation energies by comparison with states in NNDC [14] discovered by performing similar (p, t) reactions. These associations have to comply with the fact that (p, t) reactions are more selective to natural-parity states. Unnatural parity states will be suppressed in the spectrum. Another factor was that the K600 was operated at $\theta_{lab} = 0^\circ$ which selects low angular-momentum transfer reactions. A comparison was also made with Ref. [35] for consistency. The exact wire-plane position of each state is extracted by fitting with a Gaussian function and extracting the location parameter μ . See Section 4.7 for a more complete description of Gaussian spectral fits.

It can be shown as in Ref. [46] that the wire-plane positions relate directly to the momenta which, in turn, can be related directly to excitation energy with a simple conversion as in Figure 4.13. It follows that:

$$E_x = e_0 + e_1 X1_{pos} + e_2 X1_{pos}^2. \quad (4.4.2)$$

The parameters calculated from the conversion shown in Figure 4.13 are listed in Table 4.4. This example calibration is for run 3025. For the full analysis, a program is written to calibrate all runs individually in the same way. This generates a header file that saves the three calibration parameters of all 109 runs in a 2D array of size 109×3 . The excitation energy spectra (in the form of 1D histograms) are then generated. To generate the full spectrum, all the histograms are simply added together.

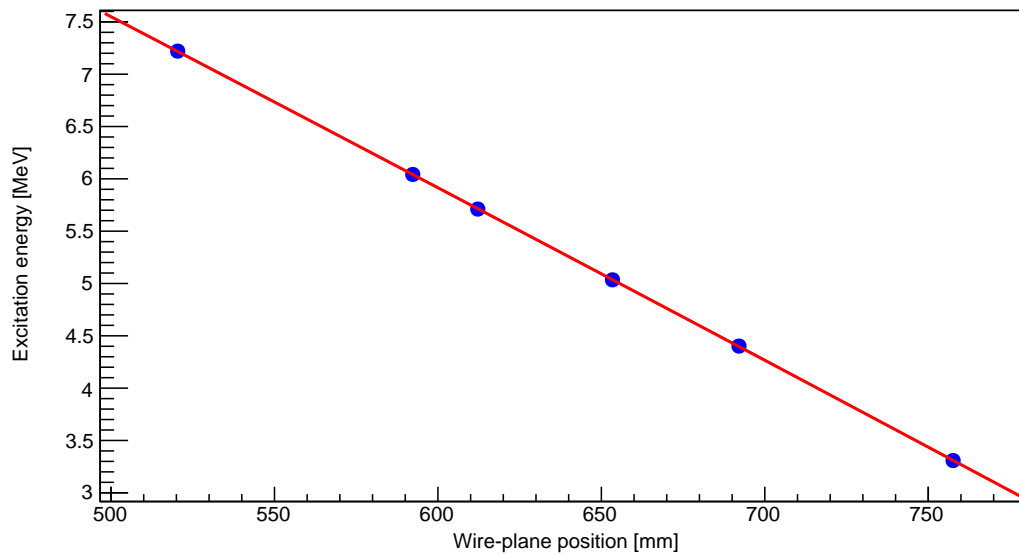


Figure 4.13: The conversion from position to excitation energy is shown for run 3025. The second-order polynomial parameters e_0 , e_1 and e_2 are extracted from the fit to convert wire-plane positions to excitation energies. The fit converges with a reduced $\chi^2_{red} \sim 1$. The errors for each point are indicated in Table 4.3 but are imperceptibly small for this graphical scale.

Parameter	Value	Error	Unit
e_0	15.501	± 0.107	MeV
e_1	-1.555×10^{-2}	$\pm 3.38 \times 10^{-4}$	MeV/mm
e_2	-7.228×10^{-7}	$\pm 2.638 \times 10^{-7}$	MeV/mm ²

Table 4.4: The parameters for the conversion from wire-plane position to excitation energy for run 3025.

$X1_{pos}$ refers to the corrected wire-plane positions. Applying this calibration to Figure 4.12 gives the excitation energy spectrum of ^{22}Mg which is shown in Figure 4.14. This is generally referred to as the singles spectrum as it is composed exclusively of focal-plane events. The energy dispersion determined from the θ_{SCAT} versus $X1_{pos}$ spectra was approximately 17 keV/mm by finding the difference in wire-plane position between two states with known excitation energies. By fitting the states in the spectrum with a Gaussian function to find the standard deviation σ , the energy resolution for the experiment was found to be 45(5) keV (full width at half maximum, FWHM).

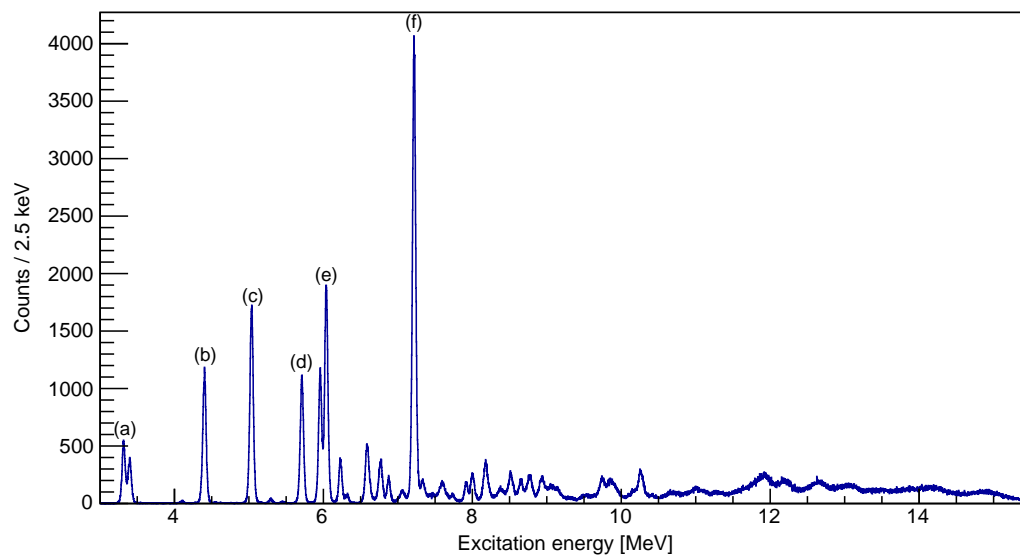


Figure 4.14: The calibrated excitation energy singles spectrum is shown. The states labelled (a)-(f) corresponds to the same states from the $X1_{pos}$ spectrum used in the calibration.

4.5 The CAKE calibration

The 5 MMM-type detectors of the CAKE each have 16 rings and 8 sectors for a total of 120 pixels. As discussed in Section 3.5.1, a total of 120 ADC channels were used. A calibration run was completed with a ^{228}Th source at the target position before the start of the experiment to determine the offset and gain of each ADC channel. This section will discuss the calibration that has to be performed before the coincidence analysis can start.

The decay chain of ^{228}Th is shown in Figure 4.15 [56]. The half-life of each step in the chain is indicated in Table 4.5. All six α particles from the ^{228}Th decay chain were detected by the CAKE as shown in Figures 4.16 and 4.17. The various decay particles are labelled α_1 to α_6 . Their respective energies and related decay schemes follow.

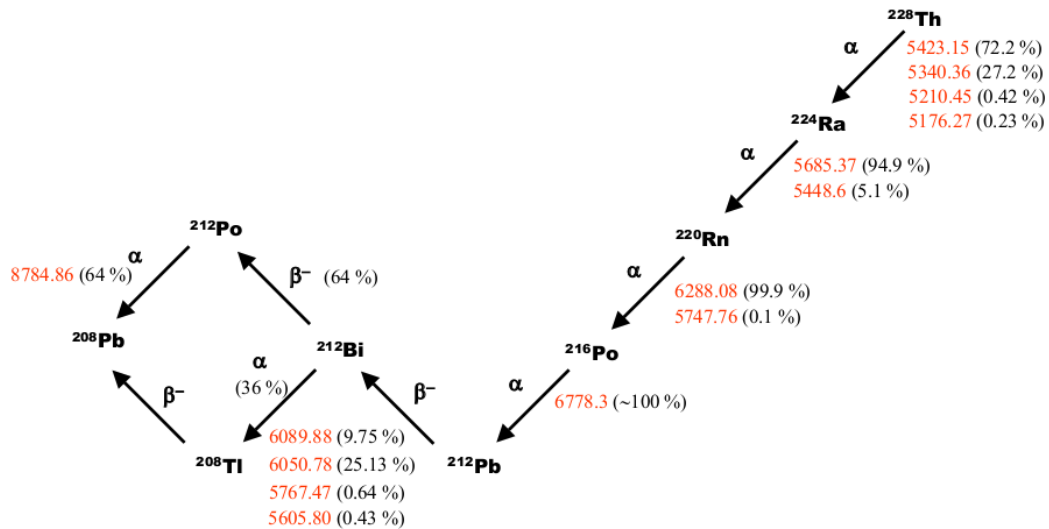


Figure 4.15: The decay chain of ^{228}Th which was used to calibrate the CAKE. From this decay chain, six distinct α particles are emitted and used to determine the gain and offset for each of the 120 ADC channels [56].

$$E_{\alpha_1} = 5.423 \text{ MeV: } ^{228}\text{Th} \rightarrow ^{224}\text{Ra} + \alpha_1 \quad (4.5.1)$$

$$E_{\alpha_2} = 5.685 \text{ MeV: } ^{224}\text{Ra} \rightarrow ^{220}\text{Rn} + \alpha_2 \quad (4.5.2)$$

$$E_{\alpha_3} = 6.050 \text{ MeV: } ^{212}\text{Bi} \rightarrow ^{208}\text{Tl} + \alpha_3 \quad (4.5.3)$$

$$E_{\alpha_4} = 6.288 \text{ MeV: } ^{220}\text{Rn} \rightarrow ^{216}\text{Po} + \alpha_4 \quad (4.5.4)$$

$$E_{\alpha_5} = 6.778 \text{ MeV: } ^{216}\text{Po} \rightarrow ^{212}\text{Pb} + \alpha_5 \quad (4.5.5)$$

$$E_{\alpha_6} = 8.784 \text{ MeV: } ^{212}\text{Po} \rightarrow ^{208}\text{Pb} + \alpha_6 \quad (4.5.6)$$

The decay loci in Figure 4.16 are used to determine the gain and offset of the ADC channels. In this way the detector calibration can be determined and added to the K600 analyser so that it is implemented when data runs are analysed.

Isotope	Half-life ($t_{1/2}$)	Decay mode
^{228}Th	1.911 a	α
^{224}Ra	3.632 d	α
^{220}Rn	55.60 s	α
^{216}Po	0.145 s	α
^{212}Pb	10.64 h	β
^{212}Bi	60.55 m	α, β
^{212}Po	0.299 μs	α
^{208}Tl	3.053 m	β
^{208}Pb	N.A.	stable

Table 4.5: Daughter nuclei in the ^{228}Th decay chain with their associated half-life and particle emission. The decay of ^{228}Th is followed by prompt α -particle emission. The branching ratio from ^{212}Bi , which can decay via α - or β -particle emission, means that a particular decay chain can emit either 5 or 6 α particles.

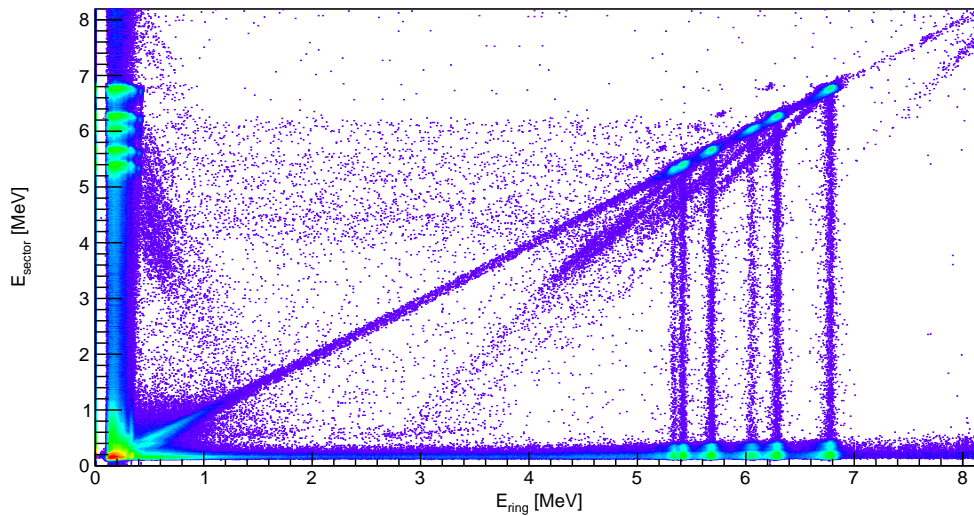


Figure 4.16: The α -particle decay loci in the front-back coincidence spectrum of the CAKE during a ^{228}Th calibration run. The six loci correspond to the six peaks as shown in figure 4.17. The weaker, oblique, vertical and horizontal structures in the spectrum correspond to particle hits near the interstrip regions of the detectors where charge is collected inefficiently across the p-n junction for the sectors and rings, respectively. The detected energies are reduced and those events are effectively lost. The weaker diagonal loci with a steeper slope result because of hits which have reduced detected energies for both the rings and the sectors.

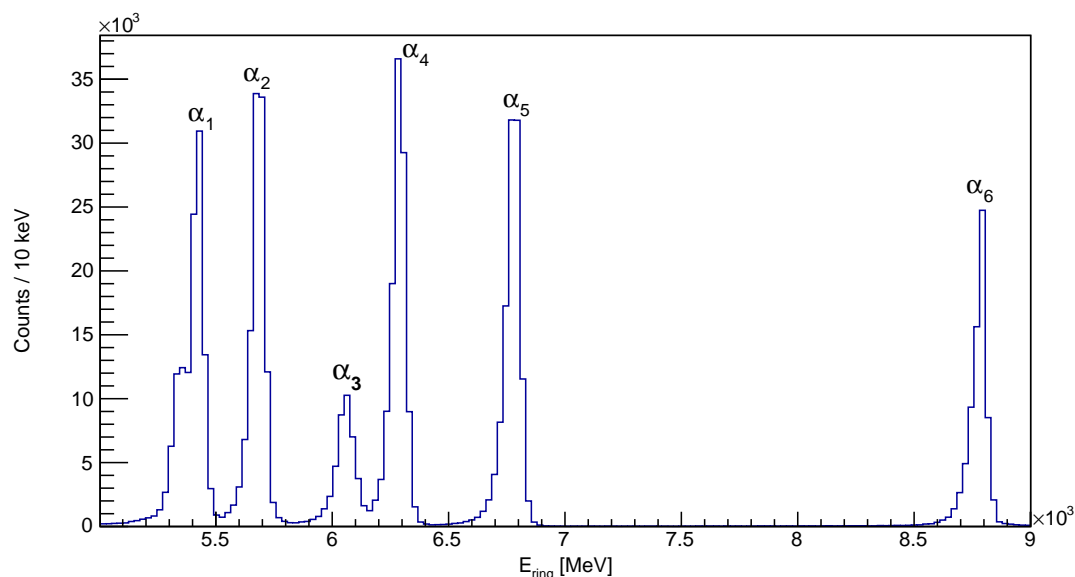


Figure 4.17: This spectrum shows the energy peaks of the α particles in the ^{228}Th decay chain as detected by the CAKE after offsets and gain matching on all ADC channels were complete. The energy resolution for each strip in the CAKE is 40-50 keV (FWHM).

4.6 Coincidence analysis

Two-nucleon transfer reactions like (p, t) are classified as direct reactions as they proceed from the initial to final state without the formation of an intermediary compound nucleus. These reactions take place over a much shorter timescale than compound reactions. Once a beam particle has impinged upon a ^{24}Mg target nucleus, the reaction will emit a triton ejectile into the spectrometer aperture and leave the excited recoil nucleus ^{22}Mg . Conservation of momentum ensures that the recoil and ejectile are emitted in opposite directions. However, because of the greater size of the recoil, it has very little kinetic energy compared to the triton ejectile and doesn't move out of the target material. Monte Carlo simulations as performed with GEANT4 (see section 3.4.2) showed that the recoil is left with a kinetic energy of about 650-950 keV on average. The recoil then starts the de-excitation process by particle emission, i.e. protons. Simulations show that the boost effect is not strong for this situation due to the low kinetic energy of the recoil. This can be seen in Figure 3.19 as the trajectories of decay particles are not backward focussed.

Once the emission of a triton into the spectrometer aperture has taken place, the excited ^{22}Mg recoil nucleus is left within the target and, in pursuit of de-excitation, proceeds via the emission of protons. Proton decays from the ^{22}Mg recoil nucleus are then detected by the CAKE. Decay will generally

proceed either to the first-excited state of the residual nucleus, ^{21}Na , or the ground state thereof. This is referred to henceforth as p_1 or p_0 decay, respectively. Figure 4.18 gives an assumed upstream view of all pixels in the CAKE. The regions between individual detectors are indicated along with their associated polar angles. The colour scale gives an indication of the number of particle hits in each detector pixel.

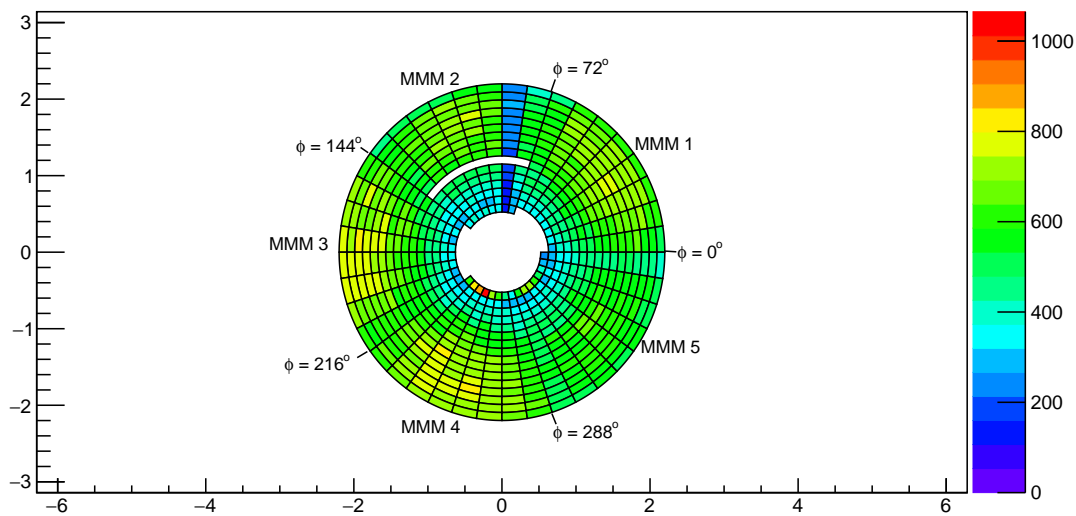


Figure 4.18: This spectrum shows a virtual plot of the CAKE without any software gates. This is used to show individual pixels of the CAKE and the total hits in each pixel. It is a good diagnostic tool with which to discover any mapping problems. Each MMM detector has 8 sectors which covers a polar angle of $\phi = 72^\circ$ [57].

The geometric limitations of the CAKE are hinted at in Figure 4.18. The inner-ring pixels have fewer counts as they cover a smaller solid angle and therefore have a lower chance of proton detection. As the ring number increases the solid angle coverage increases. This is in agreement with the simulation results for the rings as seen in Figure 3.17 of Section 3.4.2.

Figure 4.18 shows that ring 6 of MMM2 was not functional along with ring 0 of MMM1 and MMM3 whereas sector 1 of MMM2 shows lower counts. Also note the high counts seen by ring 0 of MMM4 and MMM5 which is due to beam halo. During the course of all three experimental weekends, halo levels of 20-40 Hz/pnA were detected which were within the acceptable range and can be excluded from the data by using appropriate gates. The events from these rings and sectors were discarded. This is taken into account when performing the calculations for the yields of each detector to produce the angular correlation spectra (see Chapter 5).

The ring and sector hit patterns were also generated. They generally resemble the simulation results if the anomalous rings and sectors mentioned previously are ignored. The spectra are shown in Figures 4.19 and 4.20.

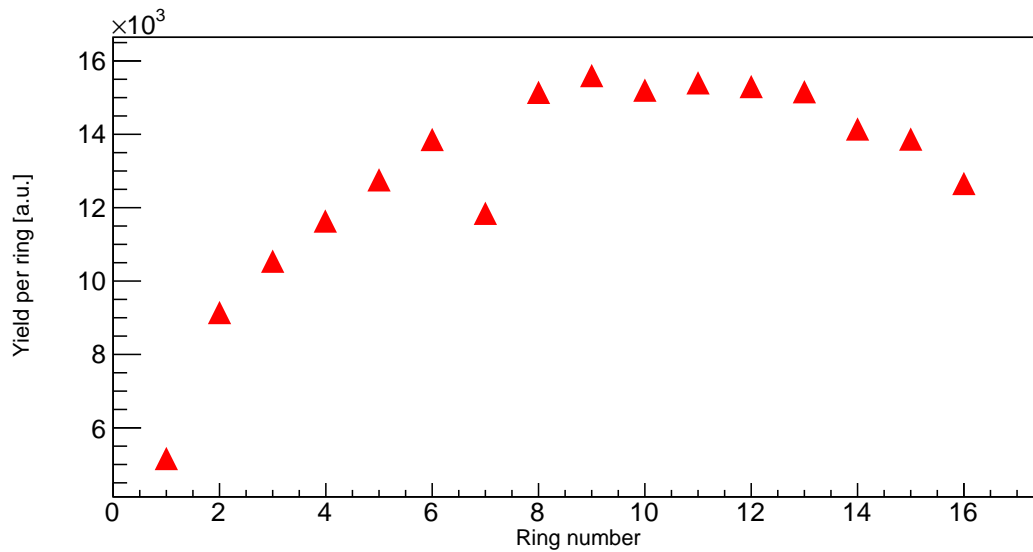


Figure 4.19: The ring hit pattern as detected by the CAKE. It is generated by gating the 2D coincidence plot on individual rings.

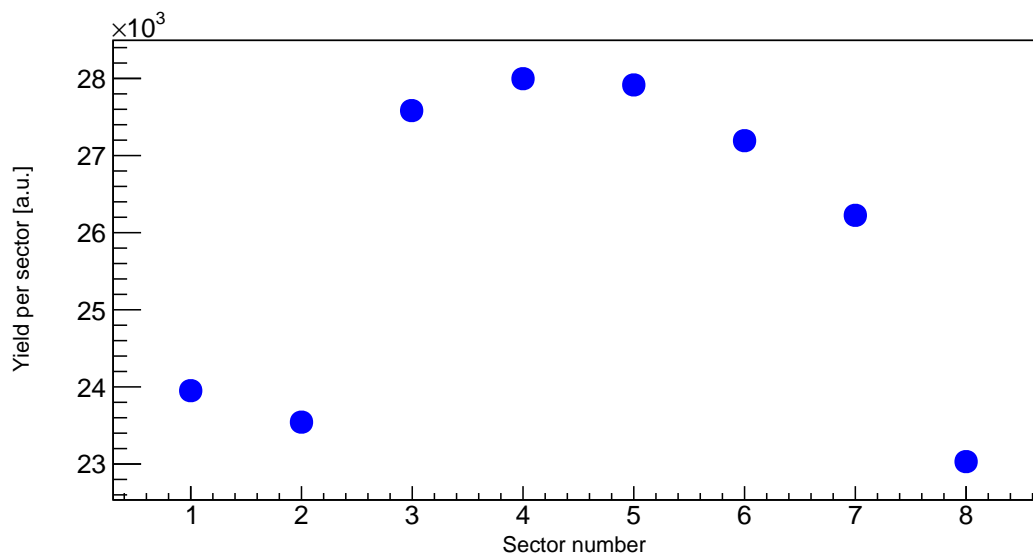


Figure 4.20: The sector hit pattern as detected by the CAKE. For this figure to be generated, each sector needs to be gated on individually.

In order to overcome the low differential cross section in the excitation energy region of interest of the ^{22}Mg nucleus, a thicker target was used to have as many possible beam-target interactions as possible. However, straggling through the target lowers the observed resolution in the CAKE. From Section 3.4, two ^{24}Mg targets were used: one with a thickness of $230 \mu\text{g}/\text{cm}^2$ and another with a thickness of $700 \mu\text{g}/\text{cm}^2$. Choosing between the two targets required a compromise between the need for both resolution and counts in the CAKE. However, there was still a clear separation of states as is illustrated in Figure 4.21 with the thicker target hence it was used for the duration of all three experimental weekends.

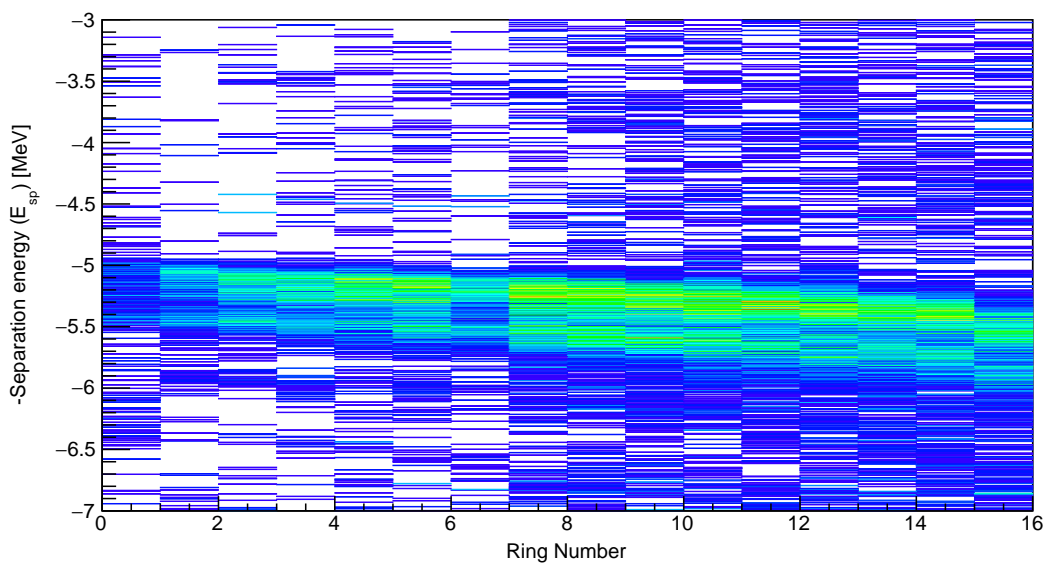


Figure 4.21: The separation energy diagram for the first experimental weekend is shown. It illustrates the separation between two states that are closely related in energy. The diagram shows that the proton straggling through the target was sufficiently low. Consequently, the DSSSD resolution was good enough for these states to be resolved. A display threshold of >2 is imposed.

For a signal from one of the MMM-type detectors to be valid and registered as a true event there has to be front-back coincidence where the ring and corresponding sector detects the same particle. This is shown in Figure 4.23 and appears as a diagonal locus running across the spectrum. To select these events, an energy condition is applied within the K600 analyser when sorting such that:

$$\left| \sum E_{ring} - \sum E_{sector} \right| < 0.2 \text{ MeV}. \quad (4.6.1)$$

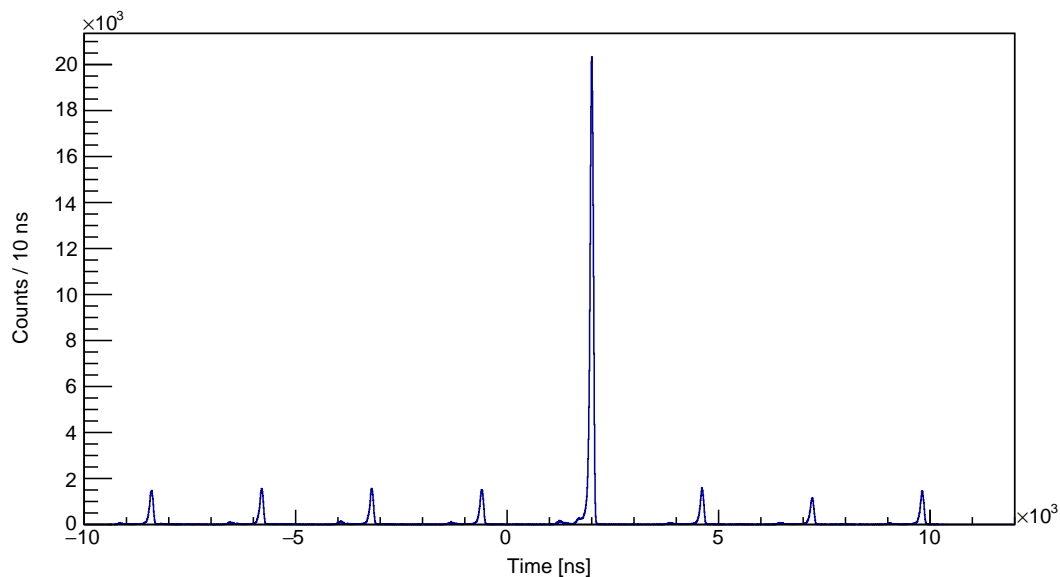


Figure 4.22: This spectrum shows the regular time structure of the SSC beam. Each peak is separate and caused by the beam pulses which are distinct and discreet. The SSC delivers the proton beam as a stream of beam packets and, with a pulse selection of 1 in 5 for this experiment, the 5th beam packet was selected to create clear timing distinctions. This is the dominant peak near 2000 ns. A software gate is applied to it to select true coincidence events.

This energy condition gates upon the real events as shown in Figure 4.24. $\sum E_{ring}$ and $\sum E_{sector}$ are the summed energies detected from the ring and sector channels, respectively. This effectively discards events from uncorrelated triggered channels.

The time spectrum for the silicon detectors had to be aligned for this experiment. Data for detector 5 were initially excluded as the events fell outside the timing gate. This could be due to various reasons including different timing on the TDC modules, different gain on the preamplifier and then a different amplification on the amplifiers, or even different cable lengths [39].

The p-side TDC channels were aligned as the n-sides of the detectors are only used to check for valid events by generating the front-back coincidence spectrum (see Figure 4.23). The offsets in the SiliconTime spectrum (see Figure 4.22) are determined by making a 2D plot of SiliconTime (the time at which the CAKE detects a particle relative to the SSC beam timing) versus TDCChannelFront (the TDC channel number corresponding to the p-side of the CAKE). A common time (2000 ns) was chosen and the time difference of each TDC channel relative to 2000 ns was calculated in order to generate the SiliconTimeOffset variable which is used to generate a gate on the valid coincidence events. The offsets are then entered into a file which is read by the analyser and the corrected SiliconTimeOffset variable is generated. The 2D

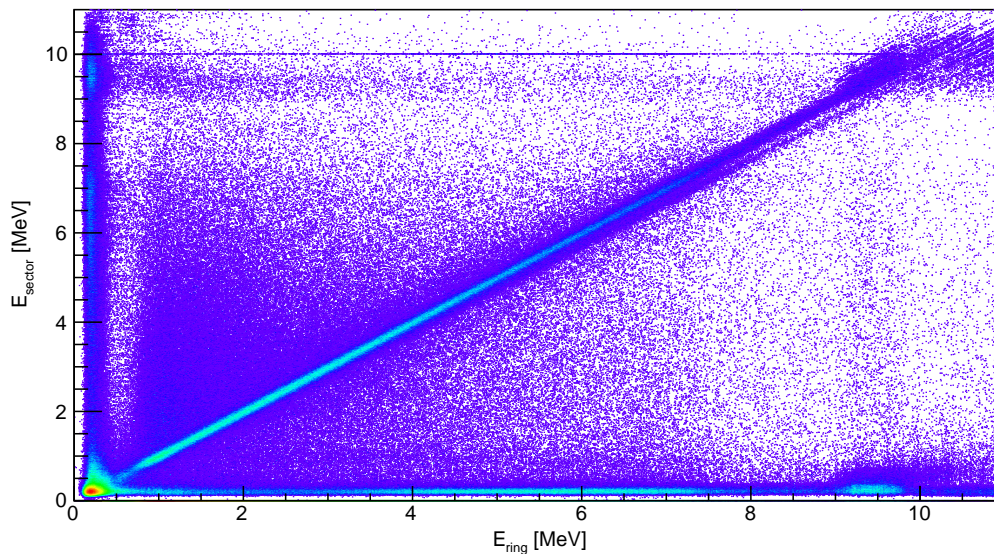


Figure 4.23: This spectrum shows the front-back coincidence spectrum for a chain of combined ^{22}Mg data runs. Requiring front-back coincidence implies that a software gate is needed in the K600 analyser to select only those events that form the diagonal locus. Beyond 9 MeV the ring and sector channels become saturated where the pulse height exceeds the capacity of the amplifier with front-back events also being saturated.

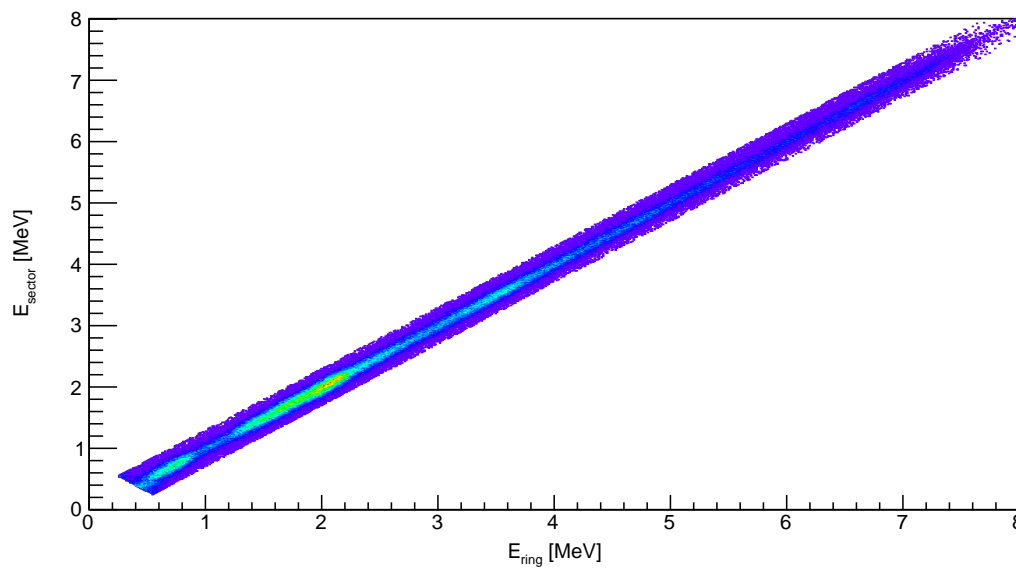


Figure 4.24: This spectrum shows the α decay locus that is gated upon by the energy condition as set out in Equation 4.6.1. Any uncorrelated events in the CAKE are thus discarded during the data-sorting process to select only true events.

time-corrected spectrum can be seen in Figure 4.25. The 1D time spectrum, as shown in Figure 4.22, is the result of projecting the 2D plot onto the x axis.

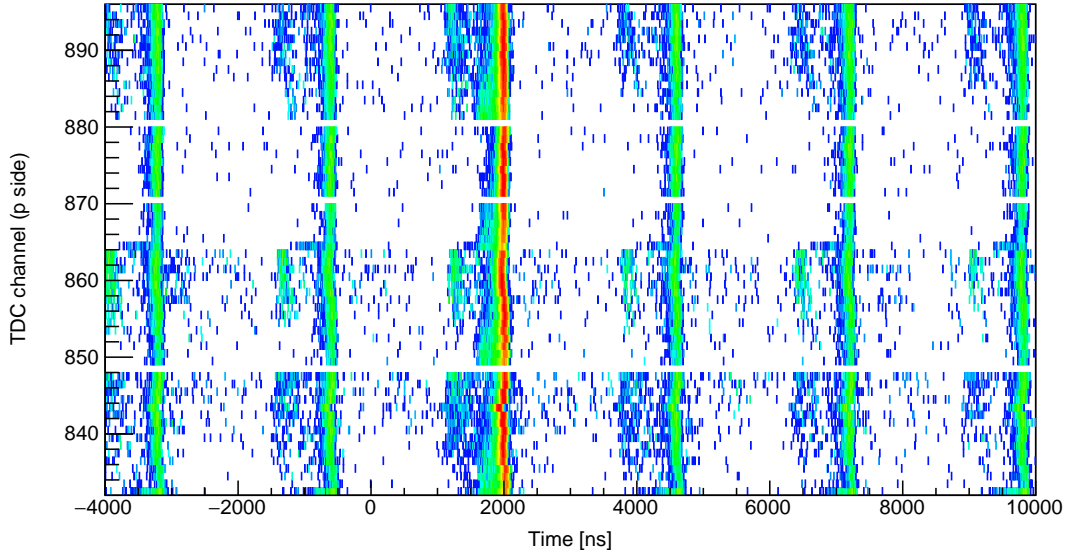


Figure 4.25: This plot shows the p-side TDC channel numbers versus the SiliconTimeOffset variable for some of the MMM detectors. The plot is in logarithmic scale to emphasize the peak of interest (around 2000 ns) that is gated on when drawing all coincidence spectra. Channels that are empty correspond to dysfunctional rings as shown in Figure 4.18.

The coincidence spectrum which plots the silicon energy signal detected in the CAKE against the excitation energy is shown in Figure 4.26. The spectrum has the previously-discussed SiliconTimeOffset gate applied to exclude random events. This is the gate placed on the dominant peak of the SiliconTime spectrum in Figure 4.22. The dominant locus in the coincidence spectrum (indicated) is the one of interest: proton decays from the recoil nucleus to the ground and first excited state in the residual nucleus, ^{21}Na . However, owing to attenuation as well as kinematic effects, broadening of the proton locus occurs. Another significant reason for this pronounced and broad nature is that decay proceeds either to the $3/2^+$ ground state or $5/2^+$ first excited state in ^{21}Na which are only separated by 332 keV [14]. The six dominant states in the spectrum are labelled by (a) to (f) and are listed in Table 4.3. Note that this spectrum and all spectra derived from this one (by applying software gates to it) were generated by adding the individual 2D histograms per run together. The reason is that it uses the same calibrations that were used for the excitation energy spectrum.

The coincidence spectra gated on detectors 1-5 were drawn to determine the effect that different detector thresholds had on the data. This impacts

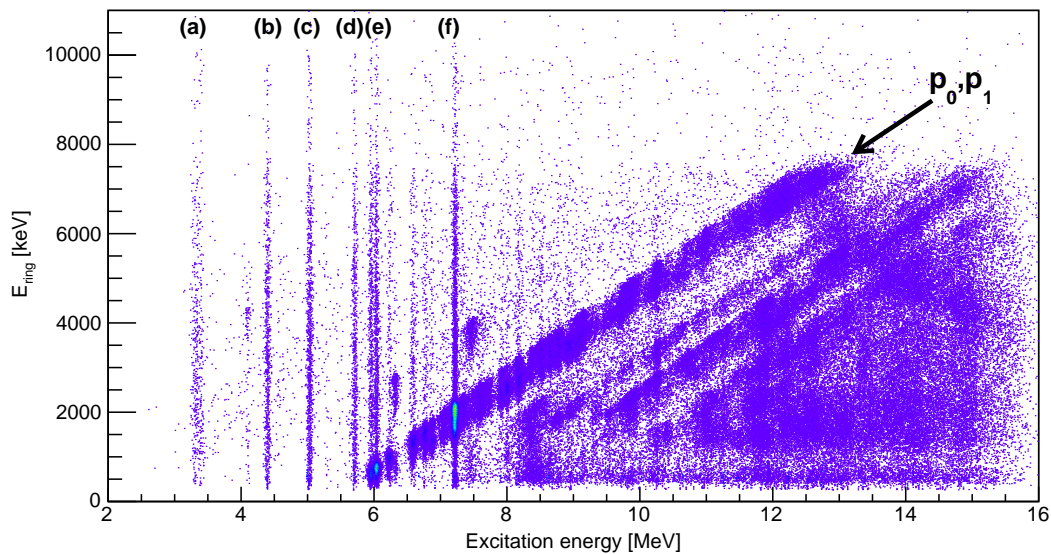


Figure 4.26: The coincidence spectrum shows the energy signals detected by the CAKE plotted against the excitation energies. A timing gate is included to exclude any data that is due to random events. The six dominant states are labelled (a) to (f) and are listed in Table 4.3. The p_0 and p_1 decay locus is indicated.

how low an energy signal a particular detector will pick up. It was determined that there was no appreciable difference as the thresholds were similar for all detectors (see Table 3.1). Therefore, all five detectors were analysed in the same way.

Gates can be placed on the rings and sectors of the CAKE as well as on separate detectors. The individual decay loci p_0 and p_1 can be seen by gating on individual rings of the CAKE. Figure 4.27 clearly shows the two different decay loci appear when ring 1 is gated on. In order to generate and fit the p_0 and p_1 spectra used in Section 4.7, the p_0 locus for all 16 rings were gated on separately and their excitation energy histograms combined. The p_1 spectrum was generated similarly. Figure 4.28 clearly shows the kinematic and attenuating effects. As protons are emitted by the recoil nucleus, still located within the ^{24}Mg target, they have to be emitted at ever greater angles to be detected by the outermost rings of the CAKE. As a result, the protons effectively move through more of the target and thus lose more energy in reaching the detectors.

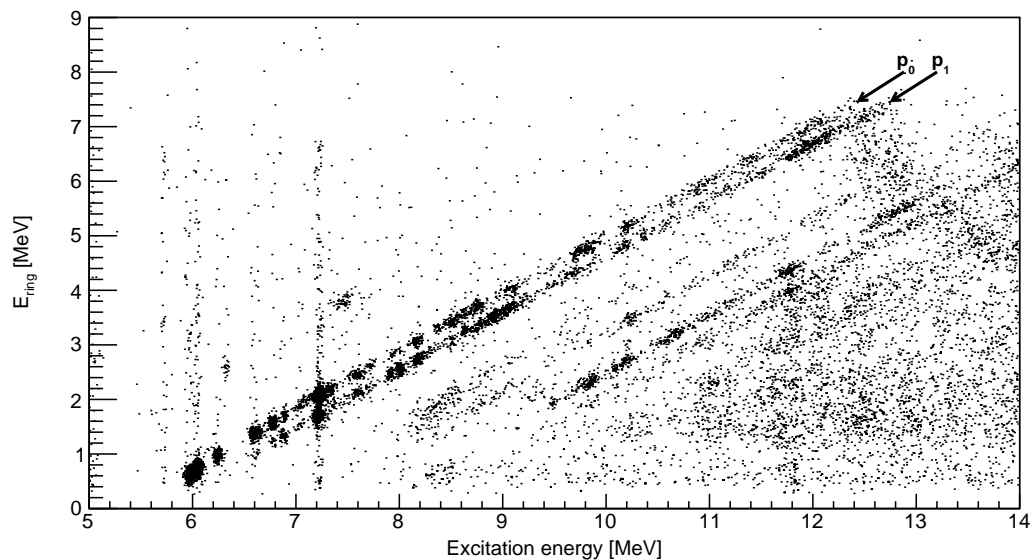


Figure 4.27: The coincidence spectrum from the CAKE gated on ring 7 is shown. Placing a gate on individual rings shows the two different proton-decay loci p_0 and p_1 .

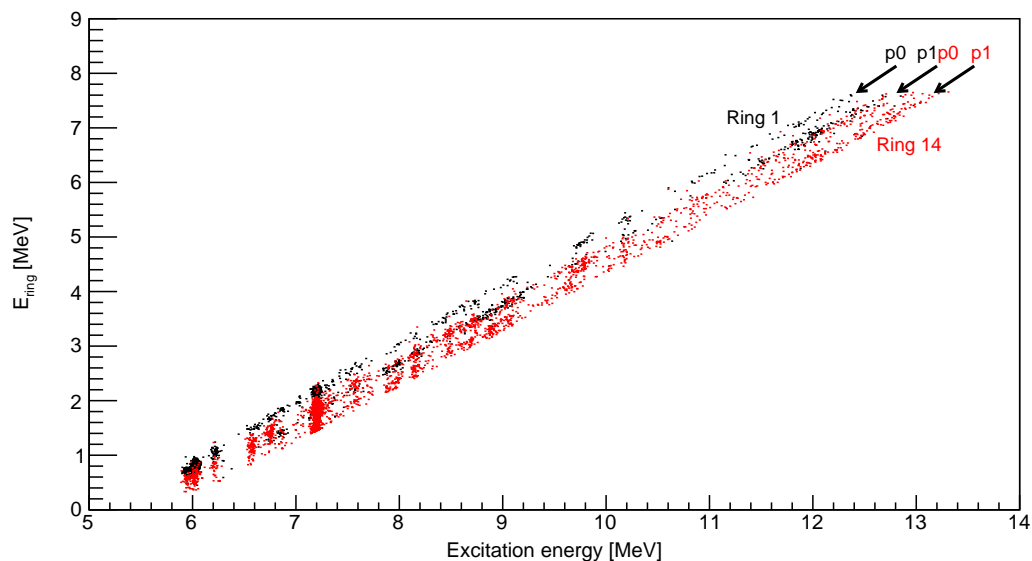


Figure 4.28: This spectrum shows the different kinematic and attenuation effects of the proton decays. The distance travelled by decay products through the target depends on the angle of emission w.r.t. the beam axis. The ring channels of the CAKE subtend different polar angles. Therefore, the target attenuation is dependent on the ring number that detects the particle which is why it is clearly seen when different ring channels are being gated on.

4.7 Excitation energy spectra fits

As part of the data analysis various excitation energy spectra were fitted with Voigt profiles to extract information regarding the yields of the resonances. The Voigt profile results from the convolution of the Gaussian and Lorentzian distributions. Distinction was made between which states to fit with a pure Gaussian or a Voigt function as states with a width significantly less than the measured experimental resolution (47(5) keV) would have their respective widths set to 0 and thus treated with a Gaussian distribution.

The Lorentzian function, L , resembles the proper shape of a resonance with width Γ . The Gaussian function, G , represents the practical resolution of a detector. Therefore, the Voigt function which is the convolution of the functions L and G is the best representation of measured resonances. For very narrow resonances you are thus limited by detector resolution which is why narrow states are fitted only with G in the following spectra.

For each fitted spectrum there were three parameters for each state (one for the resonance energy (E_r), width (Γ_r) and amplitude) and three additional parameters for the entire spectrum: two for the linear background and one for the experimental resolution. The processing time for each fit is proportional to the square of the number of parameters. Once known, some resonance-width parameters were fixed to reduce running time as the fit needs to converge for the covariance fit matrix to be valid and ultimately to determine the errors for the extracted parameters. The Gaussian, Lorentzian and Voigt equations follow [58]. The Gaussian standard deviation is given as σ , the Lorentzian width parameter is symbolised by Γ and the location parameters, to determine E_r , for the Gaussian, Lorentzian and Voigt functions are given as μ_G , μ_L and μ_V , respectively.

$$G(x : \mu_G, \sigma) = \frac{1}{\sigma\sqrt{2\pi}} \exp \left[\frac{-(x - \mu_G)^2}{2\sigma^2} \right] \quad (4.7.1)$$

$$L(x : \mu_L, \Gamma) = \frac{\Gamma/2}{\pi[(x - \mu_L)^2 + (\Gamma/2)^2]} \quad (4.7.2)$$

$$V(x : \mu_V, \sigma, \Gamma) = \int_{-\infty}^{\infty} G(x, \mu_G, \sigma) L(x - x', \mu_L, \Gamma) dx' \quad (4.7.3)$$

The location parameter of the Voigt function, μ_V , is always taken as the resonance energy, E_r , as the Gaussian function is always assumed to be centred making the location parameters for V and L equal. The resonances were fitted to minimise the $\chi_{reduced}^2$ so that $\chi_{reduced}^2 \sim 1$. Figure 4.29 visually illustrates the difference between these three different functions, given similar fitting parameters.

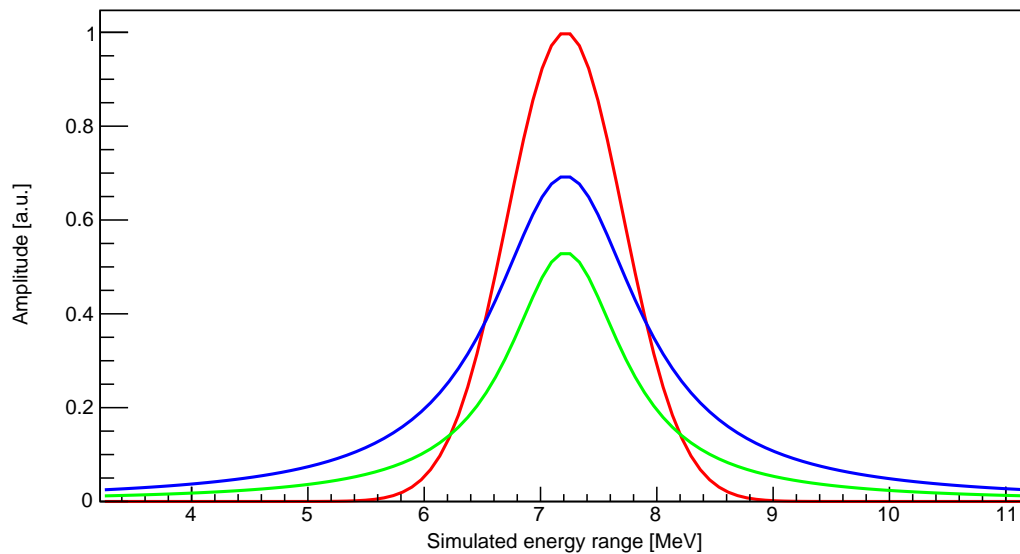


Figure 4.29: The standard Gaussian, Lorentzian and Voigt functions are compared and contrasted in this example and shown in red, green, and blue, respectively. The amplitude is normalised to 1 and the other parameters were set to $\mu = x - 7.214$ and $\sigma = 0$ for each of the functions.

The spectra that were fitted include the singles focal-plane spectrum and the coincidence spectrum. The parameters from the fit are given in Table 5.1 in Chapter 5. The p_0 and p_1 spectra were fitted as well as the p_0 and p_1 spectra gated on individual ring channels of the CAKE. However, since the number of counts from the states of interest were low (owing to an inherently low differential cross section), various rings were grouped together to overcome the geometric limitations of the solid-angle coverage of the CAKE. Rings 1 to 4 were grouped together as were rings 5 to 8, 9 to 11 and 12 to 15. For this reason, the angular correlation spectra discussed in Subsection 5.3.2 have four data points instead of fifteen, one for each group of rings of the CAKE.

The fits of all above-mentioned spectra follow. Additionally, note that the excitation energy region between 7 MeV and the dominant peak at 7.214 MeV is unresolved. From Ref. [35] it is known that there are four states in the region at 7.027, 7.045, 7.060 and 7.079 MeV which are not seen in this data set. This region is thus excluded from further analysis.

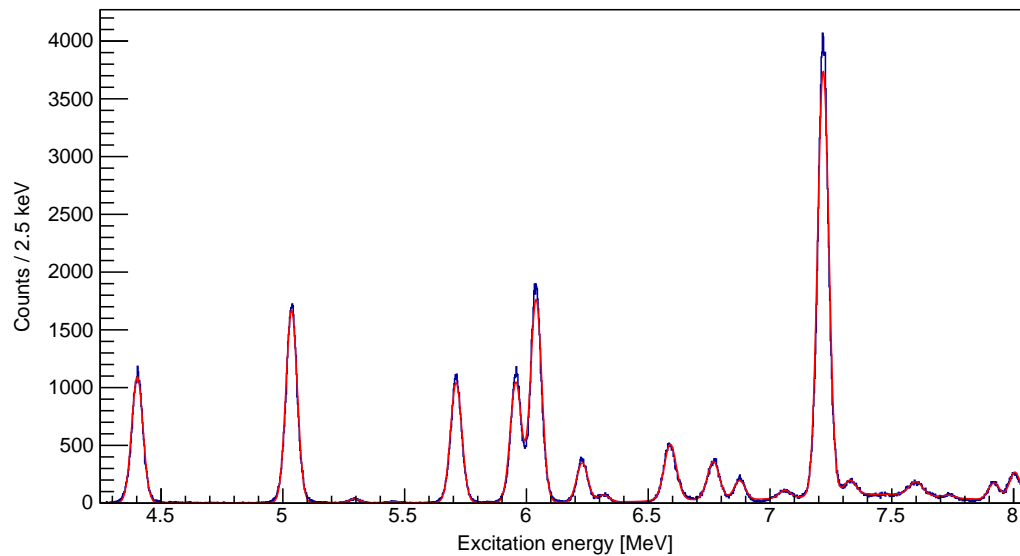


Figure 4.30: The singles excitation energy spectrum is shown. It has the largest number of parameters to be included in the fit since it has the highest number of states. The states below the proton decay threshold, S_p , at 5.502 MeV fall away once the coincidence gates are applied.

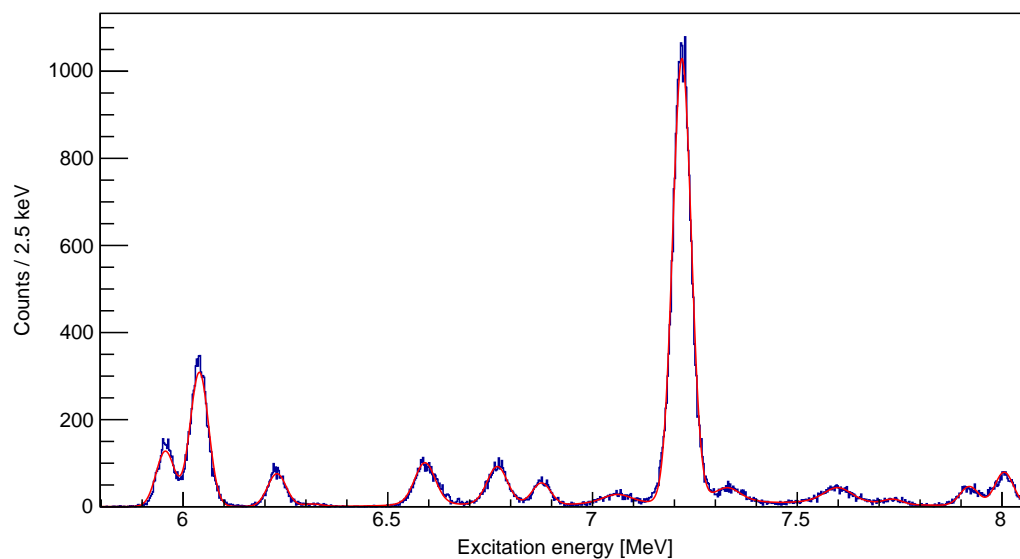


Figure 4.31: The coincidence excitation energy spectrum is shown. This spectrum has no states below 5.502 MeV which is where the threshold is for proton decay in ^{22}Mg . The spectrum shows decays to either the ground state or the first-excited state. Distinction between these two types of events is made in the following two spectra.

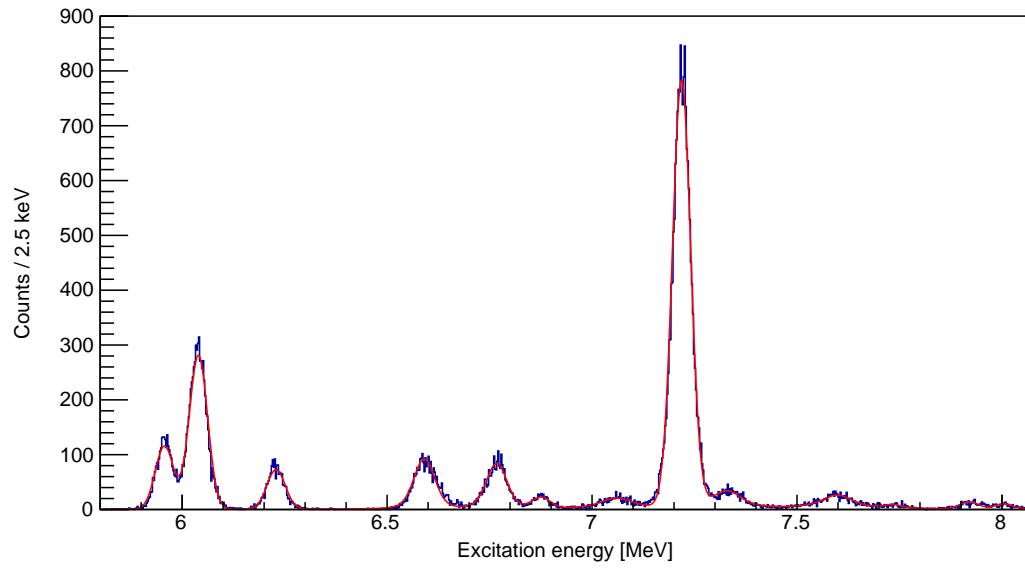


Figure 4.32: Coincidence spectrum gated on p_0 - decays to the ground state of ^{21}Na . Note the similar scale here as in the following spectrum so that it can be compared as shown in Figure 4.34.

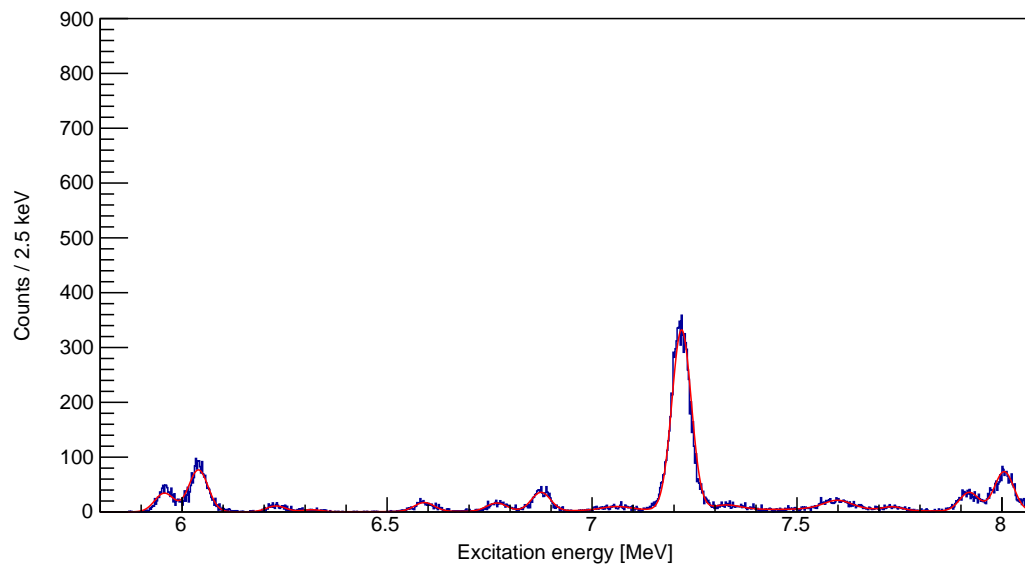


Figure 4.33: Coincidence spectrum gated on p_1 - decays to the first excited state of ^{21}Na at 331 keV [14].

When determining the branching ratios the p_0 and p_1 spectra can be superimposed over the complete coincidence spectrum. It is interesting to note that, as one would expect, the majority of states decay to the ground state but at higher excitation energies, just below the α -particle decay threshold, there are more instances of decay to the first excited state.

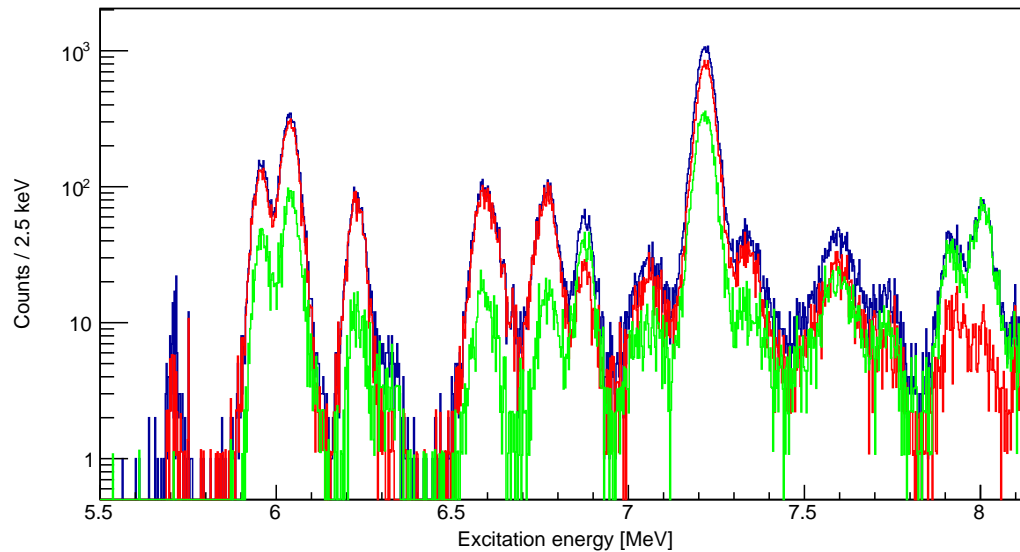


Figure 4.34: The coincidence spectra gated on p_0 (red) and p_1 (green) decay are superimposed over the complete coincidence spectrum in blue. The y axis is on a logarithmic scale and the spectrum is plotted from S_p to S_α . The spectrum with resonances above S_α is shown in Chapter 5. Note how decays to the first excited state become more preferable above ~ 7.5 MeV whereas the opposite is true below that level.

The spectra gated on decay to either the ground or the first-excited state can be gated further with regards to the rings of the CAKE. Due to geometric considerations and the inner-most rings covering a smaller solid angle, the grouping of rings are not done consistently. The following spectra are the grouped ring spectra for p_0 and p_1 decays. The scale of the y axis is kept constant in order to compare and contrast the number of counts in each group as a result of the solid angle subtended by different rings of the CAKE.

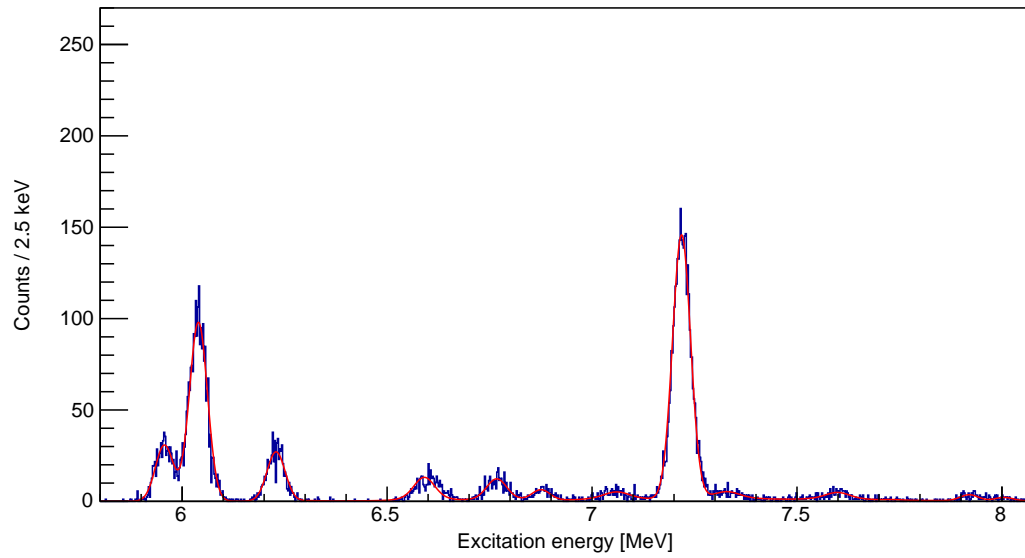


Figure 4.35: Excitation energy spectrum gated on p_0 decay and CAKE rings 1 to 4. Note the change of scale from the p_0 and p_1 spectra.

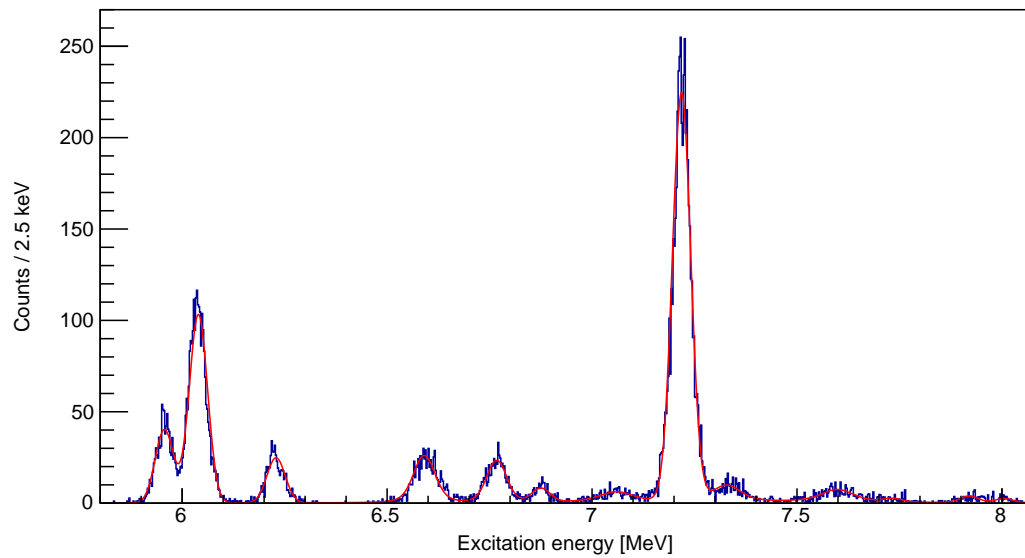


Figure 4.36: Excitation energy spectrum gated on p_0 decay and CAKE rings 5 to 8.

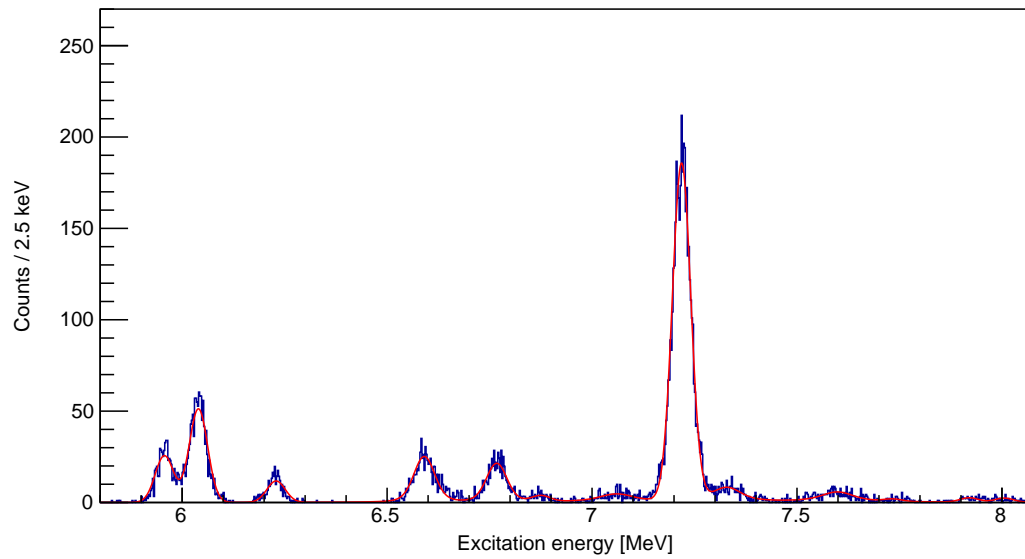


Figure 4.37: Excitation energy spectrum gated on p_0 decay and CAKE rings 9 to 11. This spectrum only contains 3 rings as rings 9 to 11 subtend the largest solid angle individually out of all of the other rings of the CAKE.

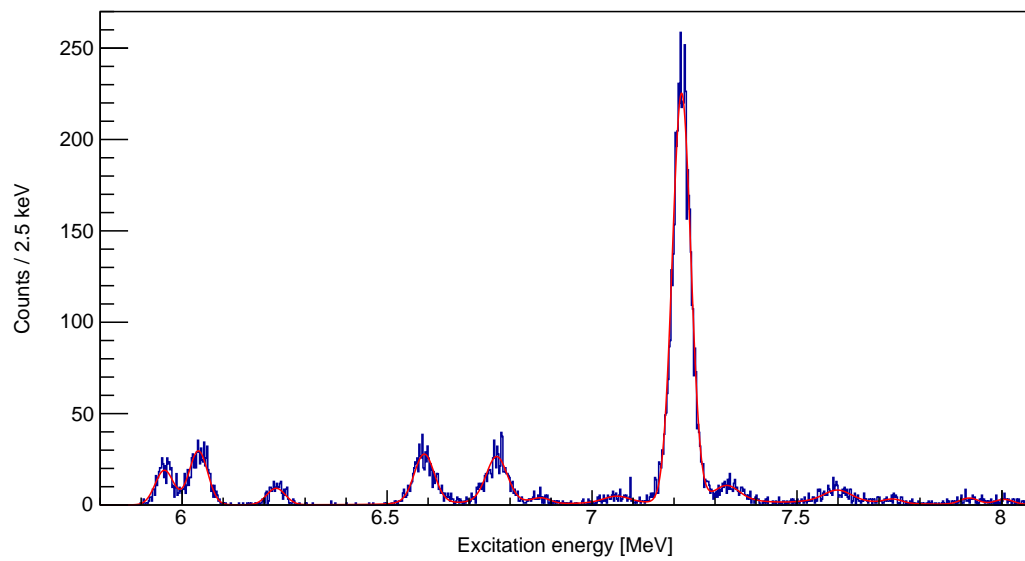


Figure 4.38: Excitation energy spectrum gated on p_0 decay and CAKE rings 12 to 15.

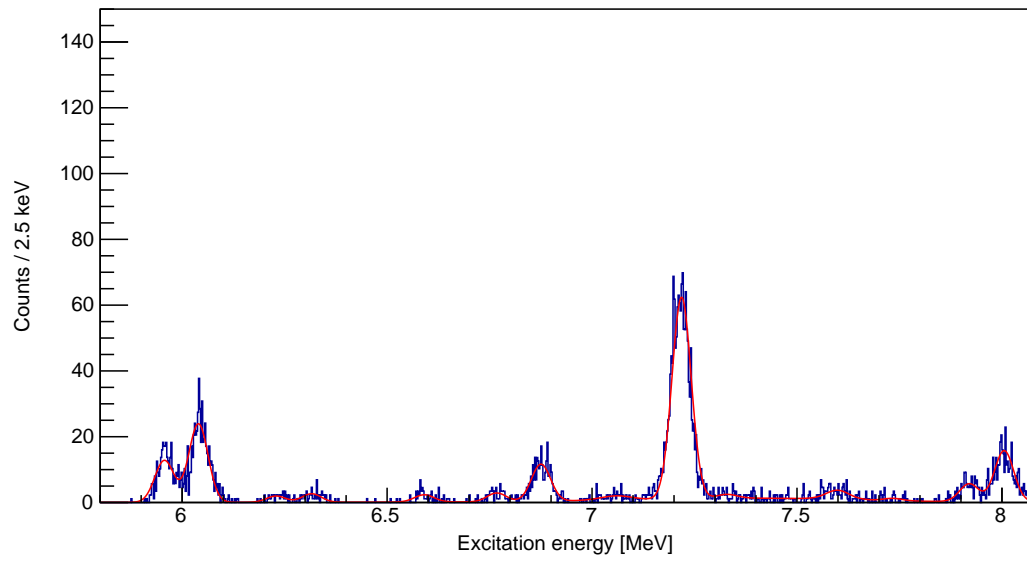


Figure 4.39: Excitation energy spectrum gated on p_1 decay and CAKE rings 1 to 4. Note the further reduction in scaling of the y axis from the previous spectra.

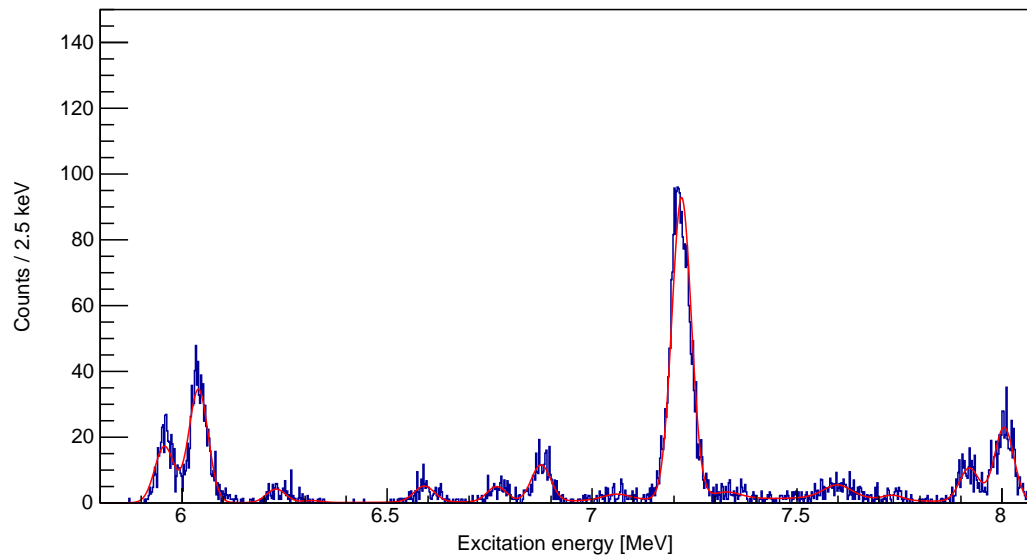


Figure 4.40: Excitation energy spectrum gated on p_1 decay and CAKE rings 5 to 8.

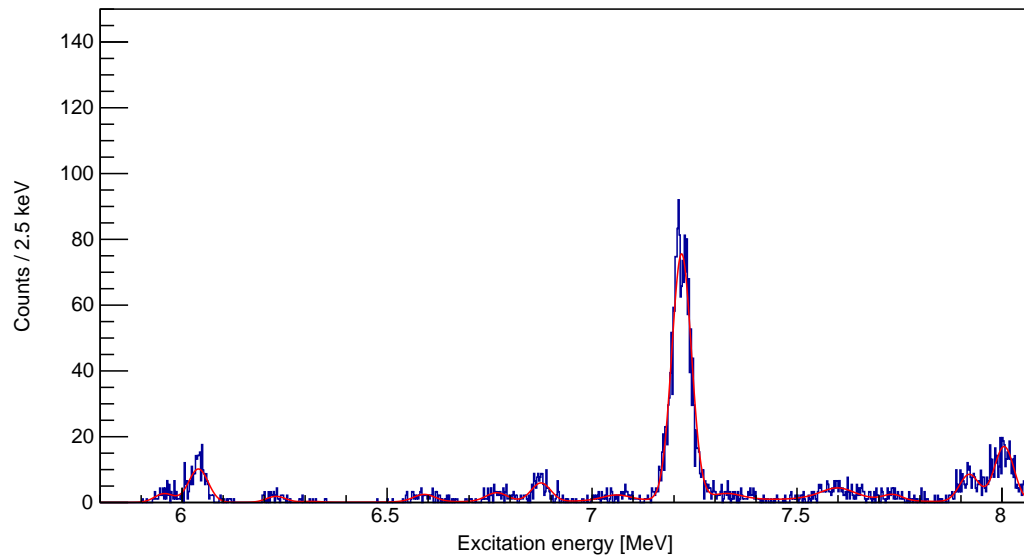


Figure 4.41: Excitation energy spectrum gated on p_1 decay and CAKE rings 9 to 11. This spectrum only contains 3 rings as rings 9 to 11 subtend the largest solid angle individually out of all of the other rings of the CAKE.

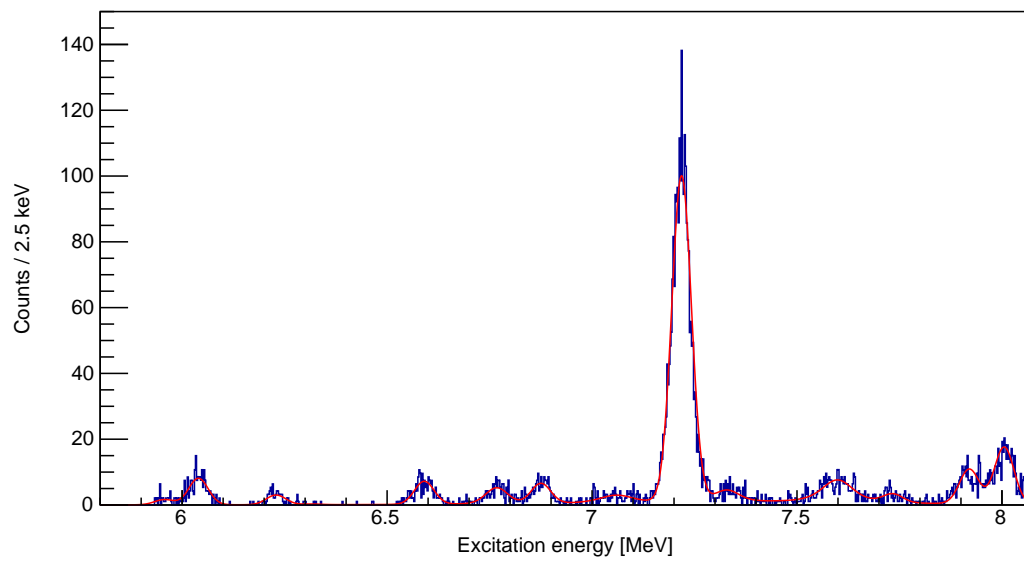


Figure 4.42: Excitation energy spectrum gated on p_1 decay and CAKE rings 12 to 15.

Chapter 5

Analysis Results

To know that we know what we know, and to know that we do not know what we do not know, that is true knowledge.

Nicolaus Copernicus

5.1 Introduction

The aim of this chapter is to determine proton branching ratios from ^{22}Mg to various excited states in ^{21}Na . The proton branching ratio to the i 'th state is B_{p_i} . This will be calculated for states below and above the α -particle decay threshold, S_α , at 8.142 MeV. To calculate them, information regarding the angular distributions of the decays are needed. Therefore, the angular correlation spectra and their associated angular correlation functions are needed to correct for the missing solid angle that is not covered by the CAKE. The CAKE only covers a limited part of the total solid angle from $\theta_{lab} = 114^\circ$ to $\theta_{lab} = 164^\circ$. Therefore, the part of the solid angle where no detection capability exists needs to be corrected for to calculate the total number of p_0 or p_1 decays and thus their respective branching ratios B_{p_0} and B_{p_1} .

Corrections to the angular correlation spectra are also needed to reconstruct the angular distribution accurately. This chapter will, therefore, show the various corrections to the data and their origin. They will be applied to the yields from the excitation energy spectra to reconstruct the angular distributions. Spin-parity assignments for states below S_α will also be discussed. The following will form part of this chapter:

- corrections to the yields,
- fit results of the coincidence excitation energy spectrum,

- angular-correlation spectra,
- ℓ -value assignments,
- angular-correlation functions ($W(\theta)$),
- proton branching ratios (B_{p_i}), and
- spin-parity (J^π) assignments.

The corrections to the angular correlation spectra are determined in the first section. The states below S_α , and above the proton-decay threshold S_p at 5.502 MeV, will be analysed individually and will form the second section. The analysis of states above S_α will be given separately in the last section as a more generalised analysis approach will be used due to the unresolved states in this region and low number of statistics.

5.2 Yield corrections

In order to reconstruct the angular distributions accurately, certain corrections have to be made to the yields that will be extracted from the excitation energy spectra. These include taking into account the solid angle subtended by each ring of the CAKE and using that to determine the ring efficiency for each ring of the CAKE. Rings and sectors that were dysfunctional also have to be taken into account when calculating the ring efficiencies. Lastly, the coordinate system transformation from the laboratory reference frame to the centre-of-mass reference frame (θ_{lab} to $\theta_{c.m.}$) will also be discussed and included in the yield corrections.

The GEANT4 simulations discussed in detail in Subsection 3.4.2 showed the solid angle subtended by each ring of the CAKE. These have to be converted to ring efficiencies. A subtlety exists when calculating the efficiency of each ring of the CAKE. Whilst it is true that the CAKE has a global efficiency of 27%, the reason for that low value is that it physically covers only a small portion of the total solid angle. In reality, the angular-dependent ring efficiencies are much higher. The true efficiencies calculate the chance of the CAKE detecting a particle that is emitted into its physical region. In Appendix A Section A.2 calculations are made to show the factor that the solid angle of each ring is multiplied by to convert it to a ring efficiency. A factor that lowers the detection efficiency is e.g. the printed circuit board (PCB) structure between MMM detectors. The next correction to take into account is the dysfunctional rings and sectors.

Figures 5.1 and 5.2 show the spectra for the front (p-side) and back (n-side) ADC channels. Each set of 16 rings or 8 sectors follow the trends shown by the ring or sector simulations, respectively, in Section 3.4.2. Dead rings or sectors can be seen as bins in the spectra that have no counts or bins that clearly have

fewer counts. This was also discussed in Section 4.6 using the polar plot of the pixels of the CAKE in Figure 4.18.

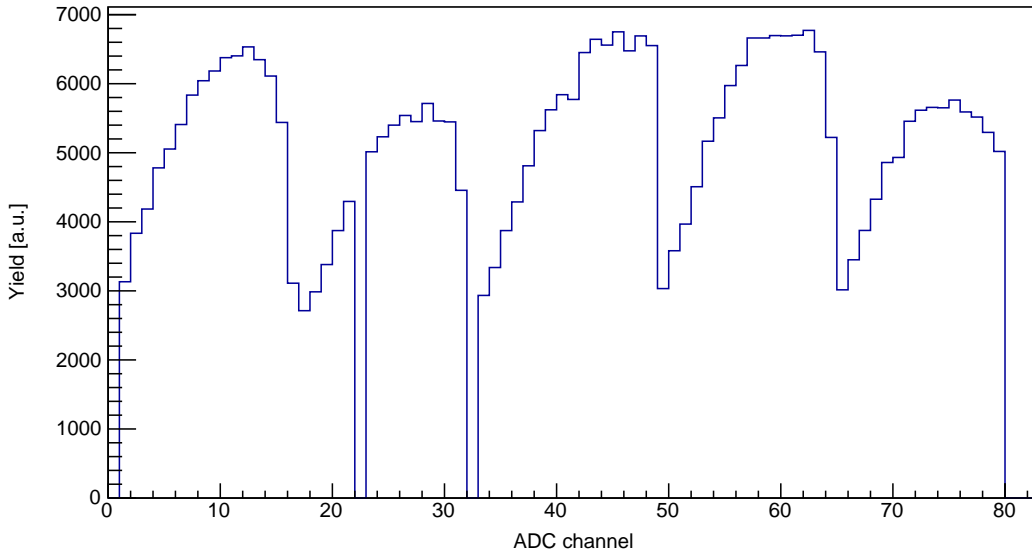


Figure 5.1: The yield spectrum for the ADC channels that correspond to the p-side (rings) of the CAKE for the entire dataset. There are 16×5 channels that range from channel 0 to 79.

Certain sectors and rings were discarded altogether due to the lack of data seen in them. Ring 0, the innermost ring closest to the beam axis, had two sectors that were dysfunctional showing no counts. Two of the three functional sectors showed anomalously high counts likely resulting from beam halo. The data from ring 0 was thus discarded altogether given that potentially only one sector recorded good data and that it subtends the smallest solid angle of all the rings in the CAKE. Other sections that were discarded was ring 6 of detector 2 and sector 1 of detector 2.

Each ring has 40 sector pixels. Due to the dead sector, 1 out of 40 sector pixels (2.5%) in each ring had no data. Every ring was thus scaled by $1/0.975$. Ring 6 was scaled by $1/0.8$ as the 8 dead pixels in detector 2 represents 20% of the complete ring.

Calculations were made to see the effect of transforming from the laboratory inertial frame to the centre-of-mass reference frame. The lab angle, θ_{lab} , was transformed to the angle in the centre-of-mass frame, $\theta_{c.m.}$. The two angles were compared and found to be roughly within 0.5° of each other between 0° and 180° . The transformation thus shows little effect which is due to the recoil nucleus having a low kinetic energy with an equally low boosting effect on its decay products. Using two-body kinematics, it was found that the recoil has between $T_{lab} = 0.654$ and 0.947 MeV for an excitation energy

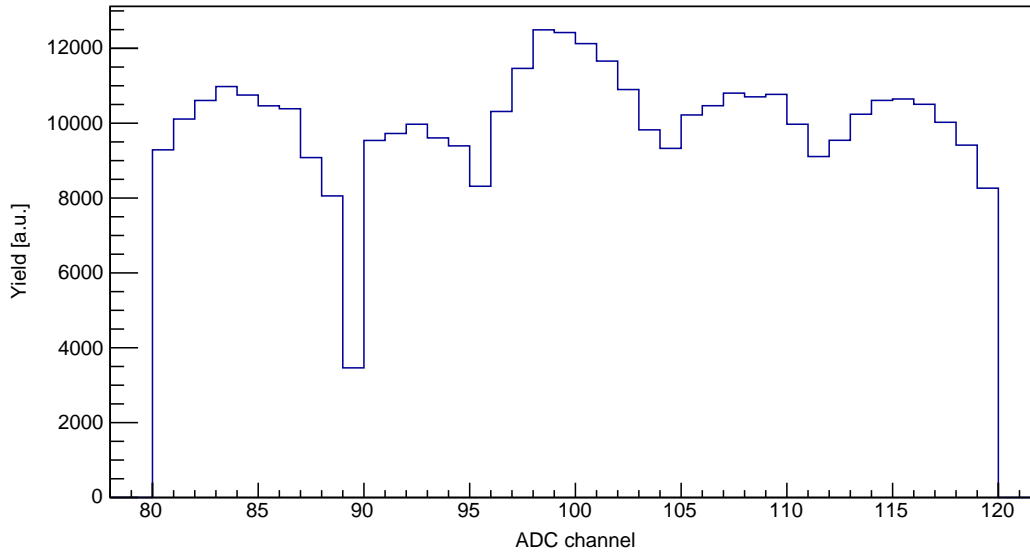


Figure 5.2: The yield spectrum for the ADC channels that correspond to the n-side (sectors) of the CAKE. There are 8×5 channels that range from 79 to 119.

between 5.502 MeV (S_p) and 13.0 MeV (proton punch through in the silicon detectors). Consequently, the transformation has little effect on the results because the difference between θ_{lab} and $\theta_{c.m.}$ is smaller than the angle binning of the CAKE array. The 16 rings of the CAKE each subtend an angle between 2.94° and 3.59° . No correction to the yields was thus made for this centre-of-mass transformation. Therefore θ_{lab} will be used throughout the rest of the analysis. Taking into account all of the corrections discussed in this section the true ring efficiencies can be calculated. This is shown in Figure 5.3.

The final correction that was made to the data is related to the yield equation for emissions into a certain angular range:

$$\begin{aligned}
 Y &= 2\pi \int_{\theta_{min}}^{\theta_{max}} W(\theta) \sin\theta d\theta \\
 &= 2\pi W(\theta_{centre}) \int_{\theta_{min}}^{\theta_{max}} \sin\theta d\theta \\
 &= 2\pi W(\theta_{centre}) (\cos(\theta_{min}) - \cos(\theta_{max})). \tag{5.2.1}
 \end{aligned}$$

The range θ_{min} to θ_{max} is the angular range of a particular ring of the CAKE. The data in Figure 3.17 showed the angles related to the central point, θ_{centre} , in each ring which are used to get the lower and upper angles of each ring by getting the value between two successive midpoints: $\theta_{centre} = (\theta_{min} + \theta_{max})/2$. The angular correlation function at that value, $W(\theta_{centre})$, is assumed to be

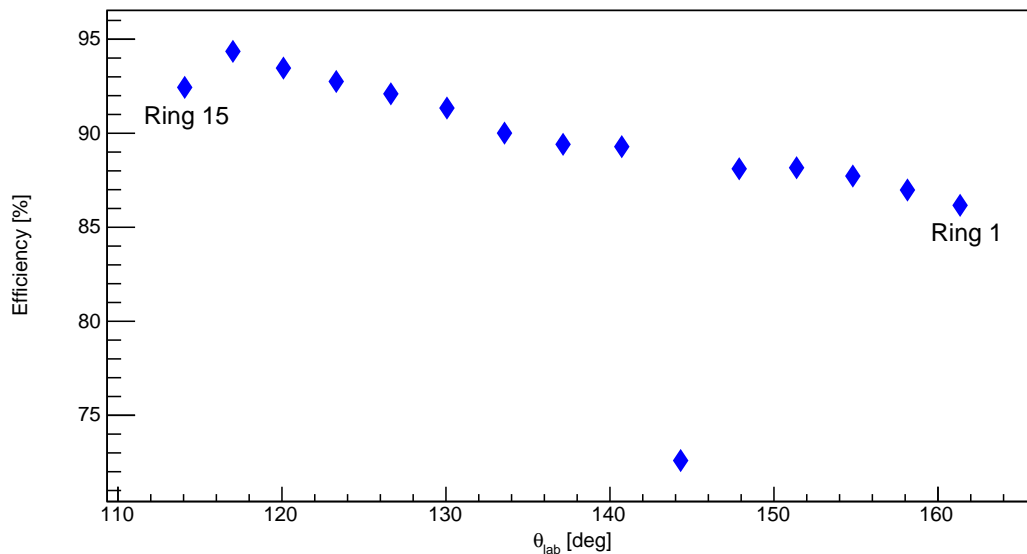


Figure 5.3: The relative ring efficiencies of the CAKE. Ring 0 is excluded. It takes into account all of the corrections discussed in this section. The data point near 144° is much lower because of the correction due to the dead ring 6 in detector 2. The effect is compounded by the additional calculations.

constant over the range of interest. The results then show that the angular correlation spectrum needs to be corrected with a factor of $2\pi(\cos(\theta_{min}) - \cos(\theta_{max}))$.

The combined effect of all the corrections can be visualised using the GEANT4 simulation results and applying the corrections to those results. The simulations were written for isotropic ($\ell=0$) decay. This is evident from Figure 3.20. Therefore, we expect to see the corrected angular correlation spectrum as a constant function. This is shown in Figure 5.4 where the simulated data (red) is corrected and the resultant graph (blue) is constant. This result is significant as it shows the validity of the corrections which is crucial for the analysis that will be discussed further in this chapter.

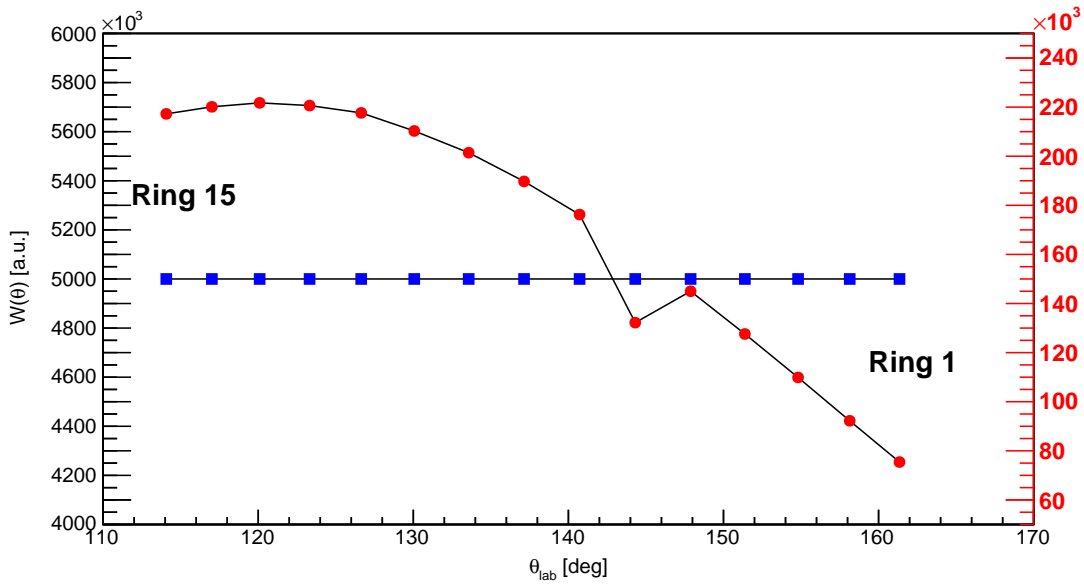


Figure 5.4: The corrected and uncorrected yield spectra of the GEANT4 simulations. The red graph (which corresponds to the latter, red y -axis) shows the uncorrected, raw simulation yields whereas the blue graph shows the corrected yield. Both have the same y -axis units. The labels indicate at which side the lower and higher rings are.

5.3 Analysis of states below S_α

5.3.1 Coincidence fit results

States below S_α were fitted to extract their resonance energies ($E_r = E_x - S_p$) and resonance widths (Γ_r). States in the spectrum with small Γ_r [30] had their widths set to zero and were fitted with a Gaussian function. Broader states were fitted with a Voigt function. Data regarding E_r from the singles fit are listed in Table 5.1 and compared to known states in Ref. [35]. The difference in E_r between literature and this study, Δ , is given in the table. The parameters that correspond to E_r and Γ_r from the singles fit are used for the coincidence fits. These parameters are then fixed as they need to be the same as for the singles spectrum. All 12 states listed in the table are from the coincidence spectrum in Figure 4.31. The unresolved state above 7 MeV is not included. The widths are also not included as they are not used further in the analysis.

The following subsections will expand on the analysis to determine B_{p_0} and B_{p_i} for all the resonances. The first step will be to use the fits of the resonances in the ring-gated spectra to extract the relevant yields and generate the corrected angular distribution spectra. The ℓ values are then determined by fitting these spectra with a Legendre polynomial. Following that, the angular

State	E_x / keV	$E_x(\text{Matic})$ / keV [35]	Δ / keV	J^π [35]
1	5957(7)	5954(6)	3	0^+
2	6040(6)	6037(8)	3	$[3^-]$
3	6229(6)	6226(10)	3	(4^+)
4	6591(8)	6580(6)	11	(1^-)
5	6767(11)	6769(12)	2	$(1^+, 2^+)$
6	6875(10)	6876(12)	1	$(2^+, 3^-)$
7	7218(10)	7218(9)	0	0^+
8	7331(11)	7338(13)	7	$[2^+]$
9	7599(13)	7601(27)	2	$(1^+, 2^+)$
10	7734(9)	7742(19)	8	(2^-)
11	7920(12)	7921(14)	1	(2^+)
12	8005(10)	8005(13)	0	$[3^-]$

Table 5.1: Fit results for states below S_α . The information is extracted from the Gaussian and Voigt fit parameters. The associated J^π values from Ref. [35] are listed. Tentative assignments are in round brackets. Where no tentative spin assignments are known, spin assumptions from mirror assignments are given in square brackets. Δ is the difference in E_x between this study and literature [35] ($\Delta = |E_x - E_x(\text{Matic})|$).

correlation function can be generated and integrated to calculate the complete and true yield of each resonance. The branching ratios are then calculated by dividing each true resonance yield by the singles yield.

5.3.2 Angular correlation spectra

The GEANT4 simulation data were used to construct an angular correlation spectrum after having the corrections applied to the data. The data were grouped in the same way as was discussed at the end of Chapter 4. The resultant spectrum was generated and is shown in Figure 5.5. It is shown as an example of what a 4-point angular distribution should look like for a resonance that decays isotropically.

The Voigt and Gaussian fits were used to extract the yields of the states below S_α to produce the 4-point angular distributions of the data as was done for the simulated data. This was done using the spectra from Figures 4.35 to 4.42 shown in Section 4.7. For every state of interest there are four points in the angular correlation spectrum as the rings of the CAKE were put into

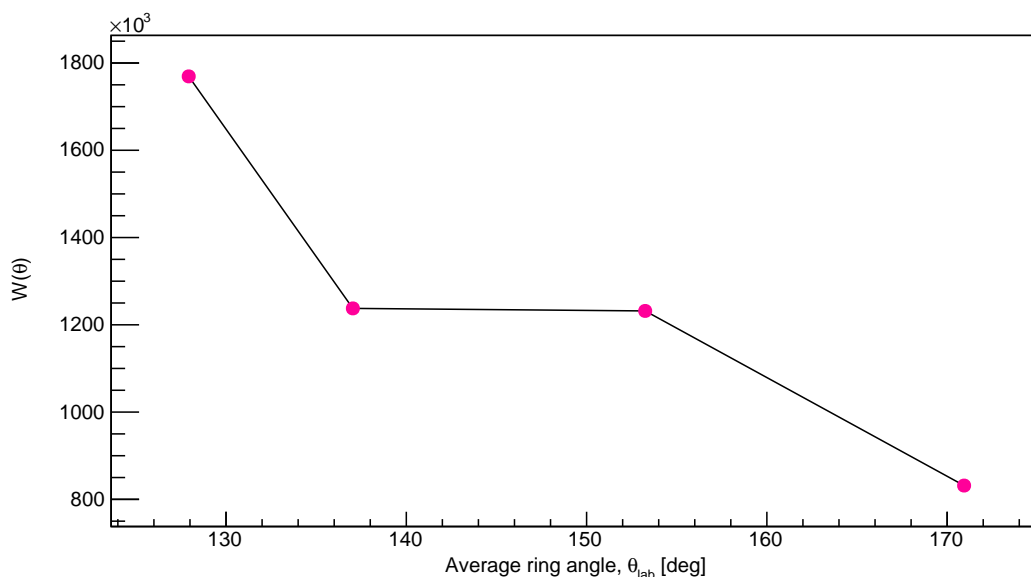


Figure 5.5: The angular correlation spectrum from the GEANT4 Monte Carlo simulations of the CAKE. The same yield corrections are made to the simulated yields. This is an example of a 4-point angular distribution for isotropic decay.

four groups. These groups are rings 1-4, 5-8, 9-11 and 12-15. The p_0 and p_1 excitation energy spectra were gated in this way.

Each ring has to be scaled by a different percentage as is evident from Figure 5.3. Consequently, as the rings had to be grouped together, the simplest solution was to scale the individual spectra before adding their histograms into groups of 3 or 4 rings. As an example, two of the angular correlation spectra are shown in Figures 5.6 and 5.7.

The following section will discuss fitting the p_0 and p_1 yield spectra with the Legendre polynomials in order to extract the ℓ values which are used to construct the angular correlation function. It is less conventional to have four data points with which to determine these values. However, the method used here to fit the spectra with Legendre polynomials is used often in literature [59]. Certain resonances have higher cross sections with exit channels that enjoy greater preference. They are thus populated more often as is evident from the coincidence spectra. Moreover, it was also seen that below S_α p_0 decay dominates. Therefore, to verify the validity of these fits, the resonances with more statistics will also be analysed using fifteen data points instead of four to reproduce the results of their analogous four-point yield spectra.

5.3.3 ℓ -Value assignments

The theoretical basis for this section was discussed in Subsection 2.7.1. The ℓ -value fits for the corrected angular distributions shown in Figures 5.6 and

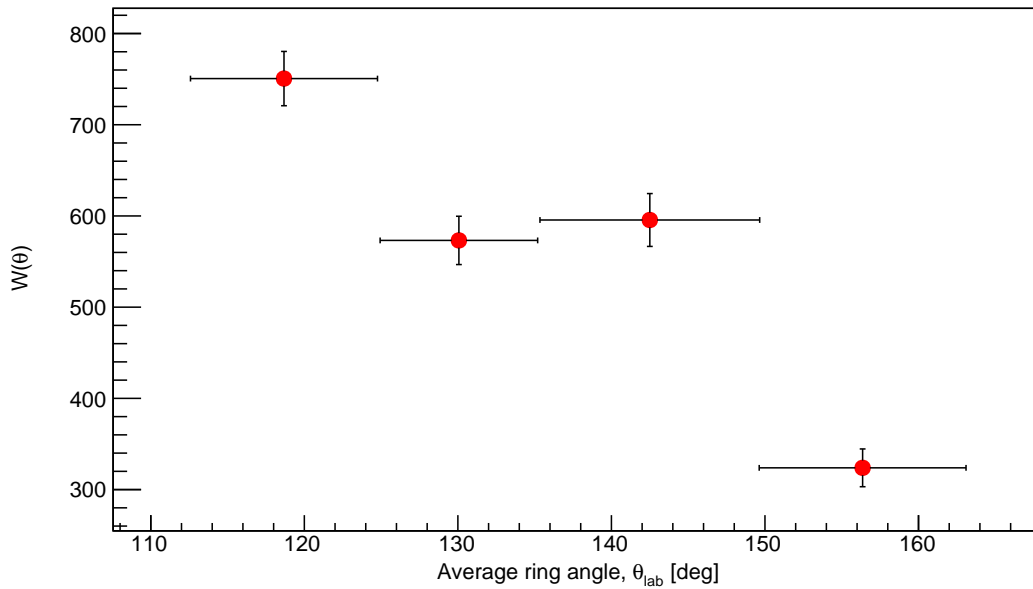


Figure 5.6: The corrected yield spectrum for p_0 decay of the 6.767 MeV state. The x -axis error bar shows the angular ranges of the groups of rings and do not represent uncertainty. The y -axis error bar consists of the statistical (counting) error, amplitude error and detector position uncertainty error (see Section A.3) all added in quadrature.

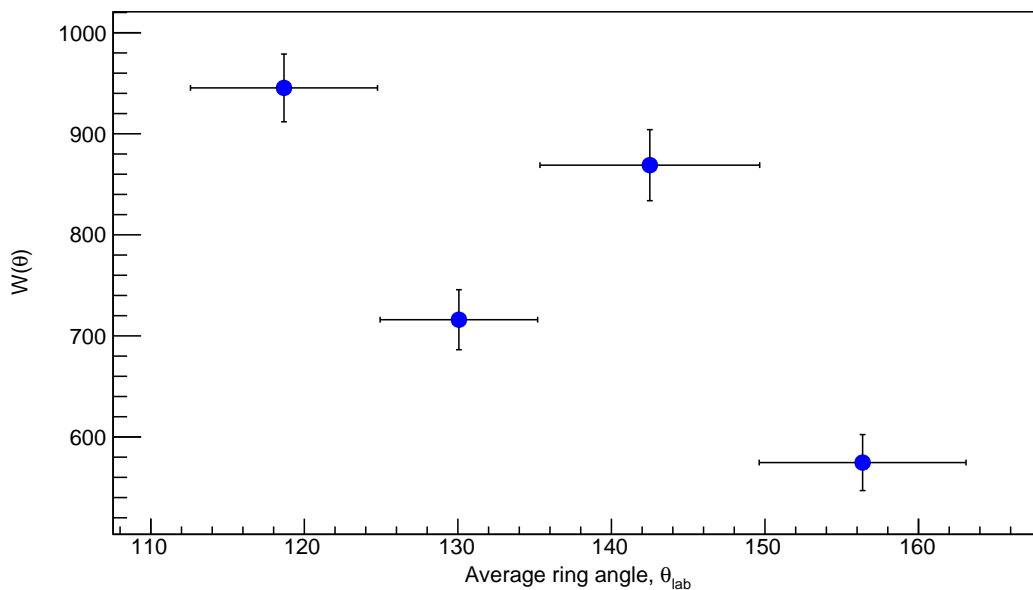


Figure 5.7: The corrected yield spectrum for p_1 decay of the 7.218 MeV state. The errors are calculated in the same as as for the previous figure.

5.7 are shown in Figures 5.8 and 5.9. Each graph shows the data with another graph drawn over it. This is the resultant function from the fit. It is drawn over the data points to give a visual idea as to how accurately the function replicates the data points. It is generated by fitting the data with the Legendre polynomials assuming a certain ℓ value. After the Legendre fit, the function describing the data is generated and the parameters minimised using TMinuit [59, 60]. The function is then integrated over the angular range of each point. The TMinuit minimisation is used to minimise the χ_{red}^2 . As each spectrum has four points there are three degrees of freedom. Therefore, the fit is generated for $\ell = 0, 1, 2$. The true ℓ value of the decay is determined by the fit that describes the data best with a χ_{red}^2 closest to 1. Higher ℓ -value transitions are not seen and are not likely in this situation as the relatively high excitation favours transitions via low ℓ values with a smaller angular momentum barrier. All of these results are listed in Table 5.2.

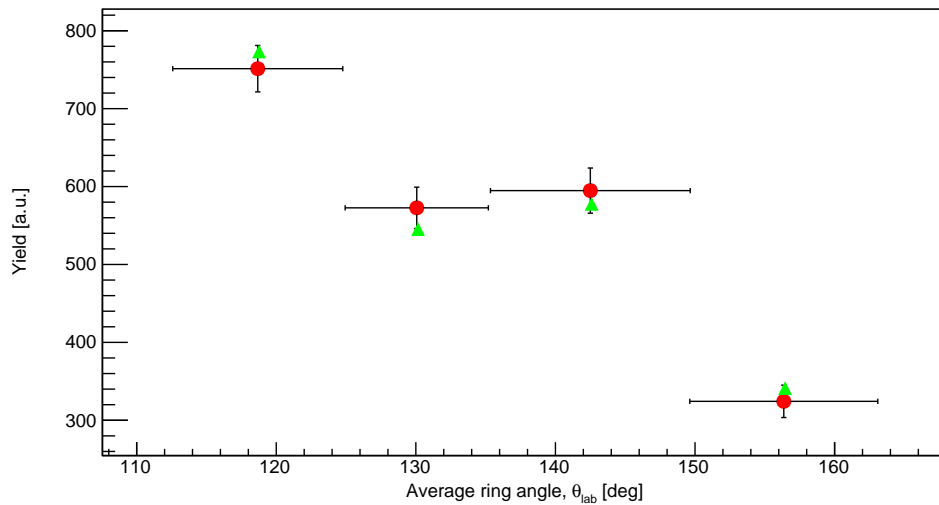


Figure 5.8: The fit for the p_0 6.767-MeV state. The grouped-yield data points are shown in red with their associated errors. The second set of data points (green) is from the fit function with the calculated yields. The fit converged with $\ell = 1$ and $\chi_{red}^2 = 1.28$.

As mentioned before, certain resonances in the coincidence excitation energy spectrum have more counts than others. It is thus possible to draw the angular correlation spectra of these resonances where the rings and, therefore, yields are not grouped together. This was done for the p_0 spectra of the 5957, 6040, 6229, 6591, 6767, 6875 and 7218-keV resonances. The spectra and resultant ℓ -value fits were used as a way to check that the TMinuit minimisation method used to determine the ℓ value from only four points was accurate and correct. Examples of these spectra are shown below in Figures 5.10 and 5.11.

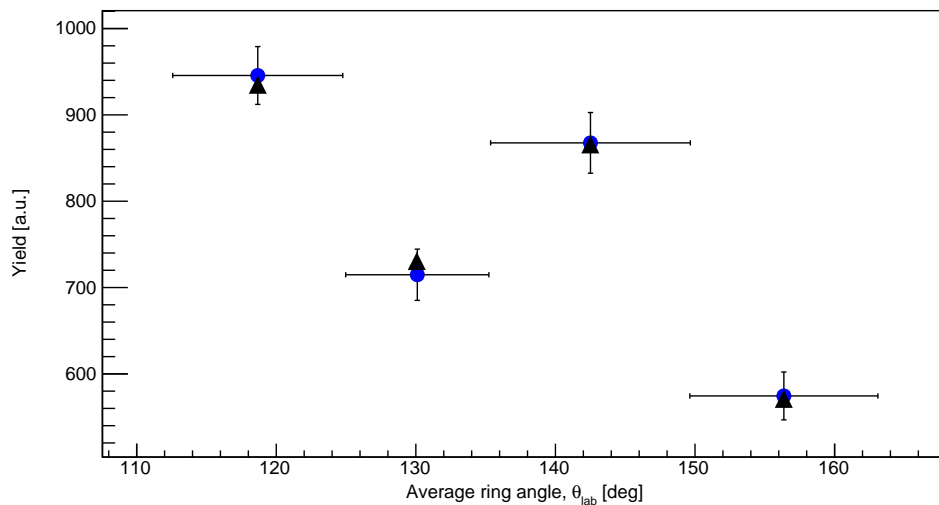


Figure 5.9: The fit for the p_1 7.218-MeV state. The grouped-yield data points are shown in blue with their associated errors. The second set of data points (black) is from the fit function with the calculated yields. The fit converged with $\ell = 1$ and $\chi_{red}^2 = 0.9$.

State	E_x / keV	p_0 ℓ value	p_1 ℓ value
1	5957	1	2
2	6040	1	2
3	6229	1	2
4	6591	2	2
5	6767	1	1
6	6875	1	1
7	7218	1	1
8	7331	2	1
9	7599	2	1
10	7734	1	0
11	7920	1	0
12	8005	0	1

Table 5.2: The ℓ value results of the Legendre fits for the p_0 and p_1 resonances below S_α is shown. The possibilities are $\ell = 0, 1, 2$.

5.3.4 Angular correlation functions

The ℓ values that were determined in the previous section are used to determine the angular correlation function for each state. It is this function that

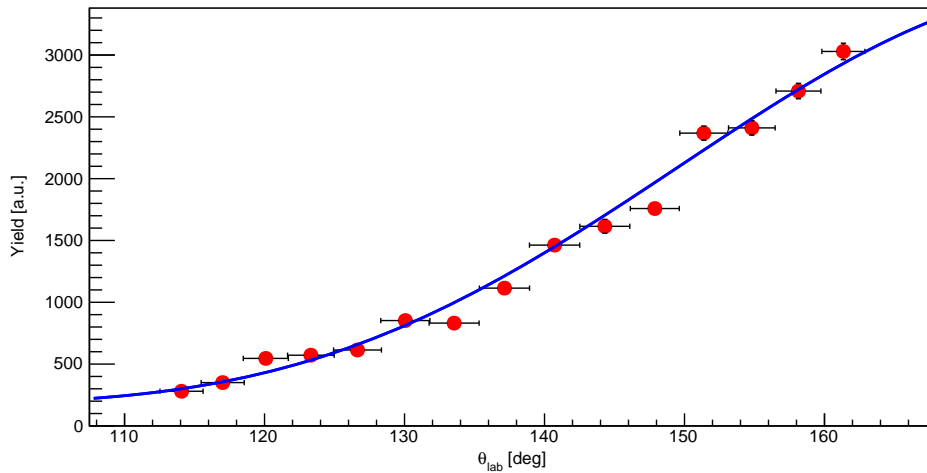


Figure 5.10: The full Legendre fit for the p_0 6.229-MeV state with $\ell = 2$.

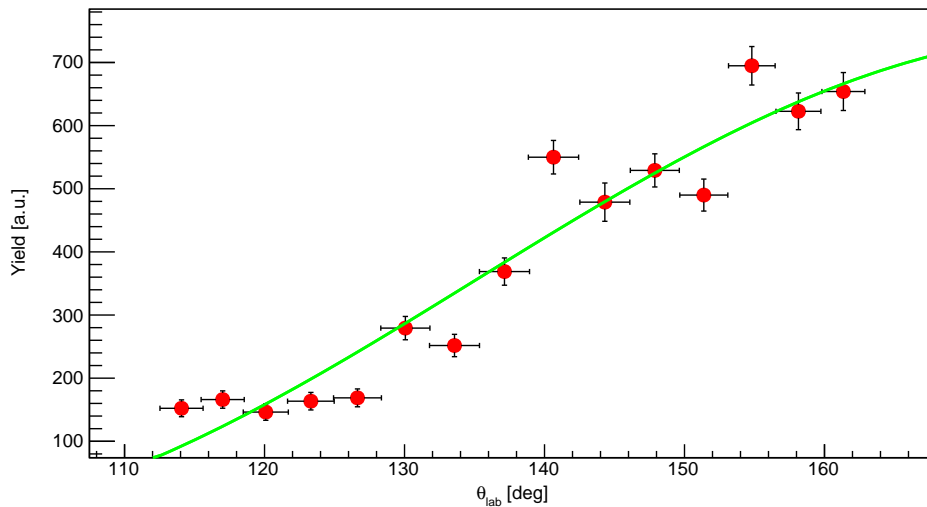


Figure 5.11: The full Legendre fit for the p_0 6.875-MeV state with $\ell = 1$.

determines the true yield of a resonance and thus leads to the determination of the branching ratio. The theory behind angular correlation functions is discussed in Subsection 2.7.2 and will be referred to in this section.

The CAKE only covers a limited region of the total solid angle from $\theta_{lab} = 114^\circ$ to $\theta_{lab} = 164^\circ$. The part of the solid angle where no detection is possible is corrected for by determining the angular correlation function of the decay and integrating the function from $\theta_{lab} = 0^\circ$ to $\theta_{lab} = 180^\circ$. This gives the total p_0 or p_1 yield of the resonance being studied. The branching ratio can then be calculated as:

$$B_{p_n} = \frac{N_c(p_n)}{N_s}, \quad (5.3.1)$$

where $N_c(p_n)$ is the total number of coincidence decays for a particular type of proton decay and N_s is the total singles yield. The angular correlations that decay particles from the recoil nuclei exhibit give insight to the rotational dynamics of the decay channels. If it is known what the angular momentum quantum numbers are for the decay products, then the spin parities for resonances of excited recoil nuclei can also be inferred. This is discussed in Subsection 5.3.6.

To calculate the true total yield $N_c(p_n)$ of a resonance, the angular correlation function is generated and integrated over the region $x \in [-1, +1]$. The function $P_n(x)$ is only defined in this region. The A_ℓ coefficients scale the function. Two generic, normalised angular correlation functions are plotted in Figures 5.12 and 5.13 for $\ell = 1$ and $\ell = 2$, respectively. For $\ell = 1$ the function is a linear combination of $P_0(x)$ which is a constant and $P_2(x)$ which is parabolic. The linear combination to determine $W(\theta)$ for $\ell = 2$ includes $P_4(x)$ (see Figure 2.5). For $\ell = 0$ it is simply a constant $P_0(x)$ which is not shown here.

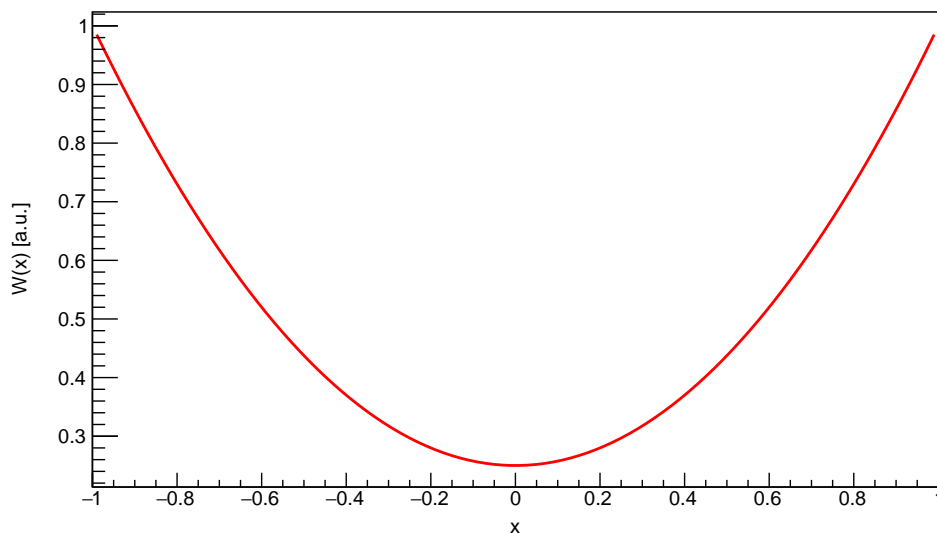


Figure 5.12: The normalised angular correlation function for $\ell = 1$.

The angular correlation functions for resonances below the α -particle threshold for p_0 and p_1 decay were calculated and the respective branching ratios determined. The results are summarised in the following section.

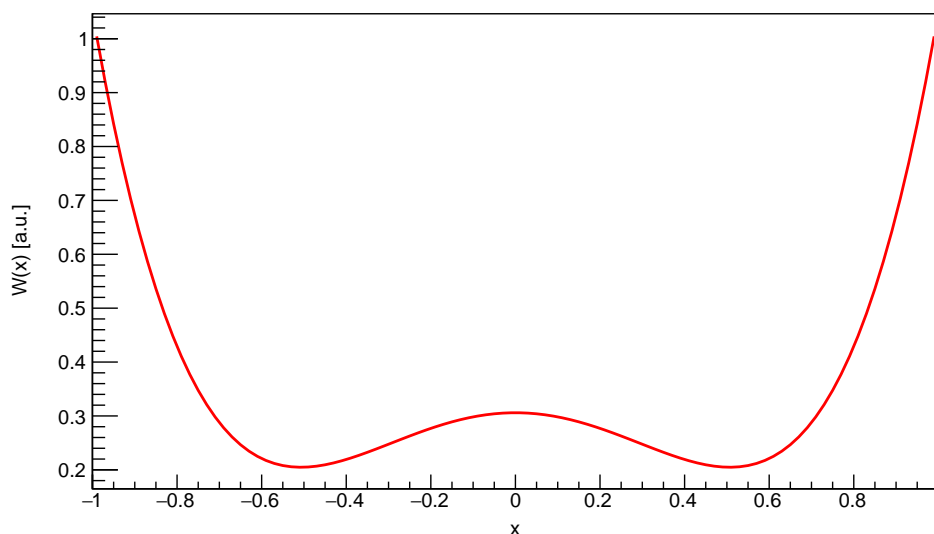


Figure 5.13: The normalised angular correlation function for $\ell = 2$.

5.3.5 Branching ratios of states below S_α

B_{p_0} and B_{p_1} were the only branching ratios determined for states below S_α as higher-order decays only become more prominent at higher excitation energies. More decay channels open as the energy increases. This is evident in Figure 5.17 where it is seen that the higher-order decay loci only start after 8 MeV.

The angular correlation functions for the p_0 and p_1 decays for all 12 resonances below S_α were determined and integrated to calculate the true yield of each. The yields of these resonances in the singles spectrum were determined previously (see Figure 4.30). The branching ratio B_{p_0} or B_{p_1} is then simply calculated as the ratio of the two. The singles yield is the total number of times a certain resonance in the nucleus ^{22}Mg was populated. The p_0 or p_1 yield is the number of times that excited state decayed via the emission of a proton to the ground state or 1st excited state, respectively. The results are summarised in Table 5.3. The errors are determined by the log-normal distribution of the errors of the p_0 or p_1 yield and the singles yield. This was discussed in greater detail in Chapter 2. The branching ratios and their use in determining the $^{21}\text{Na}(p, \gamma)^{22}\text{Mg}$ reaction rate will be discussed further in Section 6.2.

B_{p_0} and B_{p_1} for each state should add to 100%. However, it is evident that some of the higher-lying states have branching ratios greater than 100% for either p_0 or p_1 . The reason is that resonance strength does not entirely originate from a single resonance as the states are not resolved. Another reason is the size of the error estimates which are large for those resonances with a combined branching ratio greater than 100%. The error estimates are determined with log-normal distributions (discussed in Appendix B).

State	E_x / keV	B_{p_0} / %	B_{p_1} / %
1	5957	27.0(13)	4.7(2)
2	6040	32.3(15)	8.7(4)
3	6229	43.7(21)	9.7(4)
4	6591	51.7(25)	13.3(6)
5	6767	91.3(44)	16.2(7)
6	6875	26.7(12)	52.0(24)
7	7218	67.4(33)	30.5(15)
8	7331	120.2(50)	35.6(17)
9	7599	83.0(40)	78.3(38)
10	7734	107.1(48)	127.9(50)
11	7920	25.0(11)	83.6(40)
12	8005	12.5(5)	100.0(48)

Table 5.3: The results for B_{p_0} and B_{p_1} for resonances below S_α . Resonances closest to S_p show low branching ratios which are most likely attributed to the CAKE thresholds. Proton emission from these resonances have low energy (400-600 keV) and are, therefore, not detected by the CAKE with sufficient accuracy. This leads to diminished yields and incorrect branching ratios which are unavoidable with this particular experimental setup.

5.3.6 Spin-parity (J^π) assignments

From Table 5.1 it is evident that most states that feature in the excitation energy spectrum below S_α only have tentative J^π assignments as seen in Ref. [35]. When considering the J^π assignments it will be useful to note two points. Firstly, this K600 experiment was performed at $\theta_{lab} = 0^\circ$. This favours low angular momentum transfer states. It is thus unlikely to see strongly populated high-spin states. Secondly, the two-neutron pickup reaction (p, t) will have suppressed unnatural parity states ($0^-, 1^+, 2^- \dots$) as pair transfer is the main process. A two-step process would be needed to populate unnatural parity states. These two effects are alluded to in Table 5.6 which shows assignments for all the states above S_α that are based on spin assumptions from mirror assignments.

The assignments in this section will be made for the reaction $^{22}\text{Mg} \rightarrow ^{21}\text{Na} + p$. It will also be necessary to know that $J^\pi(p) = 1/2^+$ and that $J^\pi(^{21}\text{Na}_{p_0}) = 3/2^+$ and $J^\pi(^{21}\text{Na}_{p_1}) = 5/2^+$. The following calculations make reference to the discussion of J^π assignments in Chapter 2 Subsection 2.7.3.

The parity for a proton, the ground state, and 1st excited state of ^{21}Na is +1. Therefore, for p_0 and p_1 decay we can simplify the parity (see Equation 2.7.9) to

$$\Pi = \pi_1\pi_2(-1)^\ell = (+1)(+1)(-1)^\ell = (-1)^\ell. \quad (5.3.2)$$

The parity will thus be positive for even values of ℓ and negative for uneven values thereof. The possible channel spin values (see Equation 2.7.10) for p_0 decay are

$$s = |1/2 - 3/2|, \dots, 1/2 + 3/2 = 1, 2. \quad (5.3.3)$$

The possible channel spin values for p_1 decay are

$$s = |1/2 - 5/2|, \dots, 1/2 + 5/2 = 2, 3. \quad (5.3.4)$$

The channel-spin and parity values, along with Equation 2.7.12, are used to determine the values given in Tables 5.4 and 5.5. Therefore, depending on whether decay is via p_0 or p_1 and given a certain ℓ value tentative spin-parity assignments for the states below S_α can be made¹. An example of this is that any state with an ℓ -value assignment of 0 is likely a 2^+ state if it decays either to the ground state or 1st excited state of ^{21}Na .

¹According to Matic *et al.* [35] there are two known 0^+ states. These are the 5.957-MeV and 7.218-MeV states. However, their ℓ -value assignments and subsequent spin assignments from this study do not concur with Matic *et al.* [35]. Firstly, the 0^+ assignment of the 5.957-MeV state was made tentatively based on mirror-nucleus assignments which could indicate why this state in ^{22}Mg does not have the same J^π . Secondly, the 0^+ nature of the 7.218-MeV state is disputed as its assignment from a ($^3\text{He}, n$) experiment [61] is ambiguous. Further clarification using present data is needed.

^{22}Mg	\rightarrow	ℓ_p	proton	+	^{21}Na (0 keV)
J^π	\rightarrow	ℓ_p	$1/2^+$		$3/2^+$
0^+		2 (s=2)			
1^-		1 (s=1,2) or 3 (s=2)			
2^+		2 (s=1,2) or 0,4 (s=2)			
3^-		3 (s=1,2) or 1,5 (s=2)			
4^+		4 (s=1,2) or 2,6 (s=2)			
\vdots		\vdots			

Table 5.4: Possible J^π assignments for different possibilities of the ℓ value for p_0 decay. The values for s, the channel spin, with which a particular ℓ value was calculated with is indicated in brackets.

^{22}Mg	\rightarrow	ℓ_p	proton	+	^{21}Na (331 keV)
J^π	\rightarrow	ℓ_p	$1/2^+$		$5/2^+$
0^+		2 (s=2)			
1^-		1 (s=2) or 3 (s=2,3)			
2^+		0 (s=2) or 2,4 (s=2,3)			
3^-		1,3,5 (s=2,3)			
4^+		2,4,6 (s=2,3)			
\vdots		\vdots			

Table 5.5: Possible J^π assignments for different possibilities of the ℓ value for p_1 decay. The values for s, the channel spin, with which a particular ℓ value was calculated with is indicated in brackets.

5.4 Analysis of states above S_α

This section will discuss the analysis of states above S_α . The procedure has similarities to the analysis method of the previous section. Reference will thus be made to discussions and methods of the previous section. However, there are some key differences. One main difference lies in the way the yields were determined for the spectra in this energy region. This region of the spectrum was analysed by grouping bins and determining the yields in a certain bin range. The bin range was chosen to equal 100 keV, about twice the resolution.

Other differences to the previous analysis method is that higher-order proton decays will also be studied, namely p_2 , p_3 and p_4 . The reason is that these decays become possible at higher excitations (see Figure 5.17). The last variation is that individual resonances will not be studied due to the low number of counts in this region and the resolution of the experiment. Therefore, there are no spin-parity assignments. The ℓ -value assignments are also given for each energy range instead of a particular resonance.

The region above S_α was grouped into bins of 100 keV due to the limitations in the data. These included the differential cross section above S_α which is small with typical values of the order of a few $\mu\text{b}/\text{sr}$. As a result, the number of decays in this energy region are limited (see for example Figure 4.14). The resolution of the experiment was 45(5) keV (FWHM) which also meant that states were not resolved. The density of states above S_α is higher. Therefore, it was not feasible or practical to fit and analyse individual resonances. Analysis methods such as this one are used often in literature when the circumstances justify its use [62].

This section will outline the method in which the yields were determined for different proton decays. From there the ℓ values will be determined followed by generating the angular correlation functions. Once that is done the true yield for a certain bin can be calculated easily and used to determine the branching ratio for that region. Each one of these tasks is performed for every grouped bin within the energy range 8-13 MeV.

5.4.1 Singles and coincidence spectra

The spectra in this section were analysed in the energy region of 8-13 MeV. The lower limit is chosen because of S_α at 8.142 MeV. The spectrum cut-off point for the excitation energy is 13 MeV which corresponds to the proton punch through limit in the silicon detectors. This is shown in Figure 5.14. In practice, the detection capability is about 500 keV below that due to the detector thresholds.

Figure 5.15 shows the excitation energy spectrum above S_α . The coincidence spectrum is gated on the p_0 and p_1 locus and the SiliconTimeOffset gate is included. The dashed lines in the spectrum are used to label all the states from a to s. The lines are positioned in the spectrum according to E_r from literature [35]. Therefore, it is evident that there is very good agreement with literature as the centroid of each state lines up well with the assignment a to s from literature. The states are listed in Table 5.6 and note how none of the states in the spectrum are above spin $J=4$ and none are unnatural parity states (as discussed previously). This is one of the advantages of using the K600 magnetic spectrometer in 0° mode.

Previous experiments [35] also had limited counts in the corresponding spectrum above S_α . However, the J^π assignments in those studies are tentative as they are based on differential cross sections. To try and improve upon

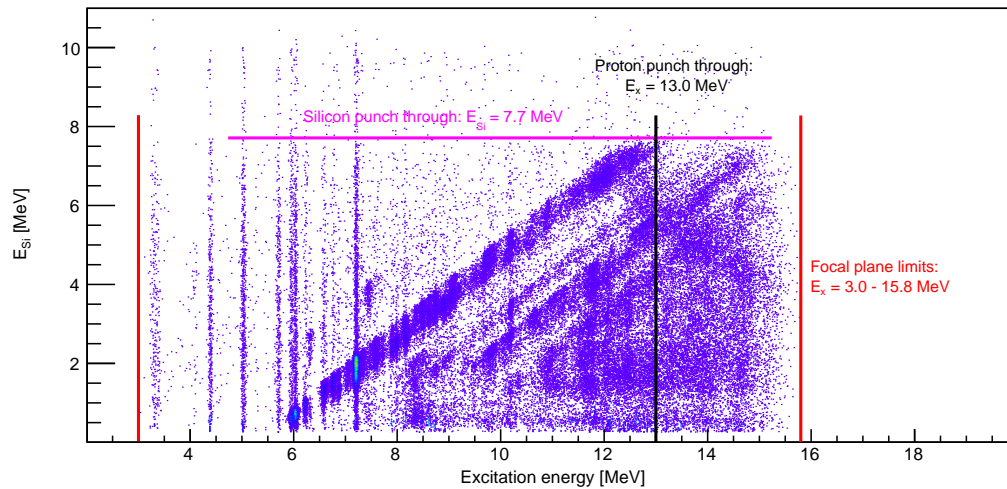


Figure 5.14: The limits of detection of the CAKE and of the VDCs. The pink and black lines are threshold limits of the CAKE. For energies higher than these punch through takes place. The red lines outline the focal plane limits. These are not physical limits as with the semi-conductor materials. The energy range is chosen by selecting a specific set of magnetic fields for the K600. See Section 3.3 and Figure 3.4.

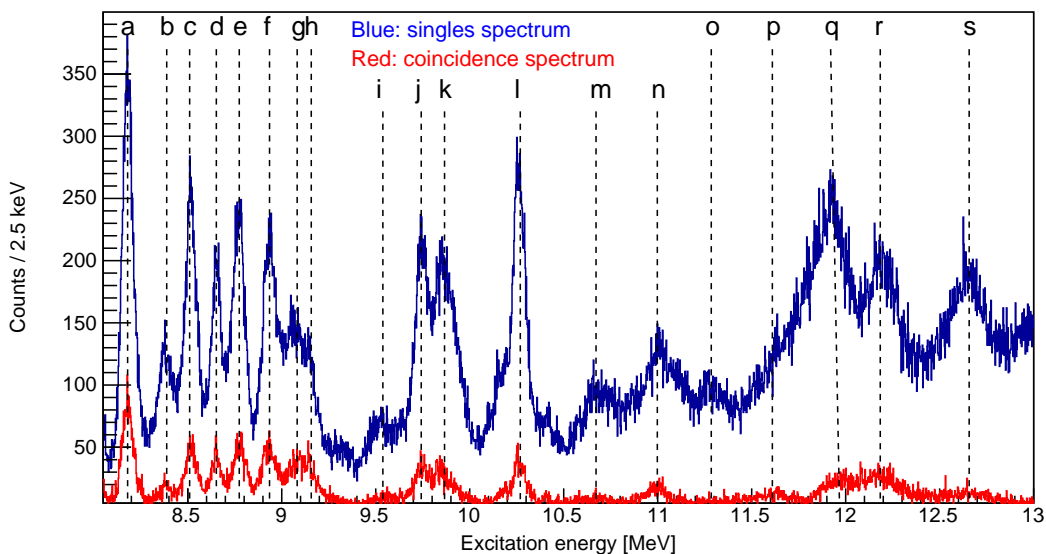


Figure 5.15: The excitation energy spectrum above S_{α} . The singles spectrum is compared with the coincidence spectrum (gated on the p_0/p_1 decay locus). The spectrum has a standard bin size of 2.5 keV.

Label	E_x / keV	J^π	Label	E_x / keV	J^π
a	8.1803(17)	[2 ⁺]	k	9.861(6)	[0 ⁺]
b	8.383(13)	[2 ⁺]	l	10.2717(17)	[2 ⁺]
c	8.5193(21)	[3 ⁻]	m	10.667(19)	[3 ⁻]
d	8.6575(17)	[0 ⁺]	n	10.999(15)	[0 ⁺]
e	8.7845(23)	[1 ⁻]	o	11.317(27)	[4 ⁺]
f	8.9331(29)	[2 ⁺]	p	11.603(16)	[1 ⁻]
g	9.082(7)	[1 ⁻]	q	11.937(17)	[0 ⁺]
h	9.157(4)	[4 ⁺]	r	12.220(30)	[3 ⁻]
i	9.546(15)	[2 ⁺]	s	12.665(17)	[3 ⁻]
j	9.7516(27)	[2 ⁺]			

Table 5.6: The excitation energies for states above S_α using assignments from Ref. [35]. All spin-parity assignments are in brackets as no tentative assignments are known and the values are based on spin assumptions from the mirror assignments.

previous studies by using the capabilities of the CAKE with its ring segmentation, the spectrum has to be gated on the rings of the CAKE as well as gated on the different proton decays. For this purpose a grouped-bin approach was used as in literature [62].

The analysis of this region of interest started by generating the various spectra with 10-keV binning and grouping those into larger, 100-keV bins (an example of this can be found in the following subsection). The individual-run calibration parameters discussed in Section 4.4 were used to have optimal alignment of the individual spectra as was discussed previously. This ensures an optimal experimental resolution. Each run is then analysed individually to create a histogram for the singles and coincidence data. The corresponding histograms for each run were then added together to generate the full singles and coincidence spectra for states above S_α with a grouped binning of 100 keV. The singles spectrum will be used when calculating the various branching ratios for each 100-keV bin. The coincidence spectrum is analysed further by applying additional software gates on p_i decays which are discussed below.

5.4.2 Spectra gated on p_i

The analysis of the region below S_α concentrated on p_0 and p_1 decays. They were the only possible decay options as the excitation energy is too low for

higher-order decays. In this section, higher-order decays (up to p_4) can be analysed along with the p_0 and p_1 decays. Figure 5.16 shows the position of the different decay types. The locus indicated with a red arrow is the p_2 proton decay locus as it contains events related to proton decay to the 2nd excited state in ^{21}Na ($E = 1716$ keV and $J^\pi = 7/2^+$). The locus indicated with the green arrow is the p_3 and p_4 decay locus with events related to decay to the 3rd ($E = 2423$ keV and $J^\pi = 1/2^+$) and 4th ($E = 2797$ keV and $J^\pi = 1/2^-$) excited states in ^{21}Na [14].

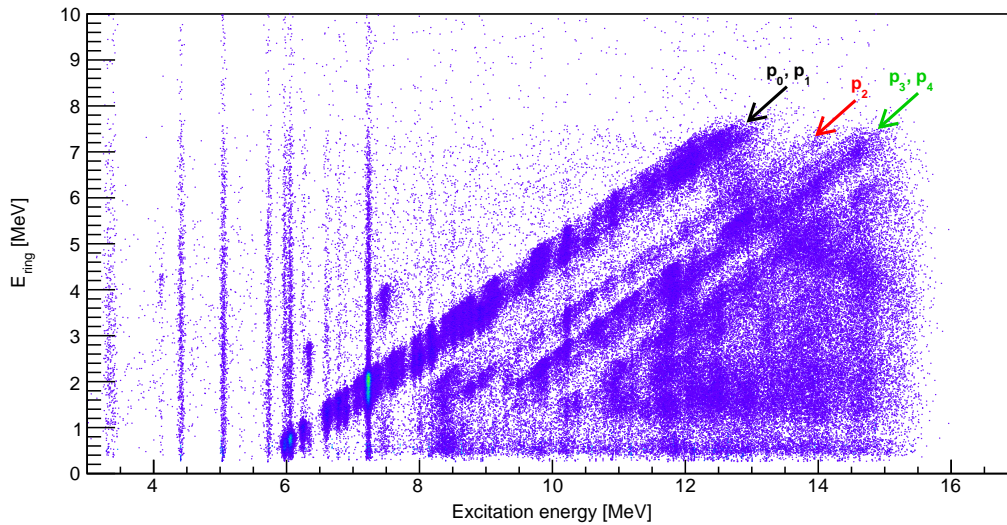


Figure 5.16: Coincidence spectrum with higher-order proton-decay loci indicated. The black arrow points to the p_0 and p_1 decay locus whereas the red and green arrows point to the p_2 and p_3, p_4 loci, respectively.

As p_0 and p_1 decays are dominant, the standard coincidence spectrum can be gated on the rings of the CAKE to separate the two loci. A different approach is needed for the other decay types. Figure 5.17 shows the coincidence spectrum drawn where a variable that is equal to the excitation energy (E_x) minus the product of the silicon energy (E_{Si}), proton separation threshold (S_p) and the ratio of the decay masses is plotted against the excitation energy. The aforementioned variable is equal to the excitation energy in ^{21}Na corresponding to each p_i (0 keV, 331 keV, 1716 keV, ...). A clear separation of decay loci emerges. Software gates can be placed on the loci using cuts to the spectrum as shown for p_2 . These are then used to select these events exclusively for further analysis. Another feature of the spectrum is that the loci are not straight. The reason is that the protons lose more energy in the target at lower excitation energies as $\Delta E/E$ increases with decreasing excitation energy.

The next step was to generate the run-by-run coincidence excitation energy spectra for states above S_α gated on p_i and gated on rings of the CAKE.

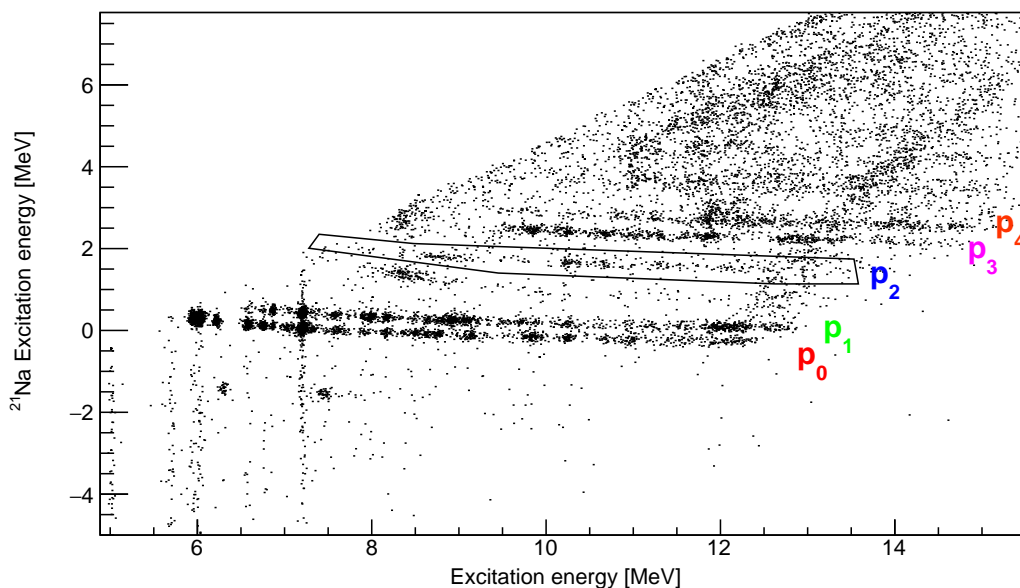


Figure 5.17: Coincidence spectrum gated on ring 4 where individual p_i loci are separated. This makes it easier to gate upon them for further analysis. Each label of p_i is to the immediate right of the associated decay locus.

Each run, therefore, has multiple histograms that are generated. One for each combination of p_i and ring number. All histograms that were gated on p_i are also added together to generate the complete p_i spectra for states above S_α . The spectra for p_0 and p_1 are shown in Figures 5.18 and 5.19. The binning was increased to 10 keV as a precursor to grouping the bins.

When comparing the p_0 spectrum (Figure 5.18) to that of p_1 (Figure 5.19) above S_α an observation can be made: more decay channels open up as the energy increases and the chance of decay to the ground state starts to decrease. The analysis data from the higher-order proton decays will be included in the branching ratio section as their method of analysis is identical to that of p_0 and p_1 . The analysis of p_0 is explained in full detail here because B_{p_0} is the main result which is needed to make corrections to the $^{18}\text{Ne}(\alpha, p)^{21}\text{Na}$ reaction rate.

The following step was to group all of the spectra according to decay type and ring number. An example of one of these spectra is shown in Figure 5.20 where the histograms of each run corresponding to p_1 decay and strip 9 were added.

The following subsections will expand on the analysis of states above S_α . The corrected yield spectra will be generated and then fitted with Legendre polynomials to determine the ℓ values of each energy bin. As was done previously, the angular correlation functions can then be determined and integrated to get the true yield of each bin region which is used to determine B_{p_i} . This

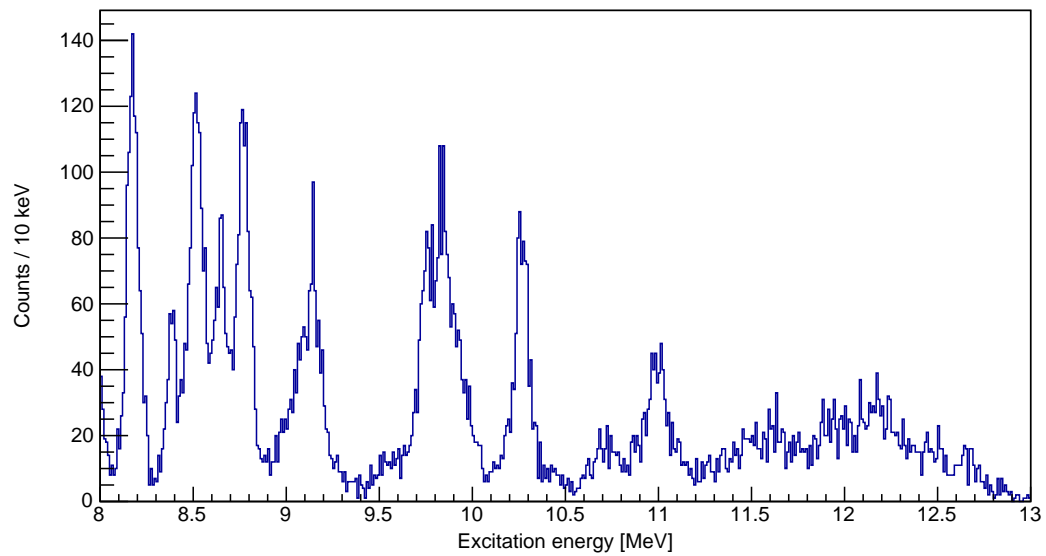


Figure 5.18: The p_0 decay spectrum for states above S_α .

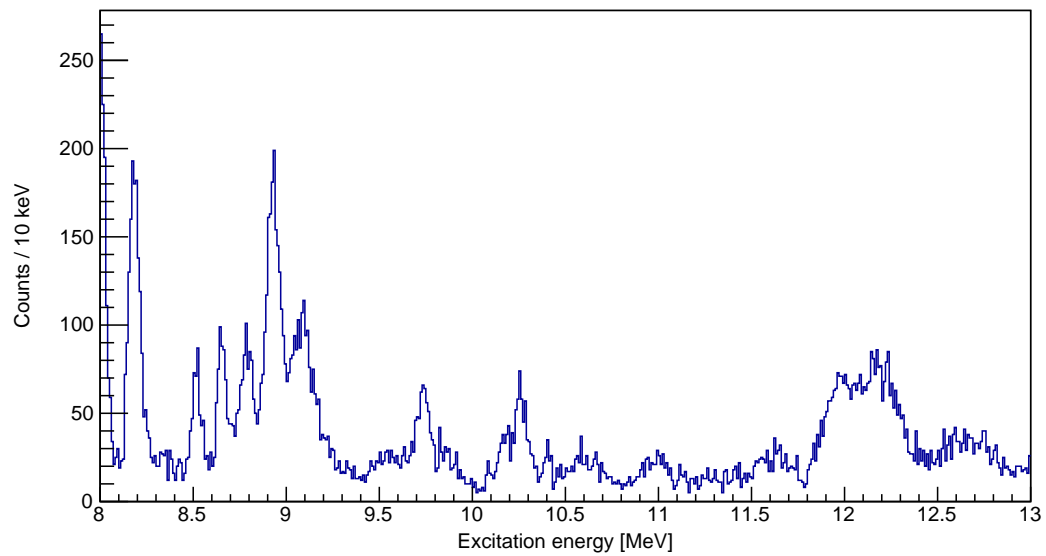


Figure 5.19: The p_1 decay spectrum for states above S_α .

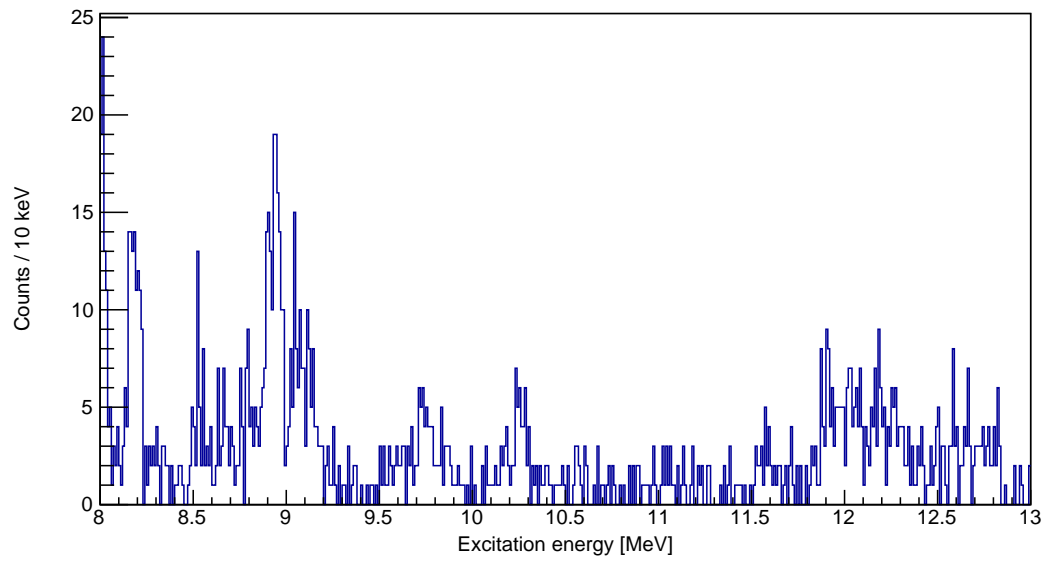


Figure 5.20: The p_1 decay spectrum for states above S_α gated on ring 9.

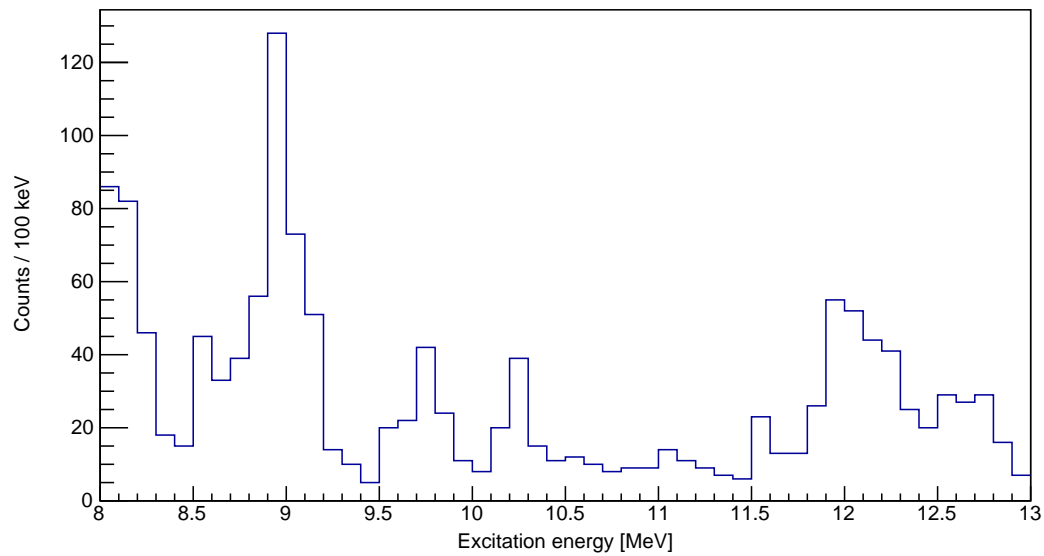


Figure 5.21: The p_1 decay spectrum for states above S_α gated on ring 9 with grouped bins. Each bin is equivalent to 100 keV.

is done for each 100-keV grouped bin in the 8-13 MeV excitation energy range which equals 50 bins.

5.4.3 Corrected angular correlation spectra

Once the histograms of all possible p_i and ring combinations are generated, the yields can be determined for each bin. Each p_i decay has 15 histograms (16 rings less ring 0). Therefore, the angular distribution for each energy bin will have 15 points. The corrections to these spectra are exactly the same as discussed in Section 5.2. The theory related to angular distributions were discussed in Chapter 2. As with the region below S_α , the angular distribution is needed as the CAKE covers a limited part of the solid angle. The decays that can not be detected due to the limitations of the CAKE need to be corrected for by reconstructing the angular distribution and generating the angular correlation function for each bin.

Figures 5.22 and 5.23 show the corrected angular distribution for bin 7 (8.6-8.7 MeV) for p_0 and p_1 . The x -axis error bars cover the angular region of each ring of the CAKE. They do not represent uncertainty. The y -axis errors consists of the statistical (counting) error and cake efficiency uncertainty error added in quadrature.

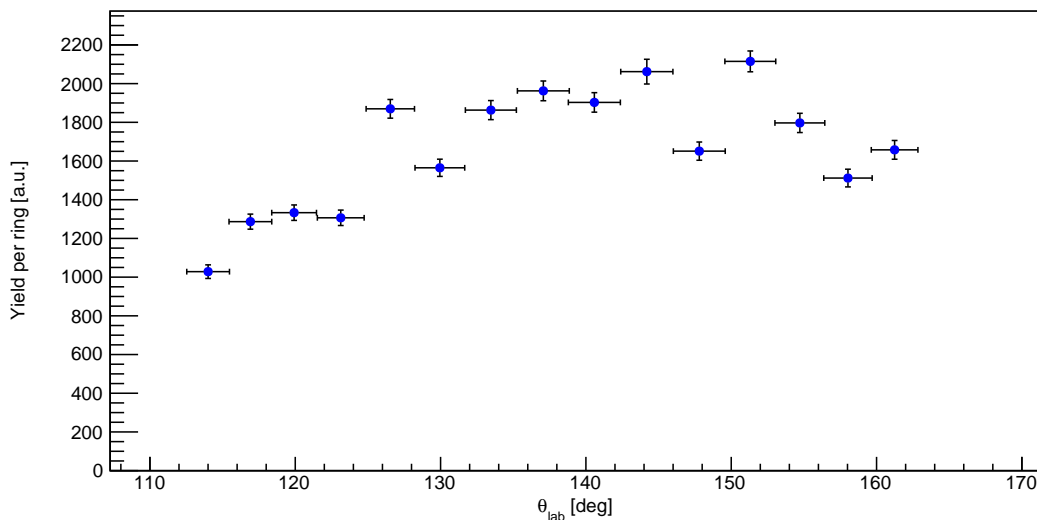


Figure 5.22: The corrected angular correlation spectrum for p_0 bin 7. It covers the energy region 8.6-8.7 MeV.

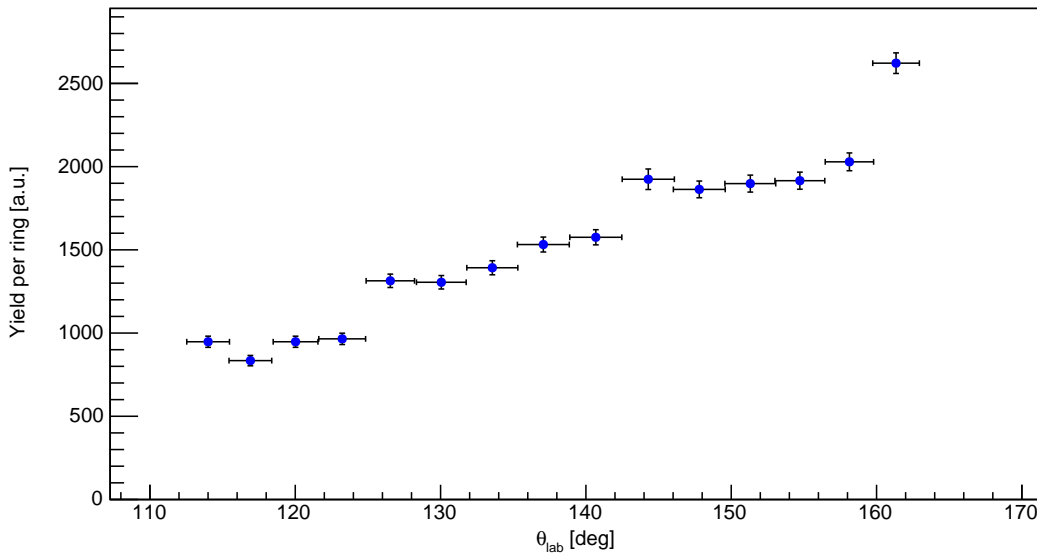


Figure 5.23: The corrected angular correlation spectrum for p_1 bin 7. It covers the energy region 8.6-8.7 MeV.

5.4.4 ℓ -Value per bin

As individual resonances are not analysed in the region above S_α as was done for the region below it, no ℓ -value assignments can be made. However, the angular correlation spectrum of each bin does exhibit an angular distribution that can be described by an ℓ value. Therefore, to correct the yield in each bin an ℓ value is determined by fitting the angular correlation spectrum with the even-numbered Legendre polynomials. No further measures had to be taken as was done for the 4-point angular distributions for states below S_α . The ℓ value of a particular bin is one where the Legendre fit converges with $\chi_{red}^2 \sim 1$ (or best convergent fit). Figures 5.24 and 5.25 show the results of the Legendre fits to the angular correlation spectra shown in the previous section. The process is repeated for each one of the 50 bins for all p_i decays. With the spectra having 15 points there are more degrees of freedom and thus more possible ℓ values but those were limited to $\ell = 2$. The reason for this has been discussed in Subsection 5.3.3.

5.4.5 Angular correlation functions

Determination of the angular correlation function for each energy range proceeds in the same way as for states below S_α . The theory has been discussed previously. Using:

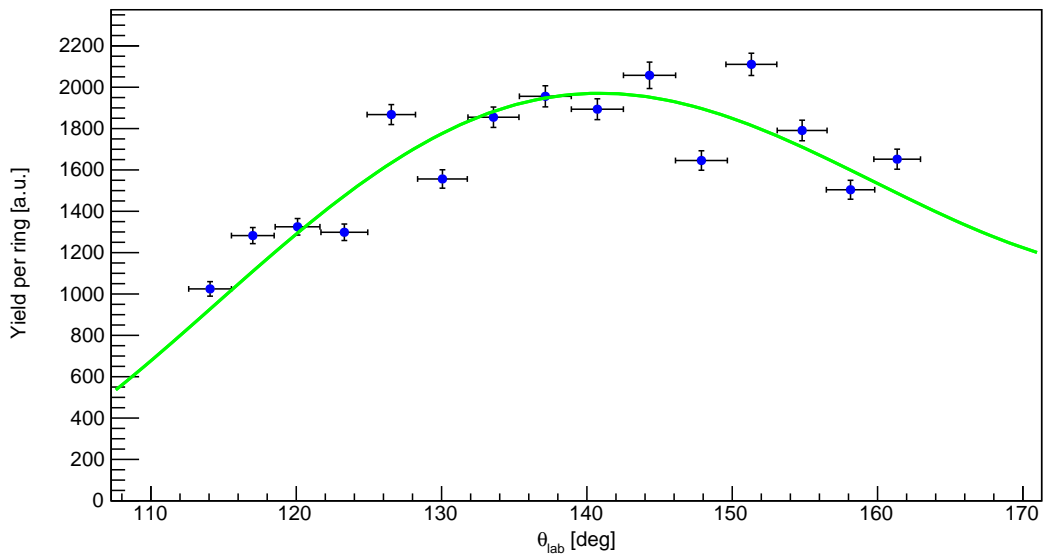


Figure 5.24: The corrected angular distribution for p_0 decay bin 7. The Legendre fit is superimposed. The fit converges with $\ell_{\text{max}}=2$ and $\chi_{\text{red}}^2=1.54$.

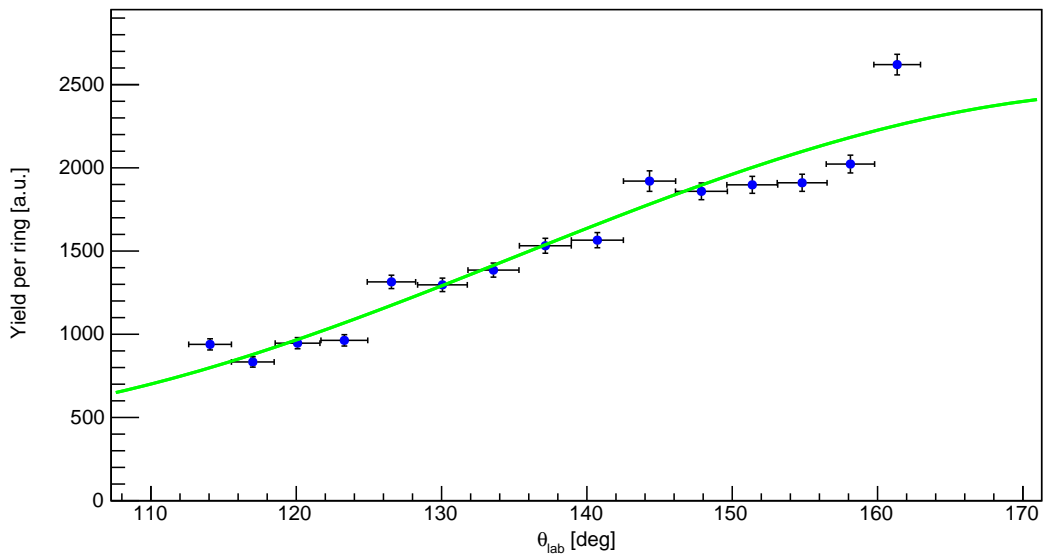


Figure 5.25: The corrected angular distribution for p_1 decay bin 7. The Legendre fit is superimposed. The fit converges with $\ell_{\text{max}}=1$ and $\chi_{\text{red}}^2=0.92$.

$$W(\theta) = \sum_{\ell=0,2,\dots}^{\ell_{max}} A_\ell P_\ell(\cos(\theta)), \quad (5.4.1)$$

the different terms of the function can be determined using the Legendre fit parameters for A_ℓ . The true yield of each bin is calculated by integrating the angular correlation function of each bin:

$$Y = 2\pi \int_{-1}^{+1} W(x) dx, \quad (5.4.2)$$

where $x = \cos(\theta)$. The spectra are shown in terms of θ whereas the calculations are done in terms of x . The angular correlation functions for bin 7 of p_0 and p_1 are shown in Figure 5.27 and 5.26. Note that the function may be inverted depending on the A_ℓ coefficients. The data points are superimposed over the functions. This serves to show the angular region that the CAKE is able to cover and the large region that it doesn't. The figures illustrate why a need exists to correct for the missing solid angle not covered by the CAKE. Integrating the full angular correlation functions thus give the total p_i yield for that particular bin.

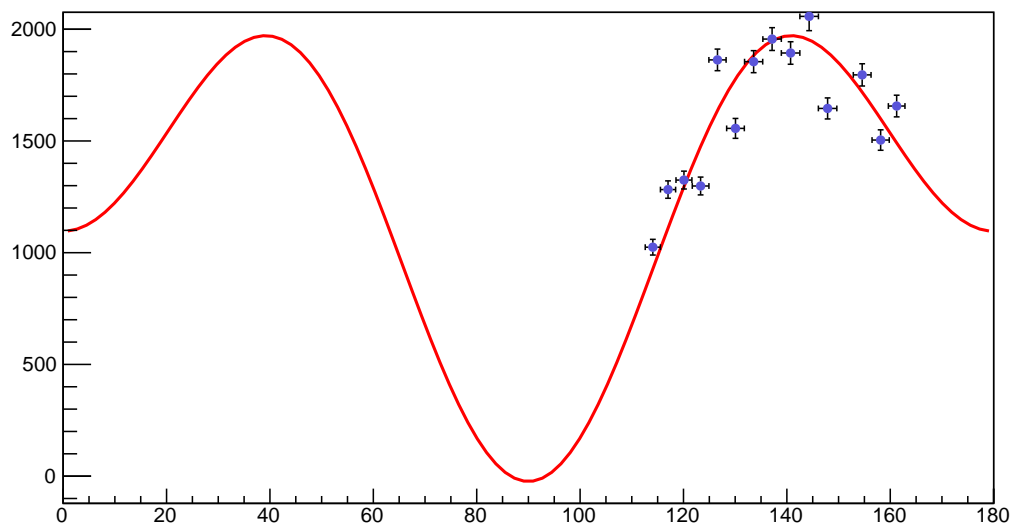


Figure 5.26: The full angular correlation function for p_0 decay bin 7. The data points are superimposed.

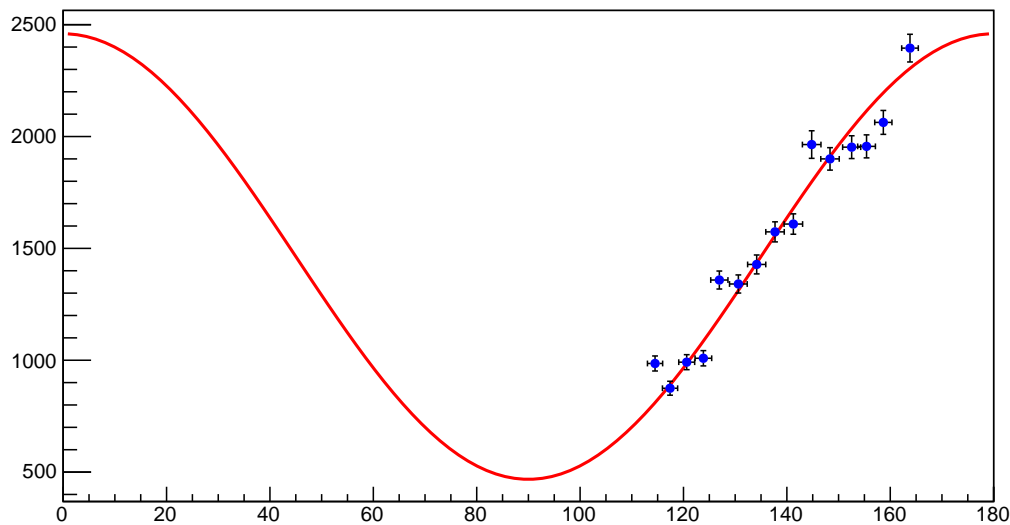


Figure 5.27: The full angular correlation function for p_1 decay bin 7. The data points are superimposed.

5.4.6 Branching ratios

The branching ratios for each energy region is calculated in the same way as was done for states below S_α . After the angular correlation functions were generated and integrated for each energy bin, the branching ratios for p_0 to p_4 could be determined. This is shown in Figure 5.28. The total branching ratio for each energy bin was also calculated. The branching ratio is greater than 1 for some bins as the error bars for certain bins are large. The branching-ratio errors for p_0 to p_4 are determined using log-normal distributions as each branching ratio is the quotient of two normal distributions (i.e. Gaussian). The method of calculating the error bars is explained in detail in Appendix B. As before, the x -axis error bars represent energy range and not uncertainty. Figure 5.29 shows the results for B_{p_0} separately as it is the main result from the analysis and used to make corrections to the $^{18}\text{Ne}(\alpha, p)^{21}\text{Na}$ reaction rate.

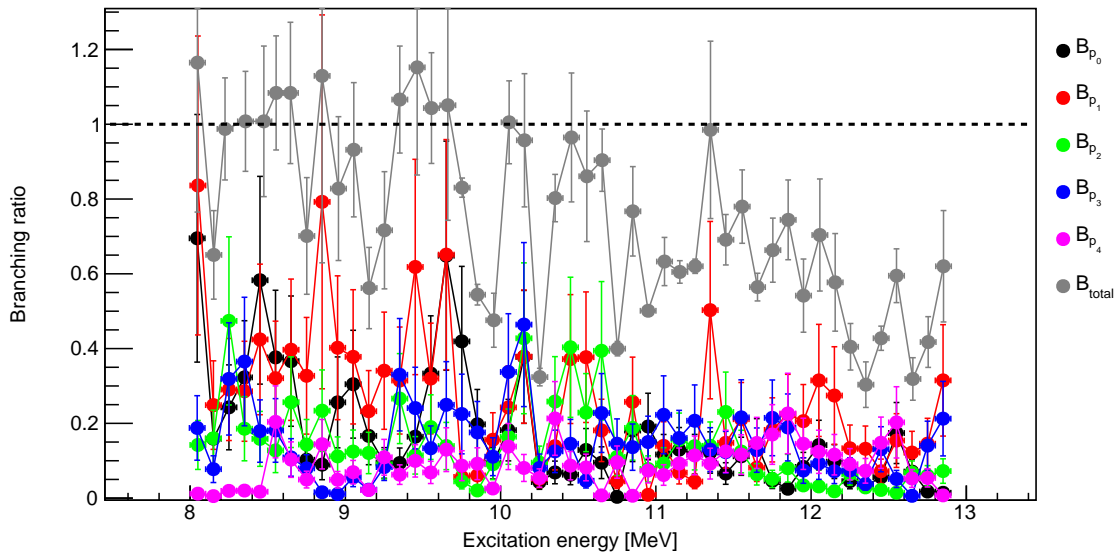


Figure 5.28: The branching ratios for p_i decay. The legend indicates which specific graph is attributed to each p_i .

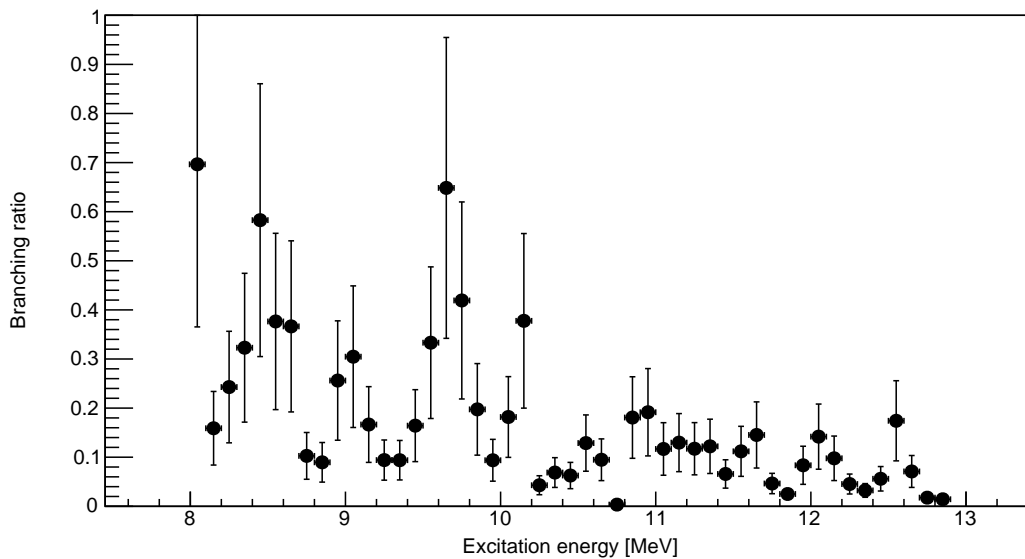


Figure 5.29: The branching ratios for p_0 decay for states above S_α . Figure 6.8 in the following chapter shows a moving-average fit that is made to this data along with a comparison to the TALYS calculations made for the p_0 branching ratios.

Chapter 6

Astrophysical Calculations and Impact

Somewhere, something
incredible is waiting to be
known.

Carl Sagan

6.1 Introduction

In Salter *et al.* [32], the $^{18}\text{Ne}(\alpha, p)^{21}\text{Na}$ thermonuclear reaction rate was calculated by doing the time-reversed reaction $^{21}\text{Na}(p_0, \alpha)^{18}\text{Ne}(\alpha)$. Consequently, the rate was determined by regarding p_0 decay only and scaling the result up by a factor of 3 to compensate for other, higher-order decay channels [32] as discussed in Chapter 1. The scaling factor was determined by regarding theoretical predictions based on Hauser-Feshbach (HF) calculations for ground-state to ground-state transitions.

This chapter will show the astrophysical calculations that were made with the B_{p_0} data, calculated in the previous chapter, to make corrections to the HCNO breakout reaction of interest, $^{18}\text{Ne}(\alpha, p)^{21}\text{Na}$. In this chapter, the energy-dependent function of the p_0 branching ratio, $B_{p_0}(E)$, will be determined and used to correct the $\sigma_{(\alpha, p_0)}$ cross section. In Salter *et al.* [32], the $\sigma_{(\alpha, p_0)}$ cross section is inferred from the $\sigma_{(p_0, \alpha)}$ cross section data using the principle of detailed balance [33]. The corrected cross section will be used to calculate the reaction rate using the particle-induced reaction-rate equation as discussed in Chapter 2.

The impact of the newly-calculated reaction rate on the X-ray burst lightcurve will then be determined by using the Modules for Experiments in Stellar Astrophysics (MESA) simulation package [63] to simulate a basic X-ray burst and reconstruct the lightcurve. The default MESA reaction rates for

$^{18}\text{Ne}(\alpha, p)^{21}\text{Na}$ will be used in the simulation and compared with simulations using the Salter *et al.* [32] reaction rate and the reaction rate calculated in this chapter. The upper and lower limits of the reaction rate will be calculated and used as input to the simulation as well. The default MESA rates are from Matic *et al.* [35]. Additionally, the reaction is treated differently in MESA. The simulation regards the reaction to the compound nucleus ^{22}Mg and then the subsequent proton emission to ^{21}Na . In doing so, the size of the calculation matrix is reduced increasing the computational efficiency for each timestep when calculating the nuclear abundances.

The previous chapter started with the analysis of resonances below S_α . Therefore, the first section of this chapter will briefly discuss the results for resonances in that region and their limitations. The majority of this chapter, however, will be dedicated to determining the X-ray burst lightcurves using present data. The second section will discuss the $^{18}\text{Ne}(\alpha, p)^{21}\text{Na}$ reaction rate from Salter *et al.* [32] and the assumptions made in that study. This will be related to simulations of cross sections calculated with TALYS [40].

This chapter will then show the recalculation of the Salter *et al.* [32] reaction rate using the cross section data. That is followed by the recalculation of the $^{18}\text{Ne}(\alpha, p)^{21}\text{Na}$ reaction rate using B_{p_0} from this study. The recalculated reaction rates will be used in the final section in the MESA simulations to generate new X-ray burst lightcurve predictions.

6.2 Resonances below S_α

The $^{21}\text{Na}(p, \gamma)^{22}\text{Mg}$ reaction rate is one of the aspects that can be studied using the $^{24}\text{Mg}(p, t)^{22}\text{Mg}$ data as both reactions populate states in ^{22}Mg . This is possible by studying the resonances $S_p < E_r < S_\alpha$ as has been done extensively in the previous chapter. The branching ratios are needed to make corrections to the reaction rate. The Gamow Window at three different stellar temperatures are tabulated in Table 6.1 [64] to show the resonance energies in ^{22}Mg that are most important for the $^{21}\text{Na}(p, \gamma)^{22}\text{Mg}$ reaction rate. The Gamow window has a maximum at the maximum peak energy E_0 with an effective width Δ and energy window $E_0 \pm \Delta/2$.

T (GK)	E_0 / keV	Δ / keV	$E_{0,low}$ / keV	$E_{0,high}$ / keV
0.50	374.5	293.4	227.8	521.2
0.75	490.7	411.3	285.1	696.3
1.0	594.4	522.7	333.1	855.8

Table 6.1: Values for the Gamow Window of the $^{21}\text{Na}(p, \gamma)^{22}\text{Mg}$ reaction for $T_9 = \{0.50, 0.75, 1.0\}$.

The maximum Gamow-peak energies E_0 are the resonance energies above the proton-decay threshold in ^{22}Mg . Therefore, they are located in the excitation energy spectrum at $E_x = 5502 + E_0$ ($S_p = 5502$). It is thus evident that decays relevant to the determination of the $^{21}\text{Na}(p, \gamma)^{22}\text{Mg}$ reaction rate have only a few hundreds of keV energy. However, the silicon detector thresholds are in the range of 400-600 keV (as seen in the coincidence spectra) depending on the individual MMM-detector threshold settings. For the data in this part of the excitation energy spectrum it was the intention to detect decay protons for states just above S_p . However, due to threshold problems this was not possible.

Notwithstanding this fact, the resonances below S_α were analysed as the density of states is lower than for the region above S_α making it an easier introduction to the analysis of the $^{24}\text{Mg}(p, t)^{22}\text{Mg}$ dataset. At the start of the analysis it was also not clear whether the resonances in the Gamow Window relevant to the $^{21}\text{Na}(p, \gamma)^{22}\text{Mg}$ reaction were observed. It was also important for the analysis of the dataset to be as complete as reasonably possible. For this reason the ℓ values, angular correlations, branching ratios and spin-parity assignments were included in this thesis if reference would ever be needed to this data. However, no further calculations can be made with the data below S_α .

6.3 Reaction rate of Salter *et al.*

In Chapter 1 it was discussed that direct measurements of the $^{18}\text{Ne}(\alpha, p)^{21}\text{Na}$ reaction are difficult due to the intensity of ^{18}Ne beams currently and the need for helium gas targets. Therefore, the study by Salter *et al.* [32] performed the time-reversed reaction $^{21}\text{Na}(p_0, \alpha)^{18}\text{Ne}$ and inferred the $\sigma(\alpha, p_0)$ cross section by using the principle of detailed balance. By performing the time-reversed reaction they were only able to observe transitions from the ^{21}Na ground state as it was used as the beam. The result of Salter *et al.* [32] is a lower limit to the rate. The results from that study were shown in Figure 1.11 and compared to other results from Groombridge *et al.* [2] and Matic *et al.* [35].

The reaction rate by Salter *et al.* [32] was calculated using $\sigma(\alpha, p_0)$ and was, therefore, only sensitive to the p_0 decay channel. However, predictions based on HF calculations showed that the reaction rate is approximately a factor of 3 higher when taking into account higher decay channels. This is indicated in Figure 1.11. Therefore, the results from Salter *et al.* [32] were scaled up by a factor of 3. This relies on assumptions of the level density which the HF calculations are sensitive to. To explore this, the following section will discuss TALYS calculations of the $^{18}\text{Ne}(\alpha, p)^{21}\text{Na}$ reaction. The energy-dependent cross sections for p_i ($i \in [0, 10]$) are determined and, therefore, their associated branching ratios. TALYS uses the HF statistical model to make predictions of cross sections. This was discussed in Chapter 2.

6.3.1 TALYS calculations of $^{18}\text{Ne}(\alpha, p)^{21}\text{Na}$

The $^{18}\text{Ne}(\alpha, p)^{21}\text{Na}$ reaction was simulated using different α optical model potentials (OMPs) as the incident particle of this reaction is an α particle. The OMPs and other aspects of the TALYS calculations were discussed in Chapter 2. The input file used a keyword, `outdiscrete y`, to generate the p_i cross section data for p_0 up to p_{10} . The data for p_0 decay for different α OMPs is compared in Figure 6.1. The TALYS calculations for p_0 decay showed the smallest amount of variation between OMPs than for any p_i . In general, the proton branching ratios do not depend strongly on the α OMPs. This was seen from the TALYS α -OMP calculations for all p_i . Therefore, the default α OMP1 from Tanikawa and Watanabe [65] was used for the calculations.

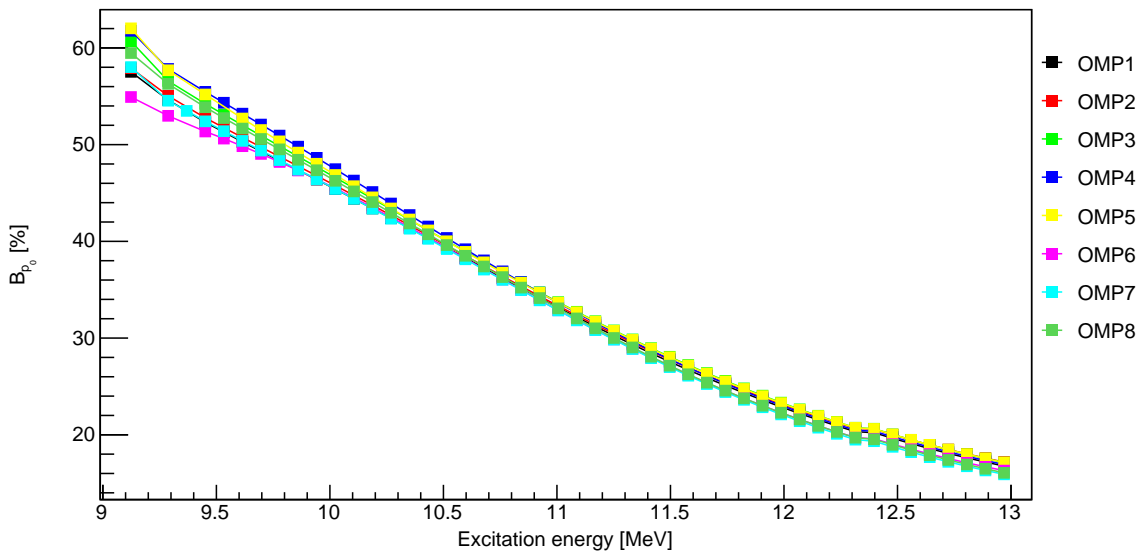


Figure 6.1: A comparison of α OMPs when calculating B_{p_0} . The data for this decay type agrees to a large extent and gives better agreement than any of the other p_i .

The branching ratios are determined by calculating the total cross section σ_T from all of the available p_i decay outputs from TALYS. The branching ratio for a particular decay is then simply calculated as:

$$B_{p_i}(E) = \frac{\sigma_{p_i}(E)}{\sigma_T(E)}. \quad (6.3.1)$$

The quantities in Equation 6.3.1 are written as functions of energy as these calculations have to be done at multiple energy points. This can be related directly to the energy bins of the B_{p_0} results in the previous chapter. The calculated results for all $B_{p_i}(E)$ are shown in Figure 6.2. The probability for

decay to proceed to any state in the daughter nucleus must be 1. Therefore, at each energy point the total branching ratio was calculated and it was indeed found to be 100%. The figure shows clearly that more decay channels open at higher energy as higher order proton decays only become possible at that point. Simultaneously, branching ratios for lower-order decays like B_{p_0} and B_{p_1} start to decrease at higher energies. This general trend is also seen in the branching ratio results presented in the previous chapter in Figure 5.28. Figure 6.3 shows B_{p_0} without the logarithmic scale to show the differences with the actual results for B_{p_0} in Figure 5.29. The TALYS calculations show different results for the branching ratios. This implies that the level density above S_α is different to those used in the theoretical HF predictions upon which the TALYS calculations are based. Thus the branching ratios were determined to make corrections to the reaction rate of which the calculations are shown in the following sections.

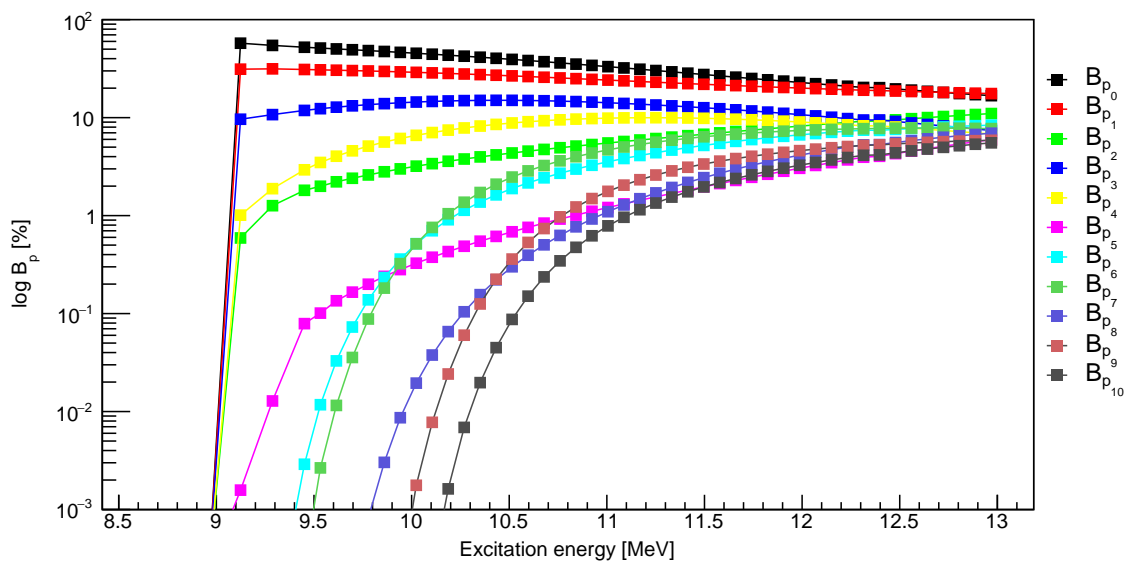
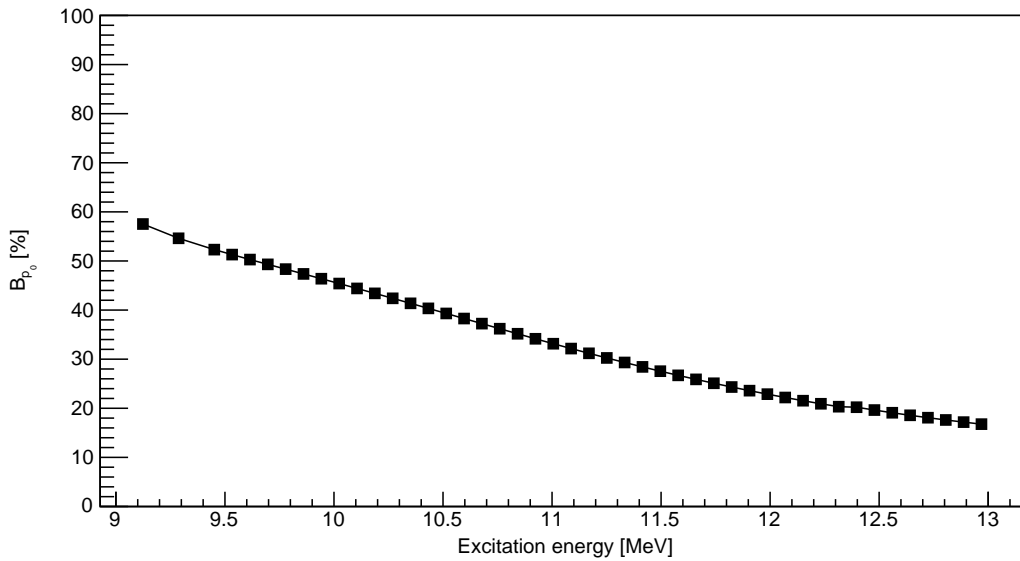


Figure 6.2: A comparison of B_{p_i} ($i \in [0, 10]$) using α OMP1 [65]. The branching ratio is given as a percentage. Note the change as the excitation energy increases.

Figure 6.3: B_{p_0} calculated with α OMP1 [65].

6.4 Recalculation of the Salter reaction rate

The next step is to use known cross section data from Salter *et al.* [32] for this reaction. The data are listed in the NNDC experimental nuclear reaction data (EXFOR) database [34]. The cross sections (in mb) and beam energies (in keV) are listed along with their error-bar values. The cross section data are generated from performing the $^{21}\text{Na}(p_0, \alpha)^{18}\text{Ne}$ reaction that gives $\sigma_{(p_0, \alpha)}$. As this is the time-reversed reaction of $^{18}\text{Ne}(\alpha, p)^{21}\text{Na}$, $\sigma_{(\alpha, p_0)}$ can be determined using the principle of detailed balance. The values for both cross sections are listed in EXFOR. The beam energy is converted to centre-of-mass energy by:

$$E_{c.m.} = E_B \frac{m_B}{m_B + m_T} = E_B \frac{18}{22}, \quad (6.4.1)$$

where E_B is the beam energy in MeV, $E_{c.m.}$ is the centre-of-mass energy in MeV, m_B is the atomic mass (in amu) of the α beam and m_T is the mass of the ^{18}Ne target (in amu). The physical motivation behind this function is that E_B in this case is for the ^{21}Na beam but we need to convert to $E_{c.m.}$ in the $^{18}\text{Ne} + \alpha$ colliding system [39]. The data are plotted and fitted in Figure 6.4. The data are fitted with a function [12]:

$$\sigma(E_{c.m.})_{\text{Salter}} = \frac{c_1 e^{-2\pi c_2 / \sqrt{E_{c.m.}}}}{E_{c.m.}}, \quad (6.4.2)$$

where the constants $c_1 = 1.23 \times 10^9$ mb MeV and $c_2 = 4.97 \sqrt{\text{MeV}}$ are the parameters of the fit.

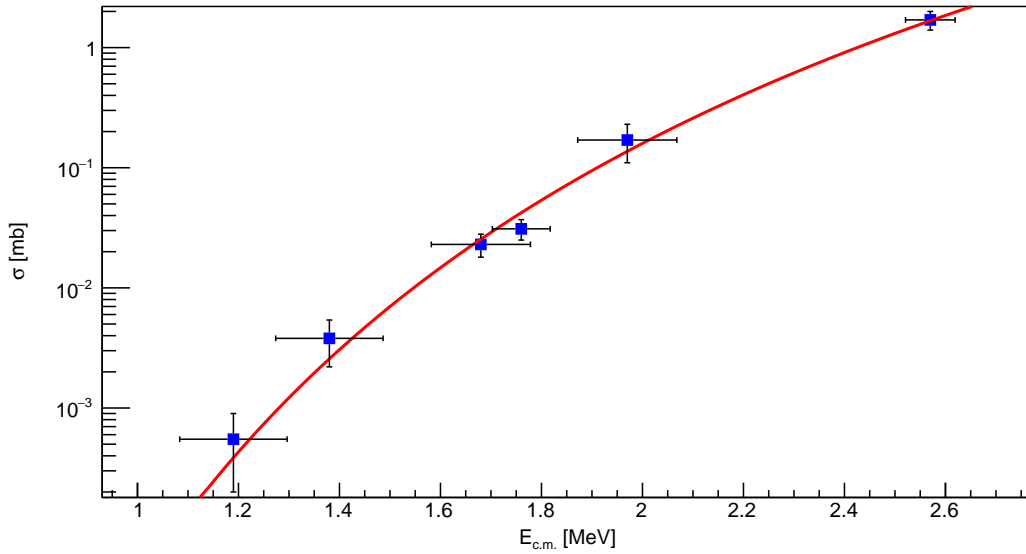


Figure 6.4: The cross section data for the $^{18}\text{Ne}(\alpha, p)^{21}\text{Na}$ reaction from Salter *et al.* [32] is plotted with the exponential fit.

The EXFOR database also lists the $^{18}\text{Ne}(\alpha, p)^{21}\text{Na}$ reaction rates at 16 different T_9 temperatures ranging from 0.95 GK to 2.45 GK (in intervals of 0.1 GK). The results from Salter *et al.* [32] were recalculated in this study using $\sigma(E)_{\text{Salter}}$ to test that the rates are reproduced accurately and that the method used is also correct. Therefore, the same method can be used when calculating the new reaction rates. The theory behind the reaction-rate calculations were discussed in Chapter 2. The particle-induced reaction rate is calculated at a particular temperature with [12]:

$$N_A \langle \sigma v \rangle = \left(\frac{8}{\pi m_{01}} \right)^{1/2} \frac{N_A}{(kT)^{3/2}} \int_0^\infty E \sigma(E) e^{-E/kT} dE, \quad (6.4.3)$$

which, after substitution of the Salter cross section function, becomes:

$$N_A \langle \sigma v \rangle = \left(\frac{8}{\pi m_{01}} \right)^{1/2} \frac{a_1 c_1 N_A}{(kT)^{3/2}} \int_0^\infty \exp \left(\frac{-2\pi c_2}{\sqrt{E}} - \frac{E}{kT} \right) dE. \quad (6.4.4)$$

In Equation 6.4.4 the fit parameters c_1 and c_2 are included and a_1 is a constant which is determined by dimensional analysis to ensure that the units of the different values and variables are corrected for to have the units of the reaction rate as $\text{cm}^3 \text{mol}^{-1} \text{s}^{-1}$. It was found that:

$$a_1 = \frac{c \text{ mol}^{-1} \text{ mb}}{\text{MeV}^2} = 3 \times 10^{-17} \text{ cm}^3 \text{ mol}^{-1} \text{ s}^{-1} \text{ MeV}^{-2}. \quad (6.4.5)$$

The integral can be determined numerically for each value of the temperature. The resultant function of the integrand for $T_9 = 1.05$ is shown in Figure 6.5. It is related to the Gamow Window discussed in Chapter 2 as the main contribution of the reaction rate is from the peak with a centroid and a width. The integrand at each temperature was drawn, integrated and the results plotted (along with data from Ref. [32]) in Figure 6.6. It is thus evident that the reaction rate data from Salter *et al.* [32] is recalculated accurately using the cross section values from.

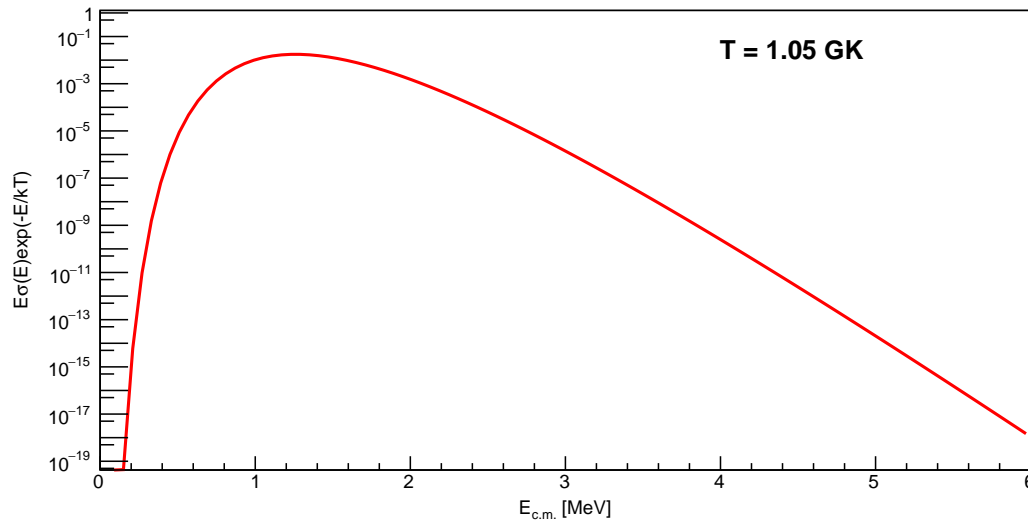


Figure 6.5: The integrand of the reaction rate integral is shown for the temperature $T_9 = 1.05$. It is the product of the energy-dependent cross section, $\sigma(E)$, with the Maxwell-Boltzmann distribution, $e^{-E/kT}$.

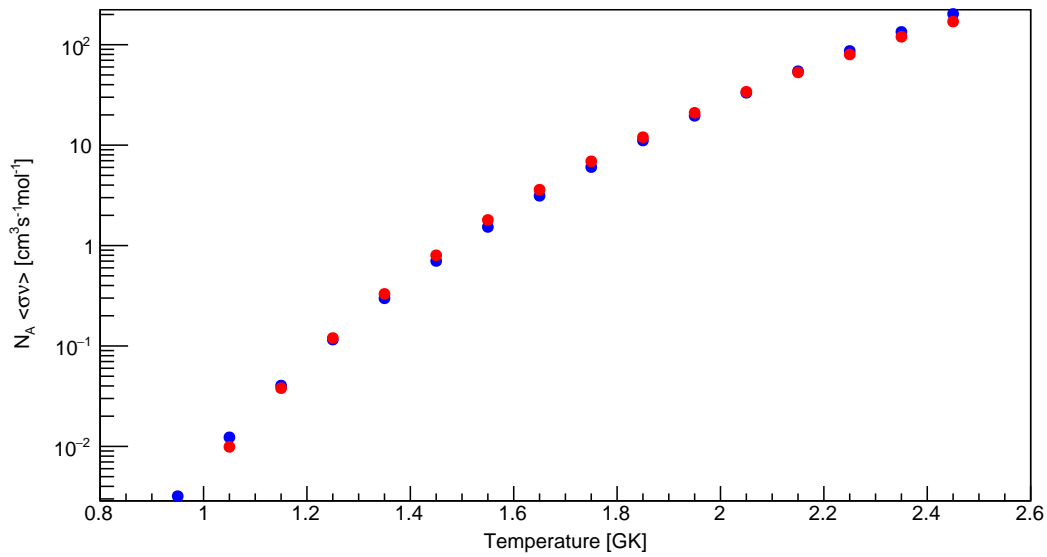


Figure 6.6: Values for the $^{18}\text{Ne}(\alpha, p)^{21}\text{Na}$ reaction rate from Salter *et al.* [32] are plotted (red) alongside the reproduction of those rates (blue) in this study.

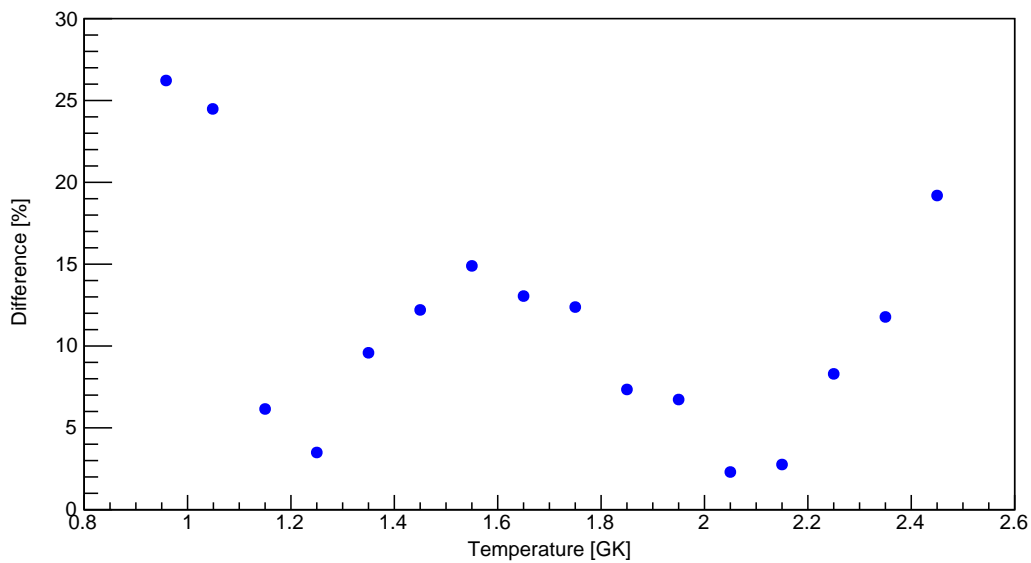


Figure 6.7: This figure shows the percentage difference between reaction-rate values shown in Figure 6.6. The largest deviation is about 26%.

6.5 Calculation of reaction rates using B_{p_0}

To calculate the corrected reaction rate of $^{18}\text{Ne}(\alpha, p)^{21}\text{Na}$ using the p_0 branching ratios B_{p_0} , the cross section as a function of energy $\sigma_{(\alpha,p)}(E)$ needs to be generated using data from Salter *et al.* [32] and the present results. The total cross section at energy, E , is related to the p_0 partial cross section by:

$$\sigma_{(\alpha,p)}(E) = \frac{\sigma_{(\alpha,p_0)}(E)}{B_{p_0}(E)}. \quad (6.5.1)$$

The function determined in the previous subsection as Equation 6.4.2 is used as $\sigma_{(\alpha,p_0)}(E)$. Thus, the next task is to determine the p_0 branching ratio as a function of energy, i.e. $B_{p_0}(E)$. This was done by using the method of a moving average to determine a general, smooth function to describe $B_{p_0}(E)$ which can then be used to determine $\sigma_{(\alpha,p)}(E)$. Within this context, the smoothness of a function is determined by the number of derivatives it has that are continuous [43]. A 5-point moving average was used. The process involves using the first five data points (1 to 5) and determining the arithmetic mean which is assigned to the centre point, point 3. The following data point is calculated by moving the 5 points by one so as to determine the geometric mean of points 2 to 6 where the mean is the assigned to point 4 etc. For this reason, the first and last two points do not have an average value. It was found that a quadratic fit best described the moving-average for the centre-value B_{p_0} data as:

$$y = b_0 + b_1 E_{c.m.} + b_2 E_{c.m.}^2, \quad (6.5.2)$$

where $b_0 = 1.9971$, $b_1 = -0.290831$ MeV, and $b_2 = 0.0109238$ MeV² (for the quadratic fit shown in black in Figure 6.8). The parameter variable names are chosen so as to not resemble variables used previously. The function generated for $B_{p_0}(E)$ using the moving average is shown in Figure 6.8 in red along with the quadratic fit in black. The actual data for B_{p_0} are in blue.

No error bars are shown in Figure 6.8. Instead, the physical quantities were used to calculate the upper- and lower-limit branching ratios for each bin. The same moving-average procedure and quadratic fit was performed with that data. The figures resemble Figure 6.8 precisely apart from the y axis being scaled. The corrected particle-induced reaction rate then becomes:

$$\begin{aligned} N_A \langle \sigma \nu \rangle &= \left(\frac{8}{\pi m_{01}} \right)^{1/2} \frac{N_A}{(kT)^{3/2}} \int_0^\infty E \sigma_{(\alpha,p)}(E) e^{-E/kT} dE \\ &= \left(\frac{8}{\pi m_{01}} \right)^{1/2} \frac{N_A}{(kT)^{3/2}} \int_0^\infty E \left(\frac{\sigma_{(\alpha,p_0)}(E)}{B_{p_0}(E)} \right) e^{-E/kT} dE \\ &= \left(\frac{8}{\pi m_{01}} \right)^{1/2} \frac{a_1 c_1 N_A}{(kT)^{3/2}} \int_0^\infty \frac{\exp\left(\frac{-2\pi c_2}{\sqrt{E}} - \frac{E}{kT}\right)}{b_0 + b_1 E + b_2 E^2} dE, \end{aligned} \quad (6.5.3)$$

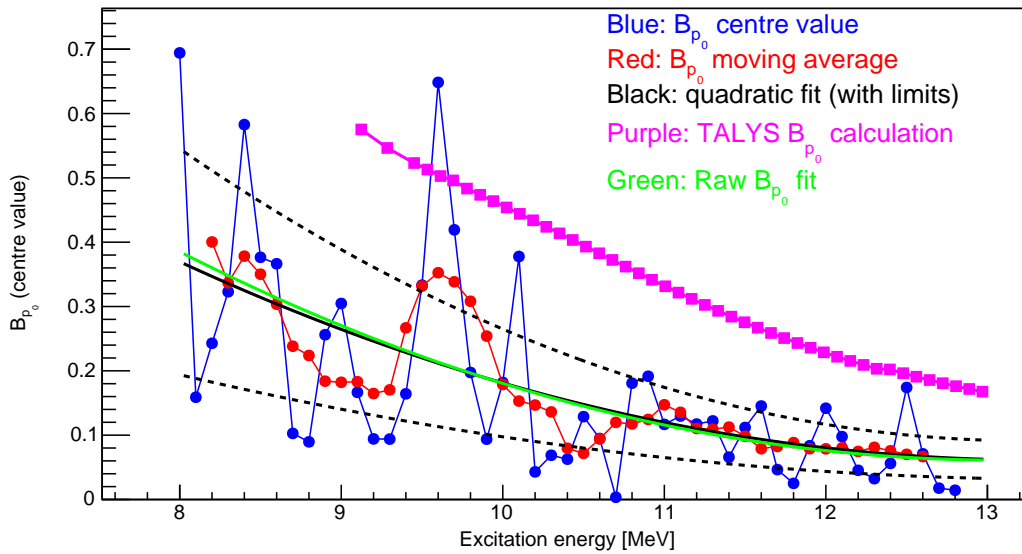


Figure 6.8: B_{p_0} data (blue) with the moving average data (red) and quadratic fit (black). A moving average is used to determine a general function for $B_{p_0}(E)$ used to calculate the corrected reaction rate. The quadratic fits for the upper- and lower-limit data of B_{p_0} is shown as black dotted lines. The TALYS results are shown in pink and show the extent to which the p_0 branching ratio is overestimated. A raw fit of the B_{p_0} data is included (green).

where E is the energy in the centre-of-mass reference frame. The integral was also determined numerically. The reaction rate was calculated at multiple temperature points from 0.1 GK to 4 GK (in intervals of 0.1 GK). To determine the reaction rate of the upper- and lower-limit branching ratios, the quadratic fit parameters for b_0 , b_1 , and b_2 were replaced. They were replaced by the fit parameters for the moving average for the upper and lower limits of the p_0 branching ratios. The results for the reaction rates calculated with the centre value of B_{p_0} is shown in Figure 6.9.

Figure 6.10 shows the comparison of the present data to literature data. The values from Salter *et al.* [32] are shown in red. Results from Matic *et al.* [35], used as the default values for this reaction rate in MESA, are shown in pink. Data from this study are shown in blue. The x -axis error bars indicate the temperature region for which that point was calculated for. They do not represent uncertainty. The y -axis error bars are determined by calculating the upper and lower reaction rates by using the error bars on the p_0 branching ratios shown in Figure 5.29. The data shown in green is taken from the results of Matic and Mohr [36]. The central, solid line represents the rates that are recommended in that paper for the $^{18}\text{Ne}(\alpha, p)^{21}\text{Na}$ reaction. The upper and lower dotted lines represent the upper and lower limit estimations, respectively, from that study. This study and others were discussed in Chapter 1.

In that study, all known data for the $^{18}\text{Ne}(\alpha, p)^{21}\text{Na}$ reaction rate from various studies were compared as some of the more recent studies showed discrepancies between them of one order of magnitude. The recommended rate is a factor of 0.55 smaller than the reference rate. The reference rate is from Matic *et al.* [35]. It is also a factor of 5 higher than the Salter rate (before being adjusted up by a factor of 3) which is used as a lower limit due to the $\sigma_{(\alpha, p; i \neq 0)}$ constraint of the experiment. The recommended rate was determined by evaluating the uncertainties and getting the most realistic overlap. Figure 6.10 is, therefore, of significance as it shows a very good agreement between all literature estimations of the reaction rate and the data from this study.

Considering the results from this section, one of the main conclusions of this thesis is that the Salter *et al.* [32] reaction rate should, at most, be scaled up by a factor of 2.3. This is the upper limit whereas the lower limit was found to be 1.4. Additionally, certain studies have given estimates as to how large the factor difference is from the Salter data. A study by Meisel *et al.* [66] estimated that the Salter rate should be scaled up by a factor of 10 but, according to data from this thesis, that would be an overestimation.

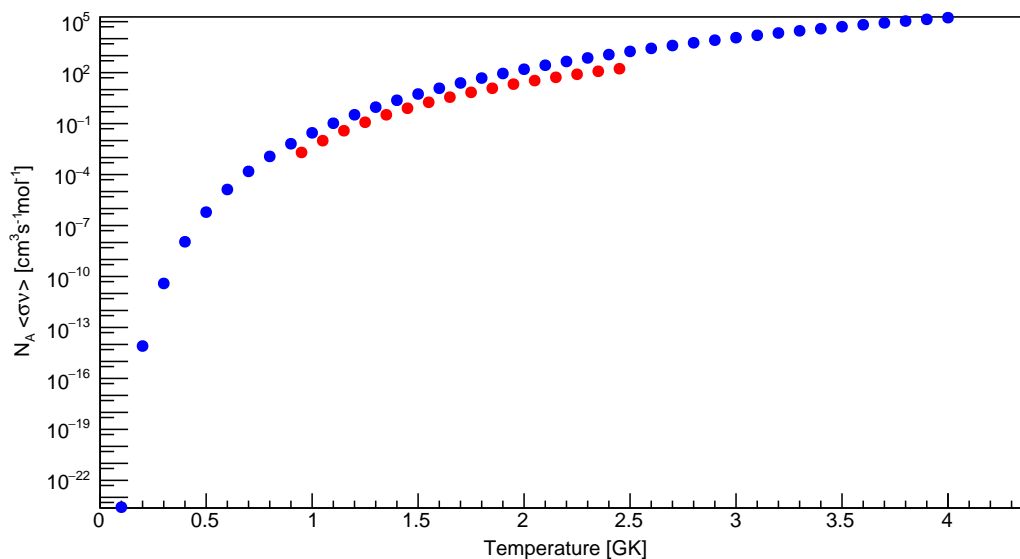


Figure 6.9: The reaction rates calculated with B_{p_0} from this study (in blue). The values of the reaction rate from Salter *et al.* [32] are shown in red.

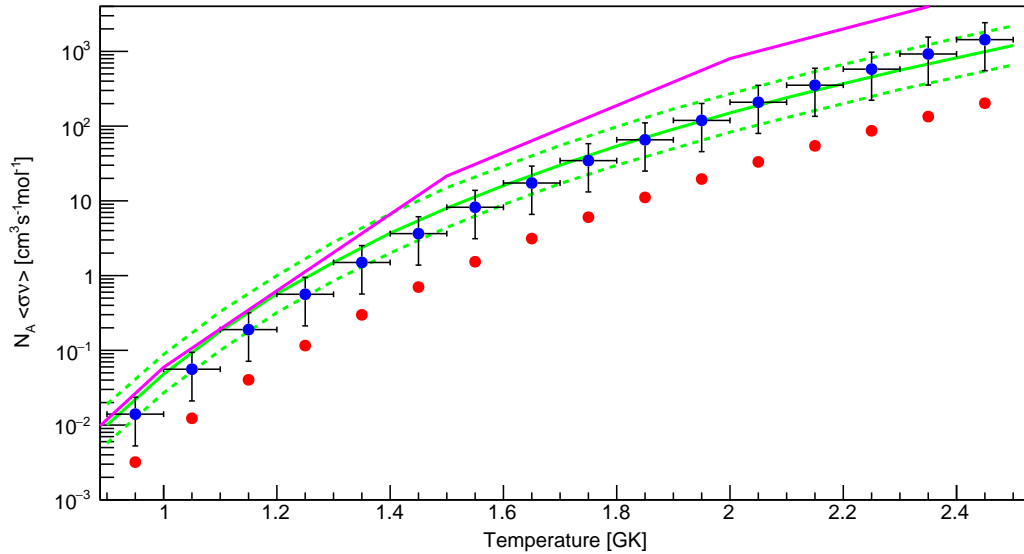


Figure 6.10: The reaction rates calculated with B_{p0} from this study compared to literature results. The red data are from Salter *et al.* [32]. The pink data are from Matic *et al.* [35]. The data from Matic and Mohr [36] are shown in green. Data from this study are shown in blue.

6.6 MESA simulations

MESA was chosen to generate the X-ray burst simulations as one of the main outputs from the MESA simulation is the lightcurve. The parameters of the simulation were kept constant while data for different $^{18}\text{Ne}(\alpha, p)^{21}\text{Na}$ reaction rates were used. This makes it possible to compare and contrast the effect that they have on the lightcurve estimations. A standard available simulation that is commonly utilised in MESA was used [63]. It was run using the full nuclear calculation network called *rp.net*. It contains slightly more than 100 nuclei from hydrogen up to ^{107}Te . A neutron star of mass $1.4M_{\odot}$ with an accretion rate of $3 \times 10^{-8} M_{\odot}/\text{year}$ was simulated. In the starting-model mass file, the inner boundary condition is set to a fixed mass, radius, and luminosity. It defines the outer regions of a neutron star above an iron substrate [63]. The 3α rate in this simulation is from Fushiki and Lamb [67]. The simulation is run each time up to model number 3000.

The output file from the simulation contains, amongst others, the time stamps and luminosities which are plotted together to generate the XRB lightcurve shown here in Figure 6.11. This particular simulation is the standard lightcurve as the default MESA values were used with the $^{18}\text{Ne}(\alpha, p)^{21}\text{Na}$ reaction rate taken from Matic *et al.* [35]. The luminosities are given in units the solar luminosity: $L_{\odot} = 3.846 \times 10^{26} \text{ W}$.

The first burst in Figure 6.11 is considered to be transient as all of the bursts

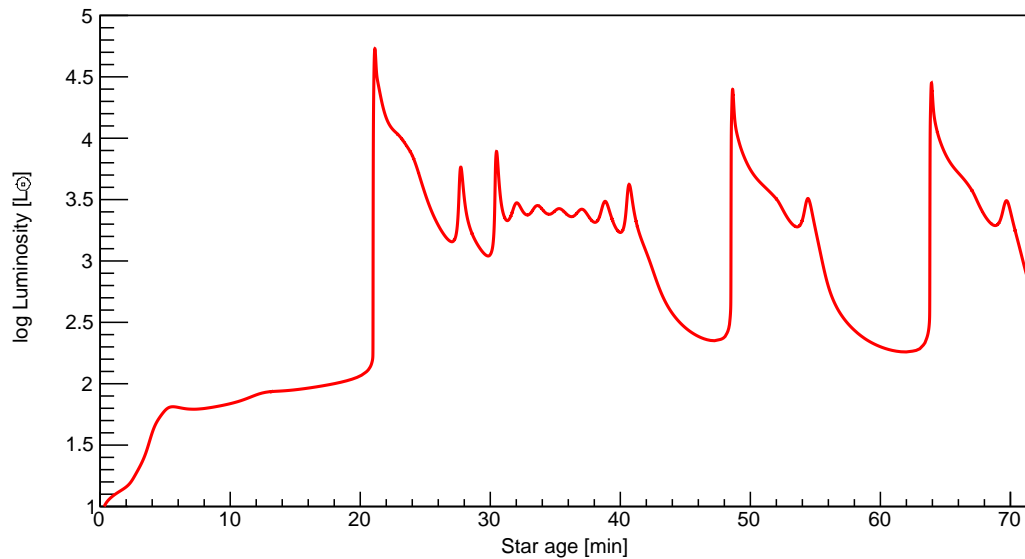


Figure 6.11: The X-ray burst lightcurve for the standard MESA simulation using the default simulation values for the $^{18}\text{Ne}(\alpha, p)^{21}\text{Na}$ reaction rate.

that follow are similar to the second burst. The reason for the differences in these bursts is due to the isotopic abundances of the CNO seed nuclei which were discussed in Chapter 1 Subsection 1.4.3. During the transient burst, more CNO seed nuclei are produced as the thermonuclear reactions commence before the occurrence of the first burst. The bursts that follow are then able to use the XRB ashes from the transient event.

Four other simulations were run with MESA. The first of these is with the recalculated reaction rates from Salter *et al.* [32] shown in Figure 6.12. The other three simulations were run with the reaction rate calculated with the centre value of B_{p_0} , shown in Figure 6.13, and with the upper- and lower-limit reaction rates shown in Figures 6.14 and 6.15, respectively. These were calculated earlier in Section 6.5 from B_{p_0} that was calculated in Chapter 5. All simulations that produced these lightcurves were run for the same number of models. However, certain lightcurves have more peaks in the spectrum making the simulation take smaller time steps in those regions. The effect is that the range of star ages differ from one simulation to the next.

The lightcurve simulated with the Salter *et al.* [32] reaction rate, in Figure 6.12, shows a higher number of bursts as compared to the standard simulation. The bursts also have identical shapes with the maximum burst peak of each diminishing in strength after each event.

The lightcurve simulated with the reaction rate data from this study, shown in Figure 6.13, predicts fewer bursts in the same period of time as the Salter simulation. All of the bursts except one show an additional, smaller burst peak after the initial explosion.

The MESA simulation shown in Figure 6.14 was generated with the upper limit of the $^{18}\text{Ne}(\alpha, p)^{21}\text{Na}$ reaction rates calculated in this thesis. It can be seen that after the first two bursts, the isotopic abundances of the seed nuclei stabilise and the shape of the bursts become more consistent. Compared to Figure 6.13, it is evident that an increase in the reaction rate resulted in more bursts in approximately the same time frame.

The lightcurve simulated with the lower-limit reaction rates, shown in Figure 6.15, resembles the shape of the lightcurve generated with the default MESA reaction rates. It also has a transient event at the start with two other bursts over a stellar age of approximately 66 minutes. However, very clear differences are apparent between this simulation and the standard MESA simulation in Figure 6.11.

The simulations in Figures 6.11 to 6.15 aim to show the vast differences between the lightcurves simulated with different reaction rates. It is clear from these simulations the extent of the effect that the $^{18}\text{Ne}(\alpha, p)^{21}\text{Na}$ HCNO breakout reaction has on the energy generation in XRBs. It is also evident that to understand these bursts and to be able to make accurate predictions of the lightcurve, accurate measurements of this reaction rate have to be available.

However, it is important to note that the changes in these MESA simulation results are not the physically observed lightcurves from an actual XRB. The changes in the bursts are much greater than what is expected when compared to the findings of Meisel *et al.* [66]. Longer burst periods need to be simulated to average out the burst-to-burst variations. In addition to that certain astrophysical factors, such as red shift, need to be calculated and included in the corrections.

Consequently, one of the main results from this thesis, as discussed previously in Section 6.5, is that the Salter reaction rate should be, at most, scaled up by a factor of 2.3 (upper-limit) which agrees with the findings of Matic and Mohr [36]. The lower limit is a factor of 1.4 higher.

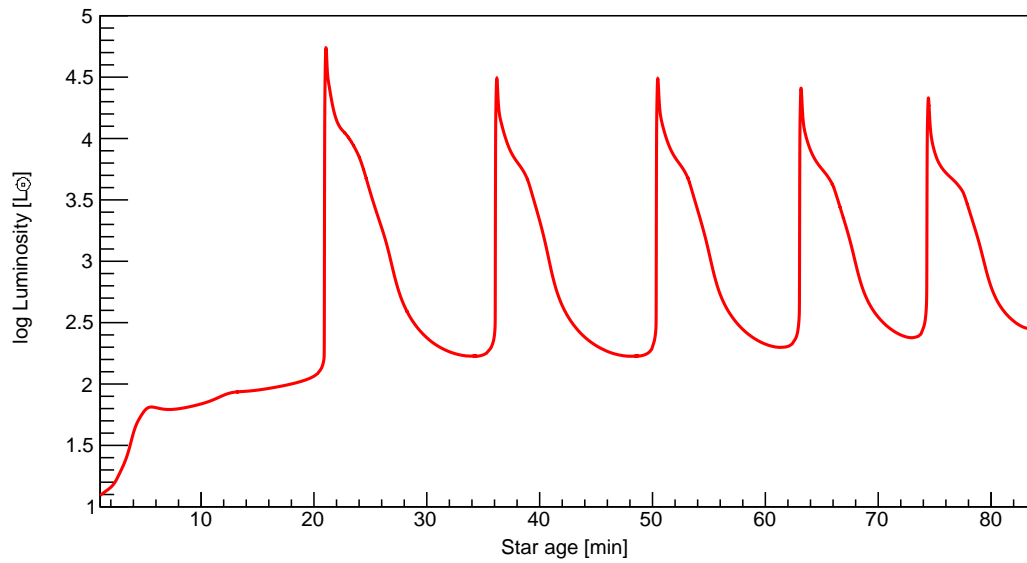


Figure 6.12: X-ray burst lightcurve simulated with the $^{18}\text{Ne}(\alpha, p)^{21}\text{Na}$ reaction rate from Salter *et al* [32].

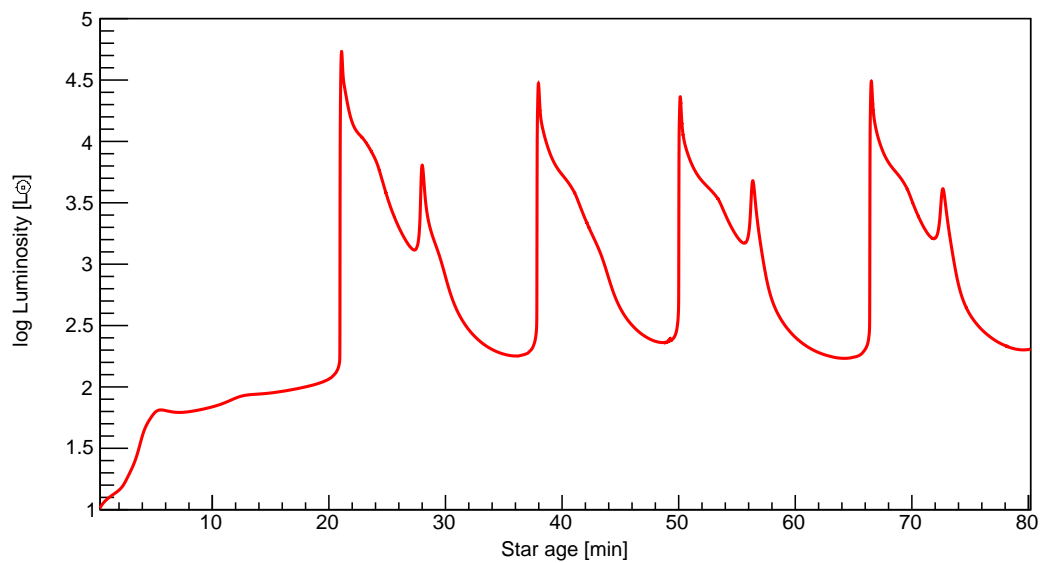


Figure 6.13: X-ray burst lightcurve simulated with the $^{18}\text{Ne}(\alpha, p)^{21}\text{Na}$ reaction rate calculated in this thesis.

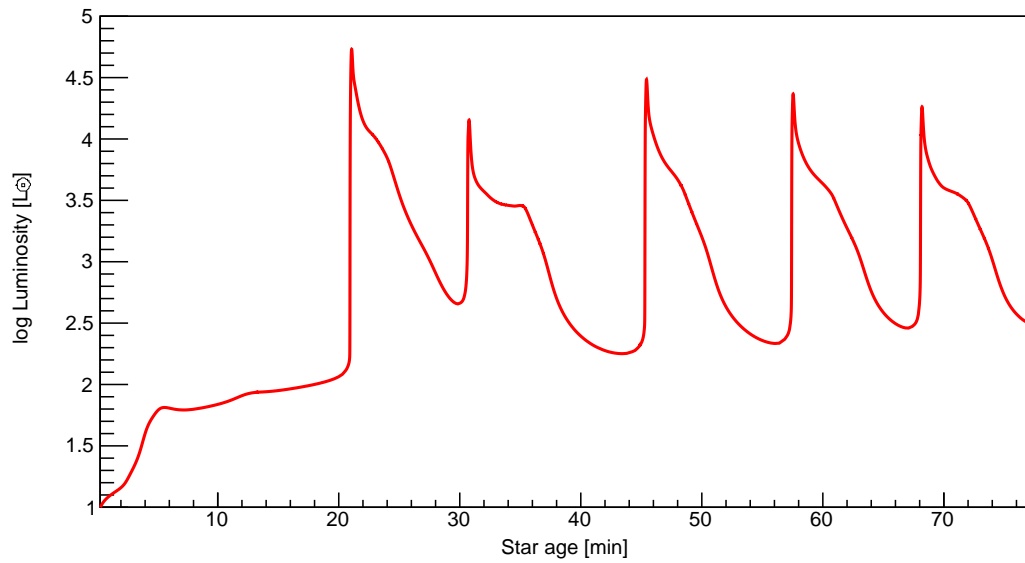


Figure 6.14: X-ray burst lightcurve simulated with the upper-limit $^{18}\text{Ne}(\alpha, p)^{21}\text{Na}$ reaction rate calculated in this thesis.

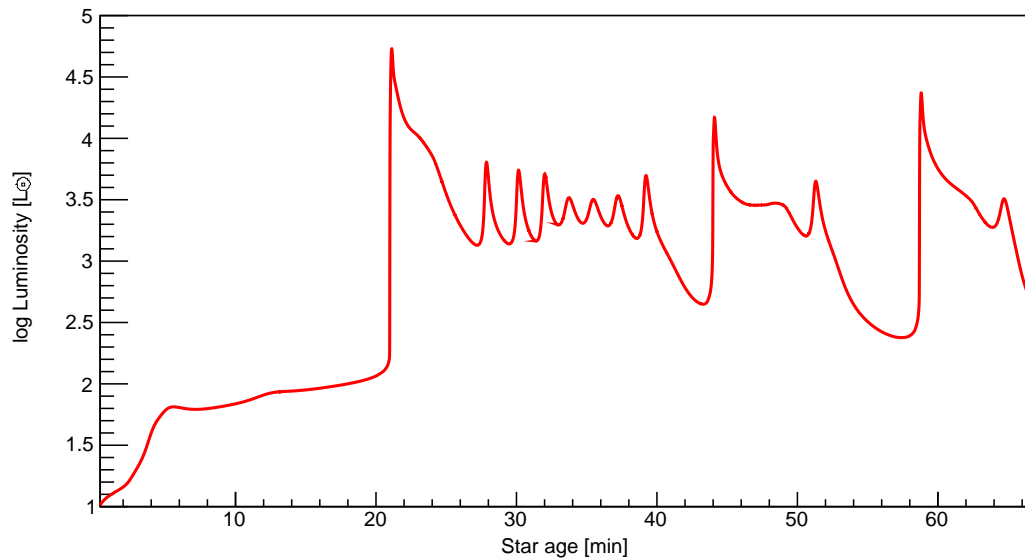


Figure 6.15: X-ray burst lightcurve simulated with the lower-limit $^{18}\text{Ne}(\alpha, p)^{21}\text{Na}$ reaction rate calculated in this thesis. The structure of the initial burst in this spectrum varies a lot when compared to the others. This is likely unphysical and rather a result of numerical anomalies in the MESA simulation package.

Chapter 7

Conclusions

If I have seen a little further it
is by standing on the shoulders
of giants.

Isaac Newton

This thesis discussed the spectroscopy of ^{22}Mg by means of the $^{24}\text{Mg}(p, t)^{22}\text{Mg}$ reaction. This reaction was performed in an experiment at iThemba LABS near Cape Town, South Africa with the K600 magnetic spectrometer in coincidence with the CAKE silicon-detector array.

The main reason for performing this experiment was to study the $^{18}\text{Ne}(\alpha, p)^{21}\text{Na}$ HCNO breakout reaction which is one of the main reactions that influences energy generation in XRBs. This made it possible to recalculate the reaction rate successfully by studying resonances in the ^{22}Mg excitation energy spectrum above S_α . Upper and lower limits to the reaction rate were also calculated to determine the amount of variation in the final answer. It was found that the results are in very good agreement with estimations by Matic and Mohr [36]. Their results were based on the most realistic overlap of uncertainties from the data of all preceding measurements that tried to calculate this reaction rate.

The study by Salter *et al.* [32] determined this reaction rate by performing the time-reversed measurement. Their results were a lower bound as it could only take into account the branching ratio to the ground state, B_{p_0} . Therefore, their results were scaled up by a factor of 3 to compensate for the missing decay exit channels. In this thesis, it was found that the reaction rate is, at most, a factor of 2.3 higher than the adjusted rate by Salter *et al.* [32].

The newly-calculated rates were used in MESA to simulate an XRB event and produce the resultant lightcurve. The default values for this reaction in MESA is by Matic *et al.* [35] which is approximately a factor of 2 higher than the result from this thesis. The lightcurve simulations showed that as the reaction rate was decreased, the number of bursts in a particular time period

increased and that the intensities of each burst increased. This also happens with a decrease in the accretion rate. This happens because the lower rates allow the burst to build up and then release a greater amount of energy when it does explode and do so more frequently. This effect was also seen by Tan *et al.* [68].

Resonances below S_α were also studied in an attempt to determine the $^{21}\text{Na}(p, \gamma)^{22}\text{Mg}$ reaction rate. The resonance energies, widths, and branching ratios were calculated and possible J^π assignments were discussed. However, it was evident that the detection thresholds of the CAKE were not low enough to detect the resonances of interest successfully in the Gamow region that influences the $^{21}\text{Na}(p, \gamma)^{22}\text{Mg}$ reaction rate. To pursue the calculation of this reaction rate, a silicon-detector array that can operate at lower physical and electronic detection thresholds would be needed. An alternative to silicon detectors would be to use active-target detectors which have very high detection efficiencies and the capabilities to detect low-energy emissions into a gaseous active region.

Appendices

Appendix A

Monte Carlo Simulations for the CAKE

Coelorum perrupit claustra.
He broke through the barriers
of the skies.

Epitaph of William Herschel

This appendix will discuss the simulations of the CAKE in more detail and is provided as documentation for future users. The first section is a simplified guide to using the basic functionality of the CAKE simulation package. The code is a GEANT4 Monte Carlo simulation written for the K600 experimental group. The sections that follow will discuss calculations of the CAKE efficiencies as well as the position uncertainties of the array in the chamber.

A.1 Running the simulation

It is assumed that the user has a working installation of GEANT4 [52], CADMesh [69] as well as the simulation program itself K600-ALBA [51]. The latter two can be found in the Git repositories of their respective authors. The CADMesh program is used to draw the mesh structures of the CAKE detectors whereas the multi-threaded version of GEANT4 makes more use of the processing threads made available by the CPU. Moreover, this guide is for users who are running on Ubuntu.

The K600-ALBA file is first extracted from the Git repository into a folder named K600-ALBA. CMake is then used to build the files in the K600-ALBA-build directory. The make command is run next to generate the executable K600 file. Very importantly, this command has to be run from the build directory every time changes are made and saved to any of the source files so that the changes can take effect. The rest of the commands will also assume the user is in the K600-ALBA-build directory.

Firstly, modify the `PrimaryGeneratorAction.cc` file according to the parameters of the experiment of the user. For instance, the `CalculateBinaryDecayKinematics()` object needs the energy of the decay threshold for the reaction at hand as its third argument. For this experiment, the proton-decay threshold of 5.502 MeV was used. Moreover, the user has to search through the file and change any values of mass and atomic number (A and Z) to suit the current experiment. The beam energy also needs to be set in the line:
`std::vector<double> reaction_T{100.0, 0.0, 0.0, 0.0};`
In this instance, 100.0 is the energy (in MeV) of the proton beam used during this experiment. The other values in the argument do not need to be changed.

One parameter in particular that needs to be measured during or right after the experiment is the CAKE arm distance. This measurement is made on the aluminium mounting arm that the CAKE is fastened to. It is the distance from the screw that attaches the CAKE to the aluminium arm to the screw that attaches the arm to the aluminium mounting bracket that is physically attached to the scattering chamber. This is shown in Figure A.1 [48]. A measurement of about 50 millimeters is typical. For this experiment it was 55.5 mm. This value needs to be entered into the `DetectorConstruction.cc` file. Find the line of code which reads:

```
double distance_CAKE_arm = <double value>;
```

Enter your measurement as the double value.

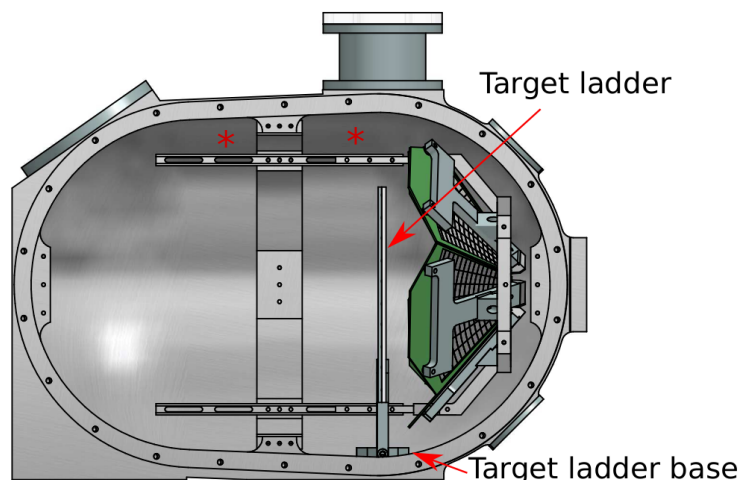


Figure A.1: The two points (noted with *) that defines the measurement of the CAKE arm distance are indicated. It is the distance between the two screws that attaches the CAKE to the bracket and frame. The target ladder frame and base is indicated for reference.

Lastly, and quite importantly, the `recoilExcitationEnergy` variable needs to be set. This can have a single value or, if the user wishes to simulate a range of energies to mirror the energy range in their excitation energy spectrum, the

line can be altered to the following:

```
double recoilExcitationEnergy = x+(y-x)*G4UniformRand();
```

In this command, x is the lower limit of the energy range and y is the upper limit. The program will then generate random numbers between the lower and upper energy limits [39] and run the simulation with that recoil excitation energy for that particular event. Every event will have a different energy.

The next step will be to enable the OpenGL visualisation if it is needed to draw the CAKE detector during the simulation. It is then possible to see the decays from the recoil nucleus impinging upon it (for reference, see Figure 3.19). Modify the `vis.mac` file in the K600-ALBA folder and uncomment the line:

```
#/vis/open OGL 800x600-0+0
```

Finally, to run the simulation while still in the build directory, type:

```
./K600
```

The program is running successfully if it displays:

```
Idle>
```

The simulation will start once the beam is switched on with:

```
Idle> /run/beamOn 1000
```

The number that followed the previous command can be changed depending on how many particles should be fired at the target. Note that the visualisation becomes saturated after about 1000 events [70]. It also slows the simulation down drastically. If it is not necessary, the line can be commented out again in the same file `vis.mac`. Depending on the CPU and number of processing cores used, the simulation will be able to run ten million events in a few minutes. Normally, the visualisation is from an upstream point of view. If a side-on view is needed (as shown in Figure 3.19 (b)) the following command can be used (this sets the values for the polar and azimuthal angles, respectively):

```
Idle> /vis/viewer/set/viewpointThetaPhi 90 0
```

The simulation runs with fictitious particles called geantinos which do not interact with the detector. The particle type can be changed firstly by opening the `PrimaryGeneratorAction.cc` file again. Near the beginning of the file the user will find the line:

```
G4ParticleDefinition* particleDefinition =
G4ParticleTable::GetParticleTable()
->FindParticle("geantino");
```

Simply change `geantino` to `alpha` or to the name of any other particle relevant to the experiment. The effect of changing the particle type to α particles is shown in Figure A.2.

To reduce the large amount of output the simulation does not by default print the kinematic information of every event to the terminal. However, this can be changed if the user requires either the kinetic energy (T in MeV) or total energy (E in MeV) or momentum (p in MeV/ c^2) of the projectile, recoil or ejectile nuclei. It will also show the angle (in degrees) of the ejectile or recoil

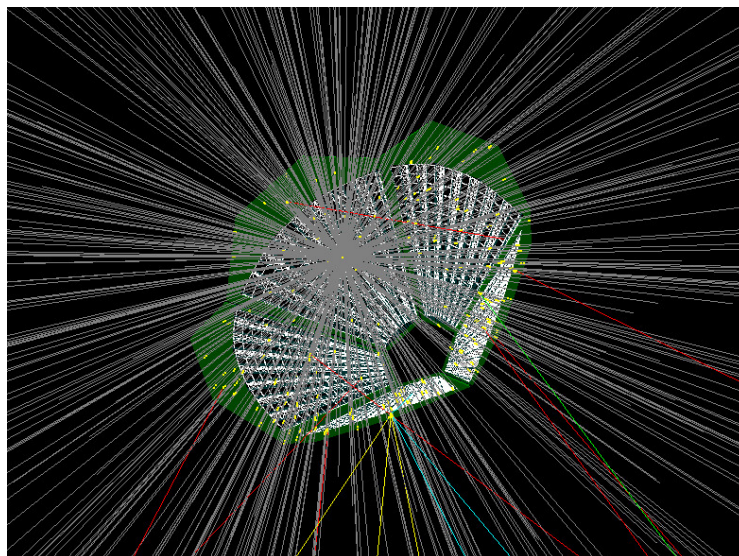


Figure A.2: The effect of changing the simulated particle from geantinos to α particles. Note that some of the trajectories have various colours which indicate secondary interactions that occur with the detector system.

nucleus w.r.t. the beam axis. If this is required, modify the `BiRelKin.hh` file and find the line which reads:

```
bool printResults = false;
```

Change this to `true` and rerun the simulation with only a few events at a time to see all of the information as listed above. If the user wishes to change the number of processing threads used during the simulation it can be done by modifying `K600.cc`. Find the line with the following code:

```
G4int nThreads = <integer number>;
```

The integer number can be lowered if more CPU cores are needed for other tasks or it can be increased if the simulation time needs to be reduced. If the CPU is an n -core system, the number of threads can be changed from 1 to $2n$.

The multi-threaded code will generate a few output files depending on how many processing threads were used to run the simulation. In the build directory, files with the name `K600Output_t<thread number>.root` can be found. The thread numbers will start from 0 up to $2n-1$.

The ROOT output files can then be analysed after they have been combined by chaining them together. The tree structure is called `SimulationTree` and if, for instance, it is necessary to see what the number of hits were in each ring of the CAKE the following commands will show that:

```
root K600Output_t0.root
SimulationTree->Draw("ga_CAKE_ringNr");
```

By combining all runs together and taking into account the total number of events that were simulated, the fraction of events detected by each ring can be calculated to determine the solid angle subtended by each ring of the CAKE

and, therefore, the efficiency of each ring by multiplying by a factor of 4π . Adding the efficiency of each ring will give the total efficiency of the CAKE. A similar procedure is followed to determine the efficiencies of the sectors. To draw the spectrum that shows the hits detected in each sector, simply execute the command:

```
SimulationTree->Draw("ga_CAKE_sectorNr");
```

A.2 Calculation of ring efficiencies for the CAKE

This section will show the derivation of the ring-efficiency equation. It is used to calculate the individual efficiency [39] of each ring of the CAKE. This is discussed in Chapter 5 under Subsection 5.2 with the results plotted in Figure 5.3. The angular correlation is given by:

$$W(\theta) = \sum_{n=0}^{n=n_{max}} A_n P_n(\cos(\theta)) \quad (\text{A.2.1})$$

Whereas the differential cross section evaluated at θ is given by:

$$\left. \frac{d\sigma}{d\Omega} \right|_{\theta} = \frac{1}{4\pi} \sigma W(\theta) \quad (\text{A.2.2})$$

Now, define that the singles yield is symbolised by N_s and assume a branching ratio at unity, $B_p = 1$, then the number of decays (N_c) in the region θ_{min} to θ_{max} is given by:

$$N_c[\theta_{min}, \theta_{max}] = \frac{N_s \int_{\theta_{min}}^{\theta_{max}} \sin(\theta) W(\theta) d\theta}{\int_0^{\pi} \sin(\theta) W(\theta) d\theta} \quad (\text{A.2.3})$$

For an isotropic distribution the angular correlation function becomes $W(\theta) = 1$ so that:

$$\begin{aligned} N_c[\theta_{min}, \theta_{max}] &= \frac{N_s \int_{\theta_{min}}^{\theta_{max}} \sin(\theta) d\theta}{\int_0^{\pi} \sin(\theta) d\theta} \\ &= \frac{N_s [\cos(\theta_{min}) - \cos(\theta_{max})]}{[\cos(0) - \cos(\pi)]} \\ &= \left(\frac{N_s}{2} \right) [\cos(\theta_{min}) - \cos(\theta_{max})] \end{aligned} \quad (\text{A.2.4})$$

Now, assume that the number of particles detected within the region $[\theta_{min}, \theta_{max}]$ is given by N_d then the efficiency η is:

$$\begin{aligned}\eta[\theta_{min}, \theta_{max}] &= \frac{N_d}{N_c[\theta_{min}, \theta_{max}]} \\ &= \frac{N_d}{N_s} \cdot \frac{2}{\cos(\theta_{min}) - \cos(\theta_{max})}\end{aligned}\tag{A.2.5}$$

Therefore, the efficiencies need to be scaled by a factor of $2/[\cos(\theta_{min}) - \cos(\theta_{max})]$. All rings have angular regions which are used to determine θ_{min} and θ_{max} for each ring. The result is that we find ring 0 to be $\sim 52\%$ efficient (as two sectors of the ring were dysfunctional) for decays into that region whereas all other rings are 86-94% efficient for decays into their respective regions. It is thus evident that the CAKE is very efficient at detecting decays incident upon it.

A.3 Efficiency uncertainties

The exact position of the CAKE mounted on its aluminium bracket inside the scattering chamber was measured immediately following the experiment. As discussed previously, that position measurement was entered into the source files of the simulation and it was of the order of 55.5 mm. To determine the error in the efficiency a position error of ± 1 mm ($\sim 2\%$) is assumed. The simulation is then run twice more with 54.5 mm and 56.5 mm as input. The total efficiency of the CAKE was calculated for each run and it was determined that the position error translates to an efficiency error range of 0.64%. This is a relative error of 2.36%. This is taken into account when calculating yields based on the efficiencies of the rings of the CAKE.

Appendix B

Log-Normal Distributions

*Non est ad astra mollis e terris
via.*

There is no easy way from the
earth to the stars.

Seneca the younger

Log-normal distributions were used to calculate the uncertainties of the branching ratios of states below and above S_α in Chapter 5. The reason is that the p_i yields and singles-yield uncertainties are distributed normally (i.e. Gaussian) and the quotient (or product) of normally distributed variables is distributed log-normally. This appendix will briefly discuss log-normal distributions and its use in determining the B_{p_i} uncertainties.

B.1 Definition and use

The definition of a log-normal distribution is that it is a statistical distribution in which the logarithm of a variable is distributed normally. Simply put, this means that if a variable x is distributed log-normally, then

$$y = \ln(x). \quad (\text{B.1.1})$$

Given that y has a normal distribution, then x is such that

$$x = e^y, \quad (\text{B.1.2})$$

has a log-normal distribution. The distribution only has values that are positive and real. The probability density function (PDF) is defined by: [71]

$$f(x) = \frac{1}{\sigma\sqrt{2\pi}} \frac{1}{x} e^{-(\ln(x)-\mu)^2/(2\sigma^2)}, \quad (\text{B.1.3})$$

where σ and μ represent the standard deviation and mean, respectively, of $\ln(x)$. An example of different PDFs with increasing σ is shown in Figure B.1.

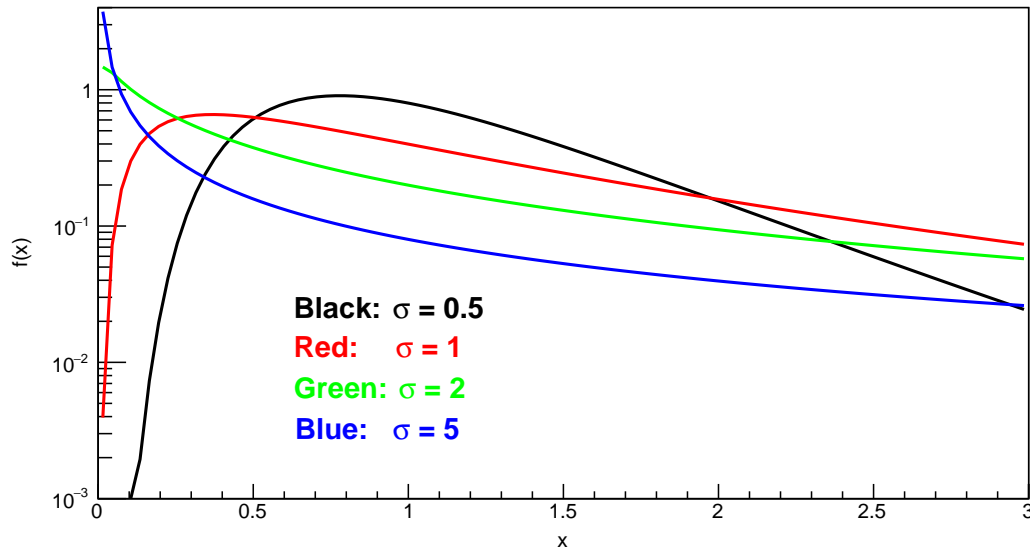


Figure B.1: Probability density function with varying standard deviation values.

The expectation value, $E[x]$, and variance, $V[x]$, of the distribution are related to the mean and standard deviation by:

$$E[x] = e^{(2\mu + \sigma^2)/2}, \quad (\text{B.1.4})$$

and

$$V[x] = e^{(2\mu + \sigma^2)} \left[e^{\sigma^2} - 1 \right]. \quad (\text{B.1.5})$$

Given the variance and expectation value, the mean and standard deviation can be calculated easily by making them the subject of the equation. This is, however, not the case here. In this study, μ and σ are determined by using the yield data points and their associated errors. As an example, consider that the branching ratios are calculated from:

$$B_{p_i} = \frac{y_{p_i}}{y_s}, \quad (\text{B.1.6})$$

where y_{p_i} is the yield for a particular decay (in a given energy region above S_α) and y_s is the singles yield in the same region. Then ey_{p_i} is the error of the decay yield and ey_s is the error of the singles yield. The decay-yield error consists of the statistical error, amplitude error (from the Gaussian and Voigt

fits), and detector position uncertainty all added in quadrature. The single-yield error only consists of the statistical error. To calculate μ and σ for the normal distributions of both yields we have:

$$\mu_{yp_i} = \ln(y_{p_i}) \quad \text{and} \quad \mu_{y_s} = \ln(y_s), \quad (\text{B.1.7})$$

and

$$\sigma_{yp_i} = \ln\left(1 + \frac{ey_{p_i}}{y_{p_i}}\right) \quad \text{and} \quad \sigma_{y_s} = \ln\left(1 + \frac{ey_s}{y_s}\right). \quad (\text{B.1.8})$$

The mean and standard deviation of the log-normal distribution is calculated as

$$\mu_{B_{p_i}} = \mu_{yp_i} - \mu_{y_s} \quad (\text{B.1.9})$$

and

$$\sigma_{B_{p_i}}^2 = \sigma_{yp_i}^2 + \sigma_{y_s}^2. \quad (\text{B.1.10})$$

These values are then used to determine the cumulative density function (CDF) for the distribution. The function used is written as [72]:

$$g(x) = 0.5 \left(1 + \frac{2}{\sqrt{\pi}} \int_0^{x_{upper}} e^{-t^2} dt \right), \quad (\text{B.1.11})$$

where the upper limit of the integral is:

$$x_{upper} = \frac{\ln(x) - \mu}{\sqrt{2}\sigma}. \quad (\text{B.1.12})$$

As an example, the CDF for B_{p_0} bin 4 (from 8.4 to 8.5 MeV) is shown in Figure B.2. Determining the uncertainty value for a 95 % confidence limit α_{CL} is indicated on the spectrum: given $P(x) = 0.95$, the value of x can be interpolated.

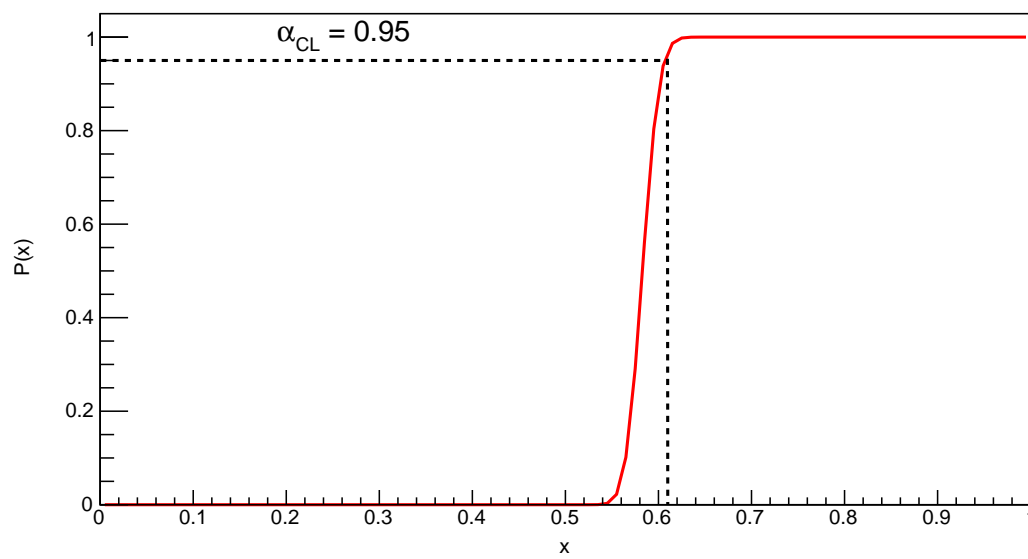


Figure B.2: Cumulative density function that shows the method of determining the value of an error using a 95% confidence limit (α_{CL}).

List of References

- [1] W. Bradfield-Smith *et al.*, *Breakout from the hot CNO cycle via the $^{18}\text{Ne}(\alpha,p)^{21}\text{Na}$ reaction*, Phys. Rev. C **59** (1999) 3402.
- [2] D. Groombridge *et al.*, *Breakout from the hot CNO cycle via the $^{18}\text{Ne}(\alpha,p)^{21}\text{Na}$ reaction. II. Extended energy range $E_{c.m.} \sim 1.7\text{-}2.9$ MeV*, Phys. Rev. C **66** (2002) 055802.
- [3] J. Grindlay *et al.*, *Discovery of intense X-ray bursts from the globular cluster NGC 6624*, Astrophysical Journal **205** (1976) L127.
- [4] R. Belian *et al.*, *The discovery of X-ray bursts from a region in the constellation Norma*, Astrophysical Journal **206** (1976) L135.
- [5] S. Woosley and R. Taam, *γ -ray bursts from thermonuclear explosions on neutron stars*, Nature **263** (1976) 101.
- [6] E. M. Basinska *et al.*, *The very long Type-II X-ray bursts from the rapid burster*, Astrophysical Journal **241** (1980) 787.
- [7] R. Prinja, *Stars: A journey through stellar birth, life and death* (New Holland Publishers, London, United Kingdom, 2008).
- [8] N. Weinberg *et al.*, *Exposing the nuclear burning ashes of radius expansion type I x-ray bursts*, Astrophysical Journal **639** (2006) 1018.
- [9] N. Bateman *et al.*, *Measurement of the $^{24}\text{Mg}(p,t)^{22}\text{Mg}$ reaction and implications for the $^{21}\text{Na}(p,\gamma)^{22}\text{Mg}$ stellar reaction rate*, Phys. Rev. C **63** (2001) 0305803.
- [10] R. Chini *et al.*, *The formation of a massive protostar through the disk accretion of gas*, Nature **429** (2004) 155.
- [11] J. Pinochet, *Brown dwarfs and the minimum mass of stars*, arXiv 1909.08575, submitted September 2019.
- [12] C. Iliadis, *Nuclear Physics of Stars* (Wiley-VCH, Weinheim, Germany, 2007).

- [13] J.J. He *et al.*, *The $^{18}\text{Ne}(\alpha,p)^{21}\text{Na}$ breakout reaction in X-ray bursts: Experimental determination of spin-parities for α resonances in ^{22}Mg via resonant elastic scattering of $^{21}\text{Na}+p$* , Phys. Rev. C **88** (2013) 012801.
- [14] Decay radiation for ^{22}Mg , <http://www.nndc.bnl.gov/chart>, Accessed 18 June 2016.
- [15] E.E. Salpeter, *Nuclear reactions in stars without hydrogen*, Astrophys. J. **115** (1952) 326.
- [16] F. Hoyle *et al.*, Phys. Rev. **92** (1953) 1095.
- [17] D.N.F. Dunbar *et al.*, *The 7.68-MeV state in ^{12}C* , Phys. Rev. **92** (1953) 649.
- [18] C.W. Cook *et al.*, ^{12}B , ^{12}C , and the red giants, Phys. Rev. **107** (1957) 508.
- [19] Image from the European Space Agency website, <http://sci.esa.int/education/35774-stellar-radiation-stellar-types/?fbodylongid=1703>, Accessed 24 May 2019.
- [20] S. Chandrasekhar, *The density of white dwarf stars*, Philosophical Magazine **11** (1931) 592.
- [21] P. Adsley, Ph.D. thesis, University of York, 2013.
- [22] D. Kasen *et al.*, *Origin of the heavy elements in binary neutron-star mergers from a gravitational-wave event*, Nature **551** (2017) 80.
- [23] NASA Hubble image, <https://apod.nasa.gov/apod/ap981230.html>, Accessed 13 November 2019.
- [24] D. Jones and H.M.J. Boffin, *Binary stars as the key to understanding planetary nebulae*, Nature astronomy **1** (2017) 0117.
- [25] Image from Swinburne University astronomy online, <http://astronomy.swin.edu.au/cosmos/r/roche-lobe>, Accessed 19 February 2019.
- [26] XRB illustration by David A. Hardy, <https://www.news.gatech.edu/2014/09/19/thermonuclear-x-ray-bursts-neutron-stars-set-speed-record>, Accessed 19 February 2019.
- [27] F. Ajzenberg-Selove, *Energy levels of light nuclei $A=18-20$* , Nucl. Phys. A **392** (1983) 1.
- [28] Nova Cygni 1992 image from F. Paresce and R. Jędrzejewski, NASA/STScI/ESA.

- [29] J. Jose, A. Coc, and M. Hernanz, *Nuclear uncertainties in the NeNa-MgAl cycles and production of ^{22}Na and ^{26}Al during nova outbursts*, *Astrophys. J.* **520** (1999) 347.
- [30] C. Ruiz, Ph.D. thesis, University of Edinburgh, 2003.
- [31] J. Görres *et al.*, *Bridging the waiting points: The role of two-proton capture reactions in the rp process*, *Phys. Rev. C.* **51** (1995) 392.
- [32] P.J.C. Salter *et al.*, *Measurement of the $^{18}\text{Ne}(\alpha,p)^{21}\text{Na}$ Reaction Cross Section in the Burning Energy Region for X-Ray Bursts*, *Phys. Rev. Lett.* **108** (2012) 242701.
- [33] W. Scheid, *Fundamentals of Physics III - Nuclear Reactions* (Eolss Publishers, Oxford, United Kingdom, 2009).
- [34] NNDC Experimental Nuclear Reaction Data, <https://www.nndc.bnl.gov/exfor/exfor.htm>, Accessed 24 October 2019.
- [35] A. Matic *et al.*, *High-precision (p,t) reaction measurement to determine $^{18}\text{Ne}(\alpha,p)^{21}\text{Na}$ reaction rates*, *Phys. Rev. C* **80** (2009) 055804.
- [36] P. Mohr and A. Matic, *Examination and experimental constraints of the stellar reaction rate factor $N_A\langle\sigma v\rangle$ of the $^{18}\text{Ne}(\alpha,p)^{21}\text{Na}$ reaction at temperatures of X-ray bursts*, *Phys. Rev. C* **87** (2013) 035801.
- [37] P. Mohr, R. Longland and C. Iliadis, *Thermonuclear reaction rate of $^{18}\text{Ne}(\alpha,p)^{21}\text{Na}$ from Monte Carlo calculations*, *Phys. Rev. C* **90** (2014) 065806.
- [38] T. Rauscher and F.-K. Thielemann, *Astrophysical Reaction Rates From Statistical Model Calculations*, *At. Data Nucl. Data Tables* **75** (2000) 1.
- [39] Private communication, P. Adsley.
- [40] <http://www.talys.eu/download-talys/>, TALYS website, Accessed 19 August 2019.
- [41] W. Hauser and H. Feshbach, *The inelastic scattering of neutrons*, *Phys. Rev.* **87** (1952) 366.
- [42] A. Koning *et al.*, *TALYS v1.8 User Manual*, Unpublished (2015).
- [43] J. Stewart, *Calculus Metric Version, 8th Edition* (CENGAGE, Boston, USA, 2001).
- [44] Guide to the K600 Magnetic Spectrometer, daq.tlabs.ac.za/facilities/k600/the-k600-manual, Accessed 20 January 2016.

- [45] K. Floettmann, *Some basic features of the beam emittance*, Phys. Rev. ST Accel. Beams **6** (2003) 034202.
- [46] K.C.W. Li, M.Sc. thesis, University of Stellenbosch, 2015.
- [47] H. Fujita *et al.*, *Realization of matching conditions for high-resolution spectrometers*, Nucl. Instrum. Methods A **484** (2002) 17-26.
- [48] P. Adsley *et al.*, *CAKE: The Coincidence Array for K600 Experiments*, J. Inst. **12** (2017) T02004.
- [49] W. Shockley, *Currents to conductors induced by a moving point charge*, J. Appl. Phys. **9** (1938) 635.
- [50] S. Ramo, *Currents induced by electron motion*, Proc. I.R.E. (1939) 584.
- [51] K600-ALBA simulation package, <https://github.com/KevinCWLi/K600-ALBA>, Accessed 18 June 2018.
- [52] GEANT4 simulation package, <https://geant4.web.cern.ch/support/download>, Accessed 18 June 2018.
- [53] <https://midas.triumf.ca/MidasWiki>, TRIUMF MIDAS wiki, Accessed 25 January 2016.
- [54] <https://root.cern.ch/content/release-53434>, ROOT CERN website, Accessed 24 January 2016.
- [55] <https://github.com/padsley/k600analyser>, K600 Analyser github repository, Accessed 26 January 2016.
- [56] J. Manfredi *et al.*, *On determining dead layer and detector thicknesses for a position-sensitive silicon detector*, Nucl. Instrum. Methods A **888** (2018) 177.
- [57] Private communication, V. Pesudo.
- [58] L.G. Sobotka *et al.*, *Proton decay of excited states in ^{12}N and ^{13}O and the astrophysical $^{11}\text{C}(p,\gamma)^{12}\text{N}$ reaction rate*, Phys. Rev. C **87** (2013) 054329.
- [59] J. Henderson *et al.*, *Localizing the Shape Transition in Neutron-Deficient Selenium*, Phys. Rev. Lett. **121** (2018) 082502.
- [60] TMinuit class reference, <https://root.cern.ch/doc/master/classTMinuit.html>, Accessed 20 July 2019.
- [61] W.P. Alford *et al.*, *Structure of ^{22}Mg , ^{26}Si , ^{34}Ar and ^{38}Ca via the $(^3\text{He}, n)$ reaction*, Nucl. Phys. A **457** (1986) 317-336.

- [62] J.M. Munson *et al.*, *Decay branching ratios of excited ^{24}Mg* , Phys. Rev. C **95** (2017) 015805.
- [63] MESA simulation package, https://billwolf.space/projects/leiden_2019/, Accessed 20 September 2019.
- [64] <http://www.kadonis.org/pprocess/gamow.php>, Karlsruhe Astrophysical Database of Nucleosynthesis in Stars website, Accessed 21 October 2019.
- [65] Y. Tanikawa and S. Watanabe, *Chirality of Tensors and Parity-Nonconserving Interactions*, Nucl. Phys. **8** (1958) 484.
- [66] Z. Meisel *et al.*, *Influence of nuclear reaction rate uncertainties on neutron star properties extracted from X-ray burst model-observation comparisons*, Astrophys. J. **872** (2019) 1.
- [67] I. Fushiki and D. Lamb, *S-Matrix Calculation of the Triple-Alpha Reaction*, Astrophys. J. **317** (1987) 368-388.
- [68] W.P. Tan *et al.*, *Measurement of the decay branching ratios of the α -unbound states in ^{19}Ne and the $^{15}\text{O}(\alpha, \gamma)^{19}\text{Ne}$ reaction rate*, Phys. Rev. C **79** (2009) 055805.
- [69] CADMesh simulation package, <https://github.com/christopherpoole/CADMesh>, Accessed 18 June 2018.
- [70] Private communication, K.C.W. Li.
- [71] R. Longland *et al.*, *Reaction rates for the $^{39}\text{K}(p, \gamma)^{40}\text{Ca}$ reaction*, Phys. Rev. C **98** (2018) 025802.
- [72] ROOT MathMore special functions, https://root.cern.ch/doc/v608/group__MathMore.html, Accessed 31 October 2019.